Title
The Application of Advanced X-ray Characterization and Modeling Approaches to Understand Behavior of Earth Materials

Author
Chandler, Brian Chase

Publication Date
2021

Peer reviewed|Thesis/dissertation

The Application of Advanced X-ray Characterization and Modeling Approaches to Understand Behavior of Earth Materials

By

Brian Chase Chandler

A dissertation submitted in the partial satisfaction of the

requirements for the degree of

Doctor of Philosophy

in

Earth and Planetary Science

in the

Graduate Division

of the

University of California, Berkeley

Committee in charge:

Professor Hans-Rudolf Wenk, Chair
Professor Raymond Jeanloz
Professor Andrew Minor

Spring 2021

The Application of Advanced X-ray Characterization and Modeling Approaches to Understand Behavior of Earth Materials

Abstract

The Application of Advanced X-ray Characterization and Modeling Approaches to Understand Behavior of Earth Materials

by

Brian Chase Chandler

Doctor of Philosophy in Earth and Planetary Science

University of California, Berkeley

Professor Hans-Rudolf Wenk, Chair

Research into the mechanical properties of materials has been a focus of study for over a century leading to sophisticated advances in our understanding of not only materials of everyday use, but also minerals within the Earth and of other planetary bodies. The conditions within the Earth range over several thousands of Kelvins (K) in temperature and several million times atmospheric pressure (stated in gigapascals (GPa)). Adding to these extreme conditions, minerals under these conditions are also undergoing continuous microstructural evolution through processes such as phase transformation, plastic deformation, and dynamic recrystallization for which no satisfactory constrains have been achieved. Several experiments have focused on determining the various properties of minerals under lower mantle conditions using diamond anvil cells combined with synchrotron radiation. While enlightening, these have been relegated to either bulk statistical approaches or individual crystal studies, both limited in the achievable spatial resolution which is a crucial aspect when trying to scale from the microstructural level to large scale physical behavior. From a computational perspective, the processes in the Earth have also been a key area of interest with several modeling attempts attempting to constrain the active deformation mechanisms in minerals that would give rise to current observations of seismic anisotropy. Many models have proven insightful, but again focused on select regions and again lacked the spatial resolution to resolve the long-wavelength anisotropic structures of the lower mantle. This thesis aims to provide a route, both experimentally and computationally, to expand the current understanding of the behavior of lower mantle minerals on scales spanning from individual grain behavior to that of a polyphase aggregate. Quantitative information of the stress environment, phase distribution, as well as crystallographic orientations and microstructural relations are obtained across a range of mantle conditions using *in-situ* high energy synchrotron radiation combined with far field high energy diffraction microscopy, a.k.a. multigrain crystallography (*MGC*). Plasticity modeling is also performed under conditions of the lower most mantle to ascertain the active deformation mechanisms at play that could give rise to the long wavelength anisotropic structure observed near the core mantle boundary (CMB).

In Chapter 2, *MGC* is applied to a sample of San Carlos olivine beginning at ambient conditions and through the olivine $\rightarrow$ γ-ringwoodite phase transition. At high pressure and ambient

temperatures, by measuring the evolution of individual Bragg reflection morphology, olivine shows profuse angular intensity broadening consistent with the onset of yielding at a measured stress of ~1.5 GPa, considerably lower than previously reported under similar conditions, which may have implications for constitutive models of lithospheric strength and dynamics. Furthermore, γ - ringwoodite phase was found to nucleate as μm (micrometer) to sub- μm grains imbedded with small amounts of a secondary phase at 15 GPa and 1000 °C. Using *MGC*, information of individual crystallites from a secondary unknown phase were extracted and refined where it was found to have a structure consistent with the phase recently named Poirierite formed from shock metamorphism and has been described in chondritic meteorites (Tomioka *et al.* 2021) but yet to be seen during high *P-T* experiments.

Chapter 3 continues deeper into the Earth's mantle applying *MGC* to investigate the microstructural evolution during the formation of bridgmanite ($(Mg,Fe)SiO_3$) and ferropericlase ((Mg,Fe)O) from olivine. A weaker ferropericlase forms with random orientations as a fine-grained (< μm - 2 μm) interconnected matrix around a larger (2-9μm) and higher stressed *bridgmanite* phase; a configuration that has been implicated in slab stagnation as well as plume deflection in the upper part of the lower mantle through influences on the local viscosity structure surrounding subducting slabs. Pairs of individual twins in the bridgmanite phase are extracted with μm-scale spatial resolution confirming a previously reported {110} twinning relation previously only seen in *ex-situ* experiments which appears to act as a more energetically favorable mechanism of stress relaxation during grain growth compared to plastic deformation. When combined with the random orientations of ferropericlase, this twining mechanism in bridgmanite would act to reduce any seismic anisotropy from the aggregate.

Chapter 4 implements plasticity modeling to investigate the possible link between plastic deformation and phase transitions with the presence of seismic anisotropy at the base of the Earth's lower mantle. To date there has yet to be consensus on the specific mechanisms that could give rise to the observed shear-wave anisotropic signatures at depths of 2500-2800 km. Strong anisotropy in magnesium post-perovskite (pPv) has been invoked, but different studies disagree on the dominant slip systems at play. In the model presented in this thesis, the most recent results from atomistic calculation and high-pressure deformation experiments are coupled with a realistic pyrolytic composition composed of 74% bridgmanite 17% and 9% calcium perovskite and a 3-dimensional geodynamic model, to compare the resulting deformation-induced anisotropy with seismic observations of the lowermost mantle. Additional complexities are included accounting for the *P-T* dependent forward and reverse phase transitions from bridgmanite to pPv. When including this feature, a strong textural inheritance is found between bridgmanite and pPv with (001) dominant slip, not seen when bridgmanite converts to pPv with (010) dominant slip. It is also seen that either dominant (001) or (010) slip can both explain the seismically observed anisotropy in colder regions where downwellings turn to horizontal flow, but only a model with dominant (001) slip matches seismic observations at the root of hotter large-scale upwellings.

Contents

1. Introduction **1**

1.2 **Introduction and Background** **2**

1.2.1 Upper mantle: crust + lithosphere + aesthenosphere

1.2.2 Transition zone

1.2.3 Lower mantle

1.2.4 The D'' region

1.2.5 Trying to bring it all together

2. Exploring the Room Temperature Strength of Olivine and the Microstructural Evolution across the Olivine to Ringwoodite Phase Transition

2.1 **Introduction and Background** **8**

2.2 **Methods** **14**

2.2.1 Formalisms, experimental methods, and considerations in MGC

2.2.2 Running HEXRD and preparing the input files

2.2.3 2D CeO_2 powder calibration

2.2.4 3D single crystal indexing, fitting, and calibration

2.3 **Calibration Results** **33**

2.3.1 Single crystal results

2.4 **Multigrain Crystallography Applied in a Diamond Anvil Cell** **39**

2.4.1 Sample preparation and experimental considerations

2.4.2 Ambient olivine results

2.4.3 High pressure and low temperature strength of olivine

2.4.4 Olivine → γ ringwoodite phase transition

2.4.5 ε-Mg_2SiO_4 and γ-ringwoodite topotaxial relationships

2.5 **Conclusions** **52**

3. Investigating the Olivine – Bridgmanite + Ferropericlase Phase Transition using Multigrain Crystallography

3.1 Introduction **53**

3.2 Methods **54**

3.2.1 Sample preparation

3.2.2 Olivine to bridgmanite + ferropericlase at high P-T

3.3 Results **59**

3.3.1 Ambient olivine results

3.3.2 Distinguishing between phases

3.3.3 Spatial distribution of bridgmanite and ferropericlase

3.3.4 Monitoring mineral microstructures at in-situ pressure conditions
3.4 Discussion **70**
3.4.1 High pressure distribution of bridgmanite + ferropericlase
3.4.2 Estimating grainsizes under mantle conditions
3.4.3 Twinning in bridgmanite and stress relaxation
3.4.4 Comparing detector capabilities and resolutions
3.5 Conclusions **76**

4. Forward Modeling the Effects of Crystal Preferred Orientation and Phase Transitions on Seismic Anisotropy in the Lowermost Mantle
4.1 Background and Introduction **77**
4.2 Methods **80**
4.2.1 3D geodynamic model
4.2.2 Plastic deformation within the slab
4.2.3 Estimating elastic properties
4.2.4 Addition of partial melting at the CMB
4.3 **Results** **89**
4.3.1 CPO evolution within the slab
4.3.2 Shear wave anisotropy
4.4 **Discussion** **98**
4.4.1 Distribution of Pv and pPv in the lowermost mantle
4.4.2 Effects of phase-transitions and partial melting on shear wave anisotropy.
4.4.3 Model limitations and assumptions
4.5 **Conclusions and Future Works** **108**
5. Concluding Remarks **109**

Appendix 1: *MGC* using the *HEXRD* Software Package **124**
Appendix 2: Auxiliary scripts for *MGC* using *HEXRD* **133**

Acknowledgments

First and foremost, I would like to thank my wife for her love, patience, and support; for being honest and strong through this journey as without her I would not have had the strength or focus needed to undertake this challenge nor complete it. My daughter Valentina for her patience and understanding of long hours, which happened often and also for her scientific curiosity. My son Aurelius, while he may not realize his contribution now, it is something he will one day come to know. Hans Rudolf Wenk for being a great advisor without whom this venture would not have been possible. His unrelenting patience which complemented my unrelenting stubbornness led to us achieving many firsts in our field and paving new ways for those to come after us. He has helped me to grow not only as a researcher but also as a person. Martin Kunz for his mentorship while a doctoral fellow at Lawrence Berkeley National Lab (LBNL) where the majority of this work was conducted and for providing numerous constructive conversations and keeping my ideas pointed in a reasonable direction, and for becoming a great friend. Andy Doran of beamline 12.2.2 for the great conversations on the beamline and always intriguing questions about what I was doing which generally led to new ideas and implementations and for comradery in general. Joel Bernier of Lawrence Livermore National Lab (LLNL) for the insight into using multigrain crystallography (*MGC*) and his software *HEXRD*, as well as allowing me to collaborate to utilize this method in new domains. Raymond Jeanloz for allowing me to partake in his group as well as his candor with respect to experiments and results interpretation; this was a general skepticism that led to me consistently questioning my results and becoming not only a better scientist, but also a better thinker. Hans Aichlmayr of LLNL for his endless patience in teaching the basis of hydrodynamic modeling while a graduate student researcher with LLNL, as well as Rob Cavallo and Vlad Georgevich for providing me with the opportunity at LLNL (which encompassed much meaningful work which is not included in this thesis). My mother and father who were always proud and let me know it. Finally, I would like to thank the Navy SEAL foundation who assisted my family at various times throughout this program and also the Naval Special Warfare (NSW) community in which I grew into the person that I am today. Specifically, Steve Lashinsky, a brother forged in fires burning around the world who to this day motivates me and of whom I am endlessly proud. To all those brothers who have made the ultimate sacrifice so that I have had the opportunity to submit this thesis and with whom I share this feeling of accomplishment. Long live the brotherhood. My research was generously supported by research grants from NSF (EAR 1343908 and EAR 1464014) and DOE (DE-FG02-05ER15637). My education was supported by the U.S Department of Defense and U.S. Department of Veterans Affairs.

Chapter 1

1.1 Introduction

To zero order the Earth can be thought of as several concentric shells of varying thickness i.e., crust, mantle, core (Fig. 1 background), each of these layers with its own physical properties shaped by the force of gravity beginning with the formation of the planetoid itself. Figure 1.1 will act as a map for the following thesis by showing the region of the planet that each chapter will concentrate. The sections below provide the relevant high-level background of the current understanding of the physical properties of upper and lower mantle minerals as well as the some of the experimental approaches that have been used to try and understand their behavior under the conditions of these locations. To provide a stage, at a high-level view Figure 1.1 shows a slice cross section that extends from the Earth's surface to the center of the inner core. The various layers (right sided labels) each housing their own mineral compositions (left sided labels).

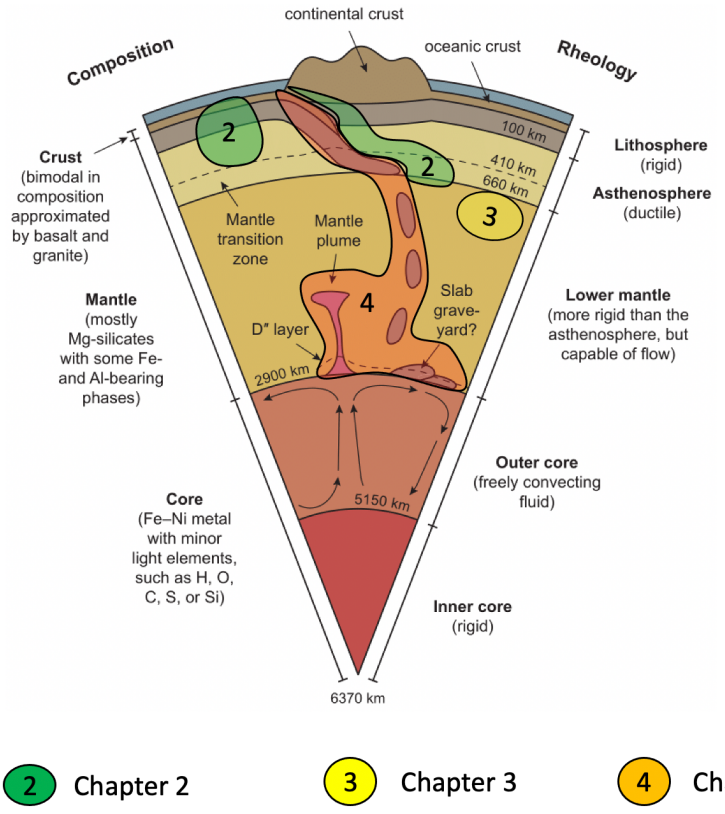

Figure 1.1 Schematic cross section of the Earth's interior. *Left side labeling the major demarcations of the Earth with associated composition and the right a finer demarcation with associated bulk rheological properties. Bottom key shows which areas of the cross section are the focus of each chapter.*

Looking closer, it is easily seen that the Earth's interior is much more dynamic than at first glance; with many large-scale processes constantly reshaping the planet. For instance, old lithospheric material known as "slabs", shown in as descending structures in Figure 1.1, are recycled at subduction zones like that in central America where the ancient Farallon slab subducts underneath the Caribbean. Because minerals portray a range of elasticity, seismic waves can be used to probe these elastic properties through recording the variations in seismic wave speeds that pass through different parts of the Earth. For instance, the above mentioned "slabs" are colder more dense material and have a faster velocity structure compared to the surrounding mantle. The slab's unique velocity structure can be imaged using various seismological techniques such as seismic tomography (e.g., French and Romanowicz 2014) or shear wave splitting measurements (Garnero *et al.* 2004, Garnero & McNamara 2008, Lay 2008) allowing recreation of a rough picture of the shape and location of the Farallon slab. Seismology provides a picture as well as insight into the elastic environment but does not answer the question of how this phenomenon specifically arises. During slab subduction the materials inside and outside of the down going structure are exposed to a wide range of physical (e.g., large variations in pressure (P), temperature (T), stress, and strain) as well as chemical (diffusion and atom partitioning) influences leading to various microscopic processes such plastic deformation, dynamic recrystallization, and with increasing pressure and temperature, phase transformations. This thesis will focus mainly on these physical influences but certain implications of chemical aspects such as composition and diffusion will be discussed since these two categories are not neatly separable.

Minerals themselves are also elastically anisotropic, meaning that the atoms are more tightly bound along certain directions and therefore they give rise to these measurable velocity differences based on the wave's propagation direction. When an acoustic wave passes through a material, in this context a seismic wave, the exit wave can also take various polarizations (e.g., horizontally polarized or vertically polarized) both with its own independent speed, called seismic anisotropy. Seismic anisotropy has been documented in various locations of the Earth, mostly concentrated near areas anticipated to have high strain environments such as subducting slabs and along the core mantle boundary CMB (see Romanowicz and Wenk 2017 for a review). While there are many phenomena that influence observed seismic anisotropy e.g., large chemical or density heterogeneities, variations in local grain sizes, layering of minerals with different anisotropy and shape preferred orientation, there are two influences that have garnered a lot of curiosity and will be a continuous theme in this thesis. (1) crystal preferred orientation (CPO) also called "texture", and (2) the effects of phase transitions on the local microstructural environment. While several studies have been successful at providing strong evidence that most of the observed seismic anisotropy in the Earth's mantle can be linked to texturing of local mineral aggregates (Romanowicz and Wenk 2017) by way of high P-T deformation experiments using diamond anvil cells (DAC) combined with plasticity modeling (Wenk *et al.* 2006, Cottaar *et al.* 2014, Miyagi and Wenk 2017, Wu *et al.* 2017), very few experiments have provided the resolution to observe the more salient phenomena such as recrystallization, twinning, and phase distribution *in-situ*.

1.2. Background

1.2.1 Upper mantle: crust + lithosphere + aesthenosphere

The outer most layer is made up of the crust + lithosphere which behaves in a brittle nature and is composed of a diverse group of silicon and oxygen-based materials with a structure based on a silicon atom surrounded by four oxygens known as a tetrahedral coordination. This region comprises the upper landscape of the planet and is subject to the accompanying forces that drive its evolution such as technique plate collision and subduction.

The upper mantle is composed primarily of the mineral olivine with the composition (Mg_x,$Fe_{1-x}SiO_4$) (Verma 1960). It is an elastically anisotropic mineral whose structure (e.g., Zha *et al.* 1998), rheological (e.g., Li *et al.* 2004, Mussi et al. 2014, Hansen *et al.* 2019) and elastic properties (e.g., Abramsom *et al.* 1997) have been studied extensively in both low (e.g., Proietti *et al.* 2016) and high pressure and temperature conditions (e.g., Meade & Jeanloz 1990). Even though olivine has been extensively studied across a wide range of pressures and temperatures its properties at lithospheric conditions (**Region 2** in Fig. 1.1) are still controversial. Understanding the rheology and strength of olivine is a crucial parameter as it is the main constituent of the upper mantle (~60% e.g., Haggerty 1995) as well as subducting slabs and therefore controls their rheology. Intermediate-focus earthquakes (at ~ 370 km) have been attributed to shear instability in olivine (Stein & Rubie 1994, Raterron *et al.* 2004) at these relatively low temperature and high-pressure regimes associated with the lithosphere. Olivine is also expected to be one of the weakest phases in the upper mantle which also includes pyroxenes, garnet, and spinel which means that its low temperature plasticity controls aspects such as the longevity of plate boundaries as well as lithospheric flexure beneath volcanic islands and the intense seismic signature seen down to 250 km depth.

Today, the deformation properties of olivin*e* are seemingly well understood and have been the compiled from various samples in a variety of conditions (see Idrissi *et al.* 2016 and Kumamoto *et al.* 2017 for reviews). While the slip systems and directions are generally agreed on with several fabric types tabulated (e.g., Karato & Weidner 2008) which explain upper mantle seismic anisotropy well and have also allowed predictions in upper mantle flow (Blackman 2002, 2007), the low temperature yield strength of olivine under lithospheric conditions (up to ~6 GPa) on the other hand remains controversial. For instance, original studies performed by Evans & Goetze (1979) predicted a very high differential yield stress of ~ 5.4 GPa at 27° C using hardness indentation tests on olivine single crystals, which lead to a flow law for olivine at temperatures < 800°C while experiments performed at room temperature and 3-7 GPa using a diamond anvil cell and powdered samples found yield stresses of only 2-3 GPa at room temperature (Meade and Jeanloz 1990, Raterron *et al.* 2004, Proietti *et al.* 2016). While this parameter has been the aim of several investigations under various conditions, it has been revisited recently (Kumamoto *et al.* 2017, Idrissi *et al.* 2016) due to the wide fluctuation in the experimentally determined values. Also, the strength of olivine has been found to be extremely sensitive to temperature (Katayama and Karato 2001) as well as water content where it has been shown that it can undergo hydrolytic weakening and shear instability (e.g., Blacic 1972, Girard *et al.* 2013). Furthermore, Jung and Karato 2001 found that the recrystallization grain size in hydrous olivine (with 800 ppm H_2O) was up to three times larger than olivine in dry conditions and having very different rheological properties.

Just below the lithosphere asthenosphere boundary is demarcated by an exchange of the brittle nature of the outermost shell with a more plastic, ductile, behavior on geologic timescales of 100's of millions of years (giga -annum or G.a.). Here, olivine rich aggregates accommodate the convection driven deformation cycle leading to crystal preferred orientation (CPO) of olivine whose seismic signatures coupled with deformation experiments have

1.2.2 Transition zone

Again, looking with finer detail, the field of thermodynamics dictates that with increasing temperatures and pressures, certain structures are no longer energetically favorable and the typical coordination of atoms within a silicate mineral begin to shift from the tetrahedral setting explained above found in the uppermost mantle into an octahedral coordination (one silicon surrounded by six oxygen). This is the case in one of the most explored structural transitions in the Earth: the $(Mg,Fe)_2SiO_4$ pathway that proceeds as olivine ↔ β-wadsleyite ↔ γ-ringwoodite ↔ ($(Mg,Fe)SiO_3$) bridgmanite + (Mg,Fe)O ferropericlase (Ringwood 1975). Each new structure along this pathway is denser and can have very different material properties, plastic as well as elastic, compared to its predecessor. This series of phase transitions is of great geophysical interest in that the olivine ↔ β-wadsleyite ↔ γ-ringwoodite transition spans from 410 – 660 km depth and has been implicated in the two large discontinuities in seismic wave speeds at these two transitions (Helffrich 2000) due to the change in elastic properties across each transition. With each phase transformation there is evidence of an initial global grain size reduction as the new phase nucleates. This is especially the case in the transition to γ-ringwoodite where a volume reduction of 6-8% can occur (Raterron *et al*. 2002). Profuse seismic anisotropy has also been observed in the transition zone although it appears much weaker than in the upper mantle (Panning & Romanowicz 2006). Furthermore, subducting slabs have also been imaged penetrating the transition zone leading to discovering correlations between the vertical material flow and the signature of vertically polarized seismic waves leading their horizontal counterparts ($V_{SV}>V_{SH}$) (Panning and Romanowicz 2006) with increased signatures appear to be associated with areas of slab subduction where the outer edges of the slab contact the surrounding mantle as it subducts leading to plastic deformation and crystal preferred orientation (CPO) in the local minerals.

Experiments on the properties of minerals in this area becomes more complicated as the pressures approach 20 GPa and temperatures to ~1500 K. The advent of large pressure apparatuses and diamond anvil cells (DACs) combined with sophisticated heating systems (laser and resistive) (Miyagi *et al.* 2013, Meng *et al.* 2015, Kunze *et al.* 2018) have provided a route to obtain quantitative but limited information in this area but we still understand little, however, regarding the inter-granular microstructure and spatial distribution of these phases as well as their evolution under the thermomechanical conditions of the lower mantle by means of plastic deformation, phase transitions and recrystallization.

1.2.3 Lower mantle

At further depths (~ 660 -750 km) the dissociative reaction that takes γ-ringwoodite to bridgmanite+ ferropericlase has been linked to the stagnation of subducting slabs as well as the seismic discontinuity at these depths. Global tomography in this area shows a 1D radial shear wave anisotropic signature of V_{SH} faster than V_{SV} (French & Romanowicz 2014) with increased signatures in and around areas of subducting slabs such as that seen near the Tonga subduction zone (Wookey & Kendell 2004). Below the 1000 km depth mark, the mantle appears mostly void of any significant anisotropy outside of subduction zones (Meade et al. 1995, Montagert & Kennent 1996, French & Romanowicz 2014), this is not the case for the lowermost mantle near the core mantle boundary (CMB). Furthermore, little is known about the spatial distribution of the newly formed bridgmanite and ferropericlase, a combination that makes up the ~90% of the bulk

lower mantle. Seismic observations can only gather local average properties on the order of kilometers and are blind to the salient features on the scale of μm to mm which control the underlaying dynamics. High pressure experiments and modeling efforts have investigated how these two phases may behave under deformation (Girard *et al.* 2016, Kaercher *et al.* 2016, Kassemer *et al.* 2021) and arrive at the conclusion that the overall properties rely on the distribution of these two phases due to their strength contrasts. For instance, if the ferropericlase were to form an interconnected network (Yamazaki *et al.* 2014) around the stiffer bridgmanite, then ferropericlase would accommodate most of the strain. On the other hand, if ferropericlase forms as isolated pockets dispersed throughout a bridgmanite background, the resulting rheology would be much different and controlled by the bridgmanite phase. Although texturing is normally attributed to lattice rotation due to dislocation glide during yielding, it can also occur due to preferentially orientated grain growth during nucleation and recrystallization during/after phase transitions (Karato 2013) but the presence of this under *in-situ* conditions has yet to be determined.

1.2.4 The D'' region

The deepest 200-300 kilometers of the Earth's mantle (bottom of **region 4**) form a complex thermal and mechanical boundary layer, named D" by Bullen 1949), where the dynamics remain elusive due to the difficulty in performing relevant experiments under these conditions. Further complicating matters, at roughly 125-135 GPa another phase transition occurs taking the moderately anisotropic bridgmanite phase to the highly anisotropic post-perovskite phase. Our current understanding of dynamics in D" , like most of the Earth's interior, is guided by seismological observations which indicate the presence of significant laterally varying shear wave anisotropy in D'', in contrast to the bulk of the lower mantle which is largely isotropic D'' is riddled with various anisotropic signatures (see review by Romanowicz & Wenk 2017) . Most seismological studies of D" anisotropy rely on splitting measurements of shear waves diffracted (Sdiff) or reflected (ScS) on the CMB (Nowacki *et al.* 2011), as well as core phases SKS/SKKS (Long 2009; Nowacki *et al*. 2011). While such observations sample D" locally, limitations in available earthquake source and receiver locations restrict azimuthal coverage. Their interpretation thus relies on simplified models of anisotropy, mainly vertically transverse isotropy (VTI, also referred to as radial anisotropy), in which the speeds of horizontally and vertically polarized waves are different (V_{SH} and V_{SV} respectively). In general, $V_{SH} > V_{SV}$ is found in areas of faster than average isotropic shear wave velocity (V_{Siso}), as imaged by seismic tomography, and attributed to the 'graveyard' of cold slabs. In contrast, $V_{SH} < V_{SV}$ or no significant splitting is found in areas of slower than average V_{Siso} such as the large low shear velocity provinces (LLSVPs) beneath the central Pacific and Africa (e.g., Cottaar & Romanowicz 2013; Lynner & Long 2014). There have also been some attempts at resolving a tilted fast axis of anisotropy (TTI) (e.g., Garnero *et al*. 2004; Pisconti *et al*. 2019).

It is assumed that perhaps large strains during flow in the deep mantle could lead to crystal preferred orientation (CPO) of anisotropic minerals such as *post-perovskite* (pPv), which could explain the seismic anisotropy observations e.g., Cottaar *et al.,* 2014, McNamara *et al*. 2002, 2003; Wenk *et al*. 2011. Testing this hypothesis relies heavily on experimentation using powders and single crystals combined with laser heated diamond anvil cells (LH-DAC) in an attempt to

elucidate the active deformation mechanisms (Wu *et al.* 2017, Miyagi & Wenk 2016, Miyagi *et al.* 2010, Merkel *et al.* 2007) which can then be forward modeled, and the resulting anisotropy calculated (Wenk *et al.* 2011, Cottaar *et al.* 2014, Tommasi *et al.* 2017). Investigations of the forward and reverse (Pv-pPv and pPv-Pv) phase transitions in the pPv analog $NaNiF_3$ has provided evidence that a strong (001) textural inheritance across these boundaries is possible if the dominant slip system in the pPv phase is also (001) which has strong implications on the strength of texture as well as anisotropy in this region.

1.2.5 Trying to bring it all together

Defining a link between the domains described above is the premise of this writing. How do we link the microscopic dynamics of mechanical properties at the grain scale which occur on the order of micrometers or smaller, to the macroscopic observables we have at our disposal? In reality, this is a simultaneous bottom-up top-down approach as the two fields of mineral physics and seismology are intimately coupled in this way, but here I will start from the bottom and work upwards and will show that there is "plenty of room in the middle*" that will require some new approaches with integrated aspects of material science, mineral physics, geodynamics, and seismology combined to investigate. This theis will show that there are currently, and remain, plenty of interesting unanswered questions, which this thesis intends to address only a few and perhaps motivate a reader to tackle some others, or re-tackle those presented here in a more clever manner.

Chapter 2 and 3 investigate mineral behavior on the micrometer (μm) scale of individual grains. Using the penetrating power of high energy synchrotron radiation combined with diamond anvil cells (DAC) and state-of-the-art laser heating technology, the mechanical properties of the most abundant minerals in the Earth's mantle, orthorhombic $(Mg,Fe)_2SiO_4$ olivine, $(Mg,Fe)_2SiO_4$ *ringwoodite*, $(Fe,Mg)SiO_3$ *bridgmanite*, and cubic (Fe,Mg)O *ferropericlase* are studied. By bringing a starting sample of San Carlos Olivine $(Mg_xFe_{1-x})_2SiO_4$ to pressures and temperatures ranging from the lithosphere to that of the upper portion of the lower mantle. Olivine*'s* high-pressure strength is investigated in Chapter 2 as well as its high-pressure phase transitions culminating in Chapte3 with the dissociative reaction into *bridgmanite* and *ferropericlase*, a reaction which is expected to occur near a depth of 660 km. The multigrain crystallography technique (*MGC*) is employed to elucidate the microstructural evolution under pressure as well as nucleation behavior and orientation relations across phase transitions *in-situ* at varying pressures after with grain scale resolution. *MGC* combines the capabilities of the standard single crystal diffraction and powder diffraction techniques and has only recently been applied to low symmetry minerals at high *P-T* conditions. Moreover, *MCG* provides the ability to probe location, orientation, and strain for several hundred individual crystallites while still providing the needed statistics for bulk sample characteristics. As this technique is yet to become mainstream, it is not without limitations as the experimental considerations and post-processing of data proves challenging, yet it remains a powerful tool for many interesting material systems. That being stated, Chapter 2 will also act to guide future experimenters using this technique by exploring the experimental considerations with respect to sample preparation, software use and data analysis, as well as experimental equipment (detectors, calibrations, software use).

Chapter 4 intends to bring the picture full circle by presenting a three-dimensional forward model of mineral plastic deformation to describe the observed anisotropic features of the Earth's lowermost mantle. A spherical 3D geodynamic model provides deformation paths within a

subducting slab impinging on the core mantle boundary. The model includes downwelling of the slab, followed by horizontal flow along the CMB, and eventually upwelling flow at the simulated edge of a large low shear velocity province (LLSVP). By using a starting aggregate composition of 72% bridgmanite/post perovskite, 19% MgO, and 9% $CaSiO_3$, 1000 grains are plastically deformed along several hundred deformation paths representing the subducting slab. Forward and reverse bridgmanite/post-perovskite phase transitions anticipated to occur in the lowermost mantle are introduced at thermodynamically determined locations leading to a topographical image of anisotropy for the D'' layer. Furthermore, by varying active deformation mechanisms in each phase, as well as orientation relations across phase transitions, which combinations of systems that can give rise to the observed signatures of seismic anisotropy are probed for the different regions of interest.

Chapter 2

Exploring the Room Temperature Strength of Olivine and the Microstructural Evolution across the Olivine to Ringwoodite Phase Transition.

2.1 Background and Introduction

The physical properties of a material are controlled by its structure, e.g., it's 3-dimensional crystalline lattice which exists on the scales of angstroms ($\AA$). Conversely, observable macroscopic properties generally occur over a range of scales from μm to *mm* to *km*. Translating any information about a material between these domains, the mesoscopic to macroscopic scale, to obtain information about material properties within the Earth's interior first requires subjecting the material to the relevant pressure (P) and temperature (T) conditions. The advent of the diamond anvil cell (DAC) (Fig. 2.1) has provided a direct path for any laboratory to reach pressures from 1 – 200 GPa (see Soignard *et al.* 2004 for a review). Over recent years the DAC has become the most versatile device for reaching high pressures during experiment. By placing a sample of miniscule size (typically 20-100 μm between the culet surface of two opposing diamond anvils (Fig. 2.1 a) a small amount of force can generate a tremendous amount of pressure transmitted to the sample with minimal force (eq. 2.1). For instance, the area of the standard 200 μm diamond culet used in these types of experiments is on the order of $7\text{x}10^{-8}$ m^2 and is easily capable of reaching pressures of 5 – 20 GPa (Fig. 2.2 b). For a review of the history of DAC the reader is directed to Basset 2009.

$$P = \frac{F}{A} \qquad (2.1)$$

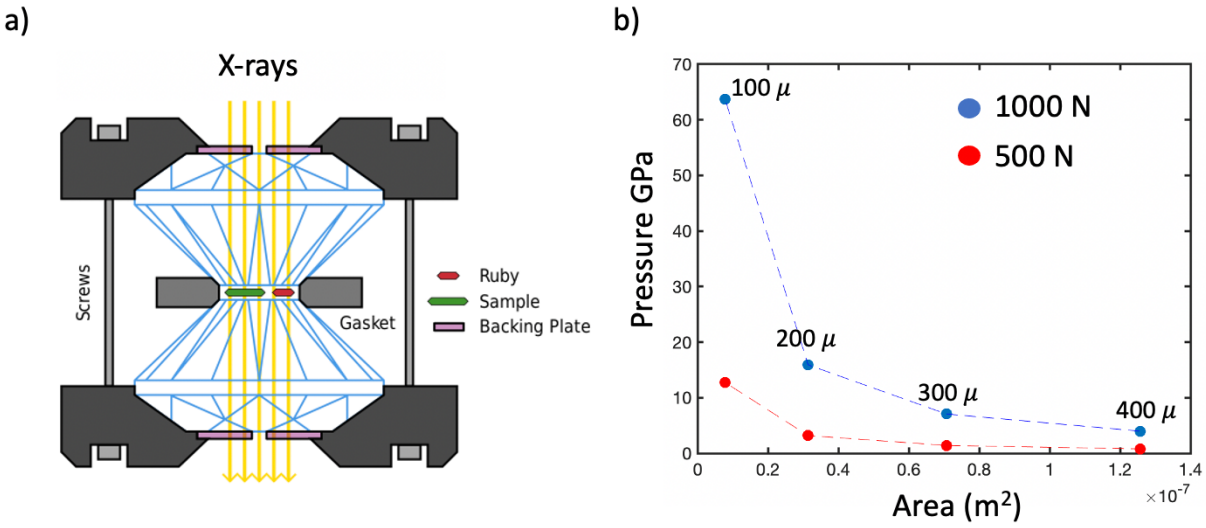

Fig 2.1. Diamond anvil cell. *(a) cross section of typical diamond anvil cell in the co-axial geometry (b)Ideal pressure (GPa) obtainable for a constant force of 500 (red) and 1000 (blue) Newtons on diamond culets ranging from 100 – 400 μm calculated from eq. 2.1.*

Additionally, the combination of a DAC with sophisticated infrared (IR) laser heating, laser-heated DAC (LH-DAC), as well as resistive heating (RH-DAC) apparatuses allows for simultaneous *in-situ* high *P-T* experimentation. Combining these approaches with the penetrating power of highly energetic synchrotron X-rays (typically in the range of 5-100 keV) provides an excellent non-destructive route to probe material microstructures under a range of conditions. Experiments using DACs to study the crystalline structure of materials rely on non-destructive X-ray diffraction approaches which can be separated based on the wavelengths used: the monochromatic (single wavelength) X-ray powder diffraction and single crystal diffraction and Laue X-ray diffraction which utilizes a polychromatic beam. There are several destructive techniques such as focused ion beam (FIB), transmission electron microscopy (TEM) each of which very power techniques but are currently not equipped for *in-situ* high pressure experimentation which is the topic here. Each of the X-ray methods mentioned above rely on crystallites being subjected to irradiation providing diffraction intensities as a function of the scattering angle (or wavelength) with respect to the incident beam (2θ) through Bragg's law (2.1). Laue diffraction which has also recently been successfully applied under *in-situ* pressure conditions, but this writing will focus on monochromatic radiation.

$$n\lambda = 2d_{hkl} \sin\theta \qquad (2.2)$$

Powder diffraction exists in the statistical realm relying on a sample of many *nm* – μm sized crystallites. Due to the numerous scattering centers in a powder sample nearly all possible crystal orientations can be sampled resulting in a cone of diffracted X-rays (Debye-Scherrer cone) from any specific d_{hkl} ; or in terms of reciprocal space many overlapping reciprocal lattices that gives a "sphere" of reciprocal lattice points satisfying Bragg's condition (eq. 2.2). By placing an instrument capable of detecting the reflected X-ray intensity in the cone path, smooth circles, or Debye Scherrer rings, can be recorded on a 2D detector face (Fig. 2.2a). These smooth rings represent the spread of orientations of systematically spaced lattice planes (*hkl*) within the crystalline structure. This 2D technique has been rigorously used to explore properties of materials in many settings in Earth and material science to include applications under a range of physical conditions allowing for phase identification, average crystallite size, determination of lattice parameters, and also insight into the active deformation mechanisms through the analysis of crystal preferred orientation (CPO) (e.g., Merkel *et al*. 2002, Wenk *et al.* 2010, Lutterotti *et al.* 2014, Miyagi & Wenk 2016, Wu *et al.* 2017). The powder method lacks however the resolution needed to levy information about individual grains, analysis of individual Bragg reflection morphology, and is also blind to any spatial distribution of phases or properties that arise from inhomogeneities in grain size or phase distribution. These information are key components when trying to understand how a polycrystalline aggregate, say comprised of two phases of varying strength, behaves on a local scale or how the physical distribution of grains of each phase might influence bulk properties.

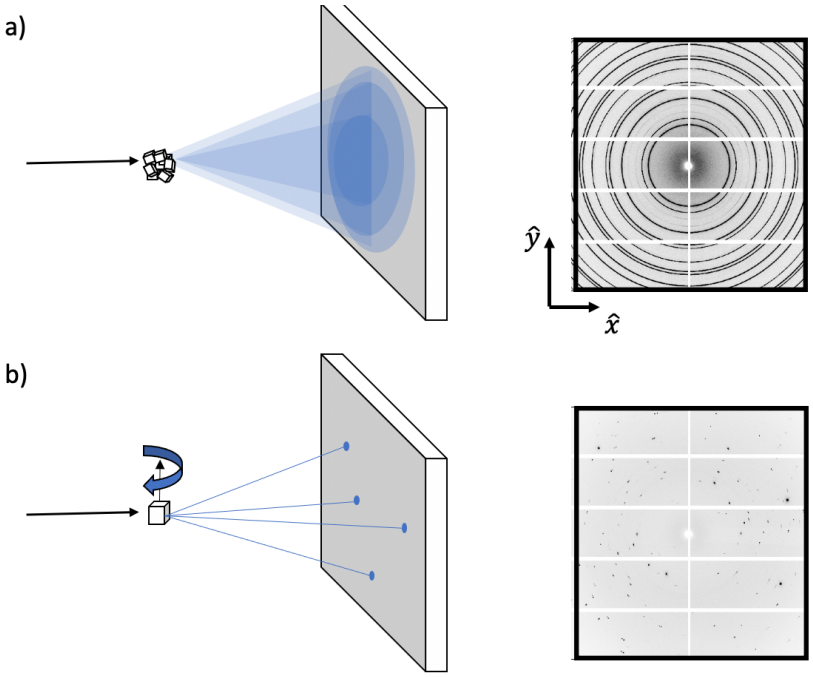

Fig 2.2 Comparison of the powder method and the single crystal method. *(a) shows resulting Debye-Scherrer cones emanating from powder diffraction and resulting complete rings on a 2D detector face. (b) single (rotating) crystal method and resulting individual Bragg reflections on a 12-independent panel 2D detector face where individual reflections lie on Debye rings.*

Single crystal diffraction, or more generally the "rotating crystal method" is a three-dimensional (3D) approach which utilizes a single individual crystallite subjected to irradiation while being rotated around a fixed axis (Fig. 2.2b) providing individual Bragg reflections as each lattice plane enters the reflection condition. This method provides excellent resolution allowing for the refinement of the crystal symmetry as well as the 6-crystal lattice parameters (three axes, and three corresponding angles between axis) (Horiuchi *et al.* 1981,1987). Single crystal diffraction also has the advantage of being able to determine the atomic position, electron density, and bond angles, and furthermore allows for the lattice parameters of an unknown material to be determined which has been used to identify and categorize new materials (e.g., Barkov *et al.* 2019) as well as study minerals within the Earth (e.g., Sasaki *et al.* 1982). While single crystal diffraction gathers surpasses the coverage of powder diffraction by moving to 3-dimensions, it lacks the capability to isolate more than a few grains/crystals and also is rendered unusable under dynamic conditions such as plastic deformation or phase transformations. In these situations, standard diffraction vector assignment to reciprocal lattice vectors G_{hkl} (a.k.a. "indexing") algorithms become overwhelmed leading to errors in crystal identification and G_{hkl} assignment. Unfortunately, since the evolution of the Earth is determined by the evolution of its constituent minerals at relevant conditions, it is again in these regimes where key information is held for understanding the Earth is locked. Furthermore, an over-arching limitation is that these two techniques are disjoint and cannot be combined in any meaningful way to leverage the information gained by both on a given sample.

Although standard diffraction methods have paved the way for our understanding of materials, they both are limited in their application during dynamic events as well as the information they can recover. For instance, the powder method relies on a finely ground crystalline

sample and while this may be applicable for materials processing where components are fabricated from powders, it may not be directly applicable to the Earth's mantle where grain sizes can vary greatly, creating a heterogenous distribution of mechanical properties. In the case of the most abundant upper mantle mineral olivine, it has been shown that grain size plays a significant role in the strength properties it exhibits (Idrissi et al 2016, Kumamoto *et al.* 2017). In those investigations, olivin*e* with grain sizes similar to that of powders (*nm*) is up to 7 times stronger than olivine grains on the order of μm to *mm* which are sizes expected throughout the upper mantle.

In reality, the more interesting dynamics of materials exist outside the grasp of both of these techniques: e.g., high *P-T* induced reactions such as phase transitions, grain nucleation and recrystallization, local stress/strain environment, and the 3-dimensional (3D) distribution of individual grains in an aggregate sample. Therefore, there is a need for a technique to bridge the gap between powders and single crystals.

Multigrain crystallography (*MGC*) (Sørensen *et al.* 2012) (a.k.a. 3DXRD, or far field High Energy Diffraction Microscopy ff-HEDM) is a 3D characterization approach that acts as a middle ground between the two above mentioned X-ray techniques. It is not a new technique in itself; but a more sophisticated analysis approach coupled with a modified experimental setup that allows both unique grain and statistical information to be extracted from a single diffraction experiment. In essence it proceeds by allowing an aggregate sample of several crystallites of varying phases to be treated as several coexisting single crystals which are analyzed individually but also by exclusion. When used in conjunction with LH-DACs and high energy synchrotron X-rays (Fig. 2.3), *MGC* provides a route to probe dynamics with grain-scale resolution even under *in-situ* extreme *P-T* conditions while still capturing information on the statistical level.

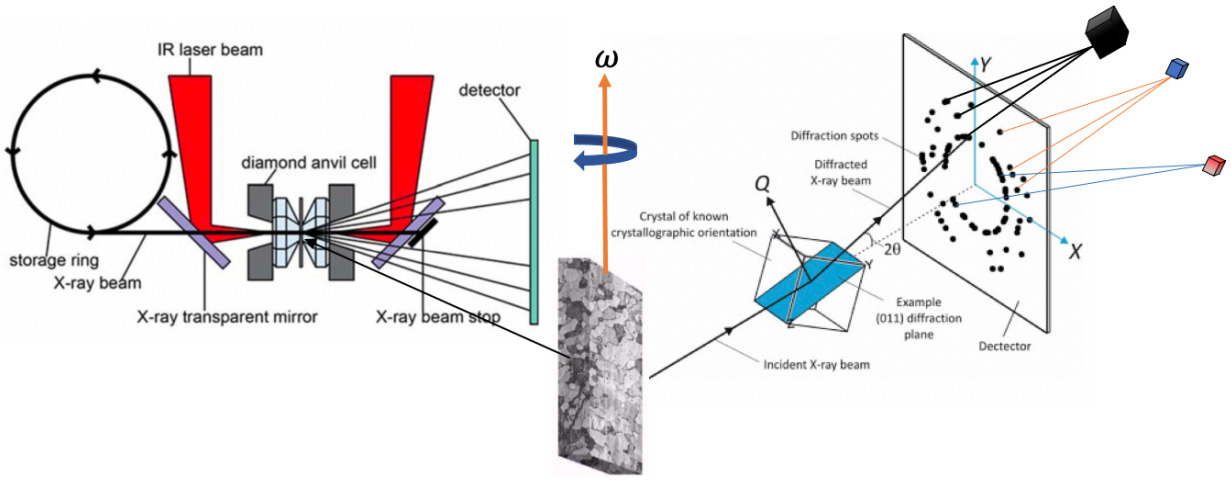

Fig 2.3 Multigrain analysis using synchrotron radiation in a DAC. *From left to right shows a pictorial overview of the experimental setup used in multigrain analysis. Starting with the circulating electron storage ring which is constantly emitting synchrotron radiation. This radiation is then shaped through a series of mirrors and apertures and directed to user end-stations where it is focused on a sample (housed in a DAC shown here). Many facilities also provide infrared laser heating capabilities (shown here) but also resistive heating equipment (not shown). The X-rays penetrating the aggregate sample housed in a diamond anvil cell leads to diffraction vectors emanating from several different grains (depicted here as black, blue, and red cubes) who's signals can then be collected by a 2D area detector.*

Originally, *MGC* was applied to a limited range of scenarios originating with the structural refinement of small number of grains in a sample consisting of pure Al_2O_3 (Schmidt *et al.* 2003), but has recently been expanded to observe microstructural evolution across phase transformations of geologic materials at modest pressures and temperatures in a diamond anvil cell (DAC) (Rosa *et al.* 2014, 2015) as well as lattice parameter refinement at high *P-T* conditions (Zhang *et al.* 2014, Zhang *et al.* 2016). *MGC* has also been successfully applied in conjunction with structural modeling approaches such as finite element methods (FEM) to find the ideal single crystal elastic moduli for materials (Boyce *et al.* 2020). For a review on the history and inception of *MGC*, the reader is directed to Paulson 2004 Sørensen *et al.* 2012, and Zhang *et al.* 2019. In this writing, the far-field variant of *MGC* is employed the by way of the *HEXRD* software package (Bernier *et al.* 2011, 2020) which was created in collaboration between Lawrence Livermore National Laboratory (LLNL) and the Advanced Photon Source (APS) of Argonne National Laboratory (ANL). Here, *HEXRD* is combined with custom scanning procedures and post processing software built by the author for the purpose of this research.

Below an introduction to the experimental considerations used when performing *MGC* analysis via *HEXRD* is given, which is followed by exploring its capabilities in two investigations. The first, a NIST standard single crystal ruby sphere (SRM 1990) as well as a single crystal quartz sample are analyzed in ambient conditions using three different detectors. These two samples are generally used to perform the 3-dimensional detector calibration due to their crystalline parameters being very well constrained, but they also serve as a baseline to show the ability of this technique in ideal conditions as well as an instructional example of the required workflow and general considerations that apply to any sample as well as provide a baseline comparison between detector platforms.

Second, addressing some of the outstanding questions in Earth science mentioned above, the microstructural evolution of a *San Carlos* olivine ($(Mg_x,Fe_{x-y})SiO_4$) sample is subjected to synchrotron radiation in an LH-DAC in an attempt to provide constraints on olivine*'s* high *P* and low *T* strength which is fundamental to understanding the evolution of the Earth's upper mantle; especially the lithosphere where olivine contains information about the stress storage capacity of local rocks (Proietti *et al.* 2016). In many portions of the lithosphere the low *T* strength of olivine influences large scale processes such as lithospheric flexure near the load of volcanoes (Zhong & Watts 2013), formation of plate boundaries (Theilman & Kauss 2012), as well as lithospheric bending at subduction zones (Buffet & Becker 2012). Large scale modeling of these types of processes involves the use of low *T* constitutive equations which are calibrated and validated through deformation experimentation where the strength of olivine is a crucial parameter. Current estimates of the manageable stress by olivine varies largely at over a half order of magnitude (Hansen *et al.* 2019) which when applied to rheological flow laws gives several orders of magnitude spread in strain rates for the Earth's lithosphere. These large variations in the measured strength of olivine facilitate a need for revisiting this parameter with a new approach.

Also, in this example, *MGC* will be used for new phase identification in a laser-heated diamond anvil cell (LH-DAC) providing evidence for the presence of ε-Mg_2SiO_4, also known as the *epsilon* phase, a high-pressure form of Mg_2SiO_4 previously only observed in recovered meteorite samples (Tomioka *et al.* 2017, 2019, 2021) but is anticipated to act as a mediator between olivine and the high pressure spineloid ringwoodite through shear mechanisms under low temperature and high-pressure conditions.

The purpose of this chapter and the next is not only to address a few outstanding questions in the Earth science community, but also to discuss the experimental aspects, considerations, and limitations to be taken into account by future users of *MGC* which has the potential to become a powerful technique for the study of minerals under high *P-T* conditions. This chapter will act as an introductory level tutorial for the use of *MGC* applied in a DAC laying much of the base understanding of the analysis process and Chapter 3 will act as a continuation applied to a more complex system at higher pressures and temperatures. It should be recognized that the functionality of *HEXRD* spans beyond the functions and capabilities used here and this is by no means an all-inclusive tutorial. It is recommended to download the software and play with it building from what is described here.

While an opening overview of the methodology and formalisms used by the *HEXRD* software is in order and is presented in the following section, a further in-depth description of the mathematical underpinning of the algorithms can be found at https://github.com/joelvbernier and also in Bernier *et al.* 2011. Throughout this chapter, references will be made to Appendix 1 and Appendix 2. These appendices and this chapter proceed in tandem. The chapter itself provides the experimental description, a step-by-step overview of the analysis using *HEXRD* and results with several references to Appendix 1, which provides further elaboration on key steps to allow the chapters main focus to remain on the experiment and results. Appendix 1 also contains descriptions of the input files used by the *HEXRD* software for these examples. Appendix 2 includes the custom scripts written for post processing and data visualization in all of these examples which makes use of the free MATLAB add on MTEX and each script will also be referenced in each image produced and are freely open for the readers use and modification.

2.2 Methods

2.2.1 Formalisms, experimental methods, and considerations in MGC

Essentially, for all intents and purposes, *MCG* is an expansion of a rotating single crystal method coupled with more sophisticated algorithms for doing the heavy lifting of crystal orientation determination and Bragg reflection intensity analysis. Fig 2.4 introduces the experimental geometry one must consider. Although the depiction in Fig 2.4 is entirely general, for this writing, experiments are performed in an axial transmission geometry meaning that the sample center, or the diamond axis in the DAC, and the detector center are along the same ray path. This configuration simplifies the geometry such that the P_0 and P_2 are coincident, therefore the rotational axis of the sample, or DAC, defined as $\mathbf{Y_l}$ with an angular variation $\Delta\omega$ must be aligned precisely on the beam path in the lab frame as shown in Fig. 2.5.

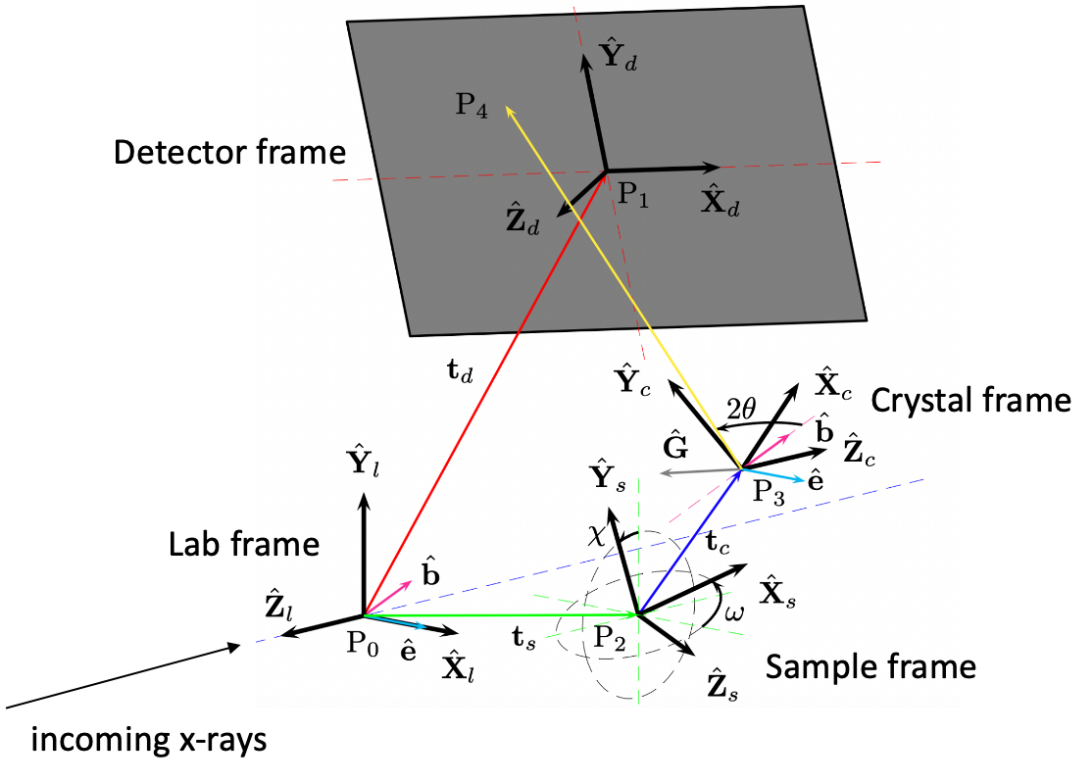

Fig 2.4 Experimental setup*. Pictorial description of associated reference frames used in multigrain analysis showing lab, sample, crystal, and detector coordinate systems.*

Diffraction images are taken through a discrete rotation of the sample ($\Delta\omega$) about $\mathbf{Y_l}$ in pre-determined steps sizes as well as predetermined exposure times. It was found in the following investigations that an angular step size of 0.25° and exposures ranging from 0.25 sec. to 1 sec. are ideal for the samples used here but this will vary based on several factors such as X-ray flux, detector sensitivity, and strength of diffraction from the sample and therefore has to be uniquely determined for each experiment. When scanning a sample in ambient conditions, i.e., single crystal or a sample not in housed in a DAC, the methodology remains the same as does the majority of the analysis procedure, but the number of experimental considerations decrease drastically. The

available scanning range of the sample becomes only limited by mechanical stage hardware, there is no structure to inhibit incoming X-rays (i.e., the DAC body), and generally the beam size can be adjusted such that the sample can be fully irradiated at all times as long as the X-ray brilliance, or "flux", remains high enough to obtain reflections from weaker reflecting reciprocal lattice vectors $\mathbf{G}_{\mathrm{hkl}}$ (in some cases depending on the X-ray source, beam spot size and flux vary inversely and must be accounted for). The resulting intensity from a particular $\mathbf{G}_{\mathrm{hkl}}$ is a function of its electron density through the complex structure factor $F(hkl)$ where incident X-rays scatter off the electron clouds in a vector direction *hkl.* The resulting intensity $I(hkl)$ is proportional to the amplitude of the structure factor $|F_{hkl}|$. This will become a very useful parameter when experiments conducted in a DAC with multiple phases explored in Chapter 3.

When using combining *MGC* and a DAC, the usable rotation range through which X-rays reach the detector is limited by the DAC body as well as the diamond seats, and furthermore the gasket material which also acts as a diffraction center if contacted by the incident X-rays (discussed further below). The gasket itself does not interfere for experiments conducted with X-ray transparent gasket material such as Boron-epoxy normally reserved for radial diffraction, but this approach is beyond the experiments described here but will be discussed in a later section. Maximizing the DAC rotational range that permits X-ray passage through the sample and to the detector in turn maximizes the amount of observed reciprocal space because rotating the sample is the equivalent of rotating the reciprocal lattice bringing more reciprocal lattice vectors into the diffraction condition. For what is shown herein, a BX-90 DAC (Kantor *et al.* 2012) was used for all experiments which has 90° opening angles along the axial direction (Fig. 2.4 b). cBn diamond seats were chosen due to their near complete X-ray transparency.

The sample chamber diameter to beam spot size ratio must also be considered. This arises because the wider the beam spot size, a smaller angular range will be available due to the edge of the beam causing diffraction from the gasket material at high angles of the rotational range. In ideal conditions the sample itself remains continuously irradiated by the incoming beam during rotation, but as alluded to previously there is a tradeoff between the amount of sample consistently irradiated and the rotational range. While it is possible to continuously irradiate a sample in a DAC for a given working range, it poses the hurdle that the gasket material is also irradiated which adds extraneous signal to the resultant image which can lead to errors in indexing reflections if:

1) The symmetry of the gasket material and the sample are similar leading to Bragg reflection overlap with the Debye rings produced by the gasket.
2) The gasket is strongly diffracting, and the intensity drowns out lower intensity reflections from the sample that lay at similar locations as the gasket reflections. This will be elaborated on in section 2.4 when experiments performed in a DAC are explored.

In many cases, a beam spot size is chosen which is significantly smaller than the sample chamber which also allows the maximum angular working range without irradiating the gasket. Fig. 2.5 shows a standard example of this effect where a 5 μm x 5μm beam is used with sample that has a face diameter of 50 μm and a thickness of 100 μm. Given that only a 60° working range is obtainable, only ~1.5 % of the sample volume is irradiated throughout the entire rotation with only a volume comparable to the chosen beam size constantly radiated during a scan.

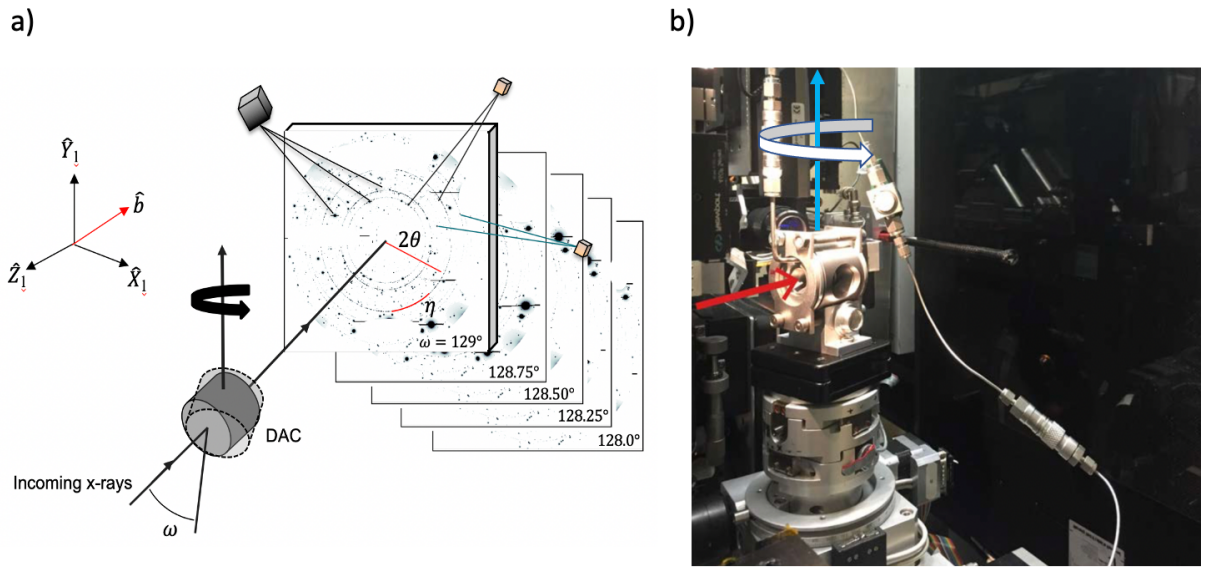

Fig. 2.5 Rotational diffraction images. *(a) Illustration of DAC in gray with incoming X-ray beam showing cell rotational axis and sample frame coordinate system. Also showing diffraction images taken in 0.25° steps (b) The BX-90 Desi DAC used mounted atop the rotational kinematic mount provided by beamline 12.2.2 of the Advanced Light Source.*

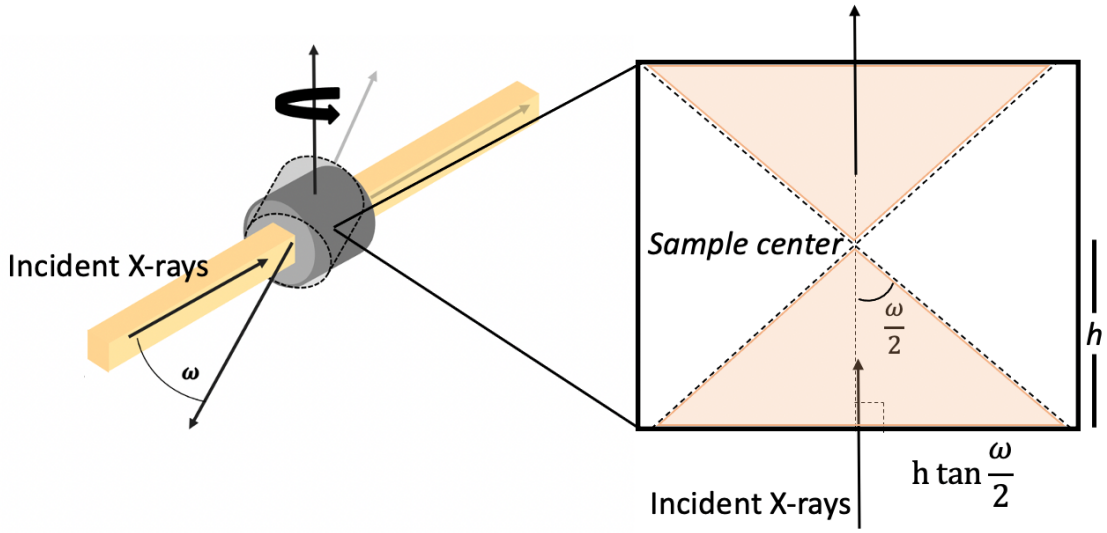

Fig. 2.6 Approximation of irradiated sample volume during MGC experiments. *Generalized approximation based on a square spot size, sample with thickness h, and cell rotation angle ω in the axial configuration. The sample radius r is not included because the working angle determines the portion of the sample diameter that is swept by the incident radiation during the DAC rotation. From here the volume of sample radiated can be determined. This can also be used to gain an upper bound on grain size under the assumption that the number of grains extracted fills the entire irradiated volume.*

As previously mentioned, while performing this technique in a DAC does not provide the ability of a full 360° scan, the working range can be increased by performing "symmetric scans", e.g., after the initial scan range is complete the cell is rotated 180° and a scan is performed over the same range from the opposite side. This introduces the ability to use Friedel pairs (e.g., diffraction vectors arising from equivalent reciprocal lattice vectors $\{hkl\} \rightarrow \mathbf{G}_{hkl}$ and $\{\overline{hkl}\} \rightarrow \mathbf{G}_{\overline{hkl}}$ which provides two observations of the same physical quantity greatly helping in constraining the grain orientation as well as position along that specific direction. For the BX-90 DAC with 90° conical openings, the two usable angular ranges were found to be [-30°-30°] and [150°-220°] where 0° defines straight transmission. An important note about this approach is that symmetric scans can only be performed when the rotation does not involve physically removing the DAC which is a mechanical limitation at the beamline set up. In the event laser heating for extended periods that requires a cooling jacket placed around the DAC to prevent cell distortion, or a pressure cannister is being used which requires external connections, symmetric scans can normally not be applied.

Other areas of consideration include the choice of diamonds as well as confining gasket material. Also, varying geometric configurations may be needed such as the radial configuration which is the common approach in texture analysis due to the orthogonality of the compression direction and the incident X-ray path. These aspects are experimentally dependent and will only be discussed in this writing.

2.2.2 Running HEXRD and preparing the input files.

Before getting started, a short description of the *HEXRD* software platform. *HEXRD* is a python based open-source package and the version of choice should be downloaded and installed from *https://github.com/HEXRD* by going to https://github.com/HEXRD/hexrdgui and following the download instructions for the desired operating system. There are two flavors of the software (1) a stand-alone GUI which is described below as well as (2) a command line-based interface (CLI). These two can be used in conjunction and typically are both downloaded into separate anaconda environments. Appendix 1 also discusses the major differences between the two which only lays in the outputs.

To maintain isolation of the *HEXRD* software and other applications it is best to create its own anaconda environment and install the package there, which is then activated whenever it is used. The installation provided from the link above also installs all the dependencies needed to run the software and therefore it is entirely self-contained. Furthermore, the scripts provided in this thesis require the use of *HEXRD* packages for the image processing and grain indexing procedures. Once downloaded and installed, the following **Command 1** will activate the *HEXRD* software environment and **Command 2** will activate the GUI interface which is used below.

Command 1: conda activate hexrd (or the name you have provided it)
Command 2: hexrdgui

Fig. 2.7 shows the initial user material screen which is the first screen upon initializing the software. The three main tabs: **materials**, **load data**, and **instrument calibration** are numbered. A set of base materials are inherent to the software (i.e., CeO_2, Ruby, diamond, Lab6, silicon and several more). New materials are also added here by creating the material name and inputting the unit cell symmetry and lattice parameters. Here the "***active material***" for an analysis can be

selected and added from the drop-down. Also, the maximum 2θ as well as the minimum lattice plane spacing (*d-spacing*) can be specified. The minimum *d-spacing* determines the number of *hkl*s made available. For these experiments the minimum was set to 0.7 *Å*, and then the maximum 2θ was set to 25° which will then act to limit the number of *hkl*s present between these two constraints.

Inside the **structure** and **properties** icons, atomic positions as well as material density and elastic properties (or compliance) can be manually input (*Appendix 1: Building material files*). Once the material has been input or selected, the **Materials Table** icon allows for selection of *hkl*s to use during analysis for the analysis while the **Materials Overlay** icon allows for selecting the material to overlay on future diffraction images as well as select the type of pattern (i.e., powder, Laue, rotational series) as shown in Fig. 2.8. Several other features are present here such as selecting *hkl*s based on d-spacing, 2θ location, multiplicity, as well as structure factor $|F^2|$. These features will be discussed as they are used in the upcoming examples. Before starting a new experiment, a working folder should be created that houses any images to be used as well as where output files will be directed. Once this folder has been created, the materials file can be saved to the experiment directory. The native materials file format is .HDF (*Appendix 1:Building material files*).

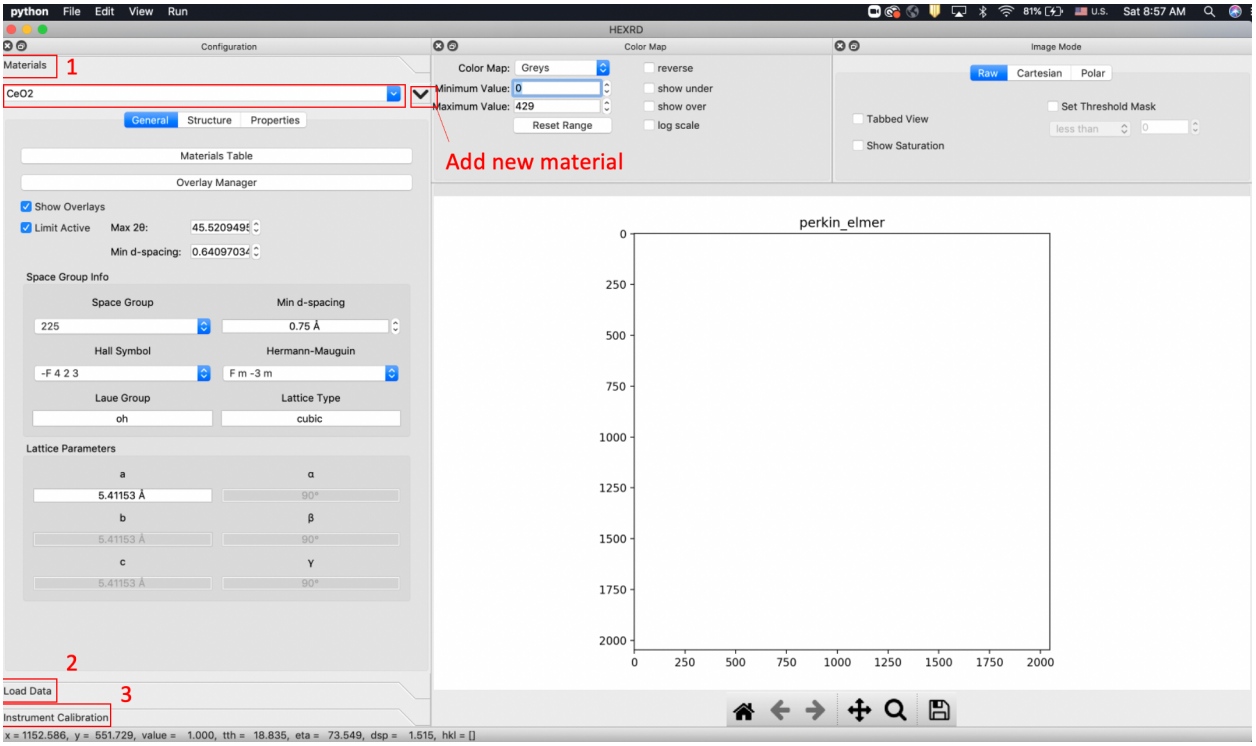

Fig. 2.7 HEXRD user screen. *The initial screen viewed during initial startup. Red boxes highlight sections requiring initial user inputs: (1) Materials input, (2) Diffraction image loading, and (3) Instrument Calibration.*

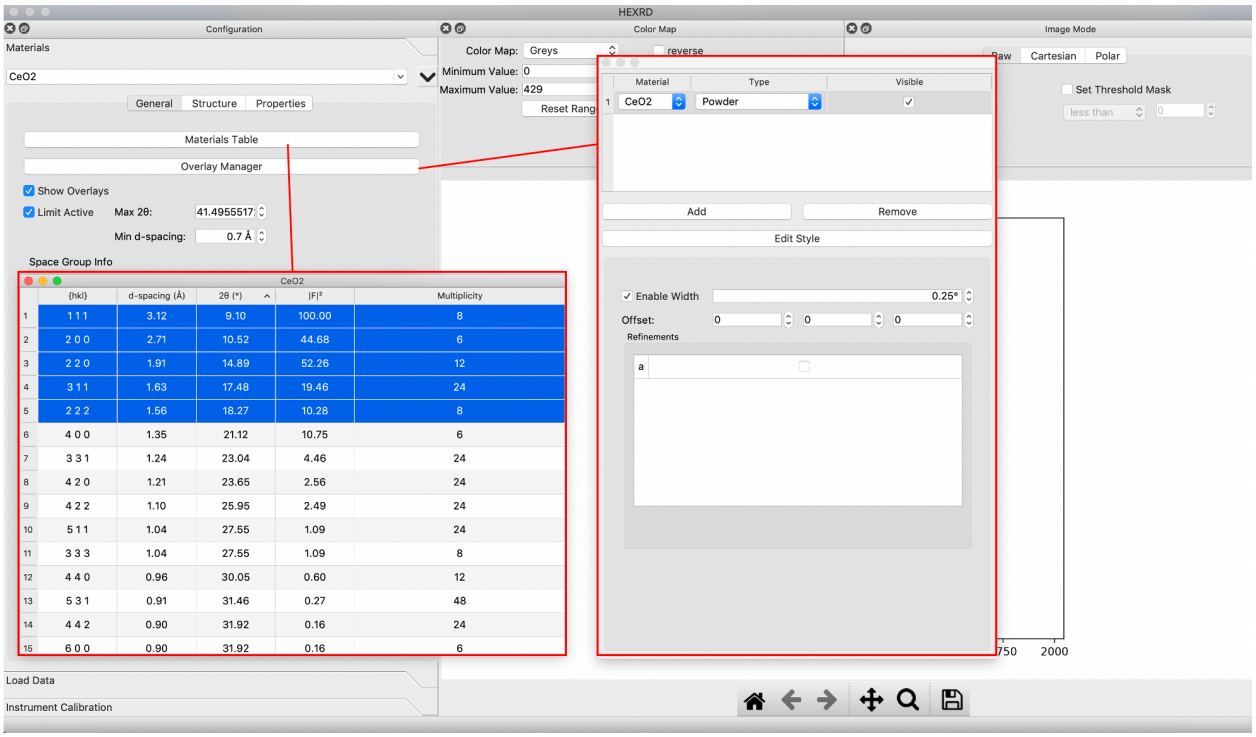

Fig. 2.8 HEXRD material input*. Initial steps of selecting hkl's to be used as well as the material overlay for diffraction patterns here showing the first 5 hkls ordered by decreasing structure factor for a CeO2 standard.*

2.2.3 2D CeO_2 powder calibration

As with standard diffraction techniques, an initial 2D powder detector calibration is generally performed when using *MGC* although not explicitly required with the *HEXRD* software when the single crystal will be used to perform the 3-dimensional calibration (such as the NIST ruby in this case). For completeness the experiments conducted using a monolithic detector (i.e., the Perkin Elmer and the marCCD) a NIST CeO_2 standard was used to obtain initial estimates of detector distance, detector tilt (non-orthogonality), and beam center coordinates using the standard non-linear least squares approach inside *HEXRD*. For experiments using the 10 independent panel Pilatus detector the initial 2D calibrations were performed using the Dioptas software package provided at beamline 12.2.2 and the initial detector parameters were then input into *HEXRD* and the 3D calibration was performed. This is because at the time of this writing the azimuthal integration algorithm to process the gaps between detectors had not been implemented into the software package.

To perform the 2D calibrations, initial detector parameters such as detector dimensions, number of pixels, pixel size (often called 'pitch'), saturation level, as well as the incident wavelength and a rough estimation of the detector distance (*mm*) should be known. The GUI offers three different ways to input the detector information under the **Instrument Calibration** tab (Fig. 2.8). The ***Form View*** of the **Instrument Calibration** tab is used to create a new detector quantity using the "+". Also, the incident X-ray energy is input here. The detector parameters are then manually input into the ***Tree View***. In the event there is another detector file from a previous experiment it can simply be loaded.

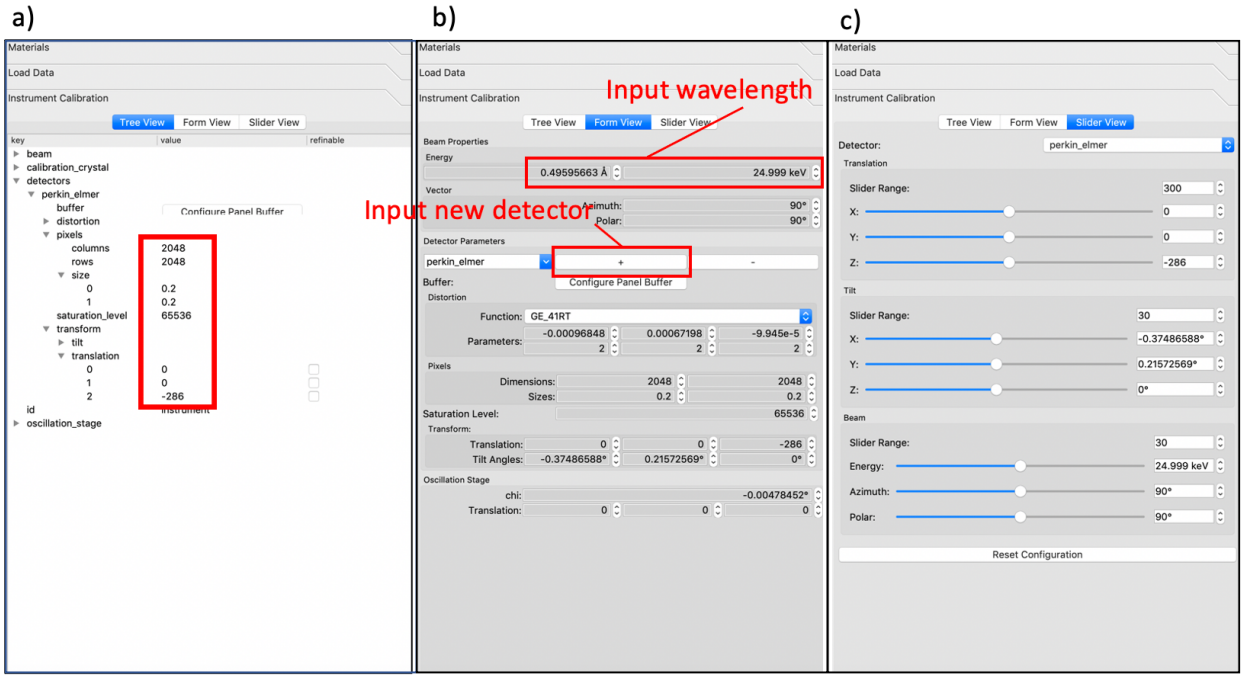

Fig. 2.9 Instrument calibration tab*. Shows the three versions of detector parameter input using the instrument calibration tab. Manual inputs of detector parameters using the (a)* ***Tree View****, Detector creation and wavelength energy input in the* ***Form View*** *(b), and manual adjustments in the* ***Slider View*** *(c).*

Once the detector has be input, the initial detector parameter file can be saved via **File > save > configuration > YAML** and providing the desired file name. This will save the "initial guess" calibration file to your experiment directory. Next, the image(s) can be loaded into the GUI using the **Load Data** tab. For powder images the *aggregation* setting should be set to **NONE**. A dark image can also be included here if available but is not required. To bring in the initial powder calibration image, the **Select Image Files** icon is used which opens a file search window. Once the desired image is found it can be loaded to the viewing screen by pressing **Read Files**. It must be insured that the intended detector is applied to the image(s) by checking the box Apply Selections to ***All Detectors***. Once the image(s) is loaded, the max and minimum values at each pixel can be chosen to increase or brighten the visibility of the Bragg reflections/Debye rings using the **Color Map** tab. In the **View** tab located along the top bar of the GUI, the **View> show live updates** option should be selected so that all modifications are updated in real-time. For each experiment described here a single image of CeO_2 powder was collected over a continuous 60 seconds a constant rotation of +/- 15° collected on a Pilatus 3M 1s detector which consists of 10 independent detector panels (i.e., non-monolithic) at a distance of 217 mm and 29.995 keV.

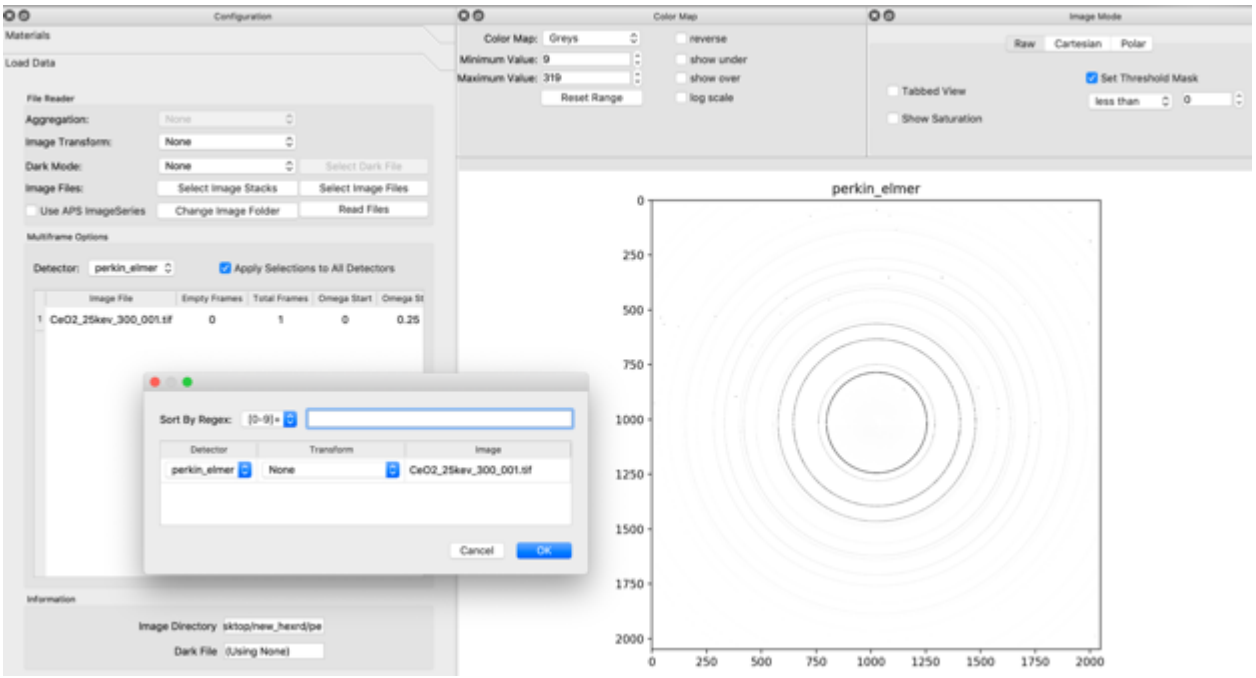

Fig. 2.10 Load Data tab*. Showing image loading procedure for a CeO_2 powder calibration image with powder diffraction image shown on the image viewing screen (right).*

By returning to the **Materials** tab and checking the **Show Overlays** box (Fig.2.7) and the preselected *hkl's* will appear in the image window at their theoretical locations based on the input parameters (Fig. 2.11a). Dashed lines also encompass the Debye Ring which act as angular thresholds during the calibration which can be increased or reduced using **Materials tab > Overlay Manager > check box *Enable Width***. The pattern can now be viewed in both the "*Raw*" detector view or sometimes it is more insightful to use the "*Polar*" integration view as the deviations in fitting is more apparent (Fig. 2.11 b). This view also provides the 1-D lineout integration of intensity vs 2θ.

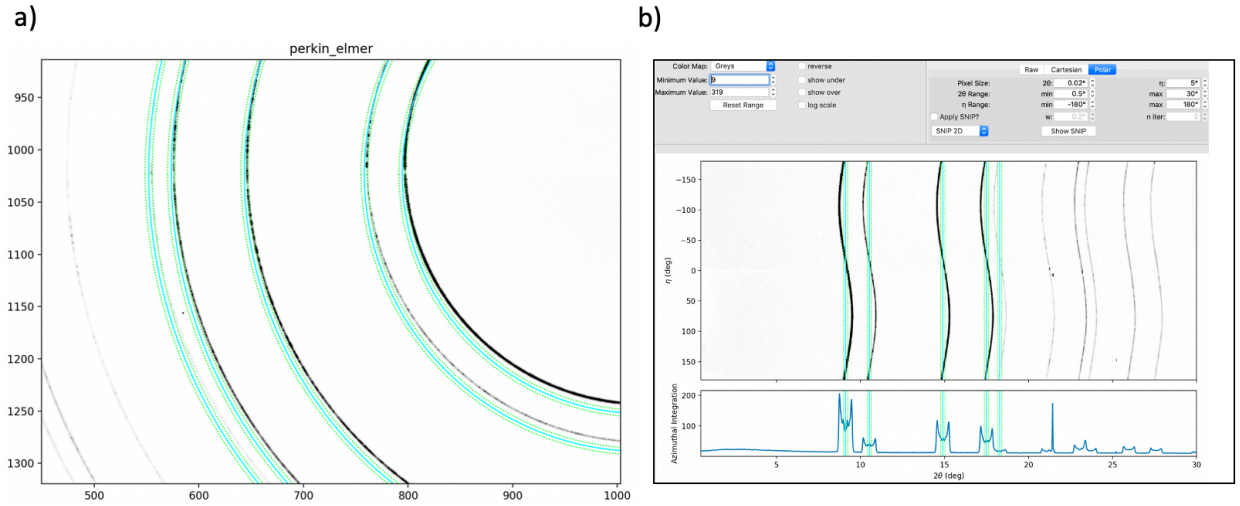

Fig. 2.11 Diffraction Image Viewing. *Image loading procedure for a CeO_2 powder calibration image in "Raw" view as well as "Polar" integration view showing a non-calibrated image. In (a) it is clear that the initial guess calibration parameters are slightly off in the x-y centering of the beam. The green theoretical rings are then manually aligned to the black measured intensities and the calibration is performed.*

Returning to the **Instrument Calibration** tab in ***Form View*** the ***refinable*** boxes can now be checked for the five detector parameters that can be refined using a powder pattern: detector translation 0-2 (where 0,1, 2 are the $\hat{x}$ and $\hat{y}$ beam center locations on the detector face and the -detector distance value in *mm*) and the first two tilt (0-1) (where 0-1 are rotations about X_D and Y_D). The third detector tilt is along the detectors own normal vector (Z_D) which cannot be fit with a powder pattern due to its axisymmetric nature but will be fit during the 3D single crystal calibration.

Next, in the **Instrument Calibration** *slider view* the Detector **Translation Slider Range**: can be used to manually align the theoretical ring overlay with the intensities from the measured powder rings. Using the **RUN** tab at the top of the GUI and selection **> Powder Calibration**, the calibration parameters 2θ and the azimuthal η binning step size can be selected as well as the number of iterations to perform and convergence limits. Fig 2.12 shows the resulting calibration after first performing an initial calibration using the eight five Debye, followed by the Debye rings out to a radial distance of 22° 2θ. In general, this is all that is needed for the 2D calibration because a follow-on 3D calibration and indexation is performed with a single crystal standard to further refine these parameters as well as the remaining tilt parameters. The fit can be iteratively performed with an increasing number of rings if needed to obtain a decent fit. The calibrated detector can now be saved by using the File tab via **File > Save > Configuration > YAML** and providing a file name *Appendix 1: CeO_2_instrument_calibration*.

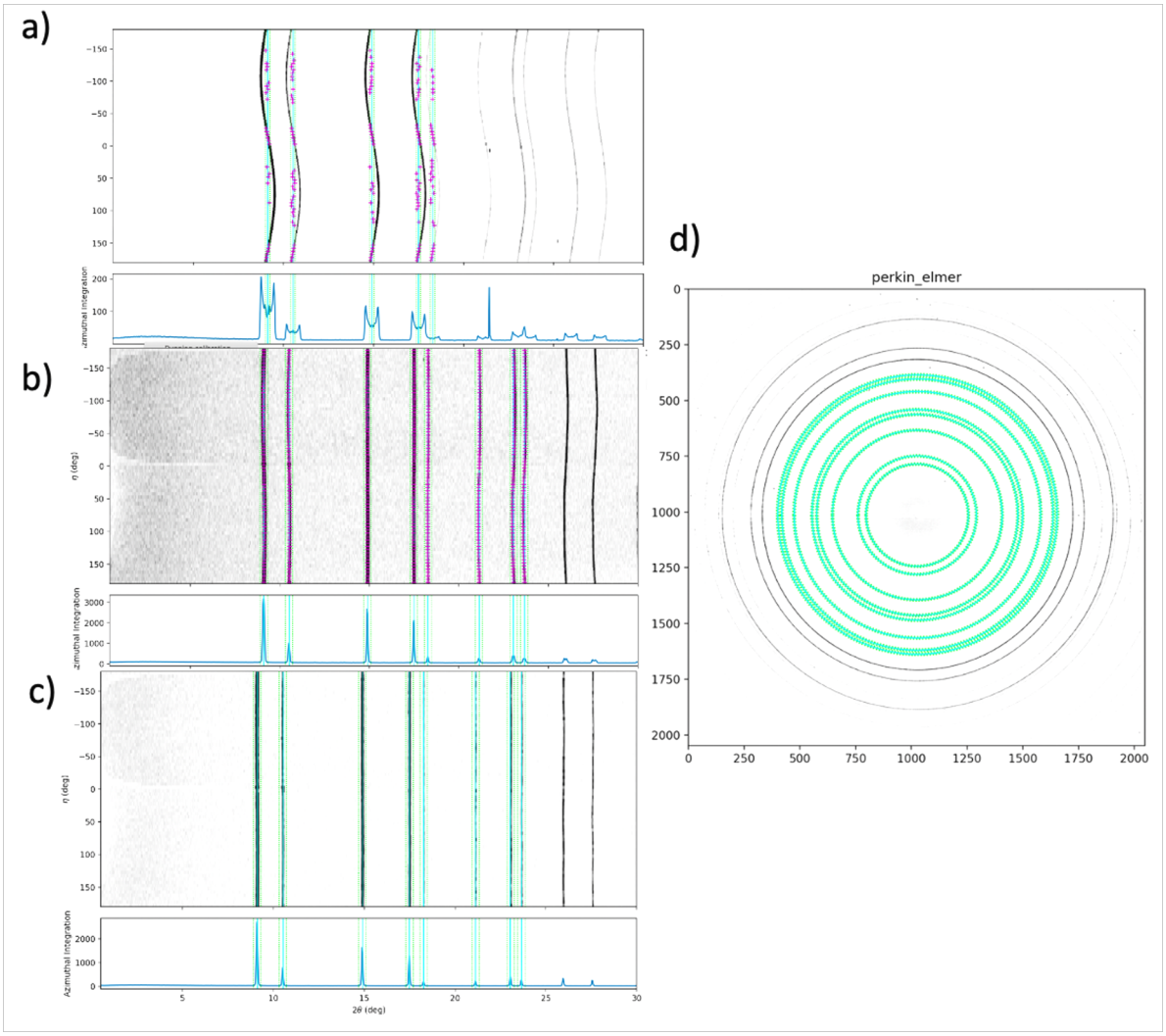

Fig. 2.12 2D calibration results. *Showing interpolation points defined during the 2D powder calibration process with iterative fitting for select hkls (green vertical lines) (a-b) resulting in the final fit (c), also shown as the raw image detector view in (d).*

2.2.4 3D single crystal indexing, grain fitting, and 3D calibration

For calibrating the detector angle of rotation about its own normal requires non-axisymmetric diffraction which is obtained using a single crystal, here a 100 μm National Institute of Standards and Technology (NIST) ruby sphere diffraction standard with precisely known lattice parameters lattice parameters a = 4.76080 Å (0.00029), c = 12.99568 Å (0.00086) as well as an SiO_2 single crystal was irradiated with 0.495937 Å (25 keV monochromatic synchrotron radiation supplied by beamline 12.2.2 of the Advanced Light Source of Lawrence Berkeley National Lab as well as beamline 16-IDB of the Advanced Photon Source. For the SiO_2 sample the specific lattice parameters were not know but as quartz has been intensely studied, those of (Gualtieri 2000) are used with a = 4.9158 Å, b = 4.9158 Å, and c = 5.4091 Å and refined after the initial analysis. In both situations each sample was rotated through 320° with 0.25 second exposures taken at each 0.25° angular step resulting in 1279 individual diffraction images (Fig. 2.13 a,b) collected by the chosen detector for each experiment. When using *HEXRD*, each recorded diffraction image taken

in the rotational scan is tagged with, and the intensity integrated over, the specific Δω step at which the image was taken to obtain an average intensity over that range. These images are then summed over the max intensities at each pixel which results in a composite diffraction pattern with each diffraction spot identified by two angular $(2\theta, \eta)$ coordinates on the detector face and one rotation coordinate in Δω (Fig. 2.13) yielding a 3D recreating of reciprocal space.

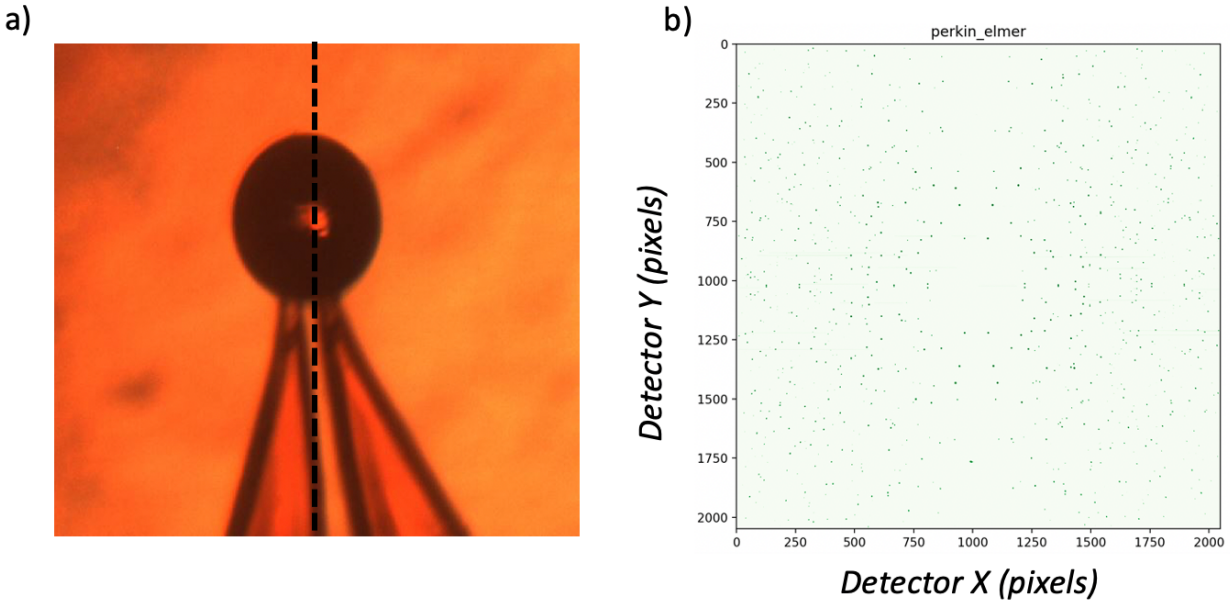

Fig. 2.13 Diffraction of NIST standard ruby sphere: *showing (a) 150 μm diameter sphere rotational axis (dashed line) aligned with beam axis (into the page) and (b) the resulting combined diffraction pattern of 1279 individual images with axes defined in pixels. Images take on a Perkin-Elmer area detector at an energy of 25 keV. (image created using Appendix 1: make_image_series.py)*

The folder containing the collected Ruby image series can be loaded into the GUI in a similar manner (See *Appendix 1:make_image_series.py*) as the initial CeO_2 image with the exception that the frame **Aggregation** should be set to **Maximum** which sums the intensities at each pixel throughout the entire scan range (Fig. 2.13 b). By changing the selected material in the **Material tab** as well as the **Overlay Manager** icon to the pre-stored Ruby material, similar to the CeO_2 select the first five $\boldsymbol{G_{hkl}}$**s** and each associated Debye ring is then overlayed onto the image (Fig. 2.14).

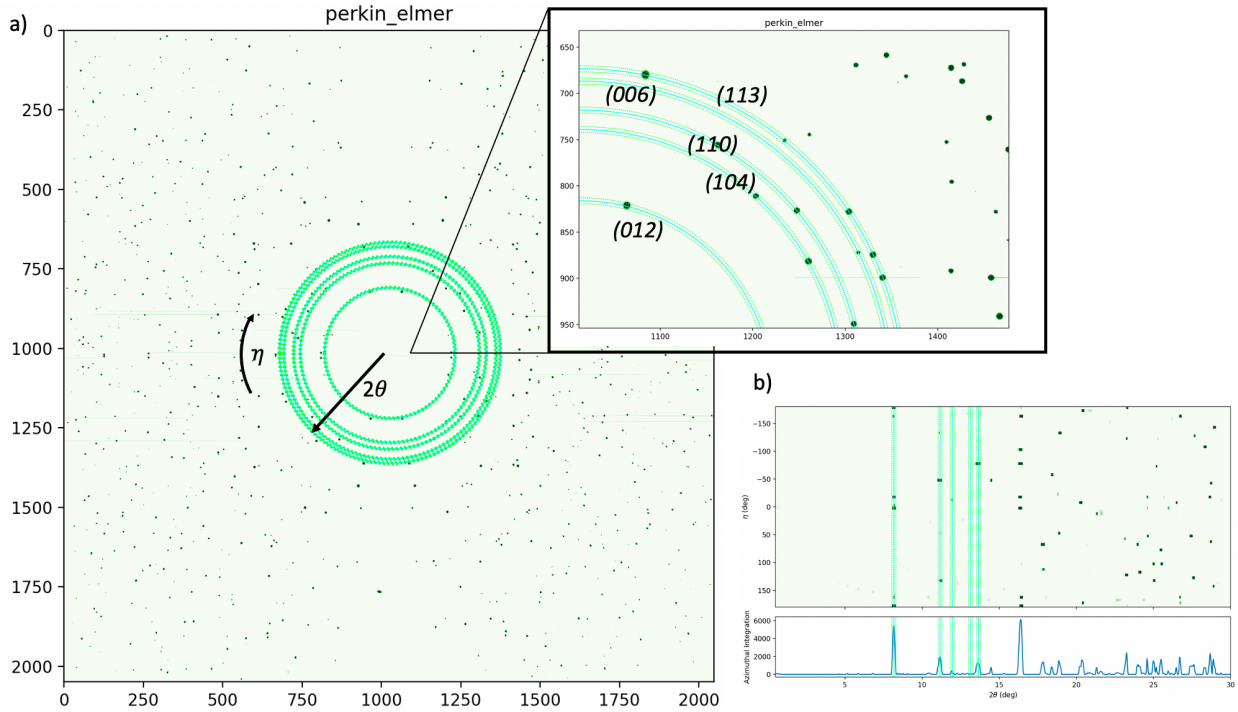

Fig. 2.14 Comparing observed diffraction vectors Q with predicted G_{hkl} for Ruby single crystal. *(a) observed diffraction vectors (Q) (reflections) as well as predicted 2θ locations of several $\boldsymbol{G_{hkl}}$ (green rings) based on reference lattice parameters, crystal symmetry, and initial 2-dimensional detector calibration. 2θ angular thresholds of 0.35° are shown as thing green dashed lines while the theoretical predicted location is solid green line. (b) "unrolled" polar integration view of the ruby single crystal.*

At this point, given that the space group is known, the lattice parameters are roughly known, and using the initial 2-dimensional detector calibration parameters, all theoretically possible $\mathbf{G}_{\mathrm{hkl}}$ locations in 2θ can be predicted and compared to the observed reflections collected from the sample (diffraction vectors **Q**). As a general guide, a typical single crystal analysis pipeline using this version of *MGC* proceeds as follows:

1) The rotational diffraction image series $(\omega_{start}{:}\,\omega_{end})$ is combined into a single aggregate diffraction image taking the max pixel intensities from each frame. Each intensity is tagged with its respective coordinates $(2\theta,\eta,\omega)$,with ω being tagged to the discretely numbered image index.

2) Initial manual thresholding is performed setting a lower bound cut-off for intensities in the event of elevated background or saturation of reflections. This is especially useful in the event of diamond reflections which can be manually masked *(this function was not used in these experiments and is not described but is a function provided by HEXRD).*

3) A priori knowledge of anticipated lattice parameters, crystal symmetry, and the 2D detector parameters are input allowing population of the complete set of predicted $\boldsymbol{G_{hkl}}$ for a given detector size, distance, and wavelength.

4) Reciprocal lattice vectors $\boldsymbol{G}_{hkl}$with unique 2θ values (i.e., dissimilar location with any other non-equivalent $\boldsymbol{G}_{hkl}2\theta$ values) are selected for a segmented search through orientation space which compares the full set of expected $\boldsymbol{G}_{hkl}$ for the target crystal lattice and symmetry to the observed **Q**s (reflections) for the experimental ω range.

5) For the list of selected $\boldsymbol{G}_{hkl}$ the image series is searched for intensity above background along each Debye ring.

6) Of the selected $\boldsymbol{G}_{hkl}$s, those cleared by the user are then defined as seeds for the search through orientation space to assign the measured intensities.

7) Trial orientations are identified as candidate grains only if they satisfy the strict user provided angular tolerances (shown below) as well as meet the user supplied completeness threshold which is defined as hit/miss in percent (see below).

- 2θ = spread around the predicted radial location of a reflection (green dashed lines in Fig. 2.14 above).
- η = azimuthal variation in reflection location.
- ω = +/- images in the series based on °. (e.g., 0.25 searches +/- 1 image if the image step size in the scan was 0.25°)
- Completeness = hit/miss. (e.g., a completeness of 0.50 means that 50% of the chosen seed reflections have to exist within the angular tolerances for a given trial orientation for it to be identified as a candidate grain).

With a well-known single crystal, initial indexation and trial orientation generation is generally achieved by using the first 3-5 $\boldsymbol{G}_{\boldsymbol{hkl}}$'s. Before this is initiated, the image may need to be intensity filtered. An idea of the amount needed to be filtered can be determined by using the *maximum* and *minimum value* fields in the **Color Bar** tab. Normally, oversaturation of peaks can be seen by streaking or "tails" that trail the observed Bragg reflections along the rotational direction of the scan. Here none were found, and the indexing can proceed to the next step as follows:

From the top scroll menu select **RUN > Indexing** and ensure the correct material is selected as well as the **Method** is set to **Generate.** The **Generate** option creates new Bragg reflection η-ω maps. Previously created maps can also be loaded by selecting the **Load** option from the drop down. Also, this provides another chance to select and ensure the intended $\boldsymbol{G}_{\boldsymbol{hkl}}$'s have been chosen. During the indexing procedure it is sometimes advantageous to filter the *hkl*s based on descending structure factor, $|F_{hkl}|$,or selecting the first couple of highest structure factor reflections. This is helpful when a phase exhibits many low intensity reflections, therefore by selecting reflections of high structure factors increases the likelihood of the reflections not being drowned out by neighboring intensities or general weakness (2.14 a). Also, *bin frames* should be set to 1 meaning the intensities are only binned image-by-image. The indexing configuration can then be accessed by **VIEW > Indexing Config** (Fig. 2.15 b). Here the only parameters that need to be set are the following:

- **Completeness:** 0.7 (70%) Having a known single crystal standard setting this value between 70-80 is acceptable. This also is dependent on the coverage obtained during the scan. A near 360° scan, 320° here, should bring nearly all lattice planes into the reflection condition. This will not be the case when inside a DAC.
- **hkl_seeds:** Ensure the total number here matches the total number intended to be used.

a) b)

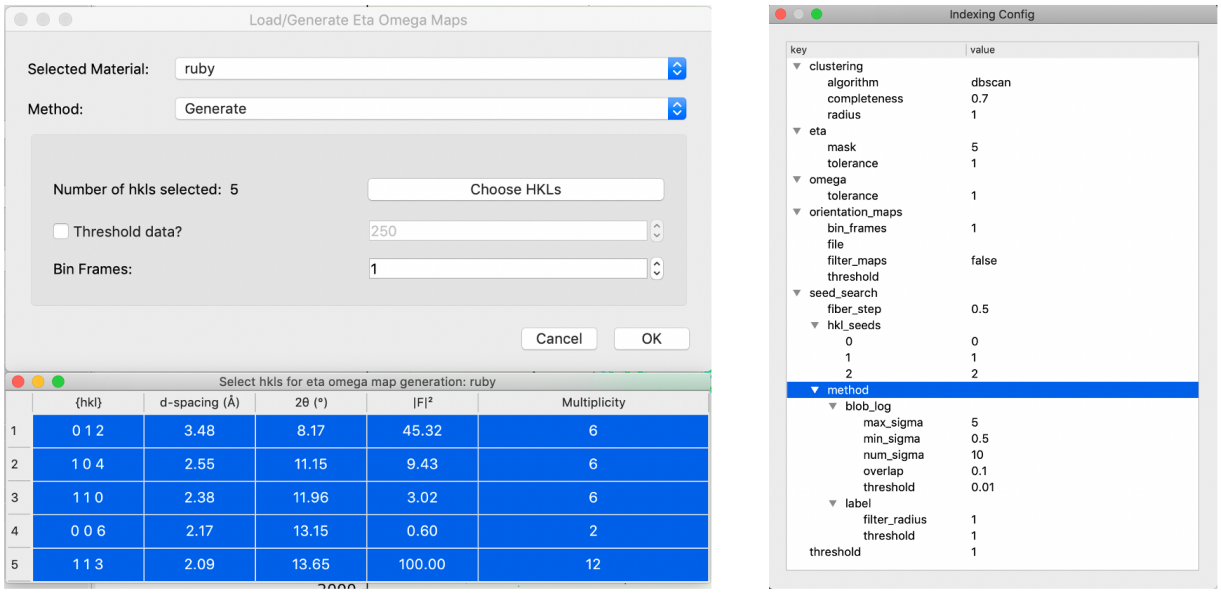

Fig. 2.15 Indexing window and indexing configuration window *(a) Indexing initiation window allowing selection of* $\boldsymbol{G_{hkl}}$*'s for the indexing procedure. (b) Indexing config allowing for setting the completeness threshold.*

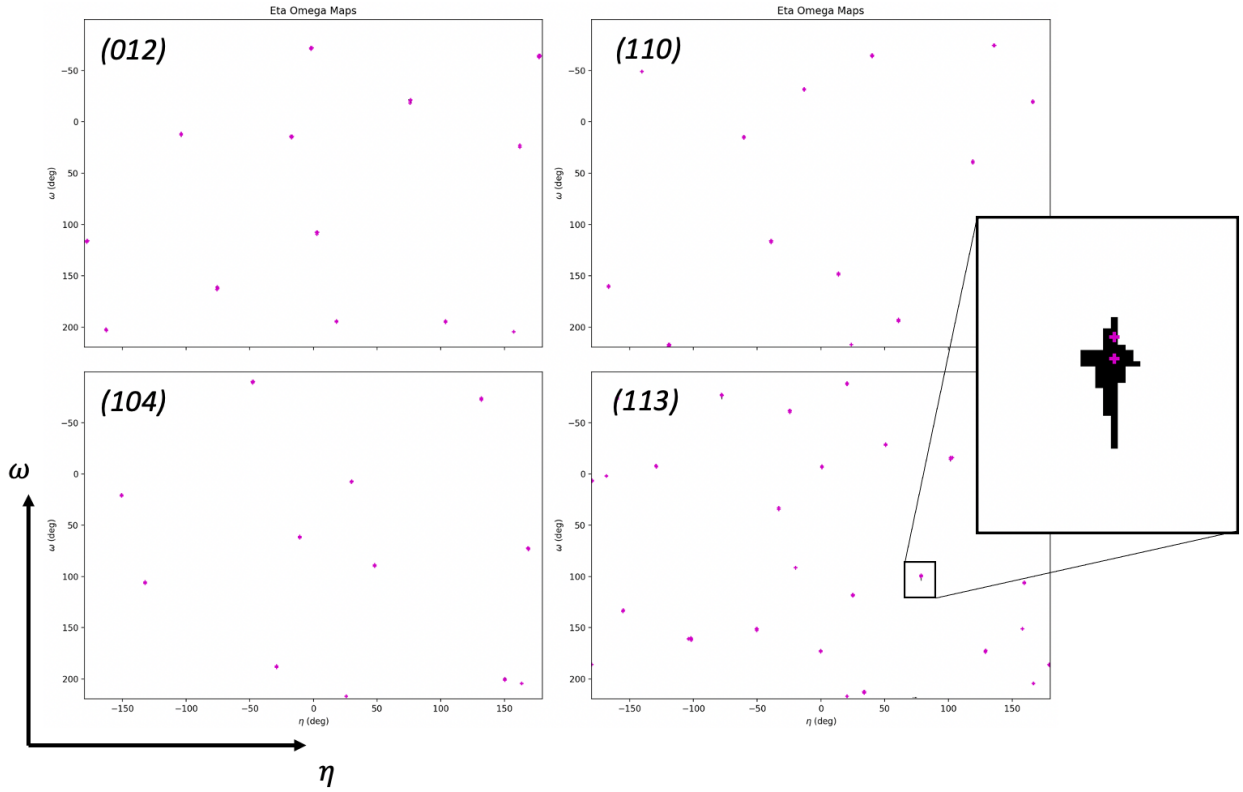

Fig. 2.16 Indexing results. *η-ω maps of* $\boldsymbol{G_{hkl}}$*'s indexation results for (012), (110), (104), (113) for the single crystal ruby sphere. Assigned intensities are marked with small red cross. Enlarged image shows individual intensity assignment for one reflection assigned to (113). Notice in the enlarged image that a cluster of assignments were made for this intensity.*

The generated maps should be investigated (Fig. 2.16), and additional thresholding applied through the form of Gaussian Laplace filtering can be added. Furthermore, the ***hkl seeds*** parameter indicates the $\boldsymbol{G_{hkl}}$'s that will be used in the seeded search for candidate orientations and should be reviewed. For instance, if the first 5 reflections were selected to generate the maps, but only 4/5 had actually identified reflections the outlier can be unchecked before proceeding since it would lower the completeness percentage which may lead to no grains being found when a grain exists. After any extraneous intensity tails have been cleaned by thresholding and recreating the maps, the orientation indexing is commenced by pressing > OK. If any orientation is successfully indexed above the preset completeness threshold the user will be prompted with the ***Fit grains*** options box (Fig. 2.16). In the event no orientation(s) could be assigned and error message informing the user of failure will appear. The inability to find any orientations satisfying the selection criterion could happen for a few reasons:

(1) The completeness threshold was set too high.
(2) The images were too aggressively thresholded leading to too few detectable intensities.
(3) The calibration may be off and needs to be redone.
(4) The wrong material (or material properties) was/were selected.
(5) The wrong detector key was selected.

As stated in the previous section, the indexing procedure provides a list of crystallographic orientations that are consistent with the measured Bragg reflections. The intensities themselves however span the entire detector face not just the initial few *hkl*s used to define trial orientations. Each Bragg reflection itself also contains a distribution of the associated intensity which is sensitive to parameters such as intragranular strain and orientation gradients. Each trial orientation is then subjected to the remaining intensities in the diffraction image out to a user defined 2θ (Fig. 2.17 a) or only a specific subset of $\boldsymbol{G_{hkl}}$'s if that is preferred. Prior to running ***Fit grains***, this is also an opportunity to take advantage of the ability to make direct angular measurements of representative reflection intensities (Fig 2.17 c) for use in the ***Fit grains*** tolerances (Fig. 2.17 a). Also in the ***Fit grains*** options window is a final threshold to be set on the raw images below which intensities will be ignored in the reflection intensity assignment. Care should be taken here in that if the image thresholds are approached with a heavy hand it can begin to remove the intensity distribution around the reflections leading to poor constraints on the intragranular parameters such as grain averaged centroid positions and strain (or stretch) tensor components. In order to ensure convergence, additional fitting iterations of increasingly tighter tolerances can be added using the **ADD** icon at the bottom of the ***Fit Grains*** Options window. With the NIST ruby sphere as well as the quartz single crystal only two iterations where necessary for the initial indexing. Below are the initial indexation parameters. After initial indexation, a 3D detector calibration should be performed until convergence using the script *Appendix 2: calibrate_from_rotational_series.py* whose results and description are also provided there. At the time of the release of this document, the single crystal 3D detector calibration should be internal to the *HEXRD* GUI and this script is no longer needed but supplied for completeness. The 3D detector calibration is a crucial step and should not be overlooked. In this example the centroid of the ruby sphere was found to be *(10, 80, 3)* μm (x,y,z) in the sample frame coordinates. Notice that the 2, y-coordinate, has the largest deviation from 0, albeit still within the volume of the ruby sphere. This is because the y-coordinate in the sample and the centroid y-coordinate are correlated. This is corrected by fixing the known y-coordinate of the ruby sphere to 0. Essentially setting the reference 0 for all proceeding analysis. This correction is also discussed *Appendix 2: calibrate_from_rotational_series.py.*

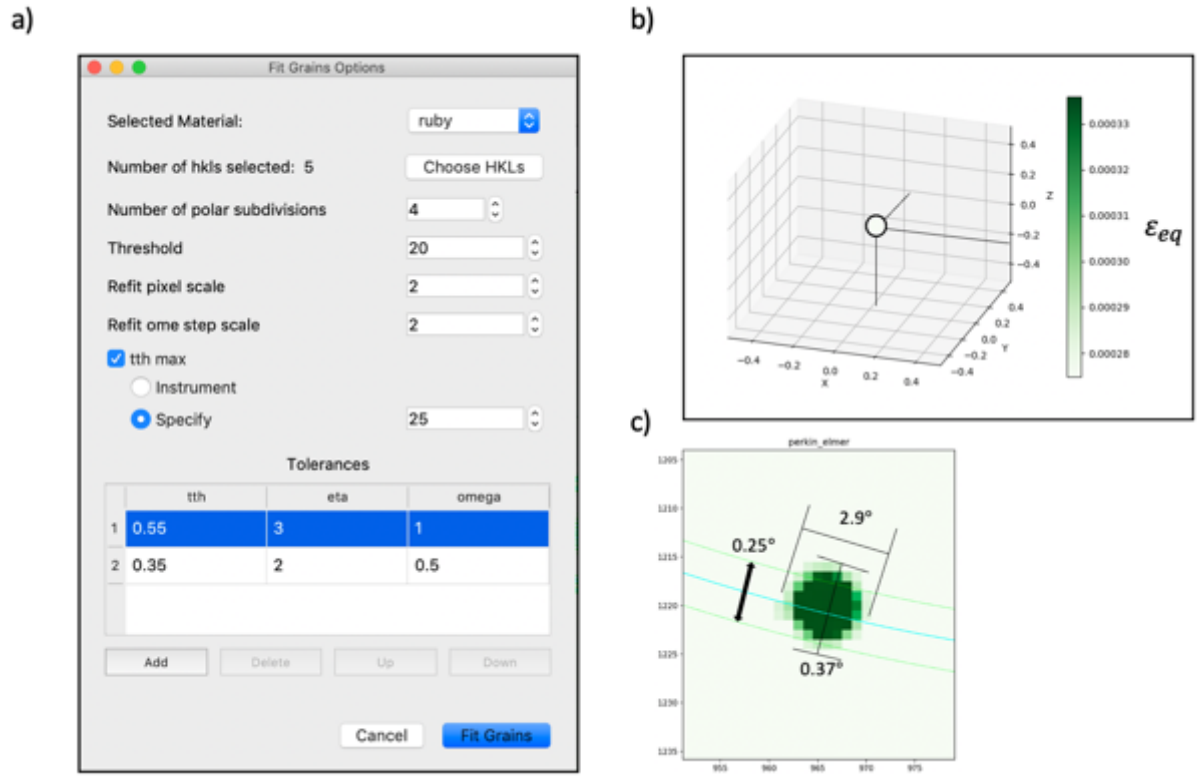

Fig. 2.17 Fit grains procedure and results. *(a) Fit grains options box showing the various thresholding possibilities for reflection intensity assignment to the list of trial orientations. (b) resulting grain centroid of 150 μm diameter ruby sphere (centroid coordinates: (10, 80, 3) μm in sample x y z coordinates as well as the Von Mises equivalent strain calculated from the fit grain.*

The ***Fit grains*** function performs a 12-parameter cell refinement (3-position, 3 for lattice orientation, and 6 for the distortion of the lattice from the reference lattice). During this process, instead of typical methods of fitting normal strains to the infinitesimal strain tensor, the full elastic strain tensor is derived by non-linear least squares fitting as many G_{hkl} as can be recorded to a deformation tensor **F** which takes the reference lattice **r** to the distorted lattice **r'** through the following finite deformation kinematics description:

$$\boldsymbol{r'} = \boldsymbol{F} \cdot \boldsymbol{r} + p \tag{2.3}$$

Polar decomposition yields a pure rotation **R** and a pure distortion (or stretch) **V.**

$$\boldsymbol{F} = \boldsymbol{V} \cdot \boldsymbol{R} \tag{2.4}$$

The right stretch tensor in the crystal frame can then be recovered via:

$$\boldsymbol{U} = \boldsymbol{R^T} \cdot \boldsymbol{V} \cdot \boldsymbol{R} \tag{2.5}$$

From which the strain is recoverable as the logarithm of the right stretch tensor components. Given estimates of the single crystal elastic constants for the experimental conditions, the stress can then be obtained under the assumption of linear elasticity and the application of Hooke's law:

$$\boldsymbol{\sigma} = \mathbb{C} : \varepsilon \tag{2.6}$$

Where $\mathbb{C}$ is the elasticity tensor and in standard matrix notation becomes,

$$\sigma_{ij} = C_{ijkl}\, \varepsilon_{kl} \tag{2.7}$$

This is simplified further by using Voigt notation (references) commonly known as engineering notation which will be the notation used here.

$$\sigma_i = C_{ij}\, \varepsilon_j \tag{2.8}$$

Once the initial grain refinement has been completed, the detector itself is iteratively to calibrate the remaining 3D detector parameters which automatically overwrites the previously created instrument file and then is used to re-index the single crystal until convergence. The final instrument file will be used for the remainder of the experiment. Fig. 2.18 provides a workflow diagram for what has been described thus far.

The grain output file consists of several useful quantities: (1) grain #, (2) completeness, (3) goodness of fit represented as a typical $\chi 2$ parameter, (4) the three-component exponential map vector describing the orientation, (5) the three grain centroid coordinates in *mm* from the beam center (0,0,0) in the sample frame, (6) 6-vector notation of the inverse stretch tensor, and (7) the 6-vector notation of the full strain tensor. It should also be noted that these values are in standard python notation with the indices beginning with 0 and not 1. Also, a second file is generated for each extracted grain (*spots_00000.out*) which contains a list of every assigned $\boldsymbol{G_{hkl}}$ for each grain as well as the integrated reflection intensity, max intensity, as well as the predicted location of each reflection on the detector face as well as the measured reflection locations (*Appendix 2: spots.out*).

** Note on ***Fit grains:*** *There are two schools of thought on thresholds for the grain fitting process. (1) Start with sloppy tolerances and tighten with iteration or (2) start with tight tolerances to nail down key spots then loosen the tolerances to grab weaker spots that might be less constrained. In these experiments both options were performed initially on the ruby single crystal and both converged to the same goodness of fit with only deviations in the strain by ~0.0002 (200 micro-strains) and 1-5 μm in centroid position for the 150 μm diameter ruby sphere***.*

From the ***fit grains*** output several useful quantities can be derived and each will be described as they are determined in the following sections. Figure 2.19 shows a roadmap of the parameters that can be directly obtained from *MGC* measurements as well as the derivable quantities that can be accessed.

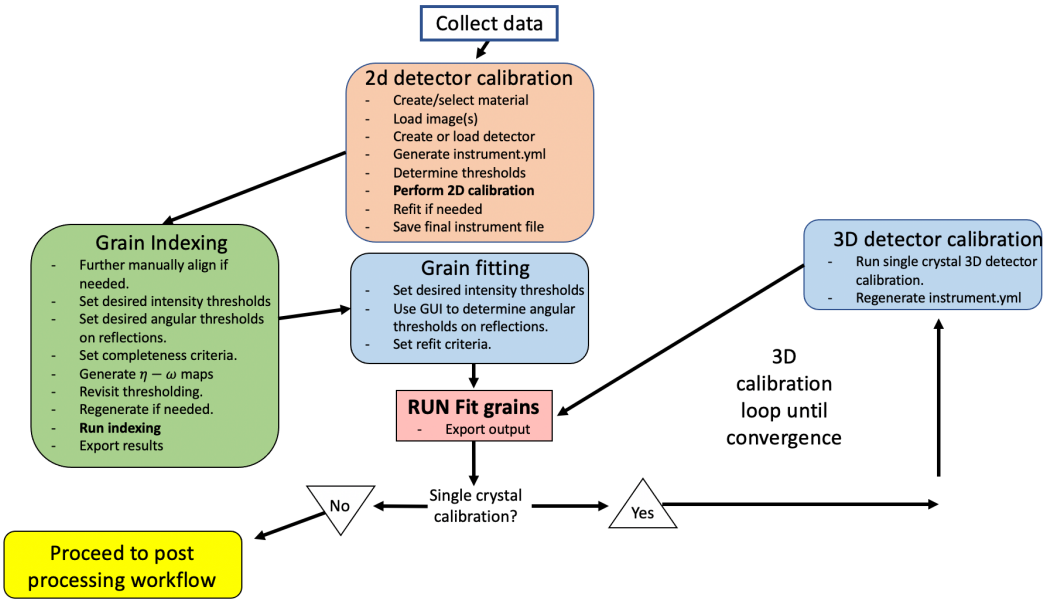

Fig. 2.18 HEXRD workflow. *Work-flow diagram describing the general analysis process with key steps and loops for 2D and 3D detector calibration.*

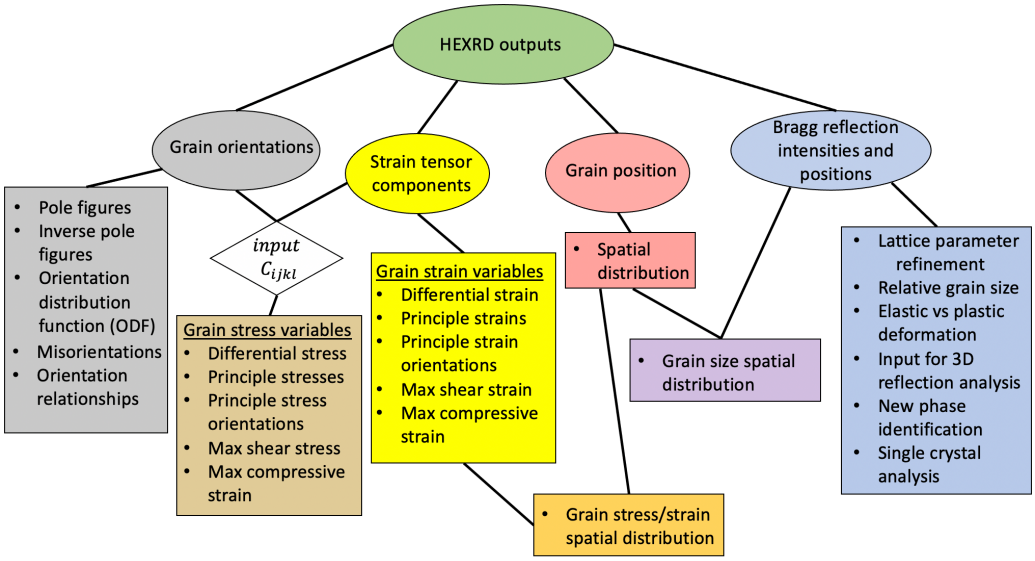

Fig 2.19 Parameters obtainable from MGC using HEXRD. *The various parameters that can be obtained from a single experiment using MGC. Circles represent the parameters directly output from HEXRD while squares represent the directly derivable variables from the output variables. Diamonds represent input variables that can be obtained and applied to derive new parameters.*

In these investigations another layer of refinement is added external to *HEXRD*, where the output is combined with a non-linear least squares refinement of the lattice parameters based on the incident wavelength and 2θ location of reflections through a combination of open access software UnitCell (Holland and Redfern (1997) and custom scripts which read the *HEXRD* output and creates a two column file consisting of all indexed *hkl*'s and the corresponding measured 2θ value that is then fed into UnitCell.

2.3 Calibration Results

2.3.1 Single crystal results

Each of the three single crystal samples were subjected to grain indexation and refinement resulting in 90% or greater of all possible reflections being assigned to a single orientation for the NIST ruby sphere out do a detector face range of 25° 2θ (Fig. 2.21 & Table 2.2) and 93.5% for the SiO_2 Fig 2.22 & Table 2.2. For the SiO_2 the results are more interesting with two initial orientations being identified of equal indexation success. For single crystal samples this can occur for a few reasons: (1) the sample was not a single crystal (i.e., fractured leading to two different orientations), or two, the sample is twinned. In this case it was determined to be the later and 93.5% and 93.5% of possible reflections for both variants being assigned. A key parameter that will be revisited throughout this writing is the crystal (grain) orientation so some care should be given to the notation used here. *HEXRD* natively provides this quantity in the exponential map formulation where the axis of rotation is defined by the direction of a vector $\hat{\boldsymbol{\omega}}$ and the angle of rotation θ, the magnitude of this vector:

$$R = e^{\theta\hat{\omega}} \tag{2.9}$$

While this notation serves several benefits over more common conventions, such as the absence of gimble lock, it is not commonplace in literature and is not readily comparable to other quantities without conversion. In this work, custom algorithms have been added (available upon request) to convert from this notation into rotation matrix form and then to the commonly used Bunge convention (eq. 2.10) designated by the three successive rotations needed to bring the crystal coincident to the sample frame. As stated above, this frame is with the $\hat{\boldsymbol{z}}$ axis coincident with the primary compression axis of the DAC.

$$(\varphi_1, \Phi, \varphi_2) = (Z_{initial}, X_{new}, Z_{new}) \tag{2.10}$$

This convention is very useful when comparing grain orientations to a known sample orientation in that the 2nd angle Φ defines the angle between the grain's c-axis and the sample $\hat{\boldsymbol{z}}$ axis and will be the notation throughout the remainder of this writing.

Upon comparing the two orientations extracted from the quartz sample and determining their misorientation, the sample was determined to be twinned through the known Dauphine twin law for quartz which involves a 60° c-axis rotation from one to the other (Fig. 2.20 a). This example also poses instructional due to the *trigonal* system taken by quartz at ambient conditions. It is rare that a crystal is perfectly 50% twinned and generally the host crystal contributes a larger volume compared to the twin. Here the relative volume between the two orientations can be estimated by

comparing diffraction intensities. Upon comparing the integrated intensities for the largest anticipated structure factor at the experimental X-ray energy (i.e., the (1 0 $\bar{1}$) reflection), one grain had twice the integrated intensity compared to the other (Fig. 2.20 b) indicating that one grain was significantly larger than the other.

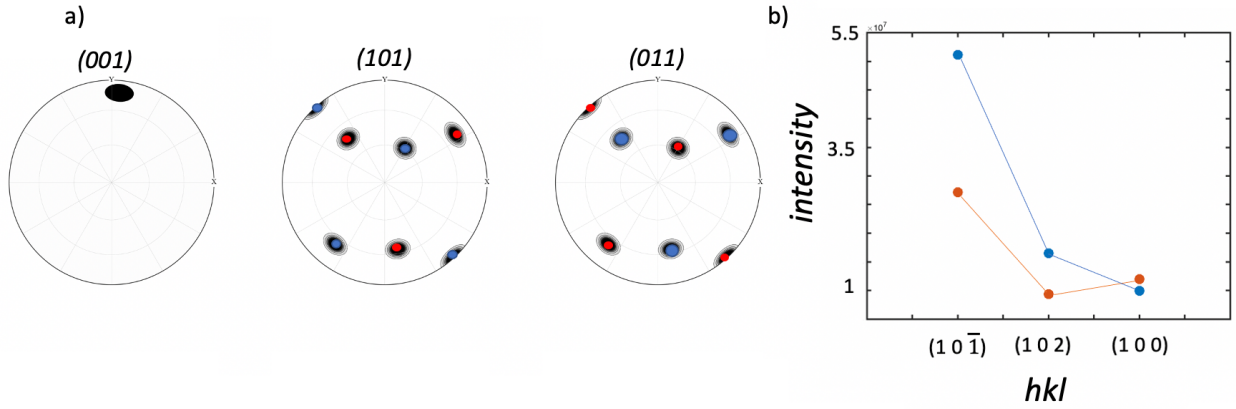

Fig 2.20 Single crystal indexation results for SiO_2. *(a) Upper hemisphere projection of two uniquely determined SiO_2 crystals showing the shared (0001) maxima and 60° about this axis indicative of twinning. Crystal 1 rhombs (red dots) was found to have orientation Euler angles (ϕ_1, Φ, ϕ_2)(175.08, 77.17, 227.55) and crystal 2 rhombs (blue dots) (175.08, 77.17, 167.55).(b) Integrated intensities from the three highest expected structure factor reflections for SiO_2 (10-1), (102), (100) at 25 keV in descending order of anticipated intensity.*

A list of assigned (*hkl*) as well as the associated intensities were then compiled and fed into an extraneous non-linear least squares refinement to check the accuracy of the lattice parameters and crystal structure. Each ruby single crystal was then used to iteratively calibrate the detector parameters in 3D for its respective experiment. Table 2.2 lists the resultant deviations comparing the location of measured diffraction vectors **Q** (reflections) to the anticipated theoretical locations for each associated $\mathbf{G}_{hkl}$ and are also shown pictorially in Figs. 2.21- 2.23. The instrument file is then saved and used for the remainder of the experiment.

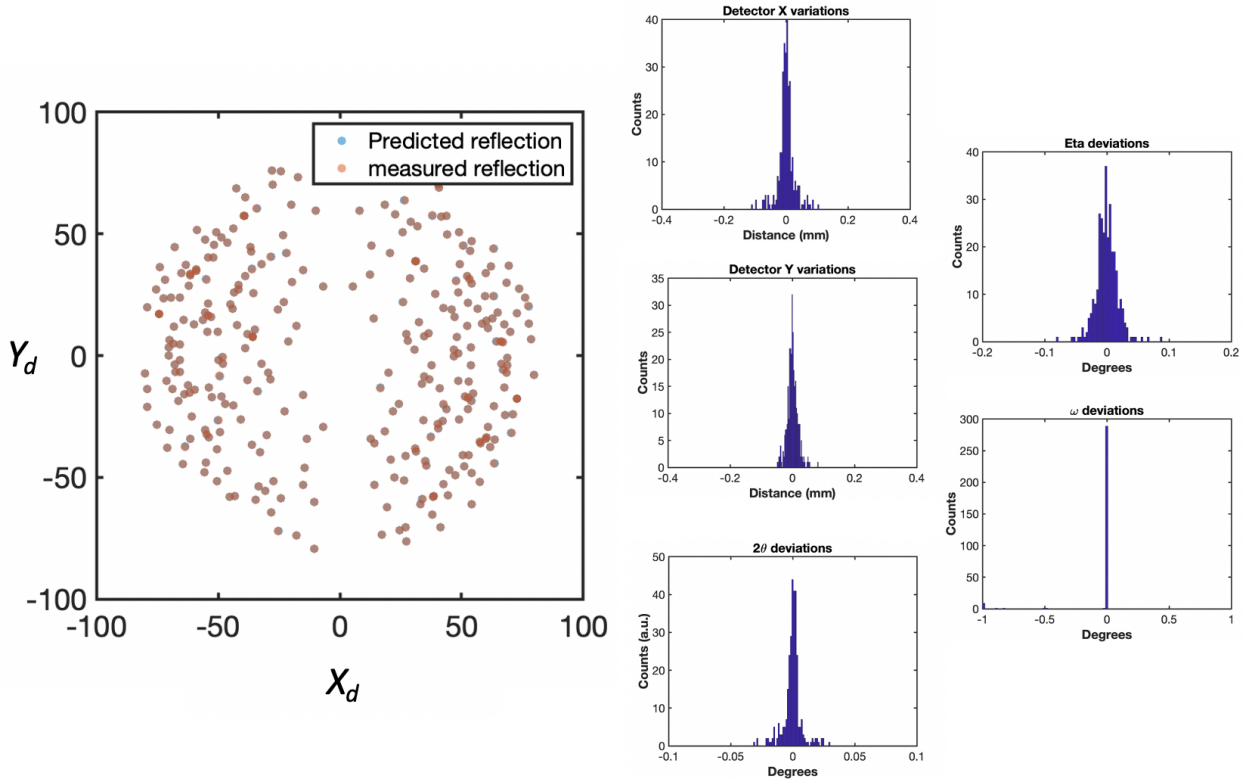

Fig 2.21 Single crystal indexation results for Ruby - marCCD *(a) Shows locations of predicted and measured Q vector locations for the ruby single crystal on the detector plane with blue circles representing the predicted location and red the experimentally measured location. (b-f) Histograms of deviations in Q vector locations on the detector plane from predicted values for detector X-Y positions as well as angular components* $\delta\omega, \delta 2\theta, \delta\eta$ *on the MARccd detector.*

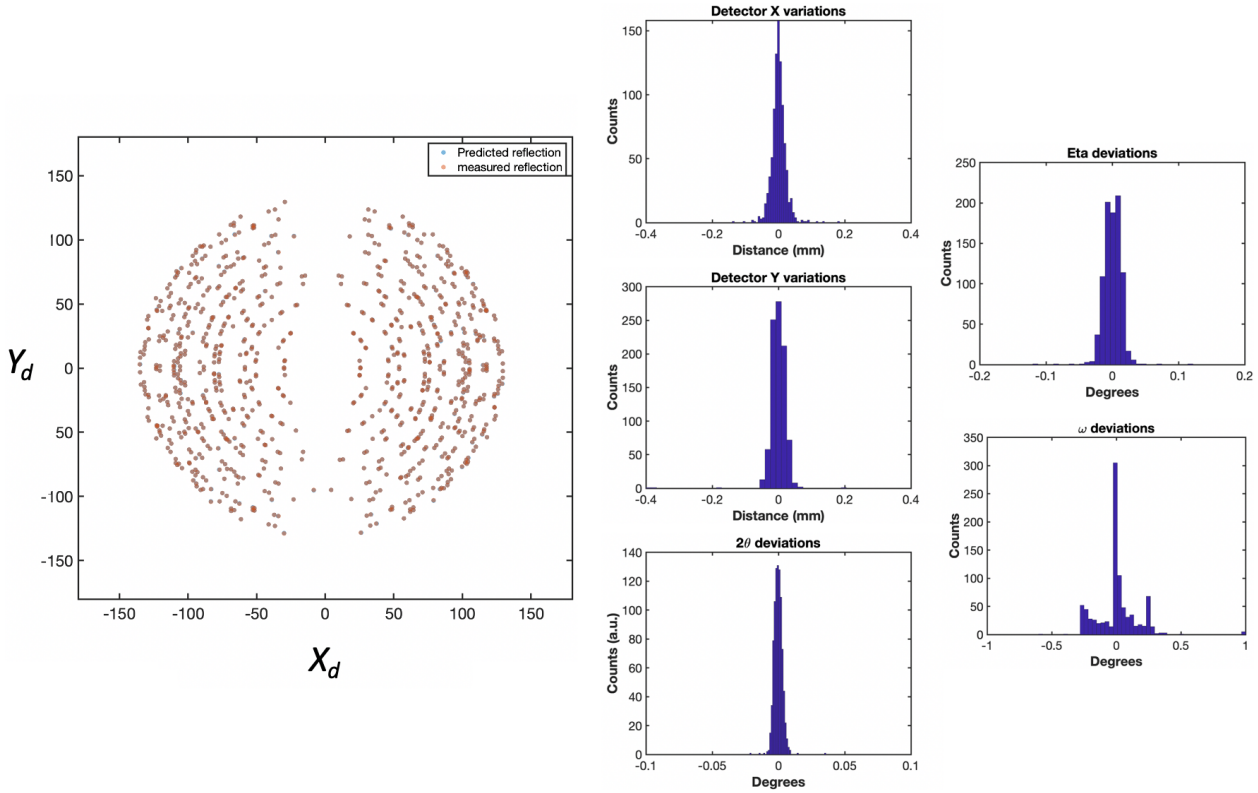

Fig 2.22 Single crystal indexation results for SiO_2 – Perkin Elmer. *(a) Shows locations of predicted and measured Q vector locations for 2 determined unique orientations on the detector plane with blue circles representing the predicted location and red the experimentally measured location. (b-f) Histograms of deviations in Q vector locations on the detector plane from predicted values for detector X-Y positions as well as angular components $\delta\omega, \delta 2\theta, \delta\eta$. Images taken on a Perkin Elmer area detector at 25 keV and a 300mm distance.*

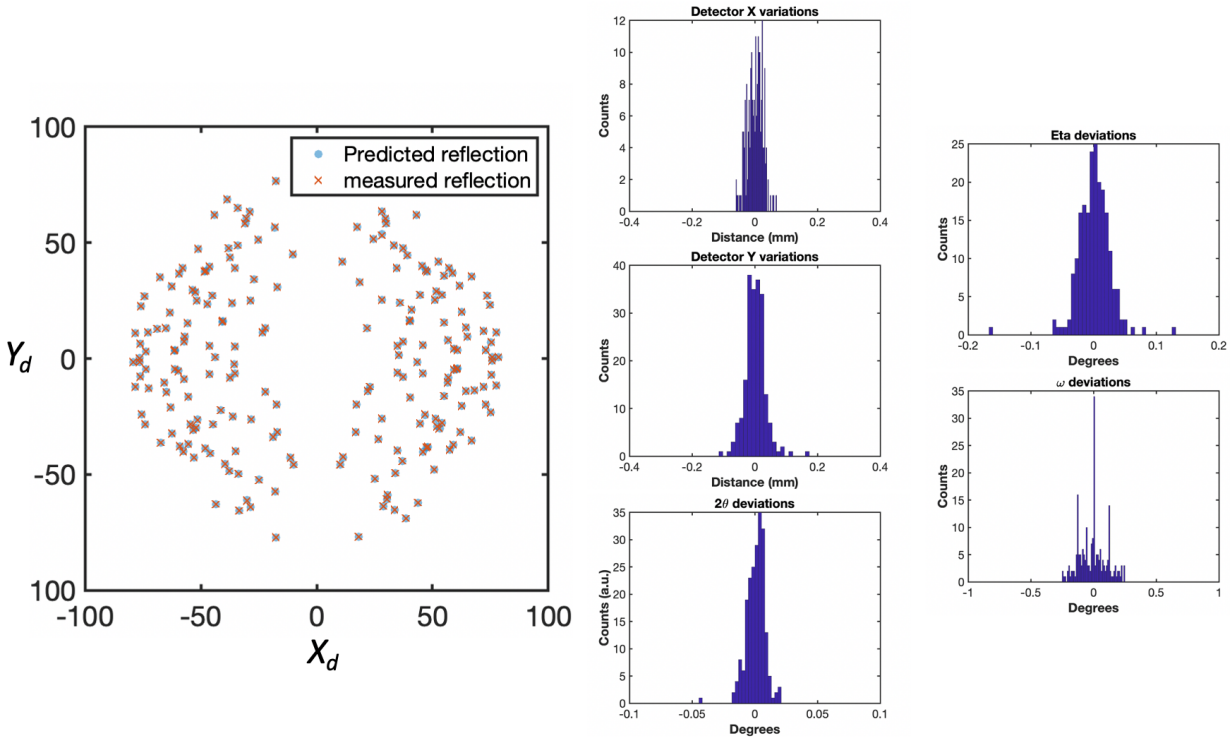

Fig 2.23 Single crystal indexation results for Ruby – Pilatus 3M 1s*. (a) Shows locations of predicted and measured Q vector locations for 2 determined unique orientations on the detector plane with blue circles representing the predicted location and red the experimentally measured location. (b-f) Histograms of deviations in Q vector locations on the detector plane from predicted values for detector X-Y positions as well as angular components* $\delta\omega, \delta 2\theta, \delta\eta$*. Images taken on a Pilatus 3M 1s area detector at 29 keV and a 217mm distance.*

Table 2.2. Indexation results for quartz (Exp.1) and ruby Exp.1 - Exp.3). *Measured lattice parameters and deviation statistics for each single crystal measured. Values are average deviations from theoretical values for each data set. Maximum value of 2θ was limited at 25° due to extraneous noise at higher values. Exp1. = Pilatus 3M 1s, Exp2= Perkin-Elmer, Exp3 = MARccd.*

Exp.	***Phase***	***No. grains***	***a(Å)***	***b(Å)***	***c(Å)***	***Comp. %***	***Avg. 2θ dev***	***Avg. η dev.***	***Avg. ω dev.***	***Detector X(mm)***	***Detector Y(mm)***
	Al_2O_3										
~	*SiO_2*	2	*4.9138(1)*	~	5.4089*(2)*	93.5%	-2.33e-04	0.0012	0.0079	3.439e-04	-4.677e-04
1	*Al_2O_3*	1	*4.7601(1)*	~	*12.9958(1)*	97%	-1.586e-04	-3.913e-04	0.0001	0.0012	3.475e-04
2	*Al_2O_3*	1	*4.7598(1)*	~	*12.9955(2)*	91%	-1.394e-04	1.089e-04	0.0002	0.0018	2.893e-04
3	*Al_2O_3*	1	*4.760(1)*	~	*12.9958(2))*	95.1%	-1.886e-04	-2.913e-04	0.0001	0.0022	3.475e-04

2.4 Multigrain Crystallography Applied in a Diamond Anvil Cell

2.4.1 Sample preparation and experimental considerations

A San Carlos olivine hand specimen with composition $(Mg_{0.88},Fe_{0.12})SiO_4$ was cut and mounted to a glass slide using water soluble crystal bond and ground to a thickness of 50 micron. Individual grains were then isolated under optical microscopy using cross polarized light and the tabulated birefringence values. Several cylindrical columns with a diameter of ~100 μm were then removed from the same grain by laser mill using systems provided by ALS.

Two modified brilliant cut diamond anvils with a culet size of 300 μm were aligned to cBN backing plates and mounted in place using a high temperature epoxy. The diamonds were aligned in a BX-90 DAC (Kantor *et al.* 2012) to near perfect parallelism within sub-micron deviation and checked using optical microscopy. A 250 μm steel disk was pre-indented to 50 μm and a sample chamber of 100 μm diameter was removed by laser milling with same system used to extract sample grains. The gasket was held in place on one diamond culet using a small piece of puddy until the cell was ready to be loaded. Several ~5 – micron ruby spheres were placed on the opposite diamond culet to be used for pressure measurements throughout the experiment by observing the ruby R1 peak shift from the reference position with increasing pressure. Due to intent of inducing plastic deformation in the samples during compression, no pressure medium was used, and the samples alone were placed in the ~ 100 μm cylindrical hole drilled in the gasket material. It has been shown (Xu *et al.* 2004) that olivine exhibits a low thermal conductivity, roughly 3 watts/m*K at 1000 K, which decreases as $T^{1/2}$ with increasing temperature. Combining this quality with trace amounts of iron in the sample leads to a system that naturally couples with the infra-red laser heating system and therefore no extra coupling agent was added to the sample chamber. This also proves beneficial when performing *MGC* in that no extraneous reflections arise from the coupling material or pressure medium which could appear in a location that also houses reflections from the primary sample. After the above prescribed detector calibration procedures, the sample chamber of the DAC was aligned on the beam center coordinates as well as the sample rotational axis. Before scanning the sample housed by the DAC, the angular working range of transmitted radiation was determined by rotating the DAC while observing the disappearance of photon count detected by an inline spectrometer placed between the DAC and the detector. The available scanning range was determined to be [-30°, 30°] and [150°, 210°] which is the standard range for a BX-90 style DAC.

The DAC containing the sample was then loaded in a gas actuated pressure membrane cannister which allows the precise control of the applied pressure on the scale of MPa. The pressure canister containing the DAC was then loaded into the beam path in the axial configuration, centered and aligned on the X-ray beam using a photo diode placed between the sample and the detector. This configuration also conveniently places the DAC compression axis parallel to the incident beam direction, i.e., $Z_S \parallel$ beam direction. Two rotational scans with 0.125° and 0.25° angular step sizes in ω were collected at each pressure step. The pressure was increased in a stepwise fashion with single images collected through a rotation of 20° and 60 second constant exposure after each pressure increment for observational purposes to check for noticeable changes to Bragg reflection morphology, which if detected, was followed by a full rotational series and *MGC* analysis. The pressure inside the DAC was measured using the online beamline assisted ruby florescence (BARF) system provided at beamline 12.2.2 which was also compared to the equation of state (EOS) for corundum as well as olivine (Knittle and Jeanloz 1987) at each step. Once Bragg

reflection distortion could be detected between consecutive pressure steps, the pressure would be released to the previous pressure step to ascertain whether the reflection morphology returned to its equilibrium state which would indicate if the reflection distortion remained in the elastic regime or if the reflection broadening remained after decompression, it can be assumed that permanent plastic deformation had occurred. MGC relies on the ability to isolate individual reflection intensities for reflection assignment to candidate orientations. When plastic deformation, or extensive elastic deformation in the sample occurs, errors in the reflection assignment algorithm increase with the magnitude of reflection broadening and erroneous non-existent orientations are identified.

Once extensive angular streaking occurred in the observed Bragg reflections rendering the data unusable for *MGC*, the pressure was directly increased into the γ-ringwoodite stability zone (20 +/- 1.5 GPa) and heated using a double-sided laser heating approach (Kunz *et al.* 2018) to a temperature of 800-1200° K using a heating spot size of 20 μm to induce the olivine → γ – ringwoodite phase transition. Table 2.3 shows an experiment overview as well as the phases observed at the various *P-T* conditions and Fig. 2.24 shows the experimental path in *P-T* space.

Table 2.3. Overview of experiment showing starting sample, observed phases and the corresponding pressures (GPa) and temperatures (K) achieved in each experiment described in this writing.

Exp.	*Starting sample*	*Phases observed*	*Pressures (GPa)*	*Temps (K)*
1	San Carlos Olivine	olivine	0 – 2	273
		ε-epsilon	15	800-1000
		ringwoodite	5-20	800-1000

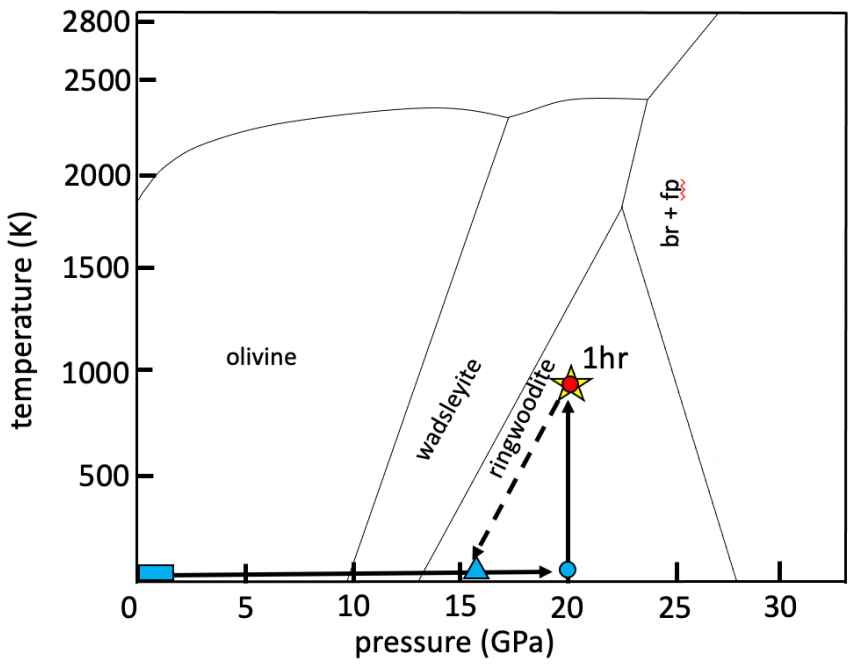

Figure 2.24 Phase diagram for olivine modified from Fei et al. 2004 showing experimental path in P-T space. *Horizontal black line shows increasing pressure, with blue rectangle representing the initial incremental pressure steps performed at ambient temperature. Vertical black arrow shows increasing temperature ~1000°C (start with red circle) to induce the* olivine *to γ phase transition. Pressure decrease due to volume collapse of phase transition shown by dashed line with diffraction images being collected at blue triangle ~(15 GPa).*

2.4.2 Ambient olivine results

A rotational series of the starting olivine sample was collected at ambient conditions (closing condition of the cell). Upon observation of the images, the sample showed visible asterism (i.e., a resolved row of individual diffraction spots for a given Debye Scherrer ring location highlighted in Fig. 2.25 (a)) in this case, pairs of reflections, similar to that described by Vinnet *et al.* 2011 when looking at Hawaiian olivine samples using *in-situ* diffraction. Because the detector has previously been calibrated in 3D only the material should be changed to that with the structural parameters of olivine followed by image thresholding, ***Indexing*** and ***Fit Grains*** procedures. Here the initial parameters were selected as follows:

Indexing:

hkls: the 5 highest structure factor reflections *(004) (011) (002) (062) (051)*

The orientation maps were then surveyed, and it was seen that the reflection conditions were not met for the (011) peak and was replaced with a clearly observed *(241)* peak.

η-tolerance: 0.5
ω-tolerance: 0.5
Completeness: 0.60
Fit grains:
2θ-tolerances: [0.35, 0.3]
η-tolerances: [0.5 , 0.4]
ω-tolerances: [0.75, 0.5]
Max 2θ: 22°

The ***Fit grains*** function was run for 3 iterations until convergence in the grain centroid positions as well as χ^2 (goodness of fit). The existence of two unique orientations seen visually in the diffraction patterns was confirmed by *MGC* which identified two unique olivine orientations (Fig. 2.25). 124 and 117 reflections (completeness of 64 and 60% to an angular distance of 22° 2θ for grain 1 and grain 2) were identified above the background owing to the existence of one larger and one smaller diffracting volume which was confirmed by comparing the integrated spot intensity of the (112) reflection (highest structure factor) of both grains with the larger grain being 90% more intense. The misorientation between the two grains ($\mathbf{G}_a\mathbf{G}_b^{-1}$, representing the active rotation to bring the two grains coincident) was found to be < 1° in agreement with the manual measurements made using the *HEXRD GUI*. The crystal c-axes of all grains were found orientated ~71° ($\mathbf{\Phi}$) from the compression axis of the DAC. Resolution allowed the elastic strain tensors to be obtained for both grains which act as a reference for the proceeding runs once pressure was increased.

The comparison of measured and predicted reflection locations between the reference lattice and the sample are on the 2D detector face are compared in Fig 2.25 c. The assigned lattice planes ($\mathbf{G}_{hkl}$) and associated 2θ values were exported for non-linear least squares lattice parameter refinement with results in good agreement with literature values (Zha *et al.* 1998) (Table 2.4).

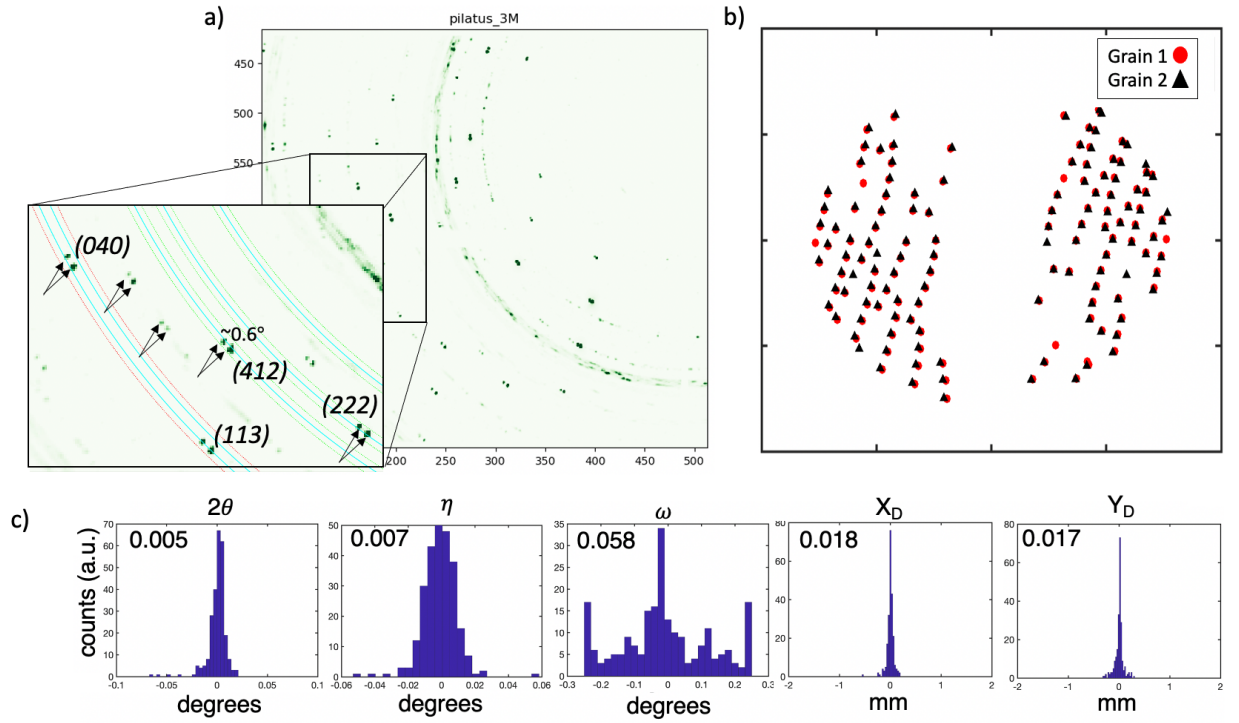

Figure 2.25 Analysis of starting Olivine sample. *(a) diffraction image collected on Pilatus 3s 1M detector of olivine sample over a range of 20° during a 60 second constant exposure showing paired diffraction intensities (asterism) due to two unique olivine grains/sub-domains (as viewed in the HEXRD GUI). (b) the aggregate diffraction image consisting of 480 images taken over 60° in 0.125° increments obtained at the same location as (a). Notice near continuous intensity rings in (b) due to diffraction from the Fe gasket material coming into contact with the beam during DAC rotation. (c) shows all assigned* $\boldsymbol{Q}$ *for both identified olivine grains. (d) shows the variations in predicted* $\boldsymbol{G}_{hkl}$ *to predicted* $\boldsymbol{Q}$ *locations as histograms with mean values shown in the upper right corner of each.*

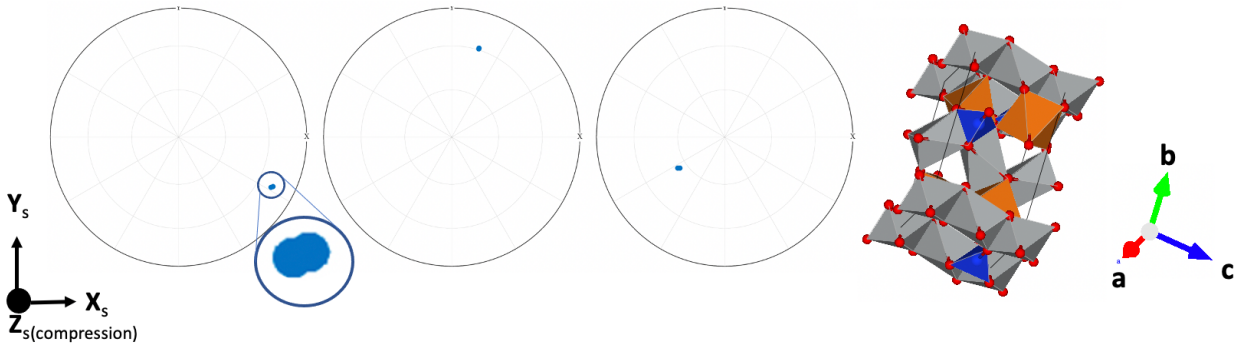

Fig 2.26 Extracted olivine orientations. *Two unique olivine orientations extracted from the sample displayed as stereographic projections of the (001), (010), and (100) lattice plane normal. Polyhedral models of the olivine structure in the appropriate orientation are shown to the right for reference. In the bottom row of the 001-pole location has been provided showing the ~1° separation between orientations detectable.*

Table 2.4. Ambient olivine indexation results. *compares the resulting olivine single crystals to the refence lattice parameters used in these study (Zha et al. 1998) as well as the number of reflections gathered for each grain and the overall completion percentage of spots assigned.*

Exp	*Grain #*	*a(Å)*	*b(Å)*	*c(Å)*	*# reflections*	*Completion %*
Reference		4.7631(14)	10.2272(9)	5.9944(10)		
Olivine	1	4.7772(4)	10.2599(3)	5.9899(4)	174	64
	2	4.7430(4)	10.2820(3)	5.9649(4)	117	60

2.4.3 High pressure and low temperature strength of olivine

While increasing pressure on the ambient olivine sample, good agreement between pressure measurements using ruby fluorescence (red line in Fig. 2.28) and the EOS (black line) were achieved with deviations being less than +/- 60 MPa up to 4 GPa with increasing divergence between the two measurements approaching at step 10. At 10 GPa, the quality of signal from the ruby spheres degraded and could no longer be distinguished and only the EOS for olivine was used.

Having access to the full strain tensor for each identified grain as well as the grain orientation allows the estimation of the stress housed by each grain under the assumption of linear elasticity through the application of Hooke's Law $\sigma_i = C_{ij}\varepsilon_j$. Single crystal elastic constants for olivine obtained under various *P-T* conditions (Abramson *et al.* 1997) were used for these calculations. Since our aim is to constrain the experimental stresses as tight as possible the increase in stiffness with increased applied pressure was accounted for through Taylor expansion to the 2nd derivative of the ambient condition elastic constants to each measured pressure step. Once determined, the Von Mises equivalent stress (as well as strain) (eqn.s 2.11-2.12) was calculated at each pressure step.

$$\varepsilon_{eq} = \frac{2}{3}\sqrt{\frac{(\varepsilon_{11}-\varepsilon_{22})^2 + (\varepsilon_{22}-\varepsilon_{33})^2 + (\varepsilon_{11}-\varepsilon_{33})^2 + 6(\varepsilon_{12}^2 + \varepsilon_{13}^2 + \varepsilon_{23}^2)}{2}} \tag{2.11}$$

$$\sigma_{eq} = \sqrt{\frac{(\sigma_{11}-\sigma_{22})^2 + (\sigma_{22}-\sigma_{33})^2 + (\sigma_{11}-\sigma_{33})^2 + 6(\sigma_{12}^2 + \sigma_{13}^2 + \sigma_{23}^2)}{2}} \tag{2.12}$$

In this experiment the differential stress is also calculated as eq 2.13 where σ_1 and σ_2 being the most extensive and most compressive stresses.

$$\sigma_{diff} = \sigma_1 - \sigma_2 \tag{2.13}$$

Between pressures of 0.1 and 0.25 GPa, an increase in asterism was observed in the diffraction patterns (Fig. 2.27 outer box step 4) resulting in a new (3rd) discernable orientation having a slightly larger misorientation gap from the original two (<1.0°). This feature was also accompanied by a drop in calculated differential stress within the sample. Increasing asterism could occur for a couple of reasons: (1) the sample contained pre-existing subdomains but with a misorientation too small to distinguish in the ambient state of the sample, (2) the crystallite was

fractured during the preparation process, (3) the sample was further fractured during initial compression before confining pressure was reached. Seeing as that no undulatory extinction could be seen during optical microscopy prior to sample loading but the extraction process involves laser drilling which imparts a rapid temperature gradient to the sample, coupled with the stress drop upon visualization, brittle fracture during compression is the most likely cause but cannot differentiate from those two with any certainty. While the orientation of the new domain was fairly well constrained, only 11% of reflections (totaling 12) could be assigned, leading to a poor overall fit on parameters such as strain tensor components and centroid position while the initial two grains remained fully constrained.

At a pressure of 0.75 GPa the observed triplet spots were replaced with the onset of spot broadening in both the azimuth and radial directions ($\Delta\eta$ increasing to 2.33° and 0.28° in $\Delta 2\theta$) markedly so on the identified (130) and (140) planes, and later at higher pressures the (110) ((*hk*0) type lattice planes) consistent with slip deformation experimentally predicted by Mussi *et al.* 2014 at higher temperatures of 1000°C as well as through first principal calculations Mainprice *et al.* 2005. It has been previously shown that observed lattice-related peak broadening along the angular directions can be used as a sign of deformation at high pressures and low temperatures Idrissi *et al.* 2016. Diffraction spots belonging to the majority of the remaining lattice planes (e.g., (240) (241)) showed little or no angular streaking at this pressure and maintained a clear distinction between the pairs or triplets with near gaussian spot morphology. The observed angular streaking in (*hk0*) type reflections remained even after pressure was slightly decreased confirming plastic deformation to the crystalline lattice. At 1.25 GPa (marked by grey bar in Figure 2.28 (center) and shown in outer box step 7) extensive peak broadening in both angular directions and increased in magnitude throughout the remaining pressure runs.

It was found that the equivalent stresses $\langle\sigma_{eq}\rangle$ steadily increased from sub GPa to 1.59 GPa just before the visualized onset of plastic yielding with an associated differential stress of 0.195 GPa. As mentioned above, it is interesting to notice that outer box 3 in Fig. 2.27 (a) represents the first indication of the newly detectible olivine orientation (the third reflection forming the triplet) and is also coincident with a sudden drop in the measured stress $\langle\sigma_{diff}\rangle$ while $\langle\sigma_{eq}\rangle$ continues to steadily increase. This event may further indicate that the newly identified orientation developed from brittle fracturing of the sample meaning that complete confinement of the sample had yet to occur this step. Similar events occurred when Proietti *et al.* (2016) performed deformation experiments using a D-DIA between 3-7 GPa. They attributed the similar low temperature drops in stress to micro fracturing. $\langle\sigma_{eq}\rangle$ and $\langle\sigma_{diff}\rangle$ could be calculated up to step 6, after which (step 7 : Figure 2.27 outer box step 7) the individual reflection centroids were no longer discernable and grain elastic strain tensors could not be quantified. At this stage, analysis would continue with powder techniques such as the Rietveld method Wenk *et al.* 1997 but that is beyond the intent of this study.

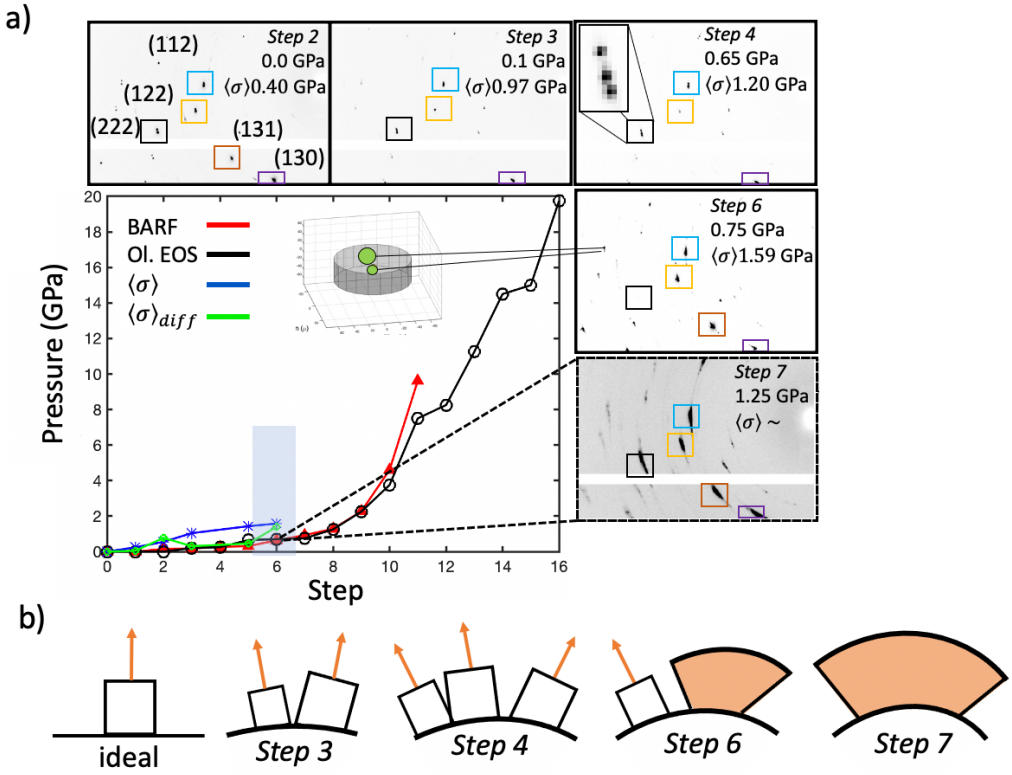

Figure 2.27 *(a) Pressure evolution within the DAC (center) and diffraction peak morphology for the (112), (222), (122), (131), (130) olivine peaks (outer boxes). Pressures obtained via BARF (red) via ruby spheres and EOS of olivine (black) as well as grain elastic stress (blue) are included. Pressure recorded from the EOS and BARF online ruby system as well as the calculated mean equivalent stress is shown select pressure steps in outer boxes. Inset also shows two identified grain centroids (green circles with size scaled by number of assigned reflections) within the 100 μm diameter sample chamber (grey structure). Increasing asterism is seen in (122) and (222) reflections with increasing pressure and the onset of plastic deformation in step 7 at 1.25 GPa. (b) depicts the evolving mosaicity observed during increasing pressure in diffraction images for each step shown in outer boxes with ideal depicting an undeformed crystal giving rise to a single reflection (orange arrow), (3-4) increased lattice flexure and visible subdomains due to inhomogeneous deformation and 5-6 indicating reflection streaking.*

2.4.4 Olivine → γ-ringwoodite at high P-T

The pressure was increased directly to a pressure of 20 GPa and was laser heated to within a temperature range of 800-1200 K for 1 hour to induce the olivine → γ-ringwoodite phase transition. After 1 hour, the sample was quenched to room temperature and diffraction images were collected which showed the disappearance of any meta-stable olivine in the scanned area and revealed the appearance of several new peaks including the distinctive (311) belonging to cubic ringwoodite (Fig. 2.28). Due to the large volume decrease that accompanies this phase transition

(estimated at ~8% (Raterron *et al*. 2008), the pressure in the DAC dropped to 15.5 GPa after quenching, but still within the stability field for γ-ringwoodite at room temperature.

MGC analysis isolated 77 unique orientations (Fig. 2.28) belonging to a cubic phase $Fd\bar{3}m$ with a = 7.9097(3) Å consistent with ringwoodite (refined and averaged from the 3 best constrained grains). It should also be noted that more than 200-300 individual orientations were found but most only contained 3-8 reflections and could not be used for further grain refinement. This is generally the case when there are many small grains, and the reflections are fairly weak pushing the limitations on the detector resolution capabilities. The isolation of ringwoodite is generally further complicated by the presence of reflections from the stainless-steel gasket (bcc) at the far angular edges of the scan where the $\{110\}_{\mathrm{Fe}}$ overlaps with the $\{400\}_{\gamma}$ as well as $\{240\}_{Fe}$ overlapping $\{440\}_{\gamma}$. Care was taken here by using the $\{220\}_{\gamma}$ and $\{311\}_{\gamma}$ peaks as constraints on the initial orientation search by requiring their presence. While this approach also lowers possible overall number of grains identified, it is necessary to minimize the possibility of mis-indexation which can lead to erroneous orientations. Here, if an orientation did not contain the $\{220\}_{\gamma}$ and $\{311\}_{\gamma}$ peaks, but did contain higher 2θ peaks, it was not considered. It is understood that this almost surely removed weakly identified ringwoodite grains and also limited the strain and centroid refinement drastically but is a necessary exclusion to prevent miss-indexation with the underlying iron peaks.

Another approach that has been taken to minimize the influence of gasket reflections is to further tighten the angular range of the scan excluding images with any indication of the gasket entering the incident beam and diffracting. This approach has been found to be successful when the grains are large and of low symmetry phases. Here, this approach was not ideal due to the few existing peaks of ringwoodite and would further decrease the angular working range to ~22° from 60°. The X-ray spot size can also be deceased which widens the angular working range slightly; this approach also comes at the cost of a proportional loss of X-ray flux which weakens the diffraction intensity, in this case for an already fine-grained weakly diffracting sample. This approach was attempted initially but greatly lowered the number of collected diffraction spots. It is also important to note that only a small subvolume of the specimen is sampled; given the initial sample volume of 3.9 x 10^5 μm^3 and the described angular range, as well as X-ray spot size; due to the axial geometry only roughly 1.5% of the sample volume is observed. Thus, the current experiment cannot capture any large-scale heterogeneities, especially those that may occur due to thermal gradients during the laser heating process. While the X-ray spot size does however remain smaller than the IR-heating laser spot size (20 μm at FWHM), and both were aligned coincident, it is assumed that the area sampled is not affected by thermal gradient effects.

The irradiated volume of the sample can be determined from simple geometry using the rotation angle of the DAC combined with an approximation of the X-ray beam size. Here, assuming a 15μm beam size, the scanned volume was found to be 1.0825 x 10^4 μm^3. Using the number of orientations extracted during analysis, an upper bound on the average grain size can be deduced under the assumption that the scanned volume is distributed between all grains found. Here it found that the average grain volume is 90.21 μm^3. Assuming an ideal cubic structure gives an estimation of the grain edge length of ~4.5 μm. This assumption is consistent with recent findings (Mahiudden et al. 2020) that found that transformed ringwoodite formed as *nm* sized grains with stresses between 1-3 GPa.

Also, at 15.5 GPa, no residual β-wadsleyite was detected in the scanning area. Due to the limited access to reciprocal space, and the cubic symmetry of γ-ringwoodite, only a 5 of the 120 identified grains provided enough reflections to provide estimates of the stress state, however the

grain centroids remained poorly constrained. Generally, this limitation can be overcome by utilizing symmetric scans (i.e., rotating the DAC 180°and performing a rotational series) which doubles the reciprocal space access and allows visualization of Friedel pairs. Here this option was not available due to the DAC being in a pressure cannister apparatus which prevents this rotation, and by removing the cell and rotating introduces the high chance of scanning a different location of the sample. Nonetheless, the orientations were well constrained with most grains containing 30-60 % of reflections out to a 2θ range of 18°. In the better constrained grains, $\langle\sigma_{eq}\rangle$ was found to be 3.055 GPa with $\langle\sigma_{diff}\rangle$ = 1.61 in agreement with Mahiudden et al. 2020, but slightly lower than the 5-6 GPa stress determined by (Raterron *et al*. 2008) through ex-situ methods as well as those determined under similar conditions where at 15 GPa *Chen et al. (2001)* (Chen *et al.* 1998) found a differential stress of ~5.5 while *Wenk et al. 2005* determined a maximum differential stress of ~ 5 GPa when deforming γ-ringwoodite between 6-8 GPa. In those cases, the stress was determined during heavy deformation after nucleation whereas in this case is only looking at stresses just after heating induced nucleation (with decompression) alone similar to that of Mahiudden et al. 2020.

Microstructurally, it is seen that γ-ringwoodite forms as a fine-grained phase caused by nucleation during heating when converting directly from olivine. The nucleated grains showed a trend for the $\{100\}_{\text{ring}}$ lattice plane maxima to be aligned with the compressions direction similar to that found by (Rosa *et al.* 2016, 2018) where *MGC* was combined with resistive heating techniques to study transition zone microstructures.

Upon further investigation, extra features were noticed in the diffraction pattern with a unique set of reflections which could not be assigned to any of the expected transformation products ($olivine$-β-γ) nor to the steel gasket material. The new reflections occurred in small, weakly reflecting, clusters indicating some form of preferred orientation, with four clusters readily visible at 2θ = 9.467° and η = 165, -159, 19, -16° (black boxes in Figure 2.28 (b,c)). The existence of an intermediate high-pressure polymorph, ε-Mg_2SiO_4 (epsilon), has been predicted by transformation models in the Mg_2SiO_4 system (Madon *et al.* 2003, Kerschhofer *et al.* 1996) where it has been implicated in assisting the straight olivine ↔ γ-ringwoodite transition through shear mechanisms (Fig. 2.28 d), and also the olivin*e* - β transition in the absence of the activation temperature needed to drive nucleation and growth, but has yet to be seen under experimental conditions. Recently ε was observed by Tomioka *et al.* 2017 in the heavily shocked Tenham meteorite which fell in Australia in 1879 (Spencer 1937).

A new material was created and added to the material file in the *HEXRD GUI* using the lattice parameters provided in (Tomioka *et al.* 2017) e.g., *Pmma* symmetry setting a = 5.78 b = 2.88 c = 8.33, provided initial search criteria in attempt to identify the origin of the new peaks. This process can be repeated for any number of materials or testing for new phases. Furthermore, the grain refinement process for phases with very different symmetries proceeds in the same manner as the single crystal. Fig. 2.28 c shows and angular section of the diffraction pattern viewed in the *HEXRD* GUI with two material overlays activated at once allowing the distinction of where reflections for both phases (γ-ringwoodite, and the suspected epsilon phase) should reside. Once the indexation has been performed for one material the grain fitting is performed until it has converged. The same process is repeated on the second or 3rd phase. Fig 2.28 d shows the resulting reflection assignment for both phases. In the event that the symmetries of the phases are very similar, and they cannot be completely separated though filtering of structure factors or a handful of unique reflections it is possible to generate a list of reflections to be excluded based during the grain fitting process but in general selecting non-overlapping reflections for the two phases is sufficient.

Due to the differing symmetries, cubic (γ-ringwoodite) versus orthorhombic (ε) reflections arising from each phase could easily be separated which allowed for isolating 17 candidate grains with 7-13 reflections each belonging to crystallites with the anticipated structural parameters for the ε-phase which structurally resembles β-wadsleyite but with ¼ size of the b axis. Due to the unknown Mg, Fe iron content or partitioning in ε, and the fact that the only recorded lattice parameters for ε were obtained at ambient conditions, allowable deviations in the 2θ direction were set to be 0.4° and then refined to 0.2°. The two best constrained grains were used for iterative least squares refinement using the software *UnitCell* (Holland and Redfern 1997, Zhang *et al.* 2014) giving the lattice parameters a = 5.7393 b = 2.81127 c = 8.3399 (Table 2.5) in very close agreement with the previous estimations. Table 2.6 provides reflections and the respective *d-spacings* emanating from one grain indexed as ε.

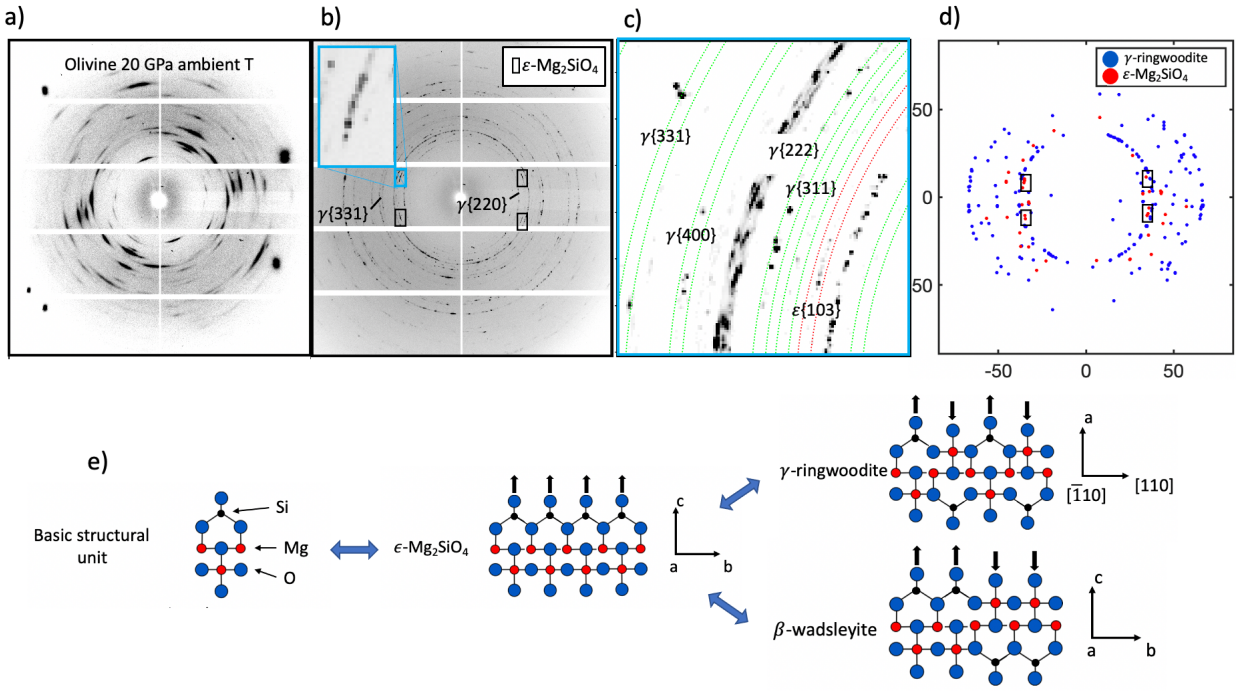

Figure 2.28. *(a) Diffraction pattern showing plastic deformation in olivine at room temperature and a compression of 20 GPa (b) sample after heating between 800 –1000°C for 1 hour. (c) separation of phases with green bounds encasing reflections emanating from ringwoodite and red the {103} of ε-Mg_2SiO_4 (d) shows the resulting indexation for both γ-ringwoodite (blue) and the possible ε-Mg_2SiO_4 (red). (e) shows the predicted transition pathway for a possible intermediate phase in the Mg_2SiO_4 pathway modified from (Tomioka et al. 2017).*

To ensure the validity of the indexation of the ε phase, multiple schemes were used: (1) It was ensured that the $\{103\}_{epsilon}$ peak family (encompassed by the black boxes in Fig. 2.28 c) was included as a seed reflection when searching for candidate orientations, along with other reflections. (2) performed the same search using only the $\{103\}_{epsilon}$ peak and a single other reflection, and (3) varied the intensity threshold on both approaches 1 and 2 to the extreme of systematically increasing the threshold high enough that no grains could be found, and low enough that the most intensities could be assigned but is most likely assigning anomalous reflections to

the candidate grains due to a small level of noise above background due to local scattering. In all cases only subsets of the original indexed set of ε grains were identified leading to the same orientations adding validity to the identification.

Table 2.5. *Comparison of space groups and lattice parameters (Å) determined for the best constrained grain from each identified phase. * indicates this study. Olivine (Zha et al. 1998), wadsleyite (Horiuchi* et al. *1981), ringwoodite (Sasaki* et al. *1982),ε-Mg_2SiO_4 (Tomioka et al. 2017)*

Phase	***Space group***	***a(Å)***	***b(Å)***	***c (Å)***	***Volume ($Å^3$)***
α-olivine(ambient)*	*Pbnm*	4.7532(4)	10.2215(3)	5.9916(4)	291.10(2)
α-olivine(ambient)	*Pbnm*	4.7631(14)	10.2272(9)	5.9944(10)	292.01(10)
α-olivine(0.1 GPa) *	*Pbnm*	4.7413(4)	10.2184(3)	5.9887(4)	290.09(3)
α-olivine(0.65 GPa) *	*Pbnm*	4.7413(4)	10.2113(4)	5.9713(5)	289.09(2)
α-olivine(0.75 GPa) *	*Pbnm*	4.7413(5)	10.2119(4)	5.9874(5)	289.94(2)
βwadsleyite	*Imma*	5.6983(4)	11.4380(7)	8.2566(8)	538.14
γ-ringwoodite*	$Fd\bar{3}m$	7.9097(3)	-	-	494.863(2)
γ-ringwoodite	$Fd\bar{3}m$	8.0649(1)	-	-	524.522(2)
ε-phase (15 GPa)*	*Pmma*	5.7393(3)	2.8112(3)	8.3399(3)	134.563(2)
ε-phase (ambient)	*Pmma*	5.78(8)	2.88(3)	8.33(14)	139(6)

Table 2.6. *Miller indices, and angular components for reflections assigned to a single ε grain extracted at 15 GPa and ambient temperature.*

h	***k***	***l***	***d − spacing(Å)***
1	0	-3	2.497
0	0	-4	1.958
-2	1	-1	2.115
3	-1	-1	1.569
0	0	-6	1.387
4	0	-2	1.350
0	0	3	2.785
-1	0	3	2.486
1	-1	2	2.153
-1	-1	4	1.596

2.4.5 ε-Mg_2SiO_4 and γ-ringwoodite topotaxial relationships

It has been hypothesized that the α-γ and α-β transition could occur through a shear mechanism when differential stresses are greater than 1 GPa (Raterron *et al.* 2002) or the pressure overstep is large. Here, the last measurable $\langle\sigma_{diff}\rangle$ in α-olivine was found to be 1.49 GPa just at the onset of plastic deformation prior to the pressure being increased to 20 GPa where it can be assumed that the differential stress increased greatly due to the lack of any pressure medium in the

sample. The final measurable stress in olivine was followed by a differential stress of 1.61 GPa in the newly formed γ-ringwoodite after nucleation at 20 GPa and then decompression to 15 GPa, therefore the differential stress during conversion lay somewhere between the two. Also, here a pressure of 20 GPa was reached before conversion was initiated providing a pressure overstep of nearly 5-6 GPa.

Furthermore, in Tomioka *et al.* 2017 the authors also identified the topotaxial relation $(001)_\varepsilon \parallel \{001\}_r$ and $(100)_\varepsilon \parallel \{110\}_\gamma$ through the use of high-resolution transmission electron microscopy (HR-TEM). Having access to the individual orientations of each identified grain we are able to probe for this relation directly. Figure 2.29 compares the obtained orientations for all three phases as upper hemisphere pole figures (p.f's). In the current study we do not find evidence for the same previously described topotaxial relation. The pole figures comparing $(100)_\varepsilon$ and $\{110\}_\gamma$ do show evidence that there is alignment of these planes (e.g., the maxima near X_S and Y_S locations around the border of both) but we do not see the described $(001)_\varepsilon \parallel \{001\}_\gamma$. However, we do see a stronger alignment of $(001)_\varepsilon$ and $\{111\}_\gamma$. We also do not find the $\{111\}_\gamma \parallel (001)_\alpha$ orientation relations seen by Tomioka *et al.* 2017. Although we do not detect these relationships here it does not mean that they do not exist in the sample, for instance, as mentioned previously; due to the rotating nature of the scan, the small 3-dimensional volume sampled, and small apparent grains size, we cannot be certain that the detected ε-phase grains and γ-ringwoodite grains are co-located in a way that would allow visualization of the expected topotaxial relationship. Furthermore, seeing as that the final orientation information that could be collected for olivine was at ~1 GPa and after laser heating there was no detectable olivine orientations to compare to the newly formed γ-ringwoodite we do not know what the transformational orientations of olivine were since there was no meta-stable olivine co-existing with γ-ringwoodite to measure. It is clear from Fig. 8 that the olivine underwent reorientation from Fig.6 during the compression from 1 GPa to 20 GPa.

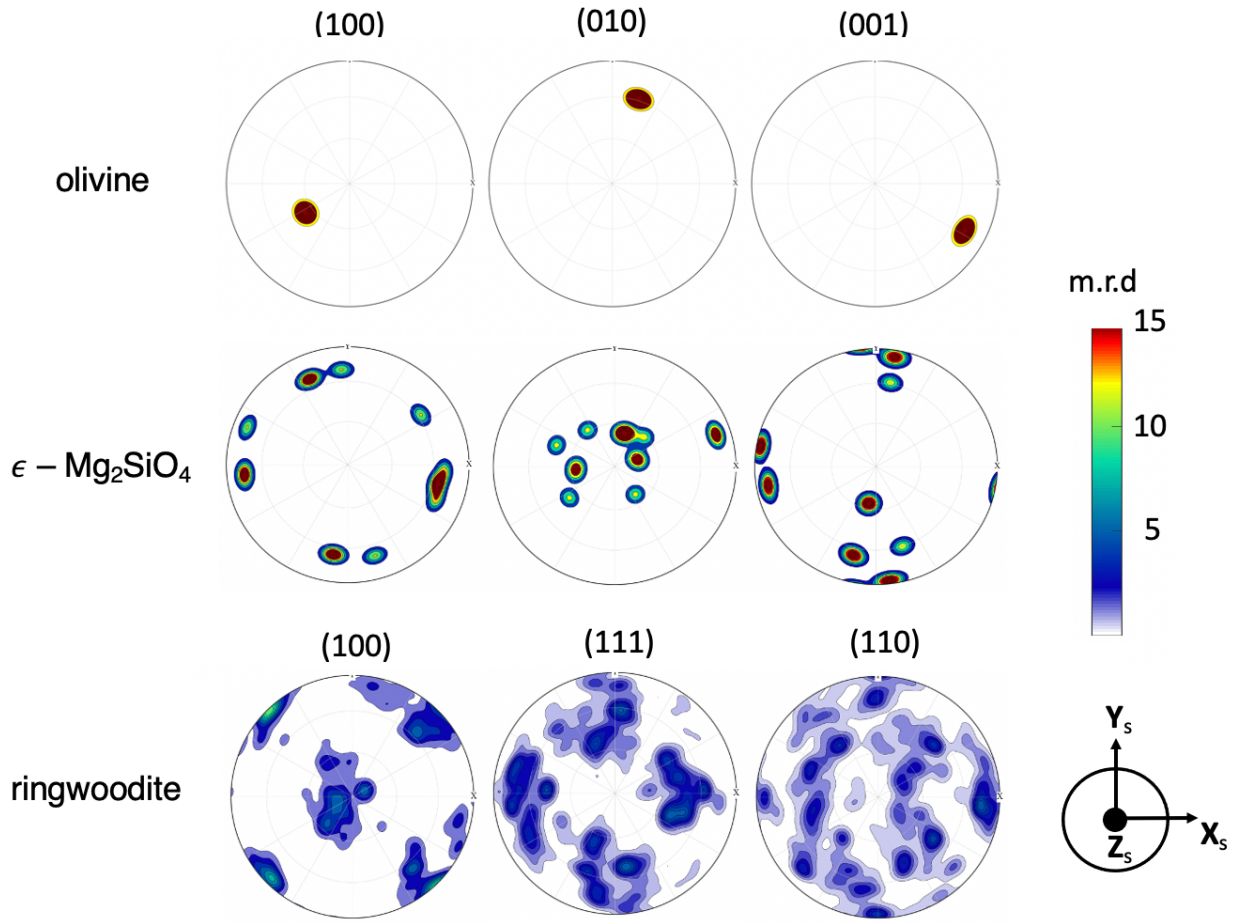

Figure 2.29. *Resulting olivine (top row) ε – Mg_2SiO_4 (middle) and γ-ringwoodite (bottom) orientations shown and olivine starting orientations as equal area pole figures. Sample coordinates are shown to the left with the DAC compression axis into the page (Z_S).*

In this study, pressure was lost in the membrane after the initial heating cycle. Extended heating at pressure would have allowed for grain growth at pressure which could have made this feature more evident and enabled a better grain refinement; (2) due to the numerous orientations of γ-ringwoodite found compared to the number of potential ε- Mg_2SiO_4 orientations, this may have been a topotaxial relationship between parent and daughter grains for which the parent grains did not have enough reflections to constrain the orientation meaning that the relationship may have existed, but we were unable to detect it.

Regardless, this is strong evidence for the experimental presence of the ε-phase seeing as that the conditions within LH-DACs can be comparable to the conditions experienced during meteorite collision which produced the discovered ε-Mg_2SiO_4 with the high strain rates and shock-heating nature of laser heating in a DAC (LH-DAC). For instance, in our study the sample naturally contains Fe which couples extremely well with the infrared laser. Once coupling between the heating laser and sample occurs, the temperatures can spike from 0° to hundreds of C° instantly before settling to a stable value. This is similar to that temperature spike anticipated during impact events. Similarities between LH-DAC experiments and impacts can also be seen in the Fe partitioning occurring in the sample, Tomioka *et al* 2017 found a highly Fe enriched γ phase

compared to the surrounding olivine when investigating the Tenham meteorite. They attributed this partitioning to solid state diffusion from surrounding melt formed in shock veins. Similar Fe partitioning has been seen in LH-DACs (Marquardt and Miyagi 2015) in the br + fp combination leading to a nearly iron depleted bridgmanite phase due to the Fe migrating away from the peak temperature hotspot from the laser system also known as Sorret diffusion (Tyrell *et al.* 1954). Also, the presence of the peaks belonging to ε-Mg_2SiO_4 were not noticed initially in this study and were not discovered until late in the data analysis process due to their weak signal and being surrounded by the fine grained ringwoodite phase. It is possible that the phase did exist in previous reported LH-DAC investigations of the Mg_2SiO_4 system but were buried in the detector noise and primary phases. This study however motivates future experiments at these conditions with an aimed attempt at confirming ε- Mg_2SiO_4 in naturally occurring samples under high *P-T* conditions.

3. Conclusions

In this chapter, the advantages of *MGC* were described in an escalating manor using first a single crystal in ambient conditions showing that it can recover the information provided by the single crystal method. This was followed by monitoring the evolution of olivine under increasing pressure at room temperature until the point of plastic yielding which revealed a much lower yield strength in olivine than previously considered which has implications for the validity of current lithospheric flexure models. This investigation was the first attempt to use *MGC* in this manner, and while preliminary, it highlights the flexibility of this technique. This was followed by increasing pressure into the ringwoodite stability zone and laser heating to induce the olivine→ ringwoodite phase transition at 20 GPa and 1000°C. Here, over 100 grains of ringwoodite where isolated and refined showing a maximum average grain size between 1 and 4.5 μm with its {100} family of place orientated near parallel with the compression direction. Furthermore, grains of ε-Mg_2SiO_4, a phase yet to be seen in a high-pressure experiment. While this technique has the ability to constrain this vast array of parameters, it is not without its experimental limitations i.e., intricate sample loading and characterization, the need for superior detector quality, as well as the need for high energy brilliant X-rays makes this technique only available to those with access to synchrotron facilities. While this technique has yet to become widely used on the geoscience community, it poses as a powerful near all-encompassing technique for the exploration of minerals in extreme environments.

Chapter 3

Exploring the Olivine – Bridgmanite + Ferropericlase Phase Transition using Multigrain Crystallography

3.1 Introduction

Continuing to more extreme conditions in *P-T* space than the previous chapter, and further down the $(Mg_x,F_{x-y})SiO_4$ transformation pathway, olivine can also undergo a dissociative reaction into cubic ferro-periclase, fp (Mg,Fe)O, and orthorhombic, *br* $(Mg_x,Fe_{x-y})SiO_3$ which defines the boundary of the mantle transition zone and the upper portion of the lower mantle. This mineral combination is expected to exist in roughly an 80/20 proportion with the presence of other minor phases such as calcium perovskite $CaSiO_3$ and make up the bulk of the remaining lower mantle all the way down to the core mantle boundary CMB at depths of ~2800 km (Ringwood 1982). The upper portion of the lower mantle appears anisotropically unassuming away from subducting slabs but poses as the first layer of the mantle with two phases contributing to the volume fraction. Several studies in recent years have been aimed at understanding the physical properties of an aggregate comprised of these two minerals by both computational, e.g., Kasemer et al 2020 using finite element methods (FEM) and experimental high *P-T* experimentation (e.g., Kaercher *et al.* 2016, Girard *et al.* 2016, Yamazaki *et al.* 2014). While *br* has been determined to be nearly 8x stronger than ferropericlase in experiments (Yamazaki *et al.* 2014, Girard *et al.* 2016), several hypotheses have been put forward into how this strength contrast may influence local dynamics under lower mantle conditions.

One idea of interest: recent experiments using DAC (Marquardt & Miyagi 2015) at lower mantle conditions have shown a 3x strength increase in fp occurred over a pressure range of 20-65 GPa due to a change in the dominant slip systems from <110>{110} to <110>{100}. If it so occurs that the weaker fp (relative to *br*) phase forms an interconnected network surrounding *br* as predicted by Yamazaki *et al.* 2014, then it is anticipated that fp would control the local rheology by acting as a soft matrix. Marquardt & Miyagi 2015 concluded that if the type of distribution described by Yamazaki et al. 2014 existed, the stiffening of the fp phase could lead to a 2.3x increase in the viscosity structure around a subducting slab leading to possible slab spreading and stagnation between 900 and 1100 km; a phenomenon frequently observed by seismic tomography and contributed to an unexplained "viscosity hill" at these depths (e.g., Fukao & Obayashi 2013, Li *et al.* 2008).

On the microstructural scale, the dynamics and microstructural evolution of the *br* + fp dissociation reaction have been investigated uses several methods. High *P-T in-situ* powder diffraction experiments studying this reaction (Miyagi & Wenk 2015) were able to determine the transformation textures when converting from San Carlos olivine and $MgSiO_3$ enstatite as well as work out the most likely active deformation mechanisms in the *br* phase finding signs of twinning in *br* during these transformations. This study however lacked the spatial resolution to determine the distribution of *br* and fp in the sample chamber. Chen *et al.* 2002 used energy dispersive X-ray diffraction and diffraction intensity analysis to study the relative strength between *br* and the

transition zone mineral ringwoodite at *in-situ* conditions where they also found evidence for (110) twinning in *br* that they attributed to an effect of the compression process concluding that it must be a more energetically favorable deformation mechanism than plastic slip by dislocation initiation. The results of Chen *et al.* 2002 are consistent with results of Wang *et al*. 1990 where both (110) and (112) twins were seen with high resolution transmission electron microscopy (HR-TEM) of *br* synthesized at 26 GPa and 1600 K although the sample had to be examined *ex-situ* and therefore the cause of twinning could not be determined.

The mechanical properties and seismic signature of the br + fp aggregate is also of interest seismologically because anisotropy provides key information needed in mapping mantle flow trajectories were outside of suspected subducting slabs the Earth's mantle is fairly isotropic (e.g., Meade *et al.* 2005, Montagner and Kennett 1996, Panning and Romanowicz 2006). Increased anisotropy in the mantle near slabs and other areas of anticipated increased strain is generally associated with plastic deformation induced crystal preferred orientation (CPO) and can be modeled using plasticity codes e.g., the visco-plastic self-consistent code (VPSC) (Lebensohn and Tome 1993). If there is a lack of significant seismic anisotropy other non-rotational mechanisms must be at play such as twinning (mentioned above) or high temperature recrystallization.

In this chapter MGC is applied at high *P* in an LH-DAC to monitor the microstructural evolution across the dissociative reaction of olivine to br + fp. Experimental considerations and results from two separate experiments at different synchrotron radiation facilities are discussed with Exp. 1 being conducted on beamline 12.2.2 of the Advanced Light Source (ALS) of Lawrence Berkeley National Lab (LBNL) and the second (Exp.2) conducted on beamline 16-IDB of HPCAT at the Advanced Photon Source (APS) of argon national laboratory. The olivine → br + fp system provides an excellent example of the extent of *MGC's* ability to spatially isolate individual grains of unique phases in a coarse-grained sample while providing the resolution at the high pressures and temperatures needed to investigate dynamics in materials at conditions of the Earth's lower mantle. While in this example, application of this method in a laser heated diamond anvil cell (LH-DAC) introduces several experimental hurdles compared to standard diffraction techniques (e.g., modified scanning routines, sample preparation, as well as custom data analysis required to maximize the data extraction) the intent here is to show that a unique method of analysis generally requires unique experimental considerations, but while the experimental preparation is more arduous, the results can be much more enlightening.

3.2 Methods

3.2.1 Sample preparation

Individual grains were isolated from the same thin section prepared in Chapter 2 using optical microscopy with cross polarized light and the tabulated birefringence values for olivine. A single cylindrical column with a diameter of ~ 100 μm was then removed from the same grain by laser mill using systems provided by the high-pressure lab at ALS or APS for the respective experiment.

While the DAC loading process and considerations are identical to Chapter 2, it has been included for completeness and the reader can skip to *section 3.2.2*. Two modified brilliant cut diamond anvils with a culet size of 300 μm were aligned to cBN backing plates and mounted in place using a high temperature epoxy. The diamonds were aligned in the BX-90 DAC (Kantor *et al.* 2012) to near perfect parallelism within sub-micron deviation and checked using optical

microscopy. A 250 μm steel disk was pre-indented to 50 μm and a sample chamber of 100 μm diameter was removed by laser milling with same system used to extract sample grains. The gasket was held in place on one diamond culet using a small piece of puddy until the cell was ready to be loaded. Several ~5 – micron ruby spheres were placed on the opposite diamond culet to be used for pressure measurements throughout the experiment by observing the ruby R1 peak shift with increasing pressure from the reference position. Due to intent of inducing plastic deformation in the samples during compression, no pressure medium was used, and the samples alone were placed in the ~ 100 μm cylindrical hole drilled in the gasket material. It has been shown (Xu *et al.* 2004) that olivine exhibits a low thermal conductivity, roughly 3 watts/m*K at 1000 K, which decreases as $T^{1/2}$ with increasing temperature. Combining this quality with trace amounts of iron in the sample leads to a system that naturally couples with the infra-red laser heating system and therefore no extra coupling agent was added to the sample chamber. This also proves beneficial when performing *MGC* in that no extraneous reflections arise from the coupling material or pressure medium which could appear in a location that also houses reflections from the primary sample. The 2D and 3D calibration procedures and sample used in these experiments were previously described in Chapter 2 (ruby sphere used for both experiments here) and are not included here. Table 3.1 shows the X-ray wavelengths and detectors used for both experiments described in this chapter. There is one key difference between the two detector platforms used in these experiments that should be pointed out which is the pixel size (or pitch) where the marCCD has a pixel size more than twice smaller than the Perkin-Elmer and it will be shown that this leads to drastic resolution differences between the two experiments. Section 3.4.4 will provide a discussion comparing the results here with those from Chapter 2 which used the 10 panel Pilatus detector which has been included as well in Table 2.1 for comparison.

Table 2.1 ***Experimental detector configurations for Exps. 1 – 2.***

Exp.	*Detector*	*Dimensions*	*Pixel pitch (μm)*	*Distance (mm)*	*X-ray energy (keV)*
1	Perkin-Elmer(ALS)	2048x2048	200x200	300	25.008
2	marCCD(APS)	2048x2048	80x80	186	30.001
Ch.2	Pilatus 3M 1s (ALS)	1078x972	178x178	217	29.995

3.2.2 Olivine to bridgmanite + ferropericlase at high P-T

In Exp. 1, after the initial analysis was performed at ambient conditions the sample directly pressed to 30 GPa and heated to a temperature of 1700-1900 K (Fig. 3.2) using the double-sided laser heating system provided at ALS and the temperature was determined using a peak-scaling technique by fitting the Plank function to the recorded sample emittance spectrum (Kunz *et al.* 2018). Four iterations of laser heating followed by quenching the sample to room temperature were conducted. After each heating iteration and quenching, a dataset with the same scanning parameters used for the starting sample was collected at *in-situ* pressure conditions.

During the first 3 iterations of Exp. 1 once the upstream and downstream laser heating spots were brought coincident, the sample was translated with the intent to partially transform a large area of the sample. This method was taken to levy the multigrain technique's ability to isolate neighboring orientations to elucidate and transformation microstructure between meta-stable olivine and the newly forming br phase. Transformation textures in this system have been previously observed via powder diffraction techniques (e.g., Miyagi & Wenk 2016) and the ability

to recreate this texture experimentally is a key point of continuity and reproducibility between experimental techniques.

In Exp. 2, the sample was also exposed to double-sided laser heating, this time that provided by APS (Meng *et al.* 2015) but after the first iteration of 30 min at 1700-1900 K and the presence of br was confirmed, the temperature was increased to 2400-2600 K for three 1hr durations with the intent to completely covert the sample within the heating spot to br + fp and induce grain growth of the new phases. In Exp.2, due to mechanical constrains on the DAC when using a water-cooled jacket for the extended high temperature runs to prevent any shifting of the cell in attempt to achieve symmetric scans; images were taken only using the [-30°,30°] angular range (single wedge scan). This restriction reduces the usable number of diffraction images to 240, from the 480 provided by the symmetric scanning procedure described above, and considerably less than the single crystal scans (1279 at 0.25° steps). The X-ray spot size remained a fixed 2x5 μm throughout Exp.2. Fig 3.1 compares single diffraction images after each heating iteration for both experiments for comparison. Table 3.2 shows the various phases observed and the corresponding *P-T* conditions. While Fig. 3.2 shows the experimental path in *P-T* space.

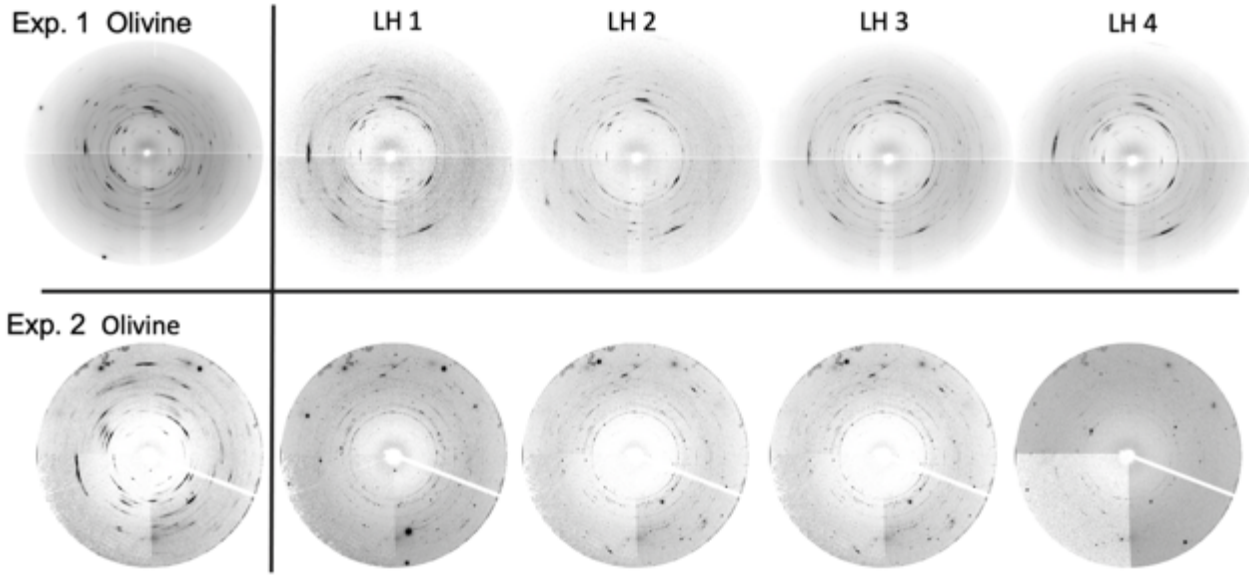

Figure 3.1 Diffraction pattern evolution from Exp. 1 & 2. *Top row shows the diffraction pattern evolution for Exp. 1 with each heating run and (bottom row) for Exp. 2. In Exp.1 remaining texture of the meta-stable olivine phase is seen to remain after all heating runs while in Exp.2 no residual olivine was detected after the 1st heating run showing only newly nucleated br and fp.*

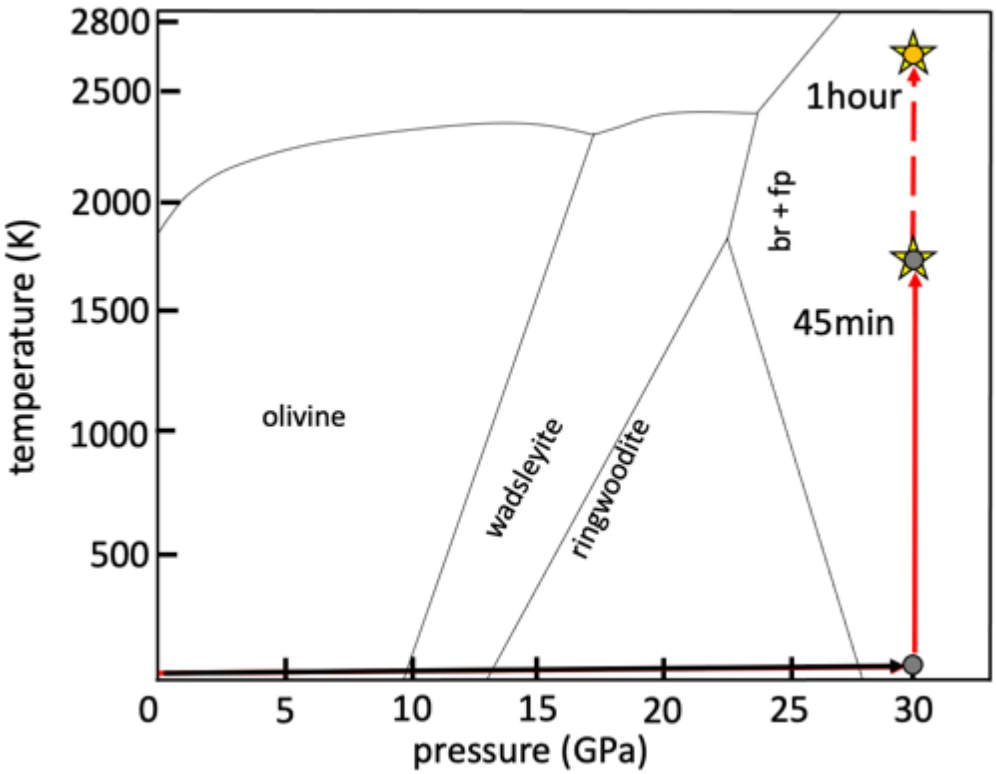

Figure 3.2 Phase diagram for olivine modified from Fei et al. 2004 showing experimental path in P-T space. *Horizontal black line shows increasing pressure. Vertical red arrow shows increasing temperature for Exp.1 and 2(star with grey circle) at 1700-1900 K and 30 GPa. Dashed red line shows increased temperature used in Exp.2 (2400-2600 K).*

Table 3.2 Overview of experiment showing starting sample, observed phases and the corresponding pressures (GPa) and temperatures (K) achieved in each experiment described in this writing.

Exp.	*Starting sample*	*Phases observed*	*Pressures (GPa)*	*Temps (K)*
1	San Carlos Olivine	*olivine*	0	273
		bridgmanite (br)	30	1800 - 2000
		ferropericlase (fp)	30	1800 - 2000
2	San Carlos Olivine	*olivine*	*30*	273
		bridgmanite (br)	*30*	1800 - 2600
		ferropericlase (fp)	*30*	1800 - 2600

During each experiment before increasing pressure after each heating iteration an initial survey diffraction image ("powder image") by collecting over a range of 10° (+/- 5° from the centered position). This is performed for two purposes:

(1) It gives the experimenter a first peak of the condition of the sample (i.e., the crystallinity) as well as an idea of the phases present.
(2) Also allows for checking for any unwanted peak saturation that may be occurring due to intense diffraction from the sample or from the diamonds if the experiment is performed in the axial geometry allowing the beam size and energy to be adjusted accordingly.

3.3 Results

3.3.1 Ambient olivine results

Along the lines of Chapter 2, for Exp.1 a rotational series of the starting olivine sample was collected at ambient conditions (closing condition of the cell). The indexing and grain fitting procedures were conducted in the same manner as the olivine sample in Chapter 2 and the indexing and grain fitting parameters used are included below for completeness. Unfortunately, upon closing the cell, the sample for Exp.2 was deformed and *MGC* analysis was not performed on the ambient sample.

Indexing parameters for ambient olivine sample:
hkls: the 5 highest structure factor reflections *(004) (011) (002) (062) (051)*
The orientation maps were then surveyed, and it was seen that the reflection conditions were not met for the (011) peak and was replaced with a clearly observed *(241)* peak.

η-tolerance: 0.5°
ω-tolerance: 0.5°
Completeness: 0.60

Fit grains parameters for ambient olivine sample:

2θ-tolerances: [0.35°, 0.3°]
η-tolerances: [0.5°, 0.4°]
ω-tolerances: [0.75°, 0.5°]
Max 2θ: 22°

The ***Fit grains*** function was run for 3 iterations until convergence in the grain centroid positions as well as χ^2 (goodness of fit).

Similar to the olivine sample in Chapter two, the ambient sample in Exp.1 also showed visible asterism (Fig 3.3) but with a larger visible misorentation between unique Bragg reflections than that found in Chapter 2. The lattice parameters were refined and the misorientation between the two grains ($\mathbf{G}_a\mathbf{G}_b^{-1}$) was found to be 2.6°. The crystal c-axes of all grains were found orientated ~71° ($\mathbf{\Phi}$) from the compression axis of the DAC but with different azimuthal locations (~35° rotated) from that found in the experiments conducted in Chapter 2 (Fig. 3.4). It is also seen that the (010) and (100) are inverted from one another which makes sense because both samples were taken from the same grain but may have been loaded upside down from one another. The comparison of measured and indexed diffraction spots compared to predicted values is shown in Figs 3.3 d with the deviations in the position and angular components of the diffraction spots and the location of the determined volume averages grain centroids. Table 3.3 summarizes the olivine crystals retrieved from the Experiments of Chapter 2 with those found here after least squares refinement of the lattice parameters.

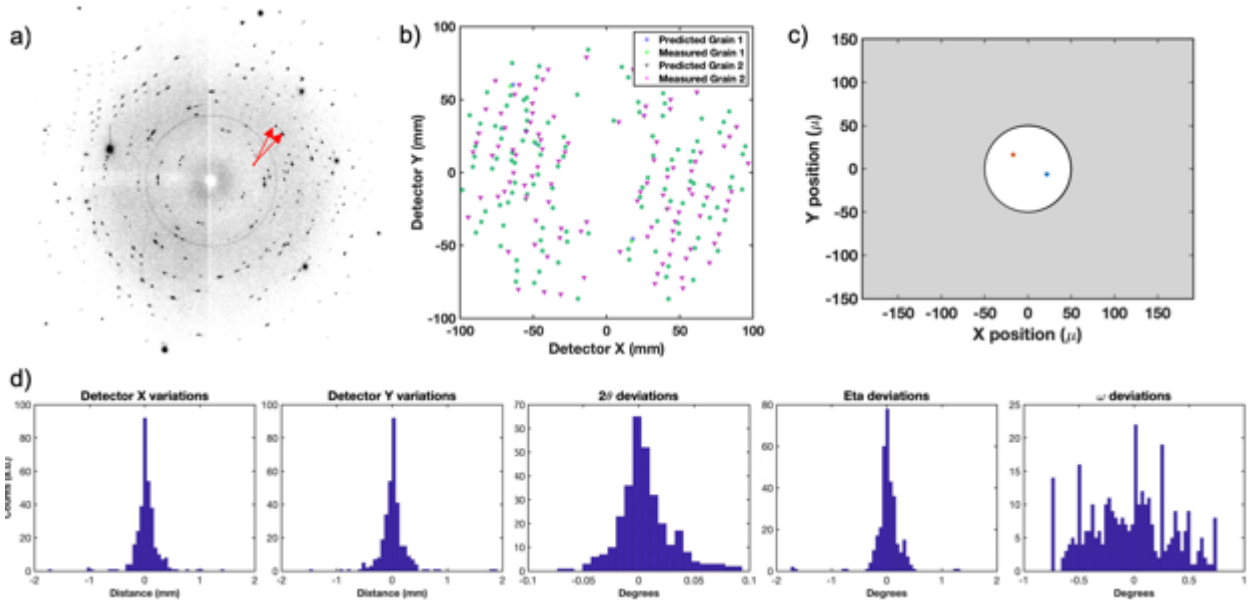

Figure 3.3 Multigrain analysis results of ambient olivine sample from Exp.1. *(a) shows initial diffraction patter taken over a 10° rotation range. (b) provides comparison of measured and predicted diffraction spot locations in the detector frame with select spot identification. (c) Spatial representation in the XY plane of diffracting volume centroids for the two identified olivine grains (red and blue circles). Here the grey boundary represents the gasket material and center circle the 100 μm sample chamber. (d) provides deviations in the spatial and angular components of all indexed diffraction spots as histograms.*

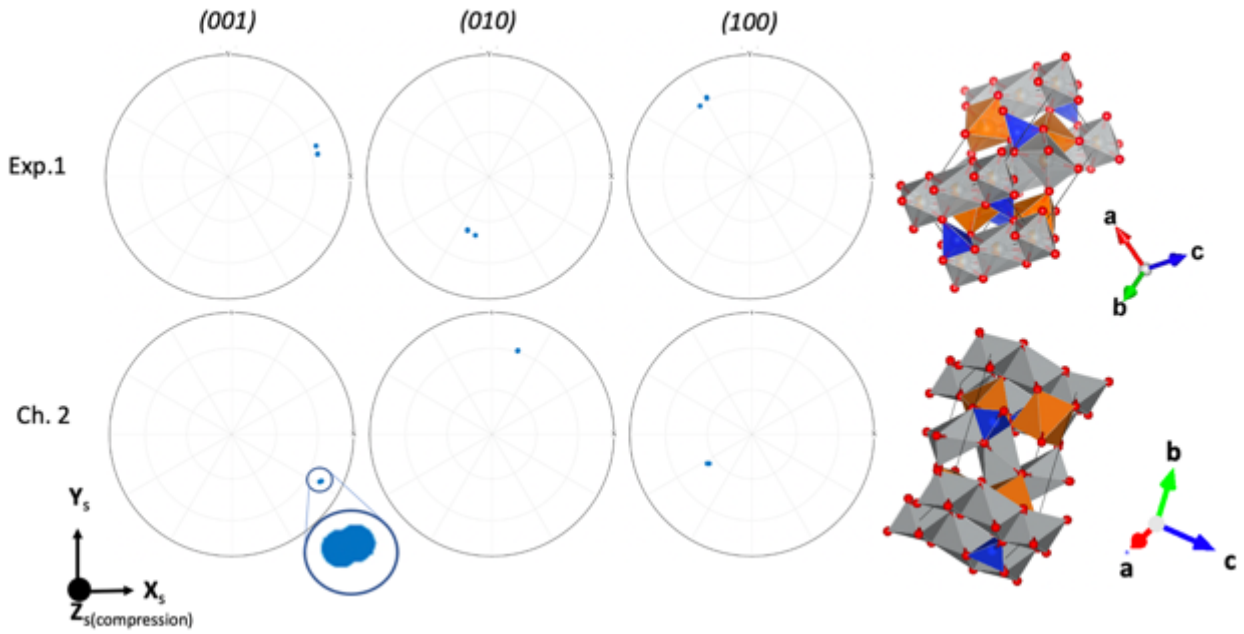

Figure 3.4 Extracted olivine orientations. *Two unique olivine orientations extracted from the sample from Exp.1 (top row) and those found in Ch.2 (bottom row) displayed as stereographic projections of the (001), (010), and (100) lattice plane normal. Polyhedral models of the olivine structure in the appropriate orientation are shown to the right for reference. In the bottom row of the 001-pole location has been provided showing the ~1° separation between orientations detectable.*

Table 3.3. Ambient olivine indexation results. *compares the resulting olivine single crystals extracted from Exps. 1 those discussed in Chapter 2 compared to the refence lattice parameters used in these studies (Zha et al. 1998) as well as the number of reflections gathered for each grain and the overall completion percentage of spots assigned.*

Exp	***Grain #***	***a(Å)***	***b(Å)***	***c(Å)***	***# reflections***	***Completion %***
Reference		4.7631(14)	10.2272(9)	5.9944(10)		
Ch. 2	1	4.7772(4)	10.2599(3)	5.9899(4)	174	64
	2	4.7430(4)	10.2820(3)	5.9649(4)	117	60
Exp.1	1	4.7532(4)	10.2215(3)	5.9916(4)	94	53
	2	4.7422(4)	10.2255(3)	5.9921(4)	84	40

3.3.2 Distinguishing between phases

When examining the multiphase sample here, the analysis proceeds in the same manner as Ch.2. the respective crystal symmetries and lattice parameters of each phase at the experimental pressure must be roughly known and each phase must be indexed separately. These experiments contained up to 3 identifiable phases during any given analysis. olivine, br, and fp all coexisted in Exp. 2 and 3. Olivine and br, who's space groups are both *Pmna,* takes special care when separating these phases during indexation. This is performed by choosing ***active hkls*** and ***seed hkls*** during the indexing procedure that are unique to each phase. For instance, selecting as many Bragg reflections as possible for each phase that at a specific 2θ does not house a possible Bragg

reflection for the other phase. Because the chosen **seed *hkls*** are used for the initial orientation indexing, this ensures that Bragg reflections are unambiguously assigned to the correct phase when constraining the orientations. There is always the possibility that two separate phases sit in an orientation such that high 2θ reflections can be wrongly assigned but the possibility decreases with tighter user provided tolerances. To assist in the indexing procedure, selecting only the highest structure factor reflections can be used which is also facilitated with the *HEXRD GUI* by overlaying all anticipated phases. This allows direct visualization of which seed *hkl's* to choose to prevent cross indexation.

The third existing phase, cubic fp, while easily separable due to a drastic difference in symmetry compared to the other present phases, also takes care due to high symmetry and few unique $\mathbf{G_{hkl}}$. Fig. 3.5 shows a typical image resulting combined diffraction pattern from Exp.2 after the 2nd iteration with select assigned diffraction spots to both br and fp as well as complete separation of both phases. The raw image in Fig. 3.5 (a) show clear distinction between the fine-grained fp reflections appearing with near Debye ring appearance. Table 3.4 shows the number of grains, average reflection assignment and deviations between the observed and predicted reflections.

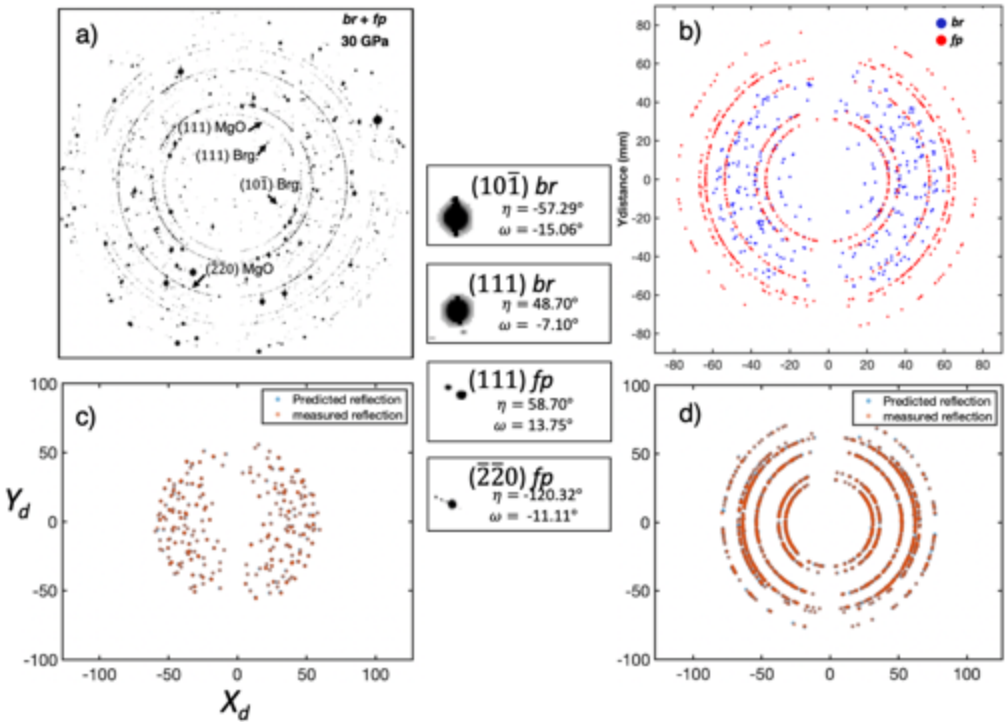

Figure 3.5 Phase identification using the multigrain analysis technique: *(a) Combined image of 240 individual polycrystal diffraction patterns containing br and fp at 30 GPa during Exp. 3 with select miller indices shown for a single br and fp grain. Middle column shows angular locations (η, ω) (azimuthal location, rotational location) of diffraction spot for the shown miller indices in (a). (b) Resulting indexation of diffraction images in (a) of both phases with blue points indicating peaks belonging to 11 individually identified br grains and red belonging to 153 fp grains. (c-d) shows the diffraction spots from (b) further separated by phase showing the locations of predicted reflection location (blue) and assigned reflection location (red).*

Table 3.4 Indexation results for Exp. 1 & 2 by phase*. Values are average deviation in diffraction vector measured locations compared to theoretical values for each data set.*

Phase	*No. grains*	*Avg. Comp. %*	*Avg. 2θ dev(°)*	*Avg. η dev(°)*	*Avg. ωdev.(°)*	*X(mm)*	*Y(mm)*
Exp 1. Starting Sample (ambient)							
olivine	2	41%	0.0079	0.0190	0.0086	0.0135	0.0302
Exp 1. Heat 1(~1900 K 30 GPa 30min.)							
olivine	40	21%	0.0177	0.0362	0.0227	0.0537	0.0055
br	15	23%	0.0156	0.0220	0.0156	0.0178	0.0286
fp	0						
Exp 1. Heat 2 (~1900 K 30 GPa 30min.)							
olivine	7	33%	0.0014	0.0156	0.0195	0.0253	0.0218
br	9	19%	0.0077	0.1330	0.0075	0.0100	0.0224
fp	16	25%	0.0721	0.0791	0.0082	0.0656	0.0639
Exp 1. Heat 3 (~1900 K 30 GPa 30min.)							
br	20	25%	0.0097	0.0331	0.0029	0.0044	0.0067
fp	0						
Exp 1. Heat 4 (~1900 K 30 GPa 45min.)							
br	20	32%	0.0052	0.0134	0.0219	0.0282	0.0283
fp							
Exp. 2 Heat 1 (~2600 K 30 GPa 45 min.)							
br	48	38%	0.0369	0.1427	0.0683	0.0107	0.0183
fp	49	80%	0.0595	0.0947	0.0062	0.0195	0.0181
Exp. 2 Heat 2 (~2600 K 30 GPa 1hr)							
br.	12	35%	0.0375	0.2216	0.2709	0.1478	0.1489
fp	88	77%	0.0213	0.1983	0.2532	0.1327	0.1121
Exp. 2 Heat 3 (~2600 K 30 GPa 1 hr)							
br	21	51%	0.0375	0.2216	0.2709	0.1478	0.1479
fp	88	77%	0.0285	0.3197	0.3525	0.1620	0.2667
Exp. 2 Heat 4 (~2600 K 30 GPa 1hr)							
br	19	44%	0.0439	0.2985	0.2957	0.2112	0.1903
fp	183	89%	0.0262	0.3048	0.3106	0.1645	0.2389

3.3.3 Spatial distribution of bridgmanite and ferropericlase

When exploring the distribution of br and fp inside the sample chamber it was seen that br grains were consistently fewer in number (decreasing from ~ 40 - 9 grains with extended heating) and immersed in a large network of fp (increasing from ~40 - several hundred grains with extended heating) in both experiments. Exp. 3 was able to spatially constrain grain centroids for 10-50

individual grains combined of both phases to within the 100 μm sample chamber as well as provide estimates of the stress/strain for each grain after each heating iteration. Although several hundred unique fp orientations were identified in each dataset, due to the high symmetry and small lattice parameter of fp mentioned above, many identified grains did not provide enough reflections to accurately constrain grain position, or strain, although the associated orientation matrix was resolved. Moreover, because the X-ray beam was focused on the same location of the sample chamber only a finite size of the target is sampled. Consequently, some grains are not being consistently irradiated during the scan but instead move in and out of the path of the X-ray beam as the DAC is rotated. Nevertheless, it was found here that there were consistently fewer, albeit larger diffracting volumes of the br phase surrounded by numerous fp in each run of Exp.2 (Fig. 3.7) and conclude this to be the case also in Exp.1 due to similar ratios in identified unique orientations between br although the same level of resolution could not be achieved with the Perkin-Elmer detector in that experiment.

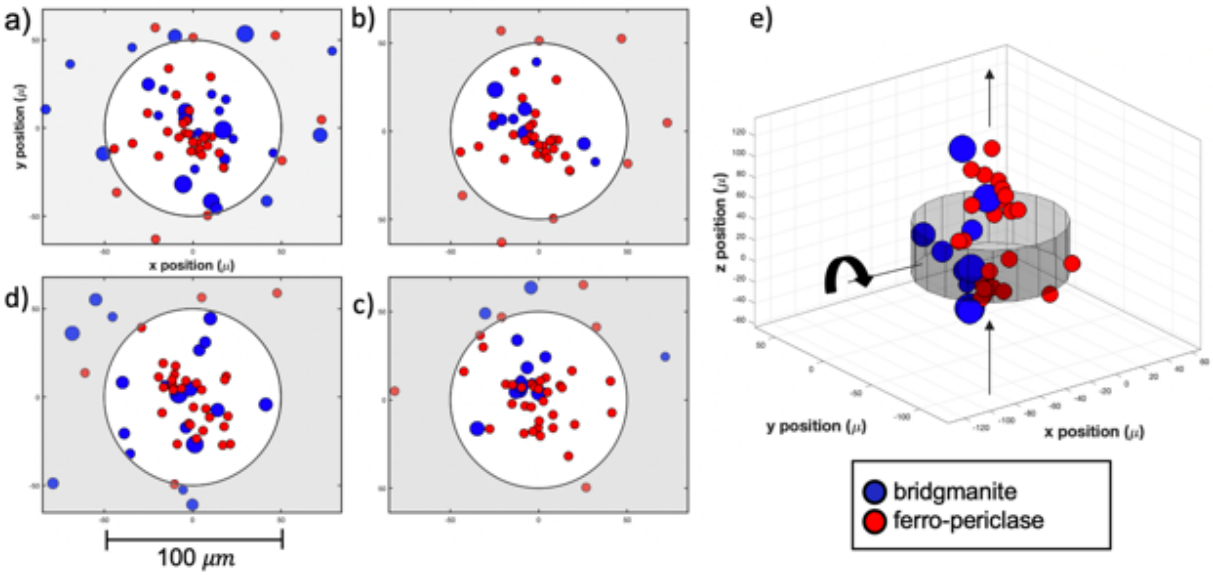

Figure 3.7: Spatial distribution of br and fp after each heating in Exp. 2: *(a) Grain distribution showing br (blue) and fp (red) with respect to the sample chamber. Grey structure represents the rhenium gasket material. Size of grains are scaled by the number of assigned reflections and view is along the incident X-ray axis. (b) Oblique view of grain distribution in (c).*

The sample from Exp.2 was recoverable after decompression and further analyzed using electron back-scatter scanning electron microscopy (BS-SEM) as well as energy dispersive spectroscopy (EDS) (Fig. 2.34). In Fig. 3.8 (a) the heated area of the sample showed several larger structures determined to be nearly completely depleted of Fe and immersed in a matrix of smaller grains of heavy Fe-Mg content but depleted of Si. Compositional analysis showed that these larger grains (1-8 µm linearly in the image) had a composition of $MgSiO_3$ while the smaller (< 1µm) network of material was found to have a composition of (Mg,Fe)O confirming the phase distribution observed *in-situ* and further endorsing that fp likely forms an interconnected network at conditions of the lower mantle. The observed disproportionation of Fe from br to fp has also been reported at higher pressures but similar temperatures of 2200-2400 K (Zhang *et al.* 2014,

Muir *et al.* 2016, Shim *et al.* 2017) indicating that the pure endmember form may be a more abundant form of the br phase in the lower mantle.

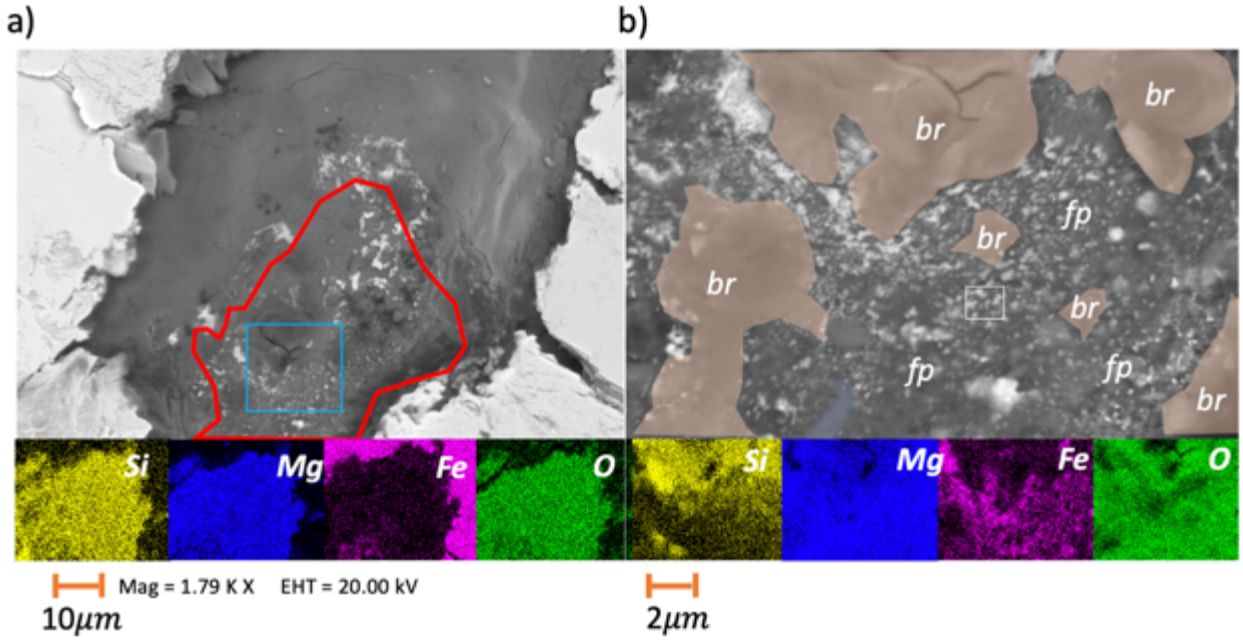

Figure 3.8: Scanning electron microscopy (SEM) and energy dispersive spectroscopy (EDS) analysis of decompressed recovered sample from Exp. 3: *(a) SEM backscatter electron image of sample laser heating spot (red border). (b) Increased magnification of area within blue border in (a). Structures determined to have composition of br shown as orange and labeled. The remaining material was found to have composition of fp. Higher Z-elements (iron in this case) appear as whitest coloring in main images.*

3.3.4 Monitoring mineral microstructures at in-situ pressure conditions

Having the exponential mapped orientation for every indexed grain allows for direct comparison of crystal orientations with the known sample or lab coordinate system, in this case the compression direction of the DAC which is coincident to the sample axis Z_s. The matrix defining each crystal orientation is then used to display the spread of orientations, or "texture", across the olivine to br + fp phase transition using custom written processing scripts created specifically for the outputs of *HEXRD* which utilizes the functions from the *MTEX* software package (Bachmann *et al.* 2010).
The orientation analysis proceeds in two ways:

1. Plotting the distribution of specific crystal plane normal vector with respect to some reference coordinate system known as a pole figure (PF). Here it is natural to choose the compression direction of the DAC which is out of the page in all figures and, also in the axial configuration, aligned with the beam axis.
2. Plotting the so-called inverse pole figure (IPF) which represents any lattice plane normal with respect to the sample coordinates. Due to the symmetry of a specific crystal being shown only a section of the figure is show which represents the symmetry of the complete figure.

Generally, this type of analysis is performed using powder samples consisting of 1000's of grains where the units are in multiples of random distribution (m.r.d). Here, enough individual grains could be simultaneously extracted to display the same style statistical orientation distribution as the powder method but also perform *in-situ* single crystal lattice parameter refinement. Both experiments showed agreement with transformation textures in the olivine to br + fp system described previously using the powder method (Miyagi & Wenk 2016) (Fig. 3.9 red box) with the transformation manifesting with a br maxima along the compression direction extending from (001) to (100) in the inverse pole figures (IPF). Pole figures after the extended heating times for both experiments are shown in Fig. 3.10.

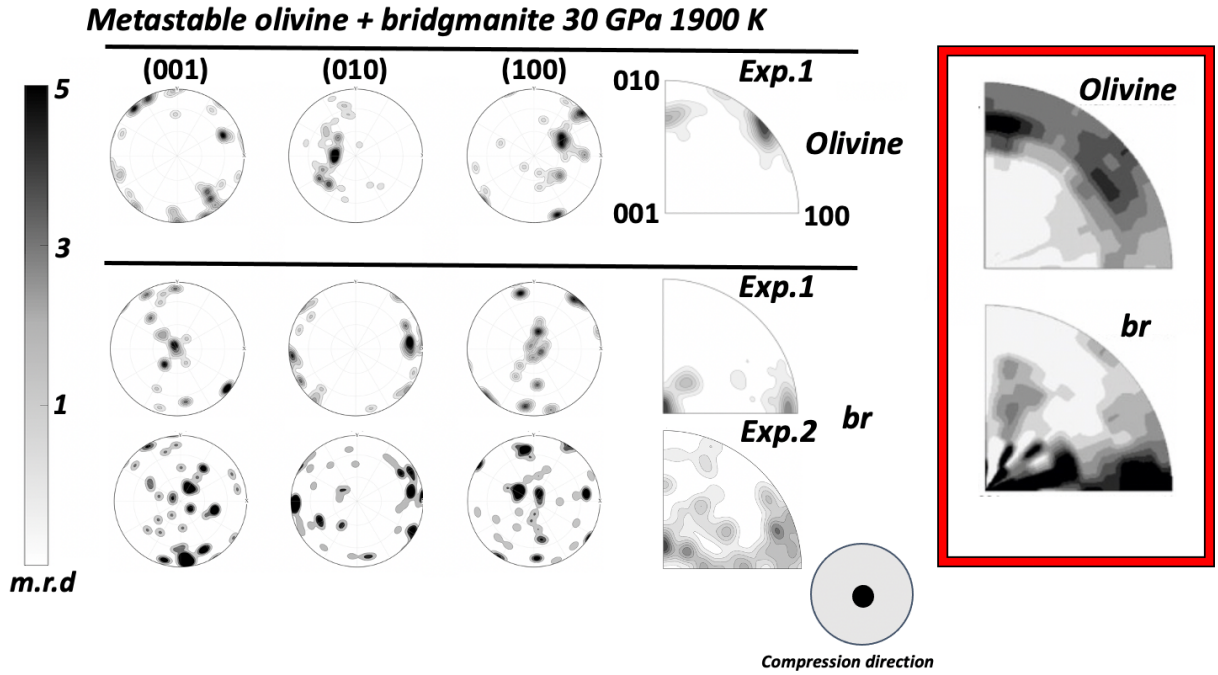

Figure 3.9. Olivine – br transformation texture from Exp.1 & 2 represented as PF and IPF's: *First row:* olivine *textures extracted from 40 unique orientations from Exp. 1. Rows 2-3: br textures retrieved from Exp. 1 (15 grains) & 2 (48 grains) after the first heating iteration at 1900 K. Red box shows* olivine *and br textures obtained by* Miyagi and Wenk 2016 *using the powder method.*

After the first heating iteration the temperature in subsequent heating events was kept at ~1900 in Exp. 2 but increased to ~2400-2600 K for extended periods in Exp. 3 to induce grain growth in the newly forming br and fp phases. With extended heating the br orientation distribution changed from the transformation texture shown above to a more symmetric distribution while the fp orientations remained near random (~1 m.r.d). This new pattern (Fig. 2.36 column 4 rows 3-4) appeared with a pseudo-mirror symmetry in the IPF's and was generally accompanied with an overall increase in the number of detectable br grains. This change in orientations can be interpreted as recrystallization and growth of *br* grains from previously formed *br* as no metastable olivine was detected at this point.

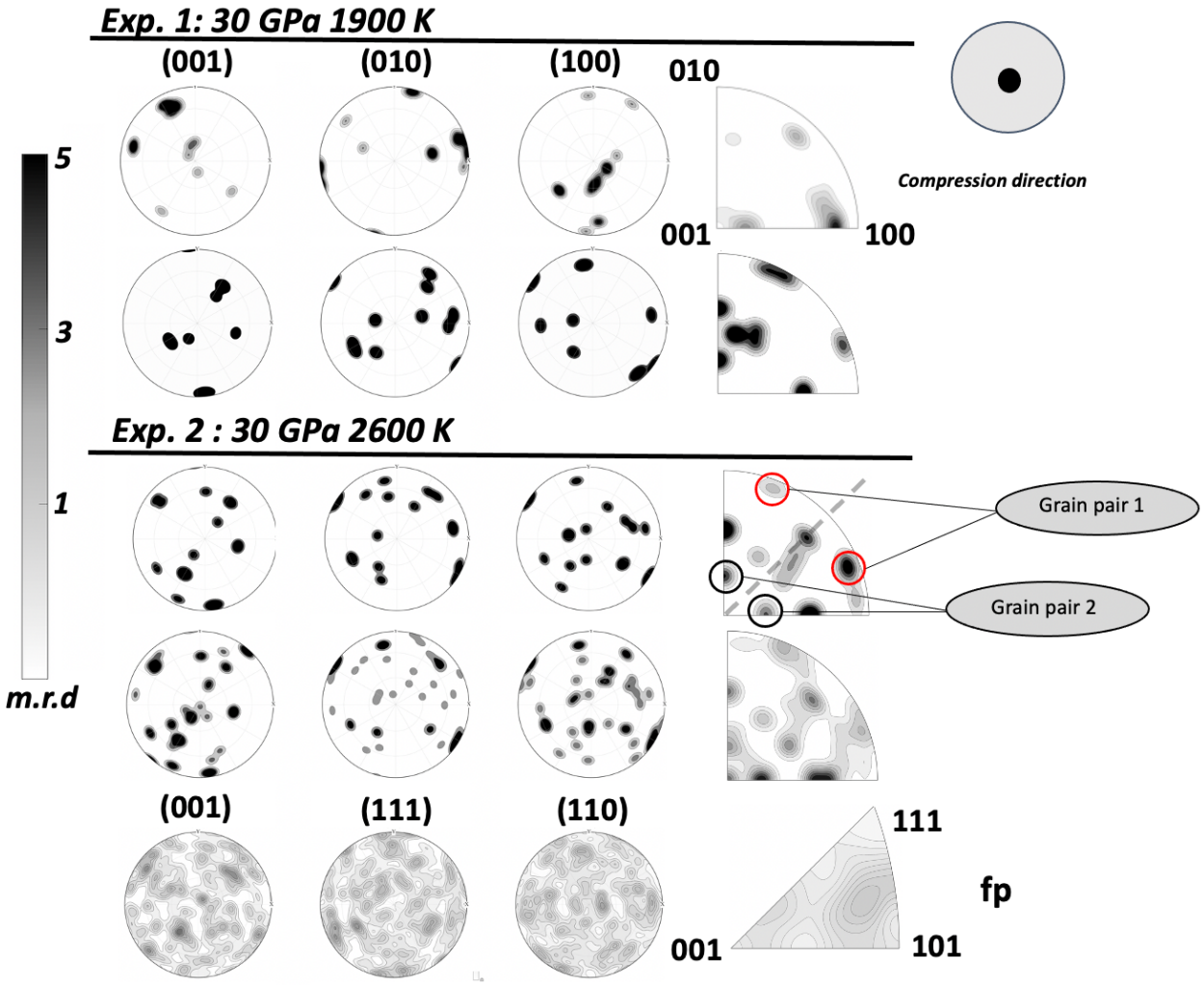

Figure 3.10. Comparing br orientation distributions from Exp. 1 & 2 after extended heating represented as PF and IPF's. *Rows 1-2 show evolving br orientations extracted from Exp.2 (9 and 18 grains respectively). Rows 3-4 extracted from Exp.2 from 21 and 19 br grains respectively. IPF's from Exp.2 with black and red circles encompassing specific orientations used for further analysis described in the text below. Bottom shows a representative distribution of nearly random fp texture consistently observed during both experiments.*

Having access to individual grain orientations as well as the grain volume averaged centroids allowed direct investigation into the origin of the newly formed br orientation distribution observed at the higher, and extended, heating iterations with grain scale resolution. After isolating 2 separate pairs of maxima from Fig. 3.10 (grain pair 1 and grain pair 2) and extracting the spatial location of the grains giving rise to each of these maxima, each pair of maxima was determined to originate from unique grain pairs with overlapping centroids and mutual crystallographic c-axes (Fig 3.11). Each pair was determined to be related by an operation that is a 90° rotation about the c-axis interchanging the *a* and *b* axes, ~ {110} $[001]_{90°}$. In terms of orientations, this equates to each pair sharing their first two orientation Euler angles and a rotation of +/-90° in the third $\left(\varphi_1, \Phi, \varphi_3 = \underset{-}{+}90°\right)$ in Bunge convention. This twinning mechanism was described previously using TEM analyses of br synthesized at 26 GPa and ~1870 K (Wang *et al.*

1990) where it was suggested that the twin formation was likely due to stress relaxation during unloading. This is at odds with findings of (Chen *et al.* 2002) where twinning was determined indirectly at *in-situ* pressure conditions. Here, *MGC* provides the ability to directly observe twinning at *in-situ* pressure conditions with *μm* resolution of grain position as well as direct orientation and stress/strain analysis of each pair.

Elastic constants in Voigt notation derived through ab-initio calculations for both br and fp (Zhang *et al.* 2016) for conditions comparable to the experimental pressure were attached to each respective grain and rotated coincident to each respective grain's rotation matrix using custom writing scripts that are available upon request. The Von-Mises equivalent strain and stress were then calculated as previously described in eqs. 2.12-2.13.

When comparing the equivalent stress in each grain with the grains that were found to obey the determined twin relation described above; each pair also consisted of one higher and one lower stressed grain (26.48 and 1.15 GPa) and (27.78 and 2.03 GPa) shown in Fig. 2.37. These findings lead to the inference that this is most likely a naturally occurring method of stress relaxation in *br* across a large temperature range and is seen here to occur at in-situ pressure conditions unlike what was anticipated by Wang *et al.* 1990.

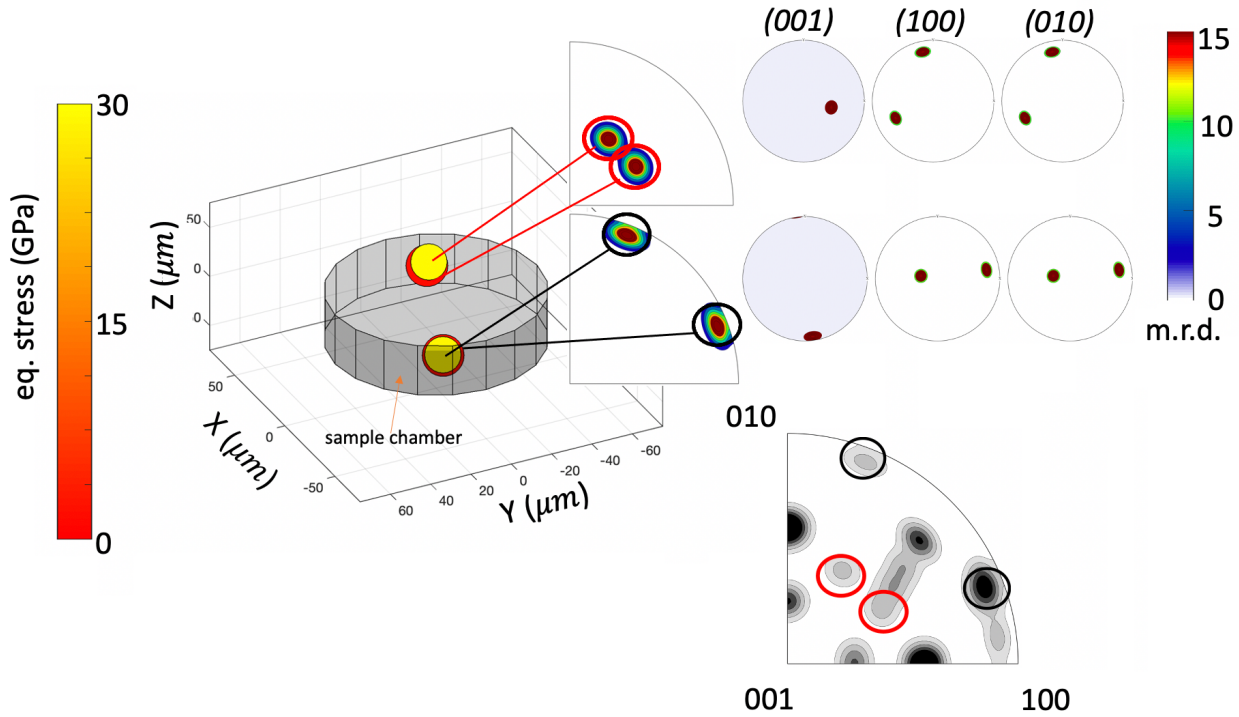

Figure 3.11 Spatially resolved twinning relation observed in bridgmanite. *Two pairs of unique grain centroids isolated from orientations shown in* ***Fig. 2.36*** *(3rd row) with intensities in PFs and IPFs emanating from each grain. Grain color shows variation in average equivalent stress (GPa). (001) pole figures show shared maxima (c-axis) between both grains in each pair. Grey structure represents 100 μm diameter sample chamber. Note: grain centroids are near overlapping therefore black lines attaching each centroid to its respective maxima in the IPF's are included to guide the reader.*

Having constrained several grain centroids to the sample chamber allows for gaining insight to the overall distribution of stress within each phase as well as spatially. This is shown in

Fig. 3.12 where each grain constrained to the 100 µm sample chamber is shown designated in color by its according Von Mises stress and its size by the number of reflections assigned to that grain for both br and fp. Fig. 3.12 also highlights some very interesting phenomenon. It was found that with increased heating, the overall stress in the sample decreased from that held its original plastically deformed state. While this trend (Fig. 3.12 (center) is expected due to typical annealing processes, a phenomenon that is well studied in metals and other materials, after the second heating iteration there was no noticeable plastic deformation so it was anticipated that another stress relieving mechanism must be at play. The global stress distributions in the br phase show in Fig. 3.12(outer) (blue circles) shows most fp grains with stresses at or below 1 GPa yet the overall average in br is 12 GPa. It was found that the larger stress values of the br phase only existed for one grain of each twin pairs.

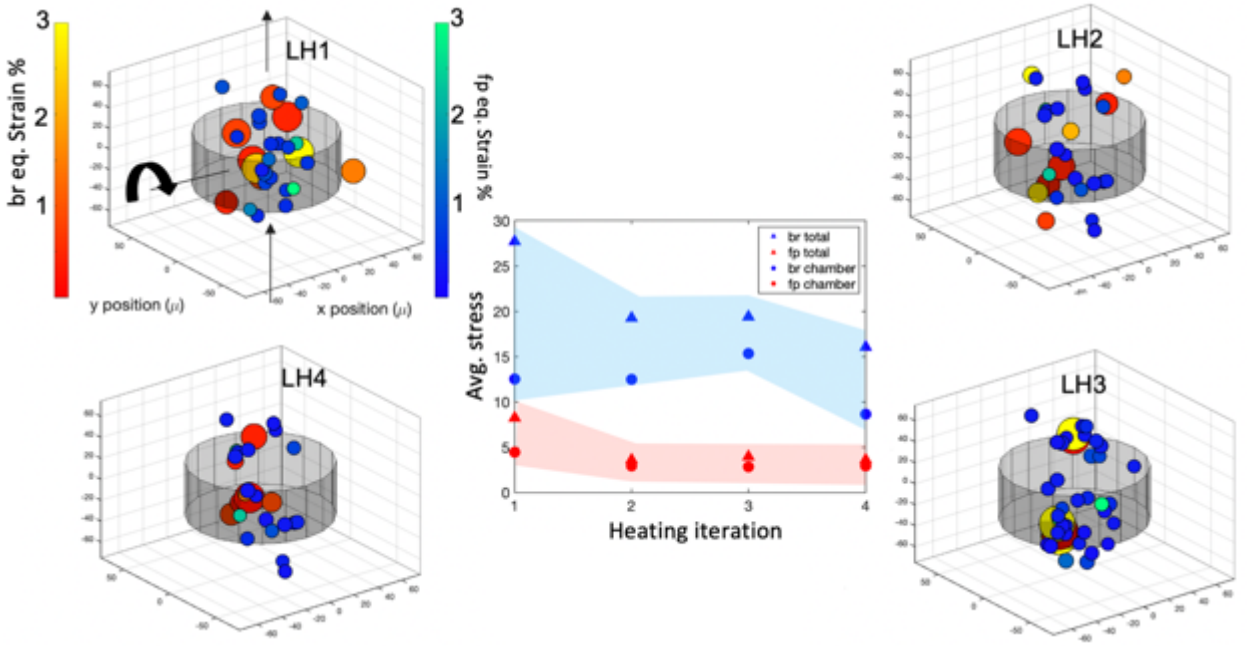

Figure 3.12 Individual grain and phase distributions: *Outer figures: 3-dimensional distributions of br and fp grains constrained within the 100 µm radius from sample center after each heating iteration (LH) in Exp.2. Black arrows represent incident beam direction as well as the rotational axis of the sample. Note that the spatial position is least constrained along z-direction (beam direction) due to the experimental geometry. Blue and red shading in (b) provided to guide the readers eye to the trend in stress. Dot sizes scaled by the number of reflections assigned to each grain. Grain colors are in % equivalent strain. Inner figure: Average equivalent stress in br (blue) and fp (red) plotted against heating iteration for both, all indexed grains compared to those constrained to the sample chamber.*

3.4 Discussion

3.4.1 High pressure distribution of bridgmanite + ferropericlase

On the sample scale, the smaller (1- sub μm) and less strained fp appears distributed around the consistently larger (up to ~ 10 μm) br grains in a configuration consistent with the formation of an interconnected network (Yamazaki *et al*. 2014). Along these lines, the observed reduction in diffraction intensity of fp coupled with the increasing number of grains after each heating cycle is consistent with grain-size reduction (described further in section 3.4.2). This effect is in agreement with the assumption that the viscosity in the upper portion of the lower mantle is affected by an interconnected fp network but in a slightly different way than described by Marquardt & Miyagi 2015 (shown pictorially in Fig. 3.13). The initial formation of the interconnected network of a weaker fp could act initially to decrease the viscosity around a penetrating slab, as proposed by Yamazaki & Karato 2001, perhaps allowing complete or partial penetration beyond the 660 km depth. As the slab pushes through the surrounding mantle, leading to plastic deformation, the increase in strength in fp predicted by Marquardt & Miyagi 2015 would act to slow the slab due to the predicted increase in the surrounding viscosity. In addition to these effects, a scenario that arises from these findings is that when considering the observed diffraction intensity increase from br with each heating cycle, which implies grain growth, it is likely that the interconnected network of fp exists only over a finite depth range. Once br has grown enough to disrupt the fp network, a rheological turnover would occur allowing the stiffer br phase to assume rheological control. This effect could lead to a compounded increase in the viscosity at the slab mantle interface and ultimately to slab stagnation. The rate of disintegration of the fp network, and therefore the depth range, would directly depend on the mantle temperature. For instance, Exp.1 and the first runs of Exp. 2, conducted at average mantle temperatures (1800 – 2000 K) may see this effect at deeper depths while the latter runs of Exp.2 conducted at hot mantle conditions (2200-2600 K) would see it sooner due to the expedient growth of br. In either case, based on these findings, it can be expected that eventually br would grow enough to disrupt this network and shift the control over the local rheology from fp to br.

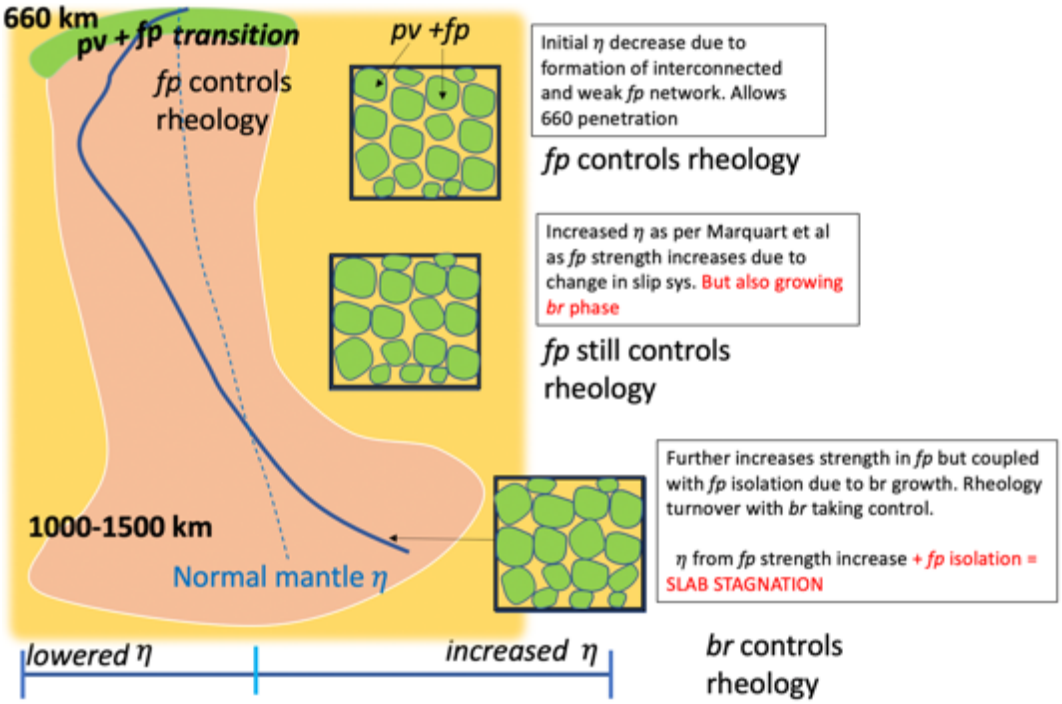

Figure 3.13 Illustration depicting route for slab stagnation due to deterioration of fp interconnected network. *Horizontal axis portrays possible viscosity slab viscosity range compared to the normal mantle. Yellow background represents surrounding mantle while tan represents slab material. In right boxes green = br while yellow = fp.*

Yamazaki *et al.* 2014 provided experimental evidence of an interconnected network of fp at similar conditions using a Kawai-type multi-anvil press, by estimating the dihedral angle of a br + fp aggregate. While our results are consistent with those findings, they report an increase in the connectivity of fp with increasing temperature and also small difference in the grain sizes between the two phases, both at odds with the current study. Key differences lie in the methods of sample preparation and heating technique. In that study, crushed powders (~ 1 μm) from a synthetically derived olivine sample were used. Using a powder would likely introduce different boundary conditions on grain growth as well as a multitude of nucleation sites and furthermore a different stress and strain conditions imparted on individual grains leading to a different microstructural evolution. Furthermore, the resistive heating mechanism in that study provides a smoother increase in temperature (reported at 100°C/*hr*) whereas the laser heating used in this study creates a temperature shock to the desired temperature upon coupling with the material and can introduce large temperature gradients and fluctuations. For example, in Exp.1 due to the gaussian nature of the heating spot, a stable uniform hotspot was observed (+/- 10 K) of ~20 μm diameter but a gradient of up to 500 K away from the hot spot. Furthermore, in both experiments short fluctuations of +/- 300 K were experienced before achieving stability at the desired temperature. These effects were minimized by maintaining the incident X-ray spot size smaller than the uniform portion of the heating spot, although influence of thermal gradients on the collected data cannot be completely ruled out due to the rotational nature of the data collection procedure where at far angles of the scan may sample areas where the gradient was present. Incorporating SEM analysis of recovered sample cross sections obtained via focused ion beam (FIB) in future experiments would allow direct comparisons of microstructure between studies and

capture any effect due to temperature gradients from the laser heating. This approach would also allow for determination of the critical br/fp grain size ratio that would lead to the predicted rheological turnover due to disruption of the fp network.

3.4.2 Estimating grainsizes under mantle conditions

Under the assumptions that the extracted orientations from each experiment comprise all grains within the sampled area upper bounds on the grain size can be determined. This is an upper bound under this assumption because if it so happens that more grains exist in the scanned region then the scanned volume would be divided up to more grains. The beam spot size in Exp.1 & 2 were both 15 μm at full-width half-max (FWHM). Given the DAC rotation range of 60° per side this leads to a scanned volume of 1.08×10^4 μm^3. In Exp. 3 the spots size was 5 μm x 4 μm. For this calculation 5 μm x 5 μm is assumed. This leads to a scanned volume of 3.60×10^3 μm^3. Based on the number of grains constrained for Exps. 1 & 2, Fig. 3.14 shows a plot of the estimated grain size of br and fp assuming an 80/20 volume fraction consistent with compositions estimations of the lower mantle. The grain sizes in br and fp follow the same trend for both experiments where after the 2nd heating iteration the br grain size increases from an initial average nucleation size (6 and 4 for Exp. 1 and 2 respectively) as would be expected due to temperature induced grain growth. Both experiments see a similar grain size reduction after the 3rd heating iteration which is consistent with high temperature recrystallization followed by the re-initiation of grain growth after the 4th heating iteration. For fp on the other hand, a consistent grain size reduction is seen consistent with the decrease in Bragg reflection intensity in the fp phase discussed above. These findings are also consistent with the SEM images taken of the recovered sample after Exp.2 where structures with the $MgSiO_3$ composition showed linear grain sizes ranging from 3-7 μm while the fp phase ranges from <1 μm to 1-2 μm.

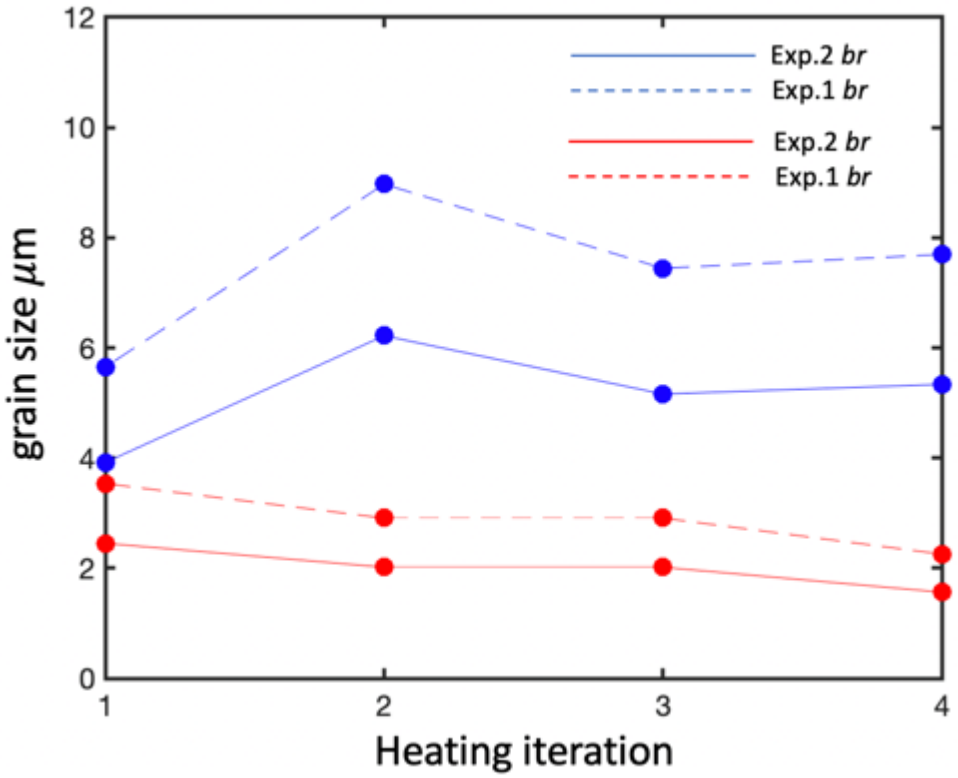

Figure 3.14 Average estimated grain size of br and fp from Exp.1 and Exp.2. *Average Upper bound grain sizes estimated for an 80/20 volume fraction of br (blue) and fp (red) from Exp.1 (dashed lines) and Exp.2 (solid lines). Grain sizes calculated under assumption of a cubic shaped grain using the estimated scan volume divided by the number of identified orientations for both phases. Grain sizes are presented as the edge length of the idealized grain ($\sqrt[3]{grain\ volume}$).*

This is an interesting observation when recalling the experiments on the size effects on the strength of olivine (Idrissi et al. 2015; Kumamoto *et al.* 2017) combined with the findings of the strength increase in fp observed by Marquardt and Miyagi 2015. If fp experiences the same "smaller is stronger" effect observed in olivine, this gradual grain size reduction may play a strong role in the increase in strength through slip system modification seen by Marquardt & Miyagi. Along the lines of the example provided above regarding mantle viscosity, the initial grain size reduction in fp which makes up a weak matrix around br would lower the viscosity around a subducting slab but over time the strength increase due to the size reduction in fp would stiffen the matrix and act to increase the local viscosity structure.

3.4.3 Twinning in bridgmanite and stress relaxation

Twinning in br has been observed in multiple studies, Wang *et al.*1992 used *ex-situ* TEM analyses of br synthesized at similar conditions (26 GPa and ~1870 K) and identified the same twinning relationship determined here although in that study it was attributed to stress relaxation during decompression. This is at odds with these findings and those of Chen *et al. 2002*. In that

study twinning was observed *in situ* at high pressure, albeit indirectly through intensity analysis. In the present work, *MGC* allows direct observation of this relation (Fig. 3.11) at *in situ* pressure with grain scale resolution of the spatial positions and estimates of the stresses/strains in the parent/daughter pairs. While this twinning was also observed in br after extended heating in Exp.1, it occurred at a higher frequency in elevated temperature runs of Exp. 2 where it was found that after the 4th heating cycle, half of all identified br grains were twinned, compared to 24% after the 4th cycle in Exp.1 (Table 3.5). These findings coupled with the anisotropic nature of thermal expansion in br Parise *et al.* 1990 leads to the inference that this is most likely a more energetically favorable way of deviatoric stress relaxation than plastic deformation by slip in br during grain growth across a large temperature range in the lower mantle as it was observed over the full experimental temperature range (1800 -2600 K) conducted here. It is expected here that the stress in the small grain of each pair that was determined to have a stress nearly 10-20x greater than the larger grain is almost certainly overestimated. This arises because of the relationship between the number of assigned reflections and the magnitude of strain which is a consequence of the non-linear least squares problem during the refinement. When there are fewer reflections to fit over a small angular range the least squares problem is no longer over defined as before in Exp. 1 and now the estimates along blind directions are less constrained.

Table 3.5. *Heating temperature, time, twinning % and Avg. Eq. stress for each iteration in Exp.1 and Exp.2 at 30 GPa.*

Iteration	***Temp (K)***	***Time***	***% Twinned***	***Av. Stress br***	***Av. Stress fp***
Exp. 1					
1	1900	15 min	0%	22.37	~
2	1900	30 min	20%	9.172	4.201
3	1900	45 min	0%	21.01	19.25
4	1900	45 min	17%	17.85	3.403
Exp. 2					
1	1900	30 min	25%	8.647	4.302
2	2400	1 hr	32%	6.527	4.201
3	2400	1 hr	33%	8.287	3.263
4	2400	1 hr	45%	7.890	3.403

Furthermore, future explorations combining *MGC* with micro-beam Laue diffraction (μXRD) (Wenk *et al.* 2020) could provide a powerful combination and place further constrains on the stresses in these phases. It is expected that widespread twinning in br could act to disperse crystal preferred orientation that may develop at the high strain interfaces of a subducting slab and the surrounding mantle. This would lead to an overall decrease in any contribution to seismic anisotropy from the br phase at these depths. When combined with the random distributions of fp that were observed in these experiments, this would be consistent with a lower mantle void of significant anisotropy (Wenk & Romanowicz 2017) away from areas where increased plastic deformation occurs, and any crystal preferred orientation develops.

3.4.4 Comparing detector capabilities and resolutions

As *MGC* becomes an increasingly popular route for diffraction-based experiments more nuances and experimental considerations will come to light. To date there has yet to be any systematic study of *MGC* across multiple detector platforms, mostly due to only a select few synchrotron sources providing the capability for the technique. This section acts to initiate this investigation comparing the experimental results across 3 different detectors using comparable X-ray energies and geometries. Detector quality and resolution plays a key factor in the effectiveness and accuracy of *MGC* analysis. To better understand these effects, a discussion between 3 detectors: (1) the Perkin-Elmer area detector and (2) marCCD used in the experiments described above and additionally the (3) Pilatus 10 panel detector is conducted.

When comparing Exps. 1 here and the results of the ambient olivine sample of Ch. 2, during Exp.1 (using the Perkin Elmer at ALS) symmetric scans were collected when using a DAC (480 images and roughly a 120° scanning range) compared to only 240 images and 60° used in Ch.2 for the olivine sample in the pressure membrane, yet the results in Ch.2 (using the Pilatus) showed better resolution of grain position as well as strain tensor components, and also collected nearly twice as many reflections from the olivine sample, but showed very comparable results for the single crystal standard. The increased resolution observed when using the Pilatus arises due to the increased dynamic range of the Pilatus over the Perkin Elmer. The Pilatus is a photon counting detector with 0 inherent background and is very efficient at preventing oversaturation due to intense reflections such as those that come from the diamonds in a DAC or large grains. This is a big advantage when performing *MGC* where rotational series are required and the diamonds will inevitably enter the field of view which then streak across several images, and while they can be manually masked, they will still wash out weak nearby reflections. In the event a photon counting detector is not available, the image stack can be "clipped" to remove the sections of the scans where the diamonds come in and out of view, but this generally takes a 60° scan range and turns it into a usable 20° scan range. This is still sufficient to constrain orientations but almost surely will not constrain grain position or strain tensors due to too few reflections. The better approach is to shrink the beam size as much as possible while maintaining X-ray flux high enough to gain reflection from smaller grains.

The pixel size between the Perkin Elmer and Pilatus are similar at $200\mu m^2$ and $172\mu m^2$ respectively which can be seen by comparable resolution in reflection location on the detector face in the single crystal calibrations. The smaller pixel size and increased dynamic range of the Pilatus also provides better constraints on the reflection morphology which is key to fitting the 2nd order parameters of strain and grain centroid. The ease of the Perkin Elmer to saturate leads to sharp edges to the reflections which does not fit well to a gaussian or Lorentzian function.

While both of these detectors can successfully be used for *MGC,* the Rayonix marCCD greatly surpasses both in resolution due its 80 μm pixel size (less than half of the other two detectors) which allows for a more robust reflection analysis (2 order of magnitude more accurate in reflection centroid location) and very precise fitting of grain position (more than 50 grains constrained within the sample chamber in Exp.2) and strain tensor components even with only a 60° scan, i.e, half the data, double the precision. One limitation of the marCCD is the ease at which it oversaturates and of course the rarity of it being in the detector pool at user facilities. Currently both ALS and APS have this detector although it is only configured for single crystal diffraction at 16-IDB of APS. A few conclusions can be made from comparing these experiments (1) detector pixel size is the driving parameter for strain measurements and grain position. (2) robustness of

results from usable angular range in ω depends directly on the resolution of the detector, i.e., a 120° symmetric scan on a detector with 200 μm pixels does not perform as well as a 60° scan collected by a detector with 80 μm pixels.

3.5 Conclusions

In this chapter, the advantages of *MGC* were described by monitoring the microstructural evolution of an olivine starting sample across the dissociation reaction into br + fp at *P-T* conditions comparable to the upper portion of the lower most mantle. Two separate Synchrotron X-ray diffraction experiments at in-situ pressure showed a weaker fp was found to nucleate as a randomly orientated fine-grained matrix around a larger and 3-4x more stressed br phase consistent with previous results observed on samples recovered from DAC experiments. The μm scale resolution provided by *MGC* allowed for the extraction of individual br grains physical location and the in-situ determination of a twinning relationship in the br phase previously only seen under *ex-situ* observations and when coupled with the random orientations seen in the fp phase provides insight as to why the majority of the lower mantle may be void of any significant anisotropy. Estimations of grain size with heating showed a fluctuation in the br phase consistent with grain growth followed by dynamic recrystallization with twinning as a mechanism for stress relief while fp underwent steady grainsize reduction. Also, *MGC* was applied on 2 detector platforms with clear distinctions discovered between the advantages and disadvantages based on pixel size as well as dynamic range which heavily effect the ability to isolate 2nd order parameters such as volume averaged strain tensor components as well as grain centroids. As a preliminary set of experiments performed using *MGC* with the *HEXRD* software on lower mantle minerals, it is shown here to be a powerful technique that grants access to both the individual crystal as well as the statistical realm of powder diffraction in a single experiment.

Chapter 4

Forward Modeling the Effects of Crystal Preferred Orientation and Phase Transitions on Seismic Anisotropy in the Lowermost Mantle

4.1. Background and Introduction

The deepest 200-300 kilometers of the Earth's mantle form a complex thermal and mechanical boundary layer, D" (Bullen 1949), where the dynamics remain surprisingly elusive. Our current understanding of D" is guided by seismological observations which indicate the presence of significant laterally varying shear wave anisotropy in this region, in contrast to the bulk of the lower mantle which is largely isotropic (see review by Romanowicz & Wenk 2017). Indeed, it has been proposed that large strains during flow in the deep mantle could lead to crystal preferred orientation (CPO) of anisotropic minerals such as the high-pressure magnesium post-perovskite (pPv), which could explain the seismic anisotropy observations (e.g., McNamara *et al*. 2002, 2003; Wenk *et al*. 2011).

Most seismological studies of D" anisotropy rely on splitting measurements of shear waves diffracted (Sdiff) or reflected (ScS) on the CMB (Nowacki *et al.* 2011), as well as core phases SKS/SKKS (Long 2009; Nowacki *et al*. 2011). While such data sample the D" locally, the limited available earthquake source and receiver locations restrict azimuthal coverage. Their interpretation thus relies on simplified models of anisotropy, mainly vertically transverse isotropy (VTI, also referred to as radial anisotropy), in which the speeds of horizontally and vertically polarized waves are different (V_{SH} and V_{SV} respectively). In general, $V_{SH} > V_{SV}$ is found in regions of faster than average isotropic shear wave velocity (V_{Siso}), as imaged by seismic tomography, and attributed to the 'graveyard' of cold slabs. In contrast, $V_{SH} < V_{SV}$ or no significant splitting is found in regions of slower than average V_{Siso} such as the large low shear velocity provinces (LLSVPs) beneath the central Pacific and Africa (e.g., Cottaar & Romanowicz 2013; Lynner & Long 2014) (Fig. 1a). Studies have also aimed at resolving a more general form of anisotropy with a tilted fast axis of anisotropy (TTI) (e.g., Garnero *et al*. 2004; Pisconti *et al*. 2019).

While plastic deformation induced CPO could is a leading candidate to explain the observed anisotropy, consensus has yet to be reached on the underlying deformation mechanisms that could give rise to the observed bulk anisotropic signatures (Cottaar *et al*. 2014; Walker *et al*. 2018; Tommasi *et al*. 2018). Some studies propose that (010) should be the preferred slip plane in pPv based on bond structure and energetic arguments which is based in theoretical computations (Goryaeva *et al*. 2016; 2017) such as molecular dynamics and density functional theory, while others favor a (001) slip plane (Nowacki *et al.* 2011, Cottaar *et al.* 2014), which was found in experimental results (Miyagi *et al*. 2010, Wu *et al*. 2017). Another candidate that has begun to make progress is anisotropic diffusion creep leading to crystal alignment (Dobson *et al*. 2019). In earlier work, dominant slip on (100) has also been proposed (Merkel et al. 2007, Walker et al 2011)

but when incorporated in previous models it provided a poor match to the observed seismic signatures (Wenk *et al.* 2011, Cottaar *et al.* 2014) so it has been excluded from this investigation.

Because an anisotropic signature is mineral unique (or combination of minerals) under specific pressure (*P*) and temperature (*T*) conditions as well as deformation geometries, all of which vary from region to region, a model that explores spatially varying environments is needed to better understand the possible causes of lowermost mantle anisotropy observations. For instance, certain parameters or configurations may explain the observed anisotropic signature during downwelling flow, but not horizontal and the vertical flow experienced during CMB traversal or during plume-like upwelling, or perhaps vice versa. By providing a model that shows continuity between each of these flow regimes a fuller picture begins to take shape.

The present model builds on multi-disciplinary work, in which considered a 3D geodynamic model of a subducting slab driven by solid state convection as it penetrates into the lower mantle and impinges on the CMB (Cottaar *et al*. 2014) (Fig. 1b). Combining the strain inferred from the flow field with a polycrystal plasticity model (Lebensohn & Tomé 1993) and knowledge of the elasticity of pure orthorhombic $MgSiO_3$ endmember phases of bridgmanite (Pv) and post-perovskite (pPv) (Zhang *et al*. 2016), as well as cubic periclase (MgO) (Karki *et al*. 2000) and Ca-perovskite ($CaSiO_3$, CaPv) (Kawaii & Tsuchiya 2015) this model calculates the resulting seismic anisotropy, including spatial and depth variations, due to deformation by dislocation glide within a slab with pyrolitic composition and compared them with seismic observations.

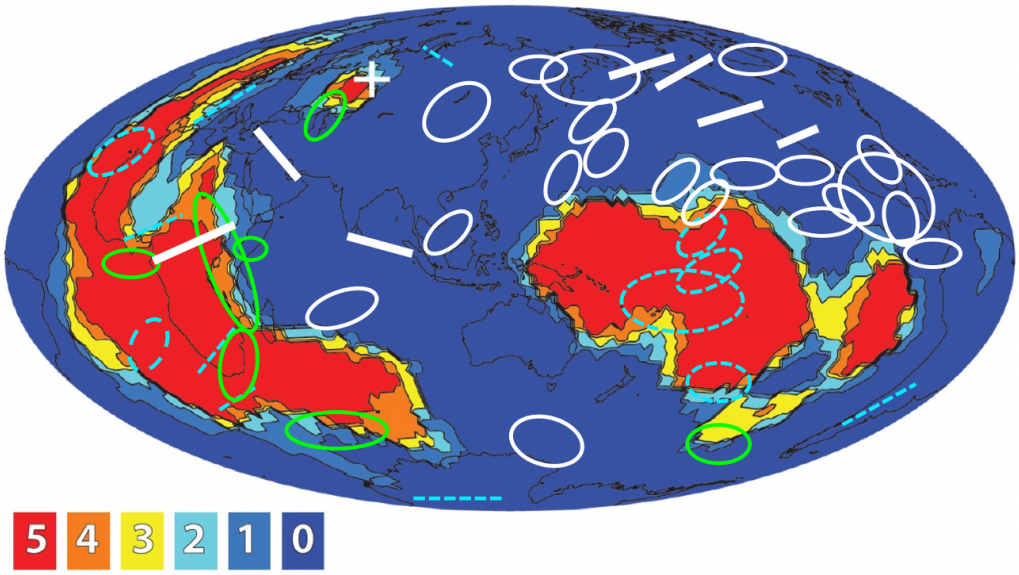

Fig. 4.1. *Observations of radial anisotropy in D". Background: "Voting map" based on 5 shear wave velocity tomographic models showing the locations in D" where the 5 models agree that Vs is lower than average (red) or higher than average (dark blue), highlighting the location of the two LLSVPs and the ring of fast velocities around them. Superimposed ellipses and lines indicate regions where shear wave splitting measurements have inferred Vsh>Vsv (white), Vsh<Vsv (magenta dashed) or the presence of strong lateral variations in anisotropy (green). The latter is found at the borders of the LLSVP and near the PERM anomaly indicated by a white cross. Modified after Romanowicz & Wenk (2017).*

The present study differs from the previous one (Cottaar *et al*. 2014) in four important aspects: 1) use of a more realistic combination of 3 minerals thought to be the dominant phases in the lower mantle in proportions consistent with a pyrolite composition; 2) it introduces a layer of intrinsically denser-than-average material at the base of the mantle, which is pushed around by the descending slab into thick thermochemical piles, from which upwellings initiate, that allows for the examination of the resulting seismic anisotropy and isotropic velocities (V_{Siso}), not only in the downwelling part of the slab but also in the region of onset of upwelling; 3) assuming pressure (*P*) as inferred from the Preliminary Reference Earth Model (PREM, Dziewonski & Anderson 1981) and considering temperature (*T*) variations throughout the geodynamic model, the forward (Pv to pPv) and reverse (pPv to Pv) phase transitions are taken into account in the lowermost mantle and the associated texture inheritance that may occur; and lastly 4) a first-order approximation of partial melting in the deepest portions of the slab at the base of upwelling is introduced in order to gain insight on the effects it may have on the anisotropic signature. Two scenarios are then compared, which differ by the choice of dominant slip systems for pPv, (001) slip for Model 001 (Miyagi *et al*. 2010; Wu *et al*. 2017), and (010) slip for Model 010 (Goryaeva *et al*. 2016, 2017; Tommasi *et al*. 2018). Maps are extracted of radial anisotropy described by the parameter $\xi = (Vsh/Vsv)^2$ and also calculation of shear wave splitting (SWS) directions and strength of splitting (as $100 \cdot \frac{2(V_{S1}-V_{S2})}{V_{S1}+V_{S2}}$) of a seismic wave that propagates horizontally in D", such as Sdiff or ScS

4.2 Methods

4.2.1 3D geodynamic model

Originally 2D geodynamic models were applied to predict seismic anisotropy in the upper part of the lower mantle (Wenk *et al*. 2006) and the D" zone (Wenk *et al*. 2011), here the focus shifts to 3D simulations. Because the 3D geodynamic model (Cottaar *et al*. 2014; Li & Zhong 2017) provides the framework for the macroscopic deformation, it will be described first. The geodynamic model used here was developed using a modified version of CitcomCU under the standard Boussinesq approximation for solving the equations of mass, momentum, and energy (Eq 1-3) (e.g., Zhong 2006) along the same lines as previous works by this group (Cottaar *et al.* 2014).

$$\nabla \cdot \vec{u} = 0 \tag{4.1}$$

$$-\nabla P + \nabla \cdot (\eta \dot{\epsilon}) = Ra(T - BC)\hat{r} \tag{4.2}$$

$$\frac{\partial T}{\partial t} + (\vec{u} \cdot \nabla)T = \nabla^2 T + H \tag{4.3}$$

where $\vec{u}$ is the velocity, P is the pressure, η is the viscosity, $\dot{\epsilon}$ is the strain rate, Ra is the Rayleigh number, T is the temperature, B is the buoyancy number, C is the composition, $\hat{r}$ is a unit vector in radial direction, t is the time, and H is the internal heating rate. The Rayleigh number is defined as:

$$Ra = \frac{\rho g \alpha \Delta T R^3}{\kappa \eta_0} \tag{4.4}$$

where ρ, g, α, κ and η_0 are, respectively, the reference density, gravitational acceleration, thermal expansivity, thermal diffusivity, and reference viscosity. The ΔT is the reference temperature which equals to the temperature different between the surface and the CMB. R is the Earth's radius. In this study, we use Ra=5.36×10^8. The buoyancy number is defined as:

$$B = \frac{\Delta \rho}{\rho \alpha \Delta T} \tag{4.5}$$

where $\Delta\rho$ is the density anomaly with respect to the background mantle. The physical parameters used in the geodynamic model are listed in Table 1.

Table 1. Geodynamic parameters used in this study.

Parameters	Reference value
Earth's radius R	6371 km
Mantle thickness	2890 km
Mantle density ρ	3300 kg/m^3
Thermal expansivity α	3×10^{-5} K^{-1}
Thermal diffusivity κ	1×10^{-6} m^2/s
Gravitational acceleration g	9.8 m/s^2
Temperature change across the mantle ΔT	3000 K
Reference viscosity η_0	1.4×10^{21} Pa s

The model domain has a longitude range of -120^o to 120^o, a colatitude range of 30^o to 150^o, and a depth ranging from the surface to the CMB (Fig. 2 a-b). The viscosity is both temperature- and depth-dependent which is expressed as $\eta = \eta_0 \exp[A(0.6 - T)]$, where A is the dimensionless activation energy and η_0 is the viscosity prefactor. In this study, A = 9.21, which corresponds to a dimensional activation energy of ~190 kJ/mol. The η_0 is varied from 1.0 in the upper mantle to 30.0 in the the lower mantle (Hager, 1984). In addition, there is a 10× linear increase of viscosity

from 660 km to the CMB, similar to that in (Li and Zhong, 2017). There are 128, 256 and 512 elements in the radial, latitudinal, and longitudinal directions, respectively. All boundaries are free-slip except the surface which has a southward constant angular velocity of 3 cm/yr in the region bounded by latitude of 0^o-30^o and longitude of -30^o-30^o and zero velocity outside (Figure 2b). The temperature is isothermal on both top (T=0) and bottom (T=1) and insulating on the sides. A non-dimensional heating rate is applied internally (H= 60). The Rayleigh number is 5.36×10^8 , scaled with the Earth's radius .

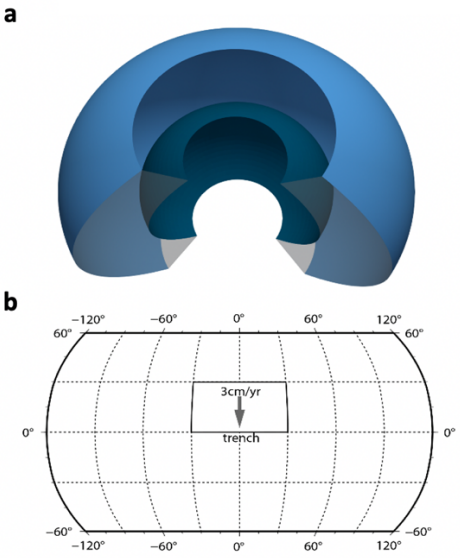

Fig 4.2. Setup of geodynamic model. a*, 3D view of the model domain that covers a depth range of from the surface (blue) to the CMB (green), a longitude range of -120º to 120º, and a latitude range of -60º to 60º.* ***b****, 2D view of the top surface of the model domain. The subducting plate, which is outlined by the solid thick black lines, is imposed with a constant southward angular velocity of 3cm/yr. The surface velocity is zero outside the subducting plate.*

The viscosity is both temperature- and depth-dependent and is defined as:

$$\eta = \eta(r)\exp[A(0.6 - T)] \tag{4.6}$$

where A is the dimensionless activation energy and we use A = 9.21, which corresponds to a dimensional activation energy of ~190 kJ/mol. The $\eta(r)$ is the depth-dependent viscosity prefactor as a function of the dimensionless radius r, and is given by:

$$\eta(r) = \begin{cases} 1.0, & r > 0.8964 \\ 30 \times (24.1 - 25.7r), & r \leq 0.8964' \end{cases} \tag{4.7}$$

such that the $\eta(r)$ increases from 1.0 to 30.0 across the 660 km discontinuity, as suggested by (Hager, 1984), and it continues to increase linearly by 10 times from 660 km to the CMB, similar to that in (Li and Zhong, 2017).

Adding complexity to our previously presented models which focused only on slab impingement on the CMB (Cottaar *et al.* 2014), here, initially a global layer of intrinsically dense material (green structure in Fig. 3 a-c) is introduced to the bottom of the mantle, with a thickness

of 300 km and a buoyancy number of B=0.8 (i.e., ~2% intrinsically denser than regular mantle). This dense material is later pushed by a subducted slab into thermochemical piles in the lowermost mantle. Passive Lagrangian tracers are allowed to subduct with slab material and record the velocity gradient (and therefore strain rate as shown in Fig. 3 d,e) at each time step which are then used to calculate the resultant deformation within the aggregate. The position, temperature, and velocity gradient at each timestep is then extracted and combined with the radial pressure provided by PREM, which is interpolated to each streamline depth to determine the pressure at each point within the model. The streamlines used in this study were selected based on a spatial distribution to sample various deformation geometries present in the slab. Therefore, 25 individual streamlines were selected with multiple sampling from areas including (1) paths nearest to the CMB, (2) paths near the edge of the slab that may experience effects due to the spreading of the slab as it impacts the CMB, (3) areas within the bulk of the slab (away from edges) and (4) sections of the top layer of the slab that fail to meet the phase transition criteria depicted in Fig.4 a. These streamlines all begin above 1000 km depth and end at various heights above the CMB in the upwelling area (radial depths of 1200 – 2000 km) and contain between 400 and 600 deformation steps.

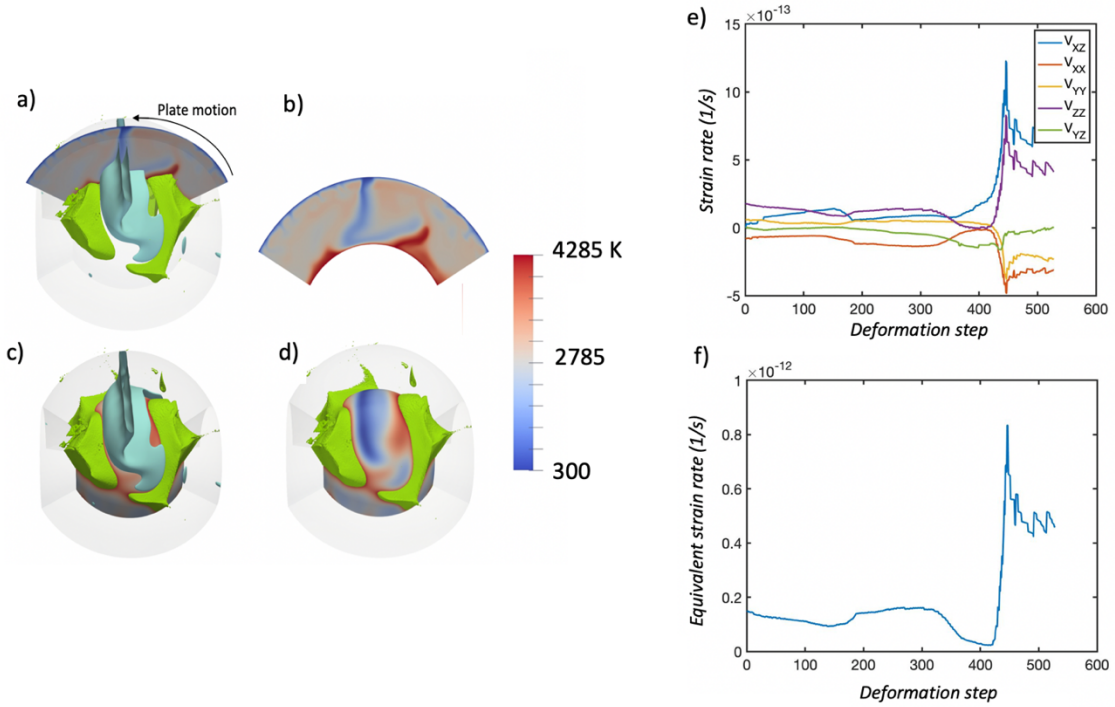

Fig. 4.3. Geodynamic model. *Showing (a) cold slab (blue) impinging on CMB pushing intrinsically dense materials into thermochemical pile (green). (b) Cross section showing non-dimensional temperature (scalebar) variations taken through the slice indicated in grey in (a). (**c**) Dimensional temperature variations in Kelvin at the base of the slab with slab removed.(e) component strain rates for a select streamline at each deformation step are shown in depicting the varying strain regimes as the slab motion evolve and Equivalent strain rate in (f).*

4.2.2 Plastic deformation within the slab

A pyrolytic composition is assumed to be composed of 3 phases (17 % periclase (MgO), 9% $CaSiO_3$ (CaPv), and 74% bridgmanite (Pv) which transforms to post-perovskite (pPv) in D’’). The

aggregate entered each streamline is represented by an initial set of 1000 randomly oriented spherical grains which are plastically deformed according to the recorded velocity gradient along the slab's subduction using the VPSC deformation code (Lebensohn & Tomé 1993). This approach allows us to simulate the plastic deformation of aggregate material by solving the constitutive equations under the Eshelby inclusion formalism in which an inclusion (here a grain) is imbedded in a fully anisotropic, yet homogenous, medium (Eshelby 1957). The self-consistent method applied here are derived under the assumption that the average of the local strain-rate coincides with the macroscopic strain rate.

The deformation in each grain can be characterized by the velocity gradient tensor in the crystal frame L_{ij}^{C} as well as the deformation gradient tensor F_{ij}^{C} (eqns. 8-9) where $\dot{u}$ is the particle velocity.

$$L_{ij}^{C} = \frac{\partial \dot{u}_i^C}{\partial x_j} \tag{4.8}$$

$$F_{ij}^{C} = \frac{\partial x_i^C}{\partial X} \tag{4.9}$$

Where X is the undeformed point in the crystal frame. Furthermore, it can be shown that:

$$\dot{F}^C = L^C : F^C \tag{4.10}$$

and,

$$L_{O_{ij}}^{C} = \frac{\partial \dot{u}_i^C}{\partial X_j} \tag{4.11}$$

Eqn. 10 is the velocity gradient in the crystal frame, which is equivalently written as the shear rates on all active slip and twinning systems (eqn. 12) where *n* and *b* are the slip plane normal and slip direction respectively.

$$L_{O_{ij}}^{C} = \sum_S \dot{\gamma}^S b_i^S n_j^S \tag{4.12}$$

Since plastic deformation is accommodated by shear and shear maintains crystal orientation, the velocity gradient tensor in the crystal frame at every recorded step along each streamline can be polar decomposed into a symmetric and antisymmetric part (eqn. 13) which represent a distortion, or strain, rate D_{ij}^{C} of the crystal followed by a rigid rotation W_{ij}^{C} that is applied at each step in the simulation.

$$L_{ij}^{C} = D_{ij}^{C} + W_{ij}^{C} \tag{13}$$

The strain rate $\dot{\varepsilon}$ is related to the applied stress σ according to the power law $\dot{\varepsilon} \propto \sigma^n$. A stress exponent n = 3 is assumed, corresponding to the dislocation creep regime. Although various deformation mechanisms have been proposed to take place in the lower mantle such as pure dislocation climb (Boioli *et al*. 2017) and diffusion (Ammann et al. 2010), these mechanisms, contrary to dislocation glide, are considered not to produce significant crystal rotations, and can act to weaken existing CPO. Contributions from such non-rotational mechanisms are incorporated here indirectly by allowing assuming 50% of the accrued strain to contribute to plastic deformation by dislocation glide along the lines of previous studies by this group (Wenk *et al.* (2011), Cottaar *et al.* (2014)). Of course, this choice of strain partitioning between rotational and non-rotational

mechanisms is not firmly based in evidence but it can be assumed that the realm of the lower mantle should be in the dislocation creep regime. Furthermore, increasing the strain partition to deformation by slip will act to increase the speed at which the texture develops as well as its intensity and decreasing the partition would have the opposite effect. It has also been argued that diffusion creep may preserve CPO (Wheeler 2009) and furthermore that anisotropic diffusion can lead to the development of CPO (Dobson *et al*. 2019), here, the concentration is only on the slab material itself where dislocation creep is expected to dominate (McNamara *et al.* (2003)).

Plastic deformation occurs on a specific slip system when the applied stress exceeds the critical resolved shear stress (CRSS). Values used in this model for each assumed active system are shown for each phase in Table 2. Values of Amodeo *et al*. (2011) were selected for pure end member MgO, of Mainprice *et al*. (2008) for Pv, of Miyagi *et al.* (2009) for $CaSiO_3$ and two variations of slip systems for the pPv phase. Model 001 contains systems based on high pressure experiments by Miyagi *et al*. (2011) while Model 010 is based on ab-initio calculations of Goryeva *et al*. (2016, 2017) also used by Tommasi *et al*. (2019). For all phases a lowest CRSS of 1 was assigned, even though there is some evidence that MgO may be weaker (e.g., Miyagi & Wenk 2016, Kaesemer *et al*. 2020) this value is kept at 1 in agreement with those used in Tommasi *et al.* (2019). Since MgO and CaPv are minor phases, the impact on the macroscopic picture is not very significant. Also note that for Pv and pPv an artificial slip system {111}<10-1> had to be included with high CRSS to close the yield surface and prevent singularities in VPSC. VPSC proceeds by iterating between measuring the response of individual grains based on the input slip systems and the mean response of the bulk "effective" medium and finds the consistent solution. Grains begin with an assumed spherical shape and are allowed to deform to a ratio of 3:1 after which only grain rigid rotation is allowed. Also, no strain hardening is implemented. Although it is anticipated that the CRSS values would evolve with the *P*, *T* conditions in the lower mantle (Lin *et al*. 2019), this is not accounted for this in the present study because of lack of data. Furthermore, dynamic recrystallization is also not taken into account in the current model even though it may be an important mechanism at lower mantle conditions. It can be incorporated in VPSC calculations (e.g., Wenk & Tomé 1999) but there is no experimental information to define controlling parameters.

Custom scripts were writing to extract the resulting crystal orientations and convert them to Euler angles in Bunge convention (ϕ_1, Φ, ϕ_2) which defines three successive rotations to bring the crystal into the simulation reference frame and then a 3D orientation distribution (ODF) is calculated, and from it pole figures are obtained which are displayed in upper hemisphere projection (Fig. 4 for a selected streamline), using the MTEX software package (Bachmann *et al*. 2010).

Table 2: Deformation mechanisms (slip systems) and relative CRSS values used for each model in this study. Relative CRSS values are provided for each system. (a) Mainprice et al. (2008), (b) Amodeo et al. (2011), (c) Miyagi et al. (2009), (d) Miyagi et al. (2011) , (e) Goryaeva et al. (2016, 2017). Slip system activity for each system is then given as % at two locations along a selected streamline at 200 steps after initiation and then 100 steps after the Pv-pPv transition. * indicates phase not present. **MgO and CaPv activities taken from 010 model.

Phase %	Slip system	CRSS	Act.% Step 200	100 steps after transition	Phase %	Slip System	CRSS	Act.% Step 200	100 steps after transition **
Pv[a] 74%	(010)[100]	1.8	2.6	*	MgO[b**] 17%	{1$\bar{1}$0}<110>	1	14.4	16.4
	(001)[100]	2.5	5.6	*		{100}<110>	1	10.2	10.9
	(100)[010]	1	15.4	*		{111}<110>	5	4.7	5.2
	(001)[010]	1	2.6	*				**29.3**	**32.5**
	(100)[001]	3.8	1.6	*					
	(010)[001]	1.6	5.1	*	CaPv[c**] 9%	{1$\bar{1}$0}<110>	1	5.7	6.4
	{$\bar{1}$10}[001]	1.9	7.6	*		{100}<110>	1.5	4.5	5.4
	(001)<$\bar{1}$10>	1.8	8.1	*		{111}<110>	3.0	0.7	0.9
	{$\bar{1}$10}<110>	2.0	11.2	*		**Total (%)**		**10.9**	**12.7**
			59.8						
pPv[d] 001 74%	**Total (%)**				pPv[e] 010 74%	(010)[100]	1	*	*22.4*
		4	*	1.1		(010)[001]	1	*	*19.5*
		4	*	9.8		{011}[100]	10	*	*2.9*
	(010)[100]	2	*	18.2		(001)[100]	20	*	*0.0*
	(010)[001]	2	*	8.9		{1$\bar{1}$0}<110>	3	*	*10.0*
	(100)[010]	1	*	20.3		{111}<110>	50	*	*0.0*
	(100)[001]	1.5	*	1.0		{111}<011>	50	*	*0.0*
	(001)[100]	3	*	0.0		**Total (%)**			**54.8**
	(001)[010]	4	*	0.8					
	{1$\bar{1}$0}<110>			**60.1**					
	{110}[001]								
	Total (%)								

The pressure *P* (obtained through interpolation using PREM) and temperature *T* (obtained from the geodynamic model) are combined with a chosen Clapeyron slope for the Pv-pPv phase boundary of 11.2 MPa/K (Oganov & Ono 2004; Tsuchiya *et al*. 2004; Hirose *et al*. 2006) is applied to each streamline (illustrated for a single streamline in Fig. 4.3) to find the location of forward and reverse phase transitions. If the transition conditions are met by a tracer crossing into the pPv stability zone, all Pv for that tracer transforms into pPv through the martensitic transformation according to the orientation relations described by Dobson *et al*. (2014) (Fig. 4.3) where it was found that $(110)_{pPv}$ was perpendicular to $[010]_{Pv}$ and maintaining the c-axis. Here the effect of the Pv – pPv phase transition is accounted for by turning each single orientation (ϕ_1, Φ, ϕ_2) into two: $\phi_1, \Phi, \phi_2 + \omega)$ and $\phi_1, \Phi, \phi_2 - \omega)$ with $\omega = 72.94°$ in Bunge convention which is equivalent to the relation described by Dobson *et al.* (2014). Correspondingly the number of MgO and CaPv grains must also double (2 copies of the same orientations). The newly formed pPv then continues to deform with the continuously deformed aggregate until the reverse transition point is met. The

pPv is then allowed to form two Pv grains following the same topotaxial relations. To maintain the grain fractions of each phase, MgO and CaPv grains are doubled again, resulting in a total 4000 grains at the end of the calculations.

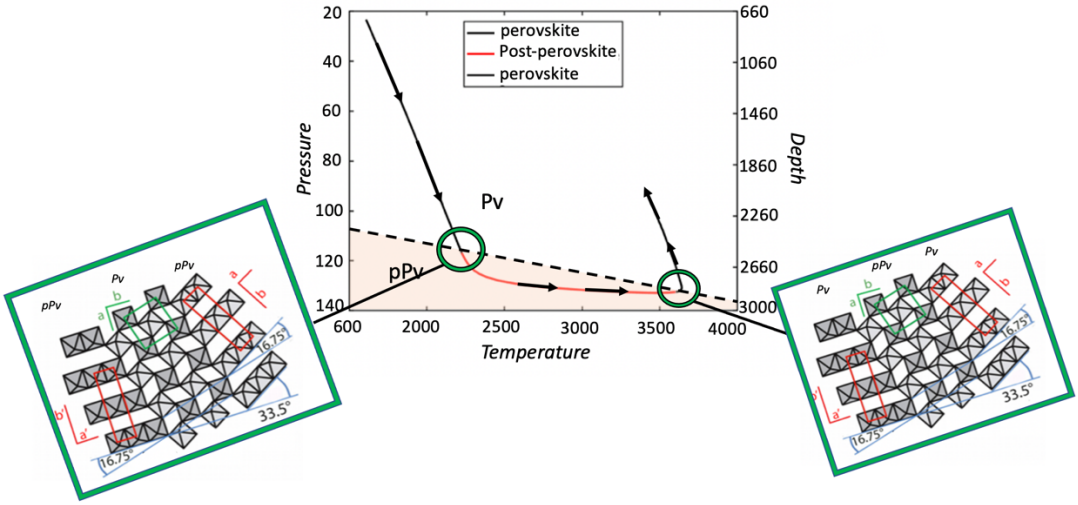

Fig. 4.3. Pv-pPv topotaxial relationship and pPv P/T locations within a streamline*. Shown is a representative deep penetrating streamline experiencing varying T conditions as a function of depth and position, leading to different depths of transformation from Pv (black) to pPv (red) and back to Pv, as the streamline reaches areas of increased temperature. Dashed line in (a) shows Clapeyron slope (Oganov & Ono 2004), and orange shaded area shows P-T conditions where the pPv phase can exist in this model. Topotaxial relationship from Dobson et al. 2014 for the Pv-pPv phase transition considered in this study with green representing the Pv unit cell and red the pPv unit cell.*

4.2.3 Estimations of elastic properties and absolute velocities

To obtain elastic constants and seismic velocities of the 3-phase aggregate, estimates of the single crystal parameters must be known. Here, the constants for pure endmembers: MgO (Karki *et al*. 2000), CaPv (Kawai *et al*. 2009), and Pv and pPv (Zhang *et al*. 2016) due to the availability of data at various $P - T$ conditions. In previous models the evolution of the elastic constants with increasing P-T were not considered and a constant reference value was used (Cottaar *et al*. 2014, Wenk *et al*. 2004), but at the high P-T conditions in the simulated lower mantle an increase of up to 300 GPa can be seen in a given elastic constant. In this study the elastic tensor components of each phase were computed for each P, T condition along the streamlines at every deformation step using a multivariable taylor expansion to the first and second derivatives in P and T (eqn. 4.14)

$$f(Cij)_{PT} = C_{ij}(P,T) + f'(Cij)_P(P,T)(P_1 - P_0) + \frac{1}{2}f''(Cij)_P(P_1 - P_0)^2 \quad (4.14)$$

After each deformation step (which occurs at every recorded point along each streamline), the resulting crystal orientations were combined with the respective elastic tensor through the self-

consistent formalism used in VPSC to determine the elastic properties of the aggregate (Lebensohn *et al.* 2007). The self-consistent approach used here provides estimates of the aggregate elastic tensor with values that fall between the upper bound Voigt which assumes the local strain in the aggregate is constant everywhere (i.e., iso strain) and the Rheus lower bound formulated under the assumption that the local stress is constant everywhere (i.e., iso-stress (Kocks 2000). At each time step along a streamline, the self-consistent aggregate elastic tensor is represented in a 6x6 matrix (21 independent values) (C_{ij}), in Voigt notation, so that each data point in the model space is described by a set of 27 values ($\theta, \varphi, r, T, P, C_{ij}, \rho$). The number of data points in each of the 25 streamlines varies depending on the length of each streamline with values ranging from 350 – 580 data points per streamline resulting in over 10,000 data points throughout the model space. The radial anisotropy parameter ξ which compares the ratio of speeds of horizontally and vertically polarized shear waves was calculated from each aggregate elastic tensor at all points for both models (Fig. 4.7,4.14) using the following equation (Browaeys & Chevrot 2004).

$$\xi = \frac{V_{SH}^2}{V_{SV}^2} = \frac{\frac{1}{8}(C_{11}+C_{22})-\left(\frac{1}{4}C_{12}\right)+\left(\frac{1}{2}C_{66}\right)}{\frac{1}{2}(C_{55}+C_{66})} \qquad (4.15)$$

Determining the aggregate isotropic velocities requires estimations of the density of the individual phases. We obtain the density of each phase at several pressures and temperatures from the literature also used to determine the elastic properties and it was then interpolated to all points within the model, together with each elastic tensor, based on pressure and temperature. As directly constraining the isotropic velocities, composition, and density are beyond the scope of this investigation, the calculated isotropic velocities are compared with PREM as a guide to the applicability of our model to observations, e.g., areas of faster and slower V_{Siso} than the 1D average. The calculated absolute velocities from the model were compared to PREM and the % difference (dVs) was calculated at each point along each streamline while the shear wave splitting (SWS) and radial anisotropy was compared to seismic observations of the lower mantle. SWS and V_{Siso} were computed using the MSAT software package (Walker and Wookey 2012) at selected points that sample different deformation geometries/ flow patterns along each streamline.

4.2.4 Addition of partial melting at the base of the lowermost mantle

In order to gain insight into the effects of partial melting that may occur at the base of upwellings, The P-T data was compared to experimental data of Nomura *et al*. (2014) which looked at the melting conditions of a pyrolytic sample across the whole range of lower mantle conditions with the *P-T* conditions within our model (Fig. 9 b), to determine model locations where partial melting may occur along each streamline. A rough approximation of the properties of a silicate-based partial melt were implemented by incorporating a phase making up a volume fraction of 1-15% of the aggregate that has the rough elastic properties of a silicate melt (Williams & Garnero 1996) and a shear modulus of 0. This phase was given the slip systems of a symmetric cubic crystal with critically resolved shear stress (CRSS) values of 0.01 (relatively no resistance compared to the other phases present) and an initial aspect ratio of 0.1 to simulate an equilibrium melt texture. The elastic properties were approximated under the assumption of isotropic elasticity (Babuska & Cara 1999).

The volume fraction of melt was tested at 1, 5, 10, and 15 %. An equivalent volume fraction was then removed from the Pv/pPv phase to accommodate the added 1-15% of partial melt. Because the model space where partial melting is observed only varies in *T* by at most 50 K and roughly 20 GPa, and due to a lack of *P* and *T* derivatives at lower mantle conditions for a partial melt, this model does not impose *P-T* variations in the elastic properties of the melt phase or the *P-T* effects to the density but rather directly impose the experimental values. As the volume fraction of melt increases the melt density contribution to the aggregate density would increase and would have to be considered.

This study only aims to observe a first order approximation of the effect from the addition of melt. Moreover, at low percentages of partial melting, the choice of volume percent partitioning was found to have little effect on the calculated signature of anisotropy from the aggregate. This is to be expected since the signature is dominated by the Pv/pPv phase where a loss of 15% at most still places it abundance more than 40% more than the second most prevalent phase, MgO. This implementation is a rough approximation but argue that it provides insight into the effects on anisotropy at the onset of melting for low volume fractions. It also provides first order insight on the trends in isotropic velocities that could be expected in these high temperature areas and then the corresponding anisotropic signature of the aggregate, and also on the complicated signatures of anisotropy and velocities that may arise due to the presence of layering of phases atop a partial melt layer near the CMB.

4.3 Results

4.3.1 CPO evolution within the slab

The CPO evolution within the slab is dictated by the evolving strain rate as the slab moves into different flow regimes. For instance, during downwelling it is found an average equivalent strain rate of ~1.15 x 10^{-13} s^{-1} and increasing by ~1.6 as the slab turns along the CMB (Fig. 4.2 e), which leads to an increase in CPO within the aggregate. The strain rate reaches a minimum once the slab material meets the pile but is then forced into upwelling flow and the rate of strain dramatically increases to ~ 8 x 10^{-13} s^{-1} (38x increase at a depth of 2296 km, ~500 km above the CMB compared to the minimum value as the slab meets the pile) and then decreases as the material travels upward away from the CMB. Figure 4.4 shows the crystal preferred orientation (CPO) developed along a selected streamline for both tested models at three important locations within the slab: 1) just before the Pv-pPv transition (first row), 2) during horizontal flow along the CMB (rows 2-3), and 3) during upwelling (post reverse pPv – Pv transition in rows 4-5). Both models are identical except for the dominant slip systems in the pPv phase. The initial Pv texture shows a strong (100) texture just prior to the phase transition ~8 m.r.d. which is immediately dispersed once the phase transition is initiated. After the phase transition occurs (signified by horizontal black lines in Fig. 4), Model 001 develops a steady increase of an (001) maximum orthogonal to the material flow direction due to “textural inheritance” from the (001) maximum developed in the parent Pv phase. While Model 010 shares an (010) distribution similar to that of Model 001, albeit weaker, the normals to the (001) and (100) lattice planes are nearly orthogonal between the two models. The secondary cubic phases MgO and CaPv both develop CPO in a girdled fashion with maxima nearly aligned with the flow direction attaining a maximum of ~5 m.r.d. during downwelling, that is maintained throughout the simulation. After the reverse pPv – Pv phase transition, the (001) texture is again inherited into the daughter Pv phase and continues to increase in strength as well as rotate with the flow direction for Model 001, reaching a maximum of ~10 m.r.d. Model 010, on the other hand,

sees an initial dispersion of CPO just after the reverse phase transition and only reaches a maximum of ~4-5 m.r.d for any slip system in the volumetrically dominant Pv phase during upwelling.

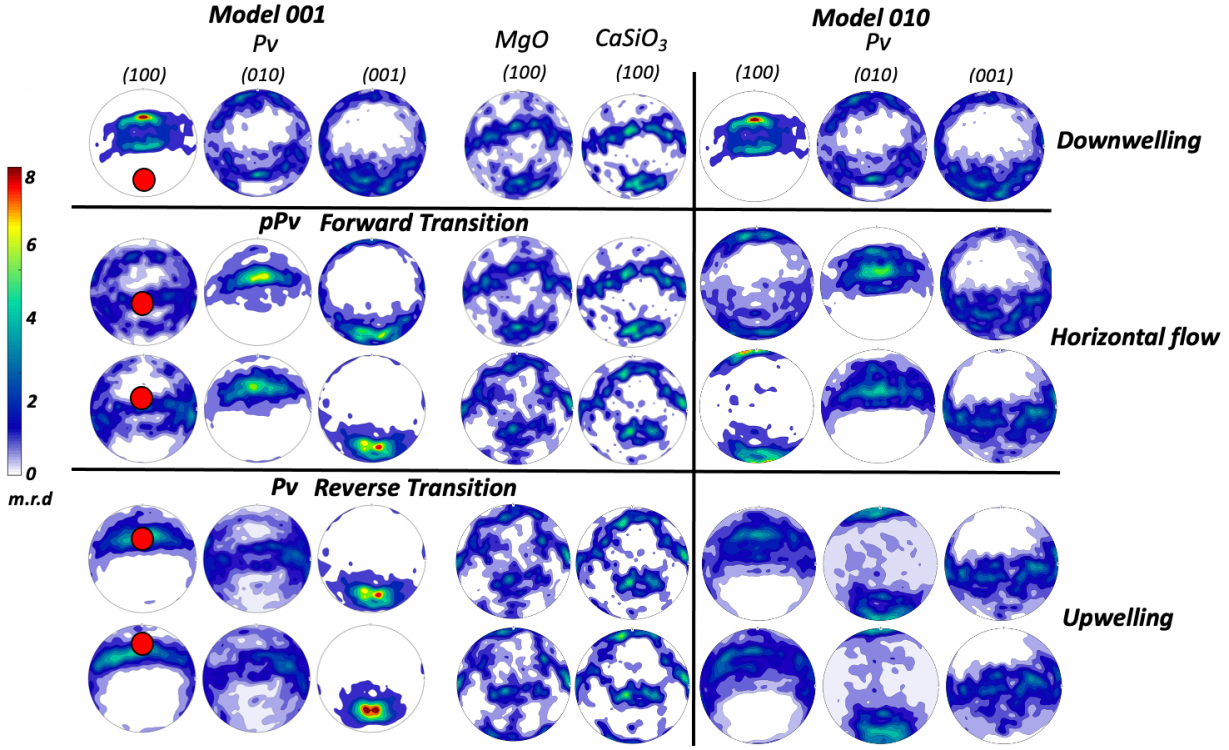

Fig. 4.4 Plastic deformation within the slab. *Deformation of Pv/pPv + MgO + $CaSiO_3$ for Model 001 and Model 010 at locations just before and after the forward and reverse phase transitions streamline 3 in Fig.8. Textures are represented as equal area upper projection pole figures and shown in a scale of multiples of random distribution (m.r.d). The CMB is horizontal in all images. Flow direction is indicated by red dots in the first column and is the same across all pole figures.*

4.3.2 Shear wave anisotropy

Given the weakly anisotropic elastic structure of the dominant Pv phase, it is found that the initial downwelling part of the slab appears largely isotropic. The forward Pv-pPv transformation occurs over a range of 50 km (2550 – 2600 km) and leads to an abrupt jump in both absolute shear (~1.5% on average, 3.5% max) and compressional (1.5% to 4.0%) wave velocities (Fig. 4.5. This measured jump in isotropic velocities is accompanied by the appearance of a lower symmetry anisotropy than the generally assumed vertical transverse anisotropy (VTI) (Fig. 4.6 with $V_{SH} > V_{SV}$ $(i.e. \xi > 1)$ (Fig. 7 a,b), with ξ steadily increasing as the slab proceeds along the CMB, in both models, from a value of 1-3% . ($\xi = 1.01 - 1.03$) to a maximum of ~6% in the deepest parts of the slab, as it impinges on the CMB. Horizontal fast axis orientation (also region highlighted in red for presence of pPv in Fig. 4.7 (c,d) continues throughout the region of horizontal flow along the CMB, in agreement with seismic observations in regions of slab graveyards (Panning & Romanowicz 2006; Sturgeon *et al*. 2019). To further highlight the key difference between the two models, the region of slab showing the strongest variations between the models is inscribed with a black circle in 4.7 c,d. Here a clear difference at the base of the intrinsically dense layer (orange

structure) can be seen in the polarizations of the fast shear wave where Model 001 is predominately changing from horizontally orientated to vertical, where in Model 010 a fast horizontal polarization stays prominent.

Due to the 3-dimensional nature of the geodynamic model, this enables the ability to investigate deformation arising from the heterogenous strains imparted along different paths through the thickness of the slab such as edges, where spreading and rolling occur as the slab impacts and traverses the CMB near the edges of the simulated LLSVP resulting in varying depth and azimuthal anisotropic signatures. Results here show a plane of highest shear wave anisotropy with a tilted axis of symmetry (tilted transverse anisotropy (TTI) with an incline of up to ~20-30° (Fig. 4.8 no. 3) similar to that observed at D'' depths beneath the Caribbean (Garnero *et al.* 2004). Included in Figure 4.8b is also a streamline (1) that fails to meet the phase transition conversion criteria and therefore retains the Pv phase. The Pv layer atop the slab exhibits a vertically oriented fast s-wave propagation direction orthogonal to the horizontally oriented fast s-wave of the underlain pPv.

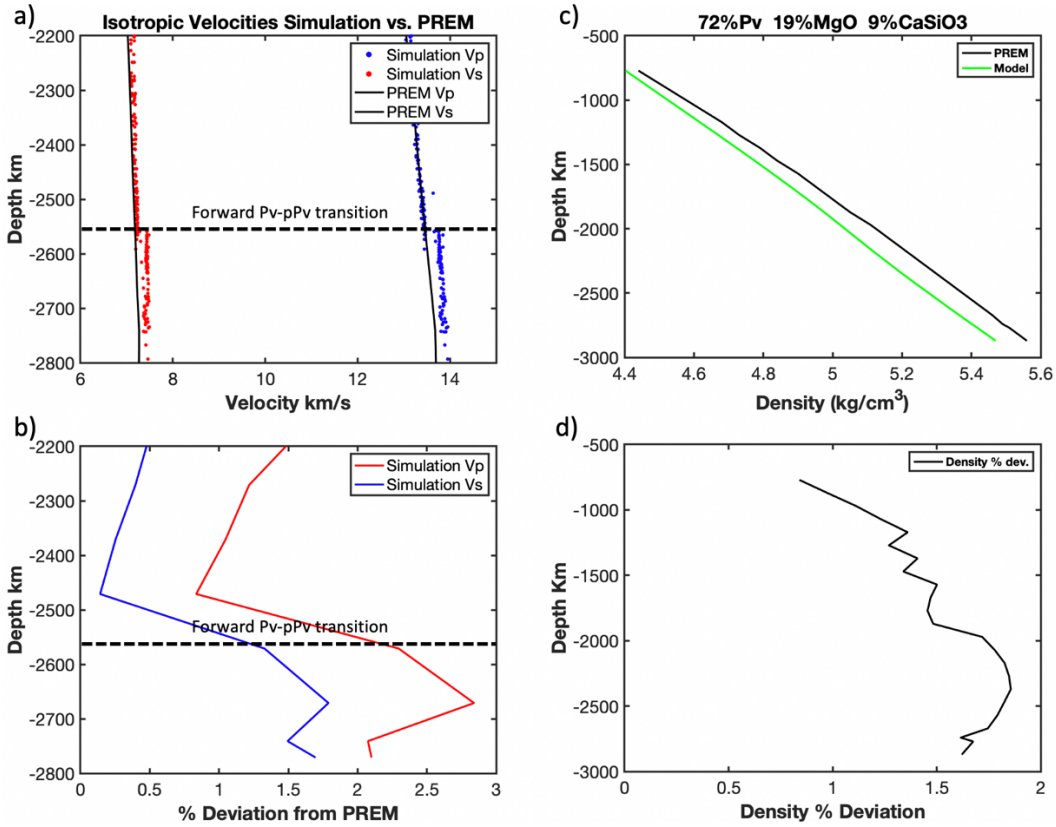

Fig. 4.5. Comparing isotropic velocities and density of the model aggregate with composition and PREM*. Model isotropic shear (red) and compressional (blue) wave speed as well as density (green) compared to PREM (black). The range of the Pv-pPv phase transition represented by grey shading and clearly demarcated by the abrupt jump in all three parameters at ~2560 expanding to just past 2600 km. Errors in density below 2000 km range from 0.4 – 1.8% compared to PREM. Units g/cc are for densities and km/s for velocities.*

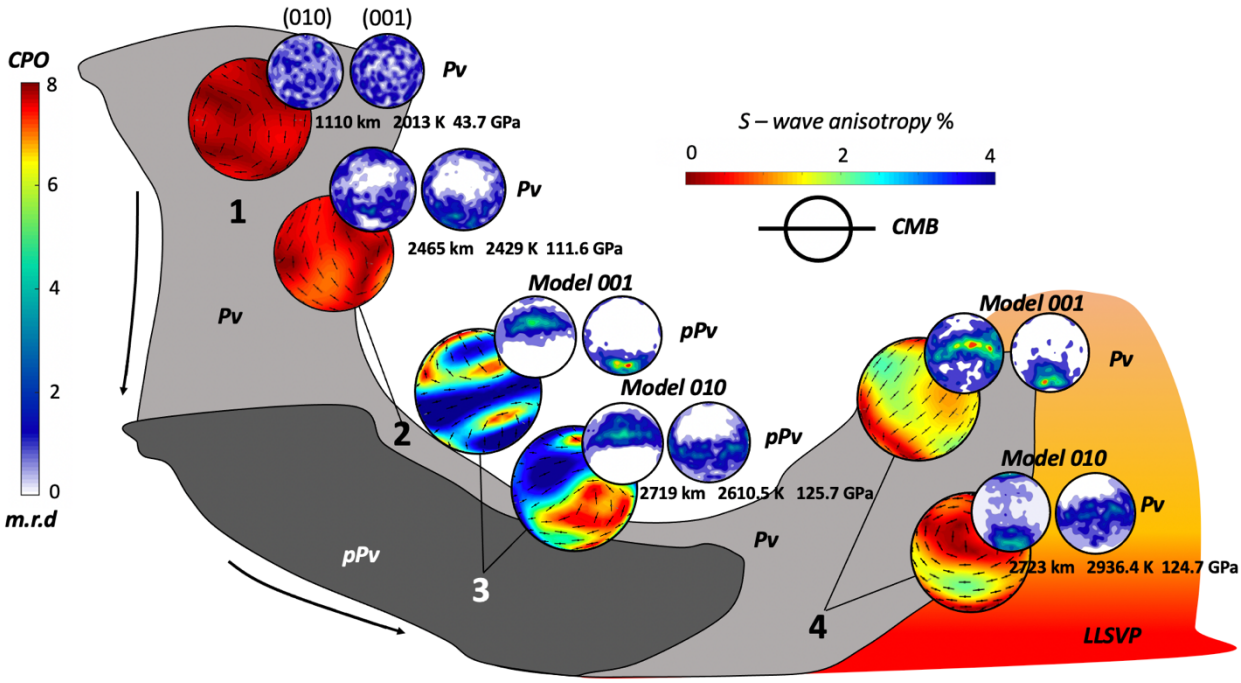

Fig. 4.6. Sketch of subducting slab highlighting the plastic deformation induced anisotropy and the presence of Pv (light grey) or the pPv (dark grey) in different areas of the slab. *Plastic deformation shown as upper hemisphere pole figures (units of multiples of random distribution, m.r.d) for the Pv/pPv phase along with associated shear wave anisotropy of the aggregate as 3D projections from different streamlines, each sampling different areas of the slab (1-4). Black ticks in velocity projections indicate fast shear wave polarization direction. Locations (3,4) show variations between Model 001 and Model 010. The CMB is horizontal as shown by the diagram upper inset. The hotter region (labelled LLSVP) and shown in shades of orange, corresponds to the pile shown in Fig. 1 (right). The top part of the slab (2) is colder, retaining the Pv phase. At the border of the hot pile, the reverse pPv to Pv occurs in the deeper parts of the slab first, so a small sliver of pPv becomes sandwiched between the newly reverted Pv beneath (2690 km to the CMB in some areas), and the never converted Pv above.*

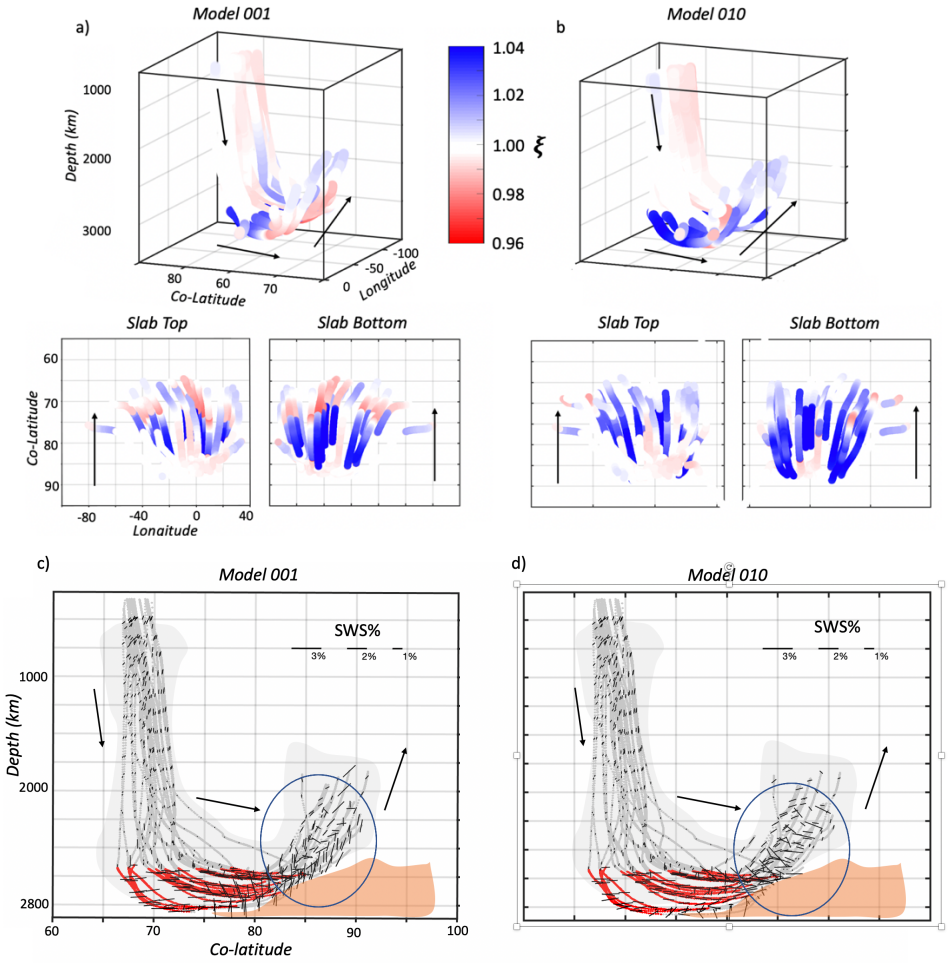

Fig. 4.7. Spatial distribution of radial anisotropy and shear wave splitting*. Top: radial anisotropy parameter ($\xi = (V_{SH}/V_{SV})^2$) computed along each streamline for Model 001* ***(a)*** *and Model 010* ***(b)*** *(25 total streamlines)****,*** *showing oblique view highlighting entire slab path (black arrow indicates slab flow direction) and views from top and bottom of the slab, respectively, for both models. Bottom: Shear wave polarization directions for waves propagating at grazing incidence to D'' for* ***(c)*** *Model 001 and* ***(d)*** *Model 010. Red paths highlight areas where the pPv phase is present. Orange areas indicate areas of increased temperature at the base of the upwelling. Black ticks indicate the fast polarization direction scaled by %. Incident seismic wave direction is into the page. Key area of difference inscribed with black circle.*

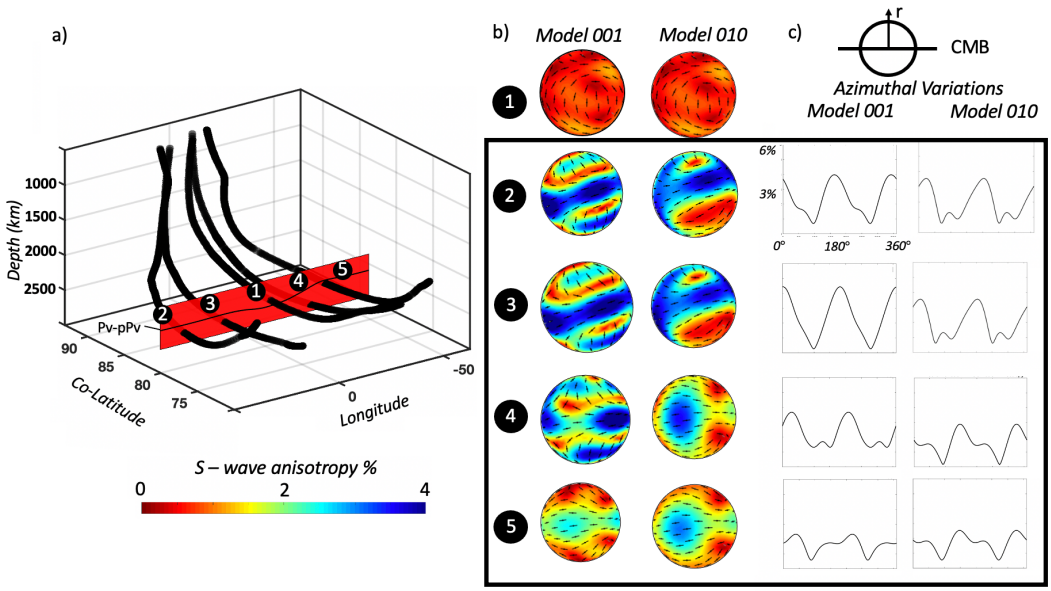

Fig. 4.8. Shear wave and azimuthal variations for Model 001 and Model 010 through transverse slice of slab at 80° co-latitude (green barrier) during slab transit along the CMB*. (**a**) View of 5 selected streamlines passing through the traverse slice of the model slab (red) as well as black line to guide reader to Pv/pPv phase transition boundary. (**b**) 3D shear anisotropy projections for the aggregate with (001) and (010) slip dominant in the pPv phase when present) for corresponding streamlines with fast direction polarization shown as black ticks, with flow direction out of page. Note that streamline (1) fails to convert to pPv and retains the Pv phase in both systems. (**c**) Azimuthal variations of the elastic tensor for each of the 3D velocity projections. The CMB is horizontal and radial direction is north in all images as depicted in the upper right inset. Flow direction is out of the page. Black box shows anisotropy from areas with pPv present.*

Several studies (Williams & Garnero 1996; Simmons & Grand 2002; Yuan & Romanowicz 2017) have suggested that a small percentage of partial melt could explain the strongly decreased velocity signatures of ultra-low velocity zones (ULVZs). As described in section 2.5 this is incorporated as a rough first order approximation. Rough estimates on the elastic parameters of a silicate-based melt are incorporated to the aggregate at the determined locations. The onset of partial melting in the model was found to occur in the deepest portion of the slab near locations with the reverse pPv-Pv phase transition. Results here show that the presence of as little as 1% melt results in a ~2.5% decrease in P-wave velocity and ~4% decrease in S-wave velocity compared to the same streamlines without partial melting added. Increasing to a melt percent of 15% leads to reductions in V_s and V_p of ~18 and 7% respectively at the base of the upwelling (Fig. 10, Fig. 9). Little deviation is observed in the direction of fast polarization in either model, but a strong increase in the amplitude of anisotropy (Fig. 4.10).

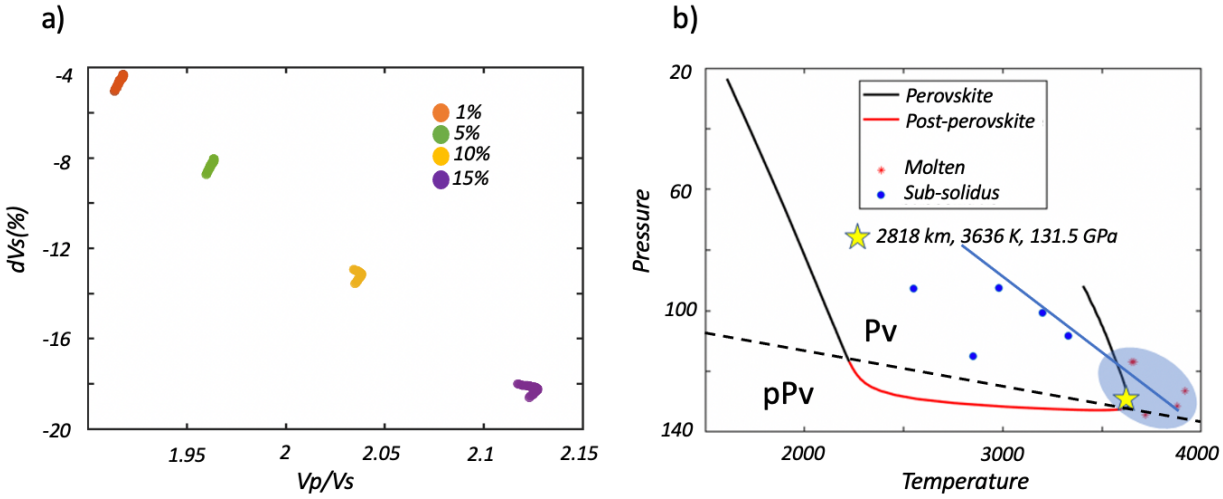

Fig. 4.9. Location and effects of partial melting on shear wave anisotropy and isotropic velocities*. (a) plot of dV_{Siso} in % deviation from PREM against the ratio of Vp/Vs for the isotropic velocities with various amounts of partial melting showing the widening gap between Vp and Vs with increased melt%. (b) Pressure-temperature trace of a selected streamline reaching the deepest level of the lower mantle at conditions of possible partial melt determined by Nomura et al. (2014). Blue circles represent data points taken from this study where no partial melting was detected experimentally (sub solidus). Red stars indicate the presence of partial melt (molten). Shaded area (grey) shows location of possible melt conditions with blue solid line the liquidus from Nomura et al. 2014, in the model and yellow star shows location of velocity projections in Fig. 4.10.*

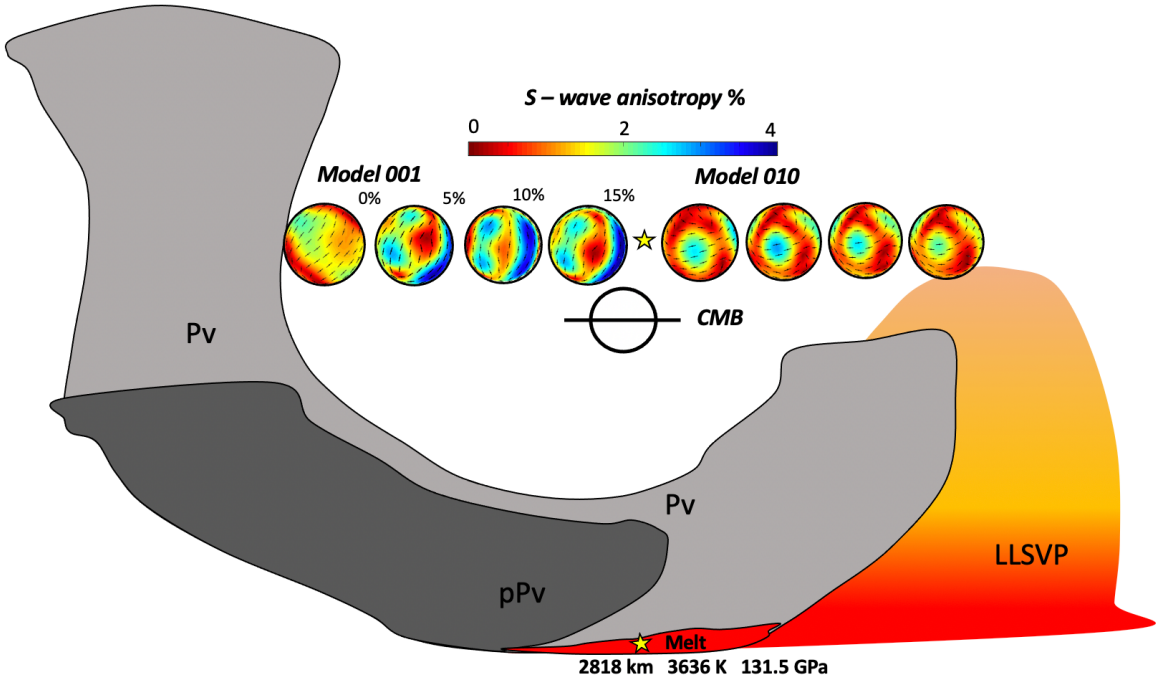

Fig. 4.10. Shear wave anisotropy resulting from various amounts of partial melting. *3D projections of shear wave anisotropy for the addition of 0, 5,10,15% partial melting at the base of the model slab near the edge of the simulated pile labeled LLSVP. Red section near the bottom of the slab depicts a section containing partial melt. Star indicates location shown by star in Fig. 9 b. CMB is horizontal in all images.*

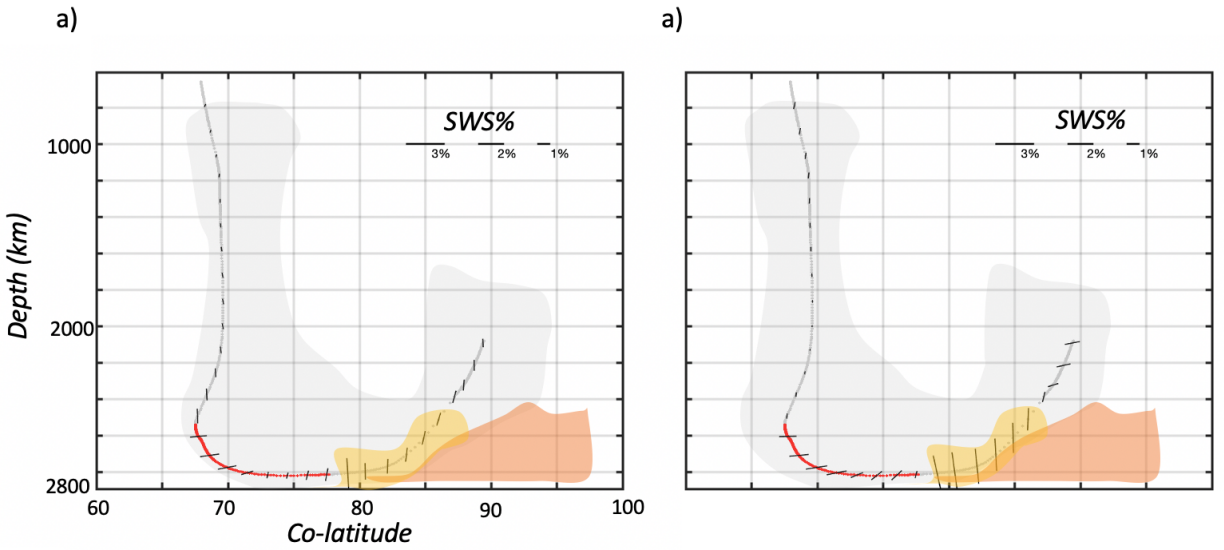

Fig. 4.11. Comparing shear wave polarization directions for waves propagating at grazing incidence to D'' for a representative streamline*.(a) without partial melting and (b), with 1% partial melt for Model (001). Black tics indicate the fast axis direction scaled by %. Red path marks the presence of pPv. The area of the slab where partial melt is present is shown in yellow, while orange represents increased temperature at the base of the upwelling. All incident wave propagation directions are into the page.*

As slab material approaches the edge of the dense hot pile, the increase in *T* initiates the reverse pPv to Pv transformation, which occurs at a range of depths depending on location in the model, but generally deeper (2595-2835 km) than for the forward transition, as anticipated due to the larger *T* near the edge of the hot pile. This is where significant differences between the two pPv models emerge in both texture development as well as anisotropy (Fig. 4, 6, 7): for Model 010, the fast axis direction with relatively larger SWS strength (~1.0-3.0%) remains horizontal after the reverse transition and the trend continues during the upwelling; Model 001, on the other hand, shows a complex pattern of mixed horizontal and vertical fast axis directions after the reverse pPv to Pv transition with ~2.0% of SWS strength, and a tilted fast axis with 1.0-2.0% SWS strength in the upwelling segment (Fig. 7 c). Interestingly, a triple layering (Fig. 6) of varying shear-wave polarization as well as isotropic velocities due to double crossing of the pPv phase boundary occurs over a 300 km depth range in Model 001. While the same triple layering of phases occurs in Model 010, the extreme reversal in fast propagation directions between layers is not as apparent. Also, Model 010 only presents small patches of $V_{SH} < V_{SV}$ at the base of the upwelling (red areas in a prevailing pattern of $V_{SH} > V_{SV}$ (blue areas) in the upwelling region). The latter is inconsistent with available seismic observations (e.g., Long 2009; Romanowicz & Wenk 2017).

4.4. Discussion

4.4.1 Distribution of Pv and pPv in the lowermost mantle

By including cubic MgO and CaPv as well as both direct and reverse phase transition from Pv to pPv, we gain a more realistic representation of the complex aggregate thought to exist in the lowermost mantle. Furthermore, an interesting observation that arises due to the temperature variations in the model is the depth dependence of the Pv-pPv and pPv-Pv phase transitions. While the forward transition is found to only vary over ~40 km in this model, the changes in elevation of the reverse transformation are more dramatic, ranging over a ~200 km depth and 15° of colatitude along the slab's path (Fig 12). This results in a situation where there exists a ~100-250 km wedge of lower-than-average isotropic velocity Pv atop the CMB at the edge of the simulated pile located beneath the faster than average pPv phase, due to a double crossing of the Pv-pPv phase transition (Hernlund *et al*. 2015). This unique feature causes a triple layering of differing shear wave anisotropies (Fig. 6) as well as isotropic velocities. This presence and extent of this feature is ultimately dependent on the value of the Clapeyron slope chosen to represent the locations of the forward and reverse phase transitions (Fig. 3a). There are also streamlines that fail to convert to pPv all together and constitute the top layer of the simulated slab. These streamlines (depicted by streamline 1 in Fig. 8) show the effect of suppressing the pPv transition and lead to very weak but vertically polarized shear waves being the fastest. This is at odds with previous studies by this group (Cottaar *et al*., 2014) but this discrepancy is understandable due to the choice of dominant slip systems in the Pv phase with (001) dominant (Wenk *et al*. 2011) compared to a mix of (001) and (100) in this study (Mainprice *et al*. 2008).

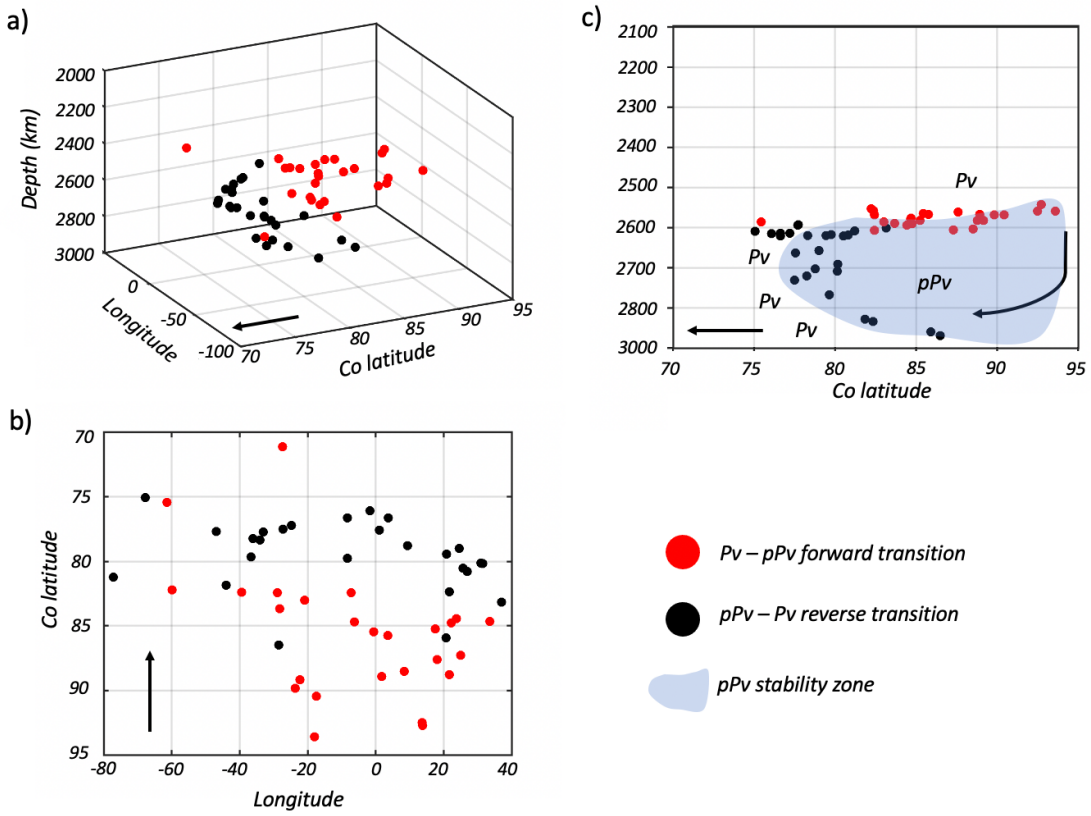

Fig. 4.12. Spatial variation of forward (red dots) and reverse (black dots) phase transitions in the slab*. 3D visualization in* ***a*** *with 2D in* ***b*** *and* ***c****. When viewed from above (****b****) the spread of the reverse pPp-Pv transition is clearly identified. Grey area in c shows the pPv stability field within the slab highlighting the deeper penetrating streamlines reverting to Pv (near 90° Co latitude) compared to shallower paths (black dots at 75-80° Co latitude). Slab flow direction is shown by black arrows in all images.*

The viscosity of the pPv phase has also been a point of recent debate where a viscocity greater than that of Pv (Karato 2010, 2011) and a "weaker" or less viscous pPv compared to that of Pv has also been investigated (Li et al., 2014, Nakagawa & Tackley 2011) each with opposite effects on the dynamics in the D'' and CMB regions. In the event of "weak" pPv, Li *et al.* 2014 showed that slab material making it to the CMB would spread more easily and also increase the heat flux from the CMB. In our model, the incorporation of a "weak" pPv could potentially have three effects: (1) a lower viscosity at a boundary layer translates into a higher strain rate which would allow for a more rapid texture development of the local minerals. (2) A higher heat flux from the CMB would directly affect the existence and spatial distribution of the pPv phase and areas of partial melting. For instance, a higher temperature at the CMB would shrink the region of pPv stability in this model and since it includes the reverse pPv – Pv transition in the hotter areas the amount of Pv along the CMB would possibly increase. As mentioned above, this model shows that the newly formed Pv at the CMB has an anisotropic signature with vertically polarized shear waves leading the horizontally polarized waves. If more Pv were to exist along the CMB, the size of patches of $V_{SV} > V_{SH}$ would increase at the cost of patches of $V_{SH} > V_{SV}$. This fact could be used in future models as a constraint on the amount of pPv present along the CMB. (3) an increase in heat flux from the CMB would also increase the size of area along the CMB where partial melting would

be found under the tested conditions. This would therefore have the effect of increasing the size of exceptionally low velocity patches found at the base of upwelling.

4.4.2 Effect of phase transitions and partial melting on deformation and shear wave anisotropy.

Along the lines of previous studies, this investigation aims to identify models that are consistent with the long wavelength seismic anisotropy structure observed in D''. In our group's previous studies (Wenk *et al*. 2011; Cottaar *et al*. 2014), the approach taken here was able to provide evidence that dominant slip on 001 or 010 in a pPv+MgO+CaPv aggregate caused by convection-driven shear deformation could provide an explanation for the anisotropic signatures of D''. Those same studies were successful showing that Pv alone as well as dominant slip in (100) in the pPv phase could not reconcile the bulk anisotropic signatures in the lowermost mantle and therefore that system is not included here. A more recent study performed my Tommasi *et al*. (2018) provided further evidence for (010) dominant slip by utilizing 2D corner flow models similar to those of Wenk *et al*. (2011). They were able to show that an (010) dominant pPv phase was capable of explaining both a horizontal (to sub horizontal) fast shear wave polarization in D'' as well as a flow-directed fast direction in upwelling areas. A key aspect of the current study is the temperature dependence of the presence of the pPv phase, and the corresponding phase transition was not taken into account in that study. In our model, pPv cannot exist thermodynamically in the hotter regions near the edges of the simulated LLSVPs, and therefore it is concluded that alternate explanations are needed to describe the observed anisotropy at the base of upwellings.

The current model corroborates the findings of Tomassi *et al*. (2018) that dominant (010) slip in the pPv phase (our Model 010) can explain the anisotropic signature during horizontal flow, this model and that of Tomassi *et al.* diverge however in the signatures seen in areas of upwelling. Nowacki *et al.* 2010 also tested (001) and (010) dominant slip in pPv through comparison of shear planes of the two systems and the measured differential shear wave splitting of S and ScS phases passing through D'' beneath the Caribbean. There they found the strongest correlation between (001) dominant slip in pPv but could not rule out (010) without further investigation. By incorporating the three distinct flow regimes here (downwelling, horizontal flow, and upwelling) this model is able to draw a clear distinction between these two systems. The difference between the two models tested here is due to the textural (001) inheritance across the pPv-Pv phase transition (Dobson *et al*. 2013) that occurs at the base of the upwelling section in Model 001, which leads to an increase in 001 texture intensity during upwelling flow (up to > 10 m.r.d), aligning the aggregate fast direction of anisotropy, on average, near the material flow direction (Fig 7). In contrast, in Model 010 an abrupt partition of deformation (Fig. 13) to the weaker MgO and CaPv phases is observed due to the fact that after the reverse transition from pPv in Model 010, Pv is in an unfavorable geometry for slip in its preferred systems (a mix of 001 and 100 in this investigation). This leads to a substantially weaker preferred orientation in the Pv phase in Model 010 as well as to (010) and (001) distributions orthogonal to those seen in Model 001 (Fig. 4), ultimately leading to the fast direction in Pv remaining near parallel to the CMB. This results in the dominantly horizontal fast direction of anisotropy, i.e., orthogonal to the flow direction during upwelling, at odds with seismic observations in the LLSVPs (e.g., Nowacki *et al*. 2011; Romanowicz & Wenk 2017). This is further illustrated by visualizing the lateral and depth dependent anisotropic structure in D'' produced by the model as a whole similar to that done in 2D by Wenk *et al*. (2011). If the effect of textural inheritance in Model 001 does occur in the lower

mantle, then it would follow that the strength of anisotropy in D'' due to pPv would be modulated by the amount of (001) texture that occurs in the precursor Pv phase, i.e., strong (001) texture in Pv would lead to a strong (001) starting texture in pPv, and therefore leading to a strong anisotropic signature emanating from a pPv dominated aggregate. This scenario could explain the variation in strength of anisotropy in areas of suspected pPv. Also, including the *P-T* dependent phase transition there exists a complicated mix of vertically and horizontally polarized shear waves dominating in the hottest regions at the base of the slab (bottom of Fig. 8) where lateral temperature variations induce reversion to Pv in some locations but not others, a feature not seen in our previous studies but consistent with seismic observations (Romanowicz & Wenk 2007, Nowacki *et al*. 2011) . Beyond these differences however, even when including the Pv-pPv-Pv transition pathway, our Model 001 although this model introduces more realistic complexity, correlates to the PPV C model proposed in Cottaar *et al.* 2014 with fast shear propagation directions aligning near the flow direction through all sections of the model.

A case was also tested in which the phase transition occurs and does not follow the topotaxial relationship but instead when the phase transition occurs the orientations of the newly introduced grains in the pPv (or Pv) phase are randomized. In the select tracers tested in this manner, because Pv (or pPv) heavily dominates the volume fraction of the aggregate an overall decrease in the calculated anisotropy occurs to near isotropic with slight anisotropy increasing at the end of horizontal flow but is then removed by the randomization once again at the reverse Pv-pPv transformation. Both areas in disagreement with the magnitudes of anisotropy observed in D''.

This model not only investigates the anisotropy developed along individual streamlines, but also collapse each deformed aggregate elastic tensor into its scalar $\xi = \left(\frac{V_{SH}}{V_{SV}}\right)^2$ value at over 10,000 points within the model which allows for a volumetric mapping of the radially anisotropic structure of the slab in both models (Fig. 14). This approach provides a volumetric image of the anisotropic structure of the slab with clear demarcations in the change from $V_{SH}>V_{SV}$ (blue) during horizontal flow along the CMB to areas of $V_{SV}>V_{SH}$ (red) during upwelling flow for Model 001 (a-d) while Model 001 only shows small patches of $V_{SV}>V_{SH}$ in those areas (Fig. 14 (h)). This approach provides a bulk view of the anisotropic signature of different areas of the slab. For instance, Figure 4.15 and 4.16 show zoomed in snapshot views of the slab as it traverses the CMB where it is seen that a stronger anisotropic signature is seen near the edges of the slab compared to the bulk center (>5% compared to ~2-3% shear wave anisotropy). The edges also show a break from the assumed radial anisotropic signature to a more general orthorhombic signature that is tilted up to 35° from the radial direction (a.k.a. tilted transverse anisotropy (TTI)). This approach also has the benefit of clearly demarcating the boundaries between different signatures of anisotropy compared to looking at individual streamlines which do not allow the capture of any spatial distribution.

As for the secondary phases, although MgO exhibits strong shear wave anisotropy (Marquardt *et al*. 2009), and at 19% volume fraction accommodates between 25-35% of the strain in this model, while the overall signature of anisotropy is dictated by the abundance of the Pv/pPv phase, which makes up 73% of the aggregate. A key limiting factor in the use of VPSC in this setting is actually the assumption of a homogenous anisotropic background. This is because as in Chapter 2 that a key aspect in the Pv – MgO distribution is that these phases very well may not be homogenously distributed. In Chapter 2 it was shown that MgO nucleates as a fine-grained phase in a matrix around the larger Pv phase. That style of distribution would almost certainly change the deformation behavior of the aggregate in terms of the strain partitioning compared to this model (Yamazaki *et al.* 2016, Girard *et al.* 2016). This limitation could be overcome by comparison to

approaches such as that of the software GEO-MIX-SELF (Matthies 2012) which accounts for grain shape as well as phase distribution in the elastic properties of an aggregate.

The resulting patterns of shear wave anisotropy found here in D" are very similar to those calculated in previous models (Wu *et al*. 2017; Zhang *et al*. 2016) when imposing 001 slip in the pPv phase. The addition of the second minor phase CaPv appears to reduce the magnitude of anisotropy, compared to the case where only a combination of Pv and MgO were considered (Cottaar *et al*. 2014) but has otherwise a minimal effect.

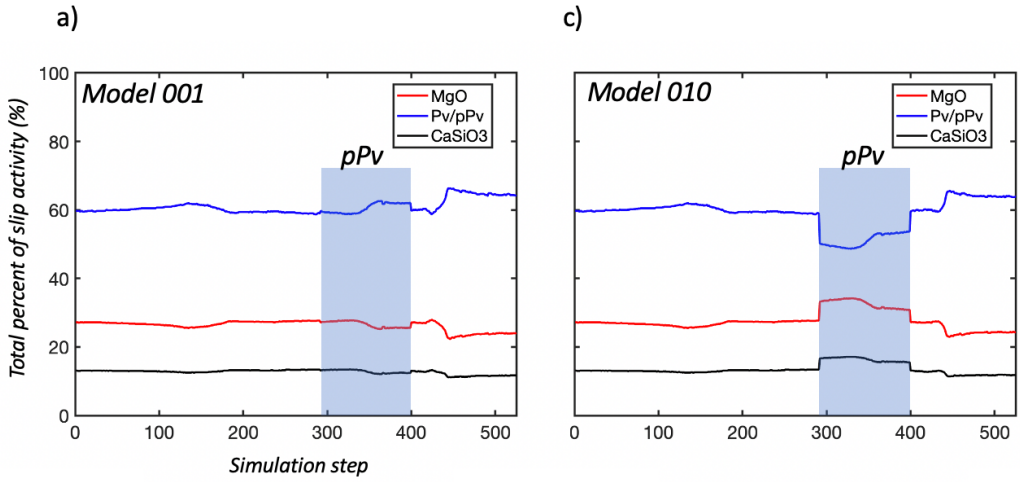

Fig. 4.13 Strain partitioning along select streamline. *Strain partitioning between Pv/pPv (blue) and MgO (red) and CaPv (black) measured as slip system activity (%) which represents the sum of relative amount of shear contributed by each phase per simulation step for streamline 3 in Figure 7, for* ***a*** *Model 001 and* ***b*** *Model 010. Shaded blue area represents the section of the streamline the pPv phase. Step 0 represents the start of the simulation and step 525 is at the end. Interestingly, in Model 010, there is sudden transfer of slip activity from Pv/pPv to MgO and CaPv at the phase transition points. This feature is also present in Model 001 but is suppressed due to the textural inheritance in the pPv phase.*

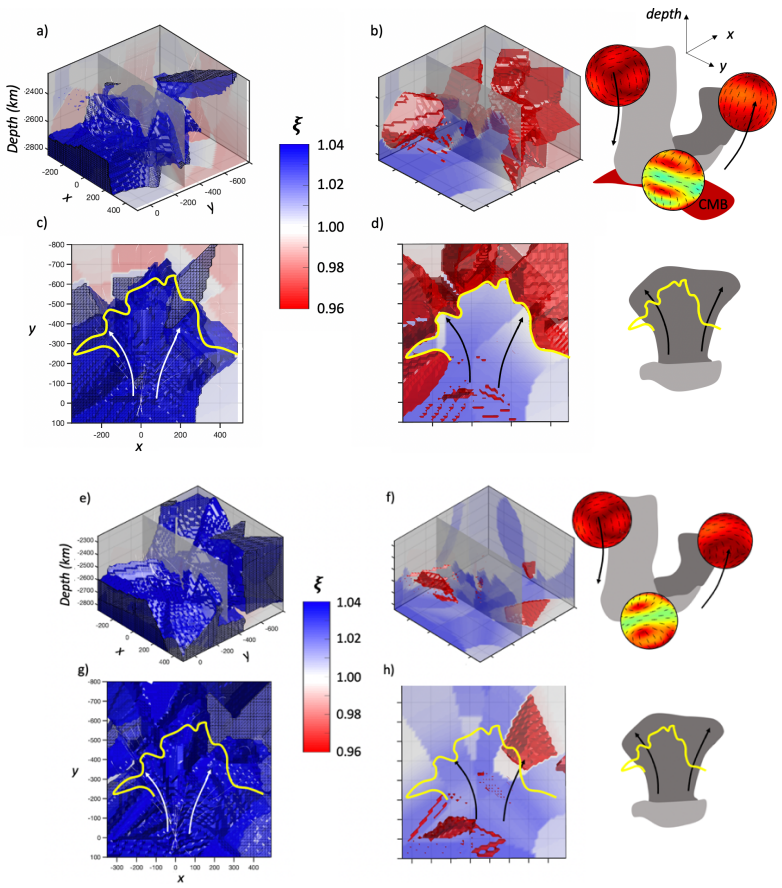

Fig. 4.14. Volumetric mapping of radial anisotropic parameter ($\xi = (V_{SH}/V_{SV})^2$) within the slab. *Model 001 (a-d) and Model 010 (e-f) showing (a), an oblique view of slab volume showing $\xi > 1$ indicated by iso-contour of constant $\xi = 1.02$ (2% V_{SH} fast) and (b) area of slab with $\xi < 1$ indicated by iso-contour of $\xi = 0.98$ (2% V_{SV} fast).(c-d) viewed from above with the pPv-Pv reverse phase transition demarcated by yellow line. Figure bound values indicated by the color. Cartoon slabs to right to guide reader of slab flow direction with 3D velocity projection of S-wave anisotropy shown for each flow section for both models. Vertical axis shows depth in km while the co-latitude (y) and longitude (x) were converted to cartesian coordinates during the meshing process.*

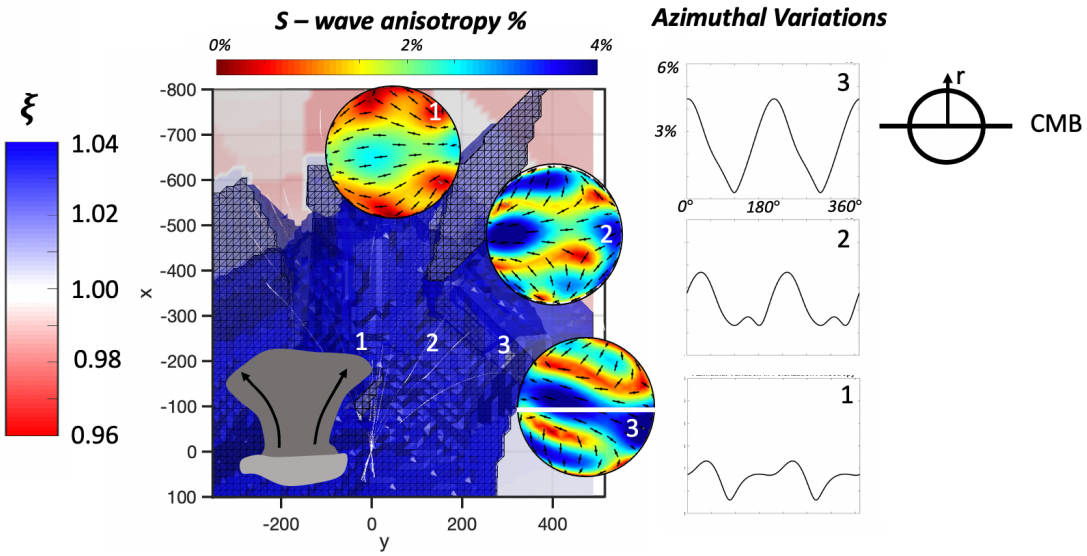

Fig. 4.15. Volumetric mapping of radial anisotropic parameter ($\xi = (V_{SH}/V_{SV})^2$) within the slab (Top View). *Top view of Model 001 showing slab spreading long CMB showing $\xi > 1$ indicated by iso-contour of constant $\xi = 1.02$ (2% V_{SH} fast) (blue structure). Background colors depicted by radial anisotropic parameter* ***ξ.*** *Cartoon slabs to right to guide reader of slab flow direction with 3D velocity projection of S-wave anisotropy shown for different flow areas. Vertical axis shows depth in km while the co-latitude (y) and longitude (x) were converted to cartesian coordinates during the meshing process.*

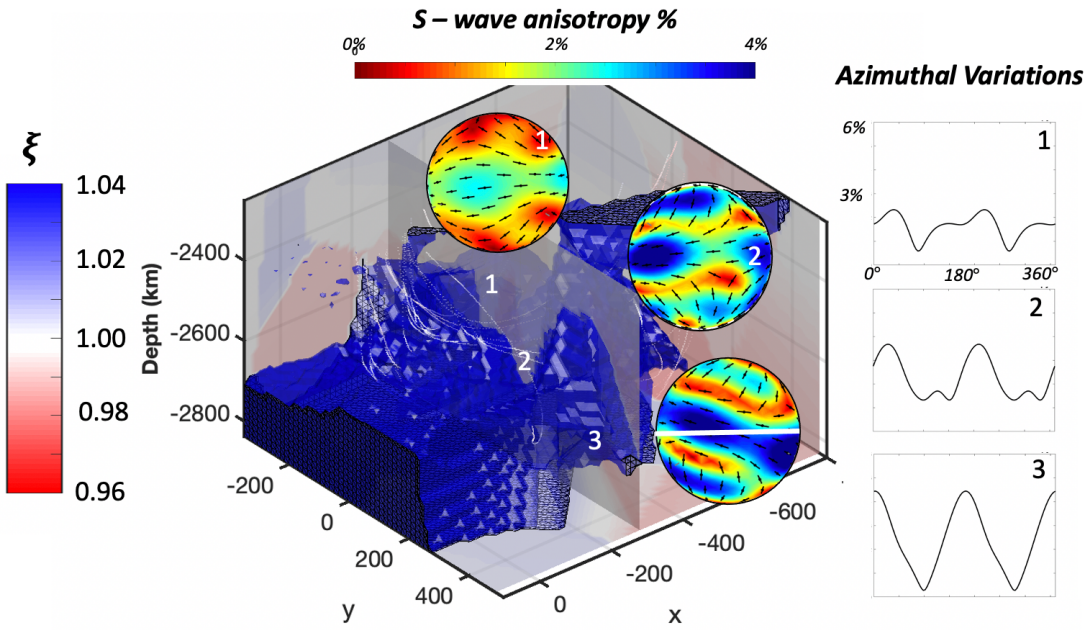

Fig. 4.16. Volumetric mapping of radial anisotropic parameter ($\xi = (V_{SH}/V_{SV})^2$) within the slab (Oblique View). *Oblique view of model 001 from 4.14 with background colors depicted by radial anisotropic parameter* ***ξ.*** *Faster that average shear wave structure (blue structure). Three 3D velocity distribution taken from 3 different areas of the slab (numbered 1-3) with their associated azimuthal variations (right column).*

In this model, thermal variations at the base of the pile meet the conditions necessary for partial melting to occur, which then acts to decrease the absolute velocities for both P and S waves (Fig. 9) while increasing the magnitude of anisotropy of the plastically deformed aggregate. This is consistent with seismic observations near the edges of LLSVPs at D" depths (Lynner & Long 2014) using SK(K)S observations along the edge of the African LLSVP. While splitting was observed near the edges, that study found little or no splitting for phases that pass through the LLSVP, also in agreement with Cottaar & Romanowicz (2013). This led the authors to infer that deformation may only occur along the LLSVP edge while the interior possibly remains undeformed. While in our model, we do not sample the interior of the simulated LLSVP but instead concentrate only the slab material near the edge of the pile that is deflected upward by its presence, future models should incorporate anisotropic signatures from material surrounding the slab. This will allow further investigation and comparison between the upwelling slab material and the signature arising from the pile interior.

4.4.3 Model limitations and assumptions.

While this revised model incorporates many new features, it still relies on several simplifications and assumptions. In particular, only elastic properties and densities determined for pure endmember phases are employed. Also, the evolution of CPO in our model has no influence on the geodynamic flow due to being introduced *a posteriori* based on the recorded velocity gradients. In the mantle, effects such as strain hardening due to plastic deformation as well as the spatial distribution and grain size of phases can have direct effects on viscosity (Marquardt & Miyagi 2015) which would affect the local strain rate is not considered.

Furthermore, although phase-transformations are incorporated into the deformation model, the associated energetic effects (Oganov & Ono 2004) as well as the choice of Clapeyron slope of this transition could also have significant effects on the local temperature and viscosity and therefore strain rates and active deformation mechanisms within the slab.

The density of the aggregate is by far the least constrained parameter as seen in Fig. 4 (green trace) where the direct temperature and pressure dependence would naturally vary laterally within the slab, not only with radial depth, as considered here, leading to larger deviations within the slab. Also, the use of pure endmember phases neglects the effects of phenomena such as electronic spin transitions observed in (Mg,Fe)O at lower mantle conditions (e.g., Antonangeli *et al*. 2011, Yang *et al.* 2015, Wu 2016) which can have a large effect on the resultant anisotropy in this phase, as well as variations in density which would affect the isotropic velocities. We anticipate that these factors most likely have a strong effect on the calculated magnitude of anisotropy contribution from the MgO phase but not necessarily a strong effect on the anisotropic signature of the aggregate (i.e., horizontally, or vertically polarized fast shear wave direction) since the contribution from the main phases Pv and pPv drastically outweighs that of MgO. Along these lines, Zhang *et al*. 2016 found that the difference in anisotropy difference between the high spin (HS) and low spin state (LS) in Pv was at maximum 1%. Future models aimed at constraining the magnitude of anisotropy should however incorporate non-pure-endmember phases and the spin transition effects on elasticity should be incorporated for the (Mg,Fe)O phase. We also do not consider the presence of any phases other than MgO, CaPv, and Pv/pPv. Some studies have mentioned evidence for other minor phases in the deep Earth such as the hexagonal H-phase (Zhang *et al.* 2014) resulting from the Fe disproportionation in iron bearing Pv to an iron depleted Pv + iron rich H-phase, or seifertite (Zhang *et al.* 2016) coexisting with pPv but without and understanding of those phases elastic properties or possible deformation mechanisms, they have been neglected in this study.

The creation of an elastic tensor field as done here is a step forward in creating a derived model space where forward modeling of synthetic seismic wave forms can be conducted. This preliminary work only covers 10,000 elastic tensors spatially distributed throughout the slab where the average interpolation length varies from 1-10 km along a given streamline but 10-300 km laterally between streamlines. This variation in the grid-space leads to a drop proportional drop in resolution laterally but may be sufficient given our current limited coverage used in tomography. In future models a denser lateral grid space should be used. By not including the surrounding mantle the interpolation scheme is blind to the variations of the anisotropic signature away from boundaries of the slab, almost certainly creating a sharper discontinuity at the edges than is realistic. Also, along these lines, the incorporation of the Pv-pPv phase transition occurs for every grain a streamline once the PT conditions are met. In reality this is almost certainly not the case. The phase transition would be time dependent which could be more accurately modeled using a sigmoid function (Fig. 4.16). In the interpolated model space, the coefficients of this function would then become a free parameter that can be fit to seismic observations of the D'' discontinuity to investigate the resulting "sharpness" which could help constrain the timescale needed to fully convert Pv to pPv in the lower mantle.

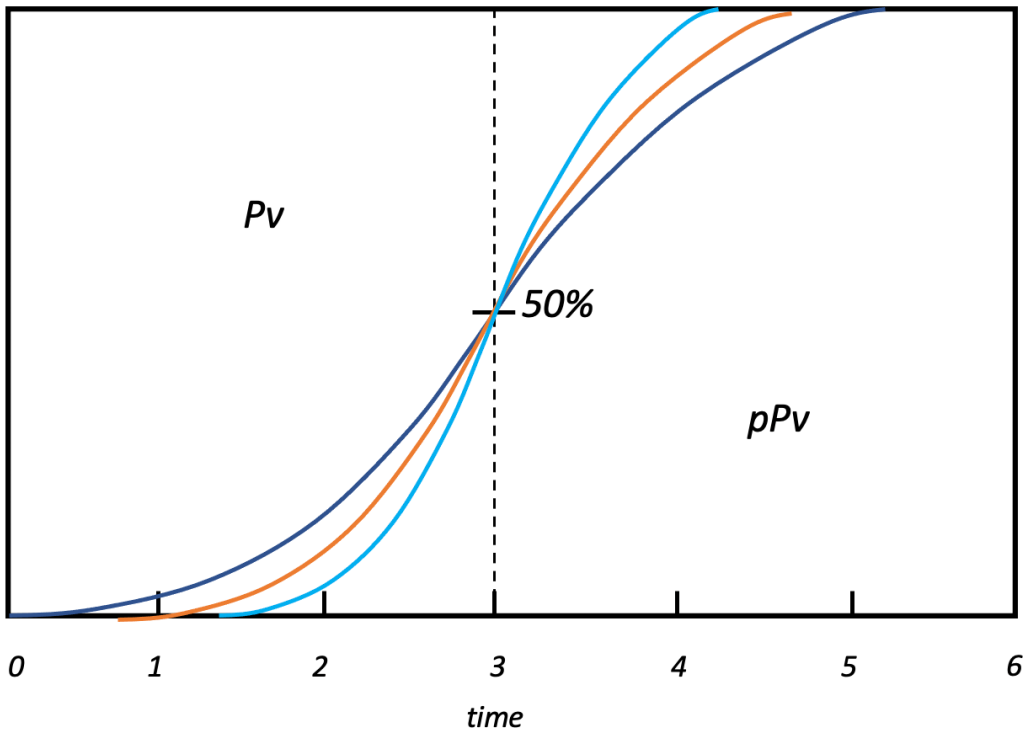

Figure. 4.16. Possible sigmoid function that could be used to model the time evolution of the Pv-pPv phase transition*. The tightness of the function to be used as a free parameter. The black dashed line represents the immediate transition incorporated in this model.*

The incorporation of melting remains a first approximation and includes several assumptions: (1) the model incorporates only pure endmember, and dry, phases, while Nomura *et al*. (2014) conducted their study on a sample containing iron as well as 400 ppm H_2O. The partitioning of water could affect the ease of deformation in the dominant Pv and pPv phases, although investigations into hydrolytic weakening of mantle minerals (Muir & Brodholt 2018) found that at low ppm (sub 200 ppm) water tends to partition to the Pv phases, while at higher amounts, water should move to the CaPv phase (2) Since only pure endmember phases are accounted for any increased density effect due to Fe that may occur in the melt and which may increase any velocity reductions is also not accounted for. (3) When testing various amounts of melt in this model the density of the aggregate is not adjusted which may be an assumption that is valid for less than 5% of melt as it is anticipated that the density of a pure end-member melt at these conditions would have a similar density to that of the surrounding aggregate and fluctuations of a few % or less would have little effect on the density contribution to the calculated anisotropy. Future geodynamic models which include the addition of partial melting would however have the effect of lowering the viscosity where melt is located which could act to increase the strain rate locally imparting effects on texture development as well as the calculated anisotropy of the aggregate. Again, here we only include the effects of partial melt from an estimated elasticity standpoint and its effects are not incorporated into the geodynamic model. Ultimately in this model the aim is to observe trends in the resulting polarization signatures of anisotropy and not precisely constrain absolute values which is poorly constrained globally as it is.

As mentioned earlier, in this deformation model recrystallization is not taken into account – nucleation of new grains and grain growth –which is likely significant at lower mantle conditions (e.g., Wenk & Tome 1999) as was shown experimentally in Chapter 2. Further studies are needed to address these technically challenging questions, coupled with more detailed measurements of seismic anisotropy at the edges of and within mantle upwellings.

4.5 Conclusions and Future Works

A model has been introduced that incorporates the effects of both forward and reverse Pv-pPv phase transitions and partial melting on seismic anisotropy in a subducting slab being deformed along the CMB as well as areas of upwelling. This study provides insights on how phase transformations in the Pv-pPv system and temperature variations related to dynamic flow patterns contribute to explaining the observed seismic anisotropy patterns in the deep mantle. Results here show that incorporating a texture inheritance for the forward and reverse Pv-pPv phase transitions is significant for interpreting observations of seismic anisotropy in D". This study provides evidence that Pv alone cannot produce the combination of isotropic shear velocities and anisotropic signatures seen in D" and therefore another phase or factor must contribute. And furthermore, only a model with (001) dominant slip for pPv provides results consistent with a strong but complicated anisotropy, with Vsh > Vsv in regions of faster than average isotropic Vs (e.g., graveyards of slabs), a tilted fast axis of anisotropy near the borders of the LLSVPs, and weak flow aligned, or absent anisotropy as observed in hotter than average regions of upwelling. While this model is more intricate than those proposed previously it creates new possibilities for expansion. Going forward, a larger model space should be used that accounts for not only the slab material but also the surrounding mantle to capture the interaction on both sides of the slab mantle interface. This approach would help to gain insight into the anisotropic signature of the surrounding mantle. Transition through the transition zone could also be incorporated to investigate the effects of a series of phase transitions. Also, having a larger model space would allow the ability to create a larger tensor field for volumetric visualization.

Chapter 5

Concluding Remarks and Future Directions

This thesis has investigated material properties in a range of environments relative to the Earth's evolution. New forms of analysis have been introduced in several experiments at both ambient conditions as well as extreme environments in a diamond anvil call (DAC). Their respective experimental considerations have thoroughly been discussed as well as a description of the processes and tools required to utilize them. While these experiments have provided enlightening conclusions on the questions they set out to answer, the results, as always, are not complete and have opened the doorway for more intricate questions and advancements on these works. There remains plenty of room for improvement so therefore these investigations act as a baseline for future researchers to continue to build our understanding of the behavior of materials and how they scale from the microscopic crystalline lattice to the macroscopic observables.

Chapters 2 & 3 presented the implementation of the multigrain crystallography (Sørensen *et al.* 2012) method through the software package *HEXRD* (Bernier *et al.* 2011) in several investigations at conditions ranging from the Earth's lithosphere to the upper portion of the lower mantle. These investigations provide examples that the *MGC* analysis can bridge the gap between standard powder diffraction techniques and the single crystal method by providing results on both the statistical front as well as simultaneously being able to extract parameters for individual grains within an aggregate sample. First, this was applied to a naturally occurring olivine sample where its low temperature and high-pressure strength was evaluated in a diamond anvil cell using synchrotron radiation. Olivine was found to have a yield strength of ~1.5 GPa, nearly a GPa less than the lowest previously report but in agreement with presdictions based on recent discoveries of a "size effect" on olivine yield strength (Kumamoto *et al.* 2017). It was also found that deformation by pyramidal slip initiated on (*hk0*) type planes in agreement with previous experiments (Mainprice *et al.* 2005) and calculation (Mussi *et al.* 2014). The sample was further pressurized and heated to convert to the high-pressure ringwoodite phase which is found to nucleate as a small fine-grained phase accompanied by a drastic volume decrease and therefore a local pressure drop in the DAC when a constant pressure is not applied to match. While this may not be the case in the deep Earth, it is relevant for meteoritic impacts. In this experiment MGC was able to extract several individual grains with reflections not belonging to any previously recorded phase in the olivine pathway but matched those belonging to the intermediate phase ε-Mg_2SiO_4 recently named *Poirierite* (Tomioka *et al.* 2021) that has only been observed in recovered meteorite samples such as that from the Tenhem site in Australia. This phase is anticipated to act as an intermediary between ringwoodite and wadsleyite or vice versa through shearing mechanism when the pressure overstep is great, or the energy needed to drive nucleation is absent on the needed time scales. Both of these conditions are met in a diamond anvil cell with laser heating where the sample is brought well above the pressure boundary for the initiation of phase transformation and is then rapidly quenched after heating. The evidence provided in this study should motivate future investigations with the intent of further isolating and constraining this phase as well as understanding its elastic properties. Given the fact that *Poirierite* was found to nucleate as a minor phase so weak it has been missed in diffraction investigations for nearly 30 years, where

it lies out of reach of standard powder or single crystal methods for the reasons described in Chapter 2 (e.g., too weak to be detected by powder methods and occurs after a phase transition excluding the use of single crystal diffraction); observing this mineral *in-situ* may require the use of *MGC*.

In a second experiment using a laser heated diamond anvil cell (LH-DAC), olivine was once again investigated in two parallel experiments at two different synchrotron facilities with Exp.1 being conducted at the Advanced Light Source of Lawrence Berkeley National Laboratory and the Exp. 2 at the Advanced Photon Source at Argonne National Laboratory. These experiments investigation the transformation of olivine to the bridgmanite and ferropericlase aggregate. Both experiments found excellent agreement with the transformation textures previously reported in these phases (Miyagi and Wenk 2016) when converting from meta-stable olivine using the powder technique. This study also highlighted the ability of *MGC* to simultaneously extract and separate statistical data for several grains of both bridgmanite and ferropericlase phases *in-situ* at high pressure. Both experiments also provided evidence that a weaker ferropericlase forms and interconnected network around a larger and stiffer bridgmanite phase. A phenomenon that has been implicated in slab stagnations in the upper portion of the lower mantle (Marquardt & Miyagi 2016). Approximations of grain sizes show a fluctuation in the bridgmanite phase consistent with grain growth followed by recrystallization while ferropericlase underwent a consistent grainsize reduction. When investigating the individual grain orientations, the appearance of profuse twinning in the bridgmanite phase was detected. The spatial location of individual twin pairs were able to be isolated and the precise crystallographic relationship between parent and daughter grains could be calculated, confirming a {110} twinning relation *in-situ* previously seen in *ex-situ* TEM studies. Furthermore, this twinning relation was accompanied by a global stress drop within the sample indicated that twinning may be a stress relieving mechanism in the bridgmanite phase at high pressures (Miyagi & Wenk 2016). Here estimations of grain sizes during heating were also collected which showed evidence for dynamic recrystallization in bridgmanite with oscillations in grain size with steady growth while ferropericlase underwent consistent grain size reduction.

Chapter 4 shifts methods again except this time from experiment to theoretical modeling where the visco-plastic self-consistent (VPSC) method was combined with a large-scale 3D geodynamic model of a subducting slab to investigate the strain induced plastic deformation during subduction of a pyrolytic aggregate with composition 72% bridgmanite 17% MgO and 9% $CaSiO_3$ with at higher pressures and temperatures br converting to the high-pressure phase post-perovskite (pPv). This study aimed at presenting a more realistic model of deformation in a subducting slab by incorporated pressure and temperature evolution in the elastic properties of each phase as well as the pressure-temperature induced bridgmanite (Pv)-pPv phase transition near the D'' region of the lower most mantle. Along the lines of previous experiments using this approach (Tomassi *et al.* 2019, Cottaar *et al.* 2014, Wenk *et al.* 2011) this version compared various primary deformation mechanisms in the pPv phase in order constrain which mechanisms could give rise the anisotropic shear wave picture gathered by shear wave anisotropy in the Earth's lower mantle. This model accurately recreates several features observed on both local and global scales including a break from the assumed radial anisotropic picture to a spatially varying one with elements of tilted transverse anisotropy (TTI) where the slab edges roll while spreading along the CMB. By incorporating the Pv-pPv phase transition this new model shows a layering of the br and pPv phases at the base of the lower mantle where the temperatures increase along the CMB causes a thin layer of br due to the temperature induced pPv-Pv reverse phase transition. A key result from this model is that the incorporation of the Pv-pPv transition also draws the needed distinction between the

two competing models of deformation in the pPv phase, here (001) is compared with (010) put forth by Tomassi *et al.* 2019. A model with (001) dominant slip in pPv that incorporates the forward and reverse phase transitions can reproduce the $V_{SH} > V_{SV}$ anisotropic signature during horizontal shearing flow as well as the $V_{SV} > V_{SH}$ signatures seen during downwelling and upwelling flow. Furthermore, the incorporation of the reversion to *br* at the base of upwelling flow also recreates the observed decrease in isotropic velocities in these areas proceeded by a fast V_s region in the pPv stability realm. While this model is more realistic than those previously presented, it only aims to constrain the relative signature observed through seismology at the largest of scales (shear wave splitting observations tomography) and it still makes many assumptions on the intricate workings in the lower mantle where there is room for much improvement.

References

Abramson, E.H., Brown, J.M., Slutsky, L.J. & Zaug, J. (1997) The elastic constants of San Carlos olivine to 17 GPa. *Journal of Geophysical Research: Solid Earth*, **102**, 12253–12263. doi:https://doi.org/10.1029/97JB00682

Aydıner, C.C., Bernier, J.V., Clausen, B., Lienert, U., Tomé, C.N. & Brown, D.W. (2009) Evolution of stress in individual grains and twins in a magnesium alloy aggregate. *Phys. Rev. B*, **80**, 024113. doi:10.1103/PhysRevB.80.024113

Aydıner, C.C. & Telemez, M.A. (2014) Multiscale deformation heterogeneity in twinning magnesium investigated with in situ image correlation. *International Journal of Plasticity*, **56**, 203–218. doi:10.1016/j.ijplas.2013.12.001

Barkov, A.Y., Bindi, L., Tamura, N., Shvedov, G.I., Winkler, B., Stan, C.V., Morgenroth, W., *et al.* (2019) Ognitite, NiBiTe, a new mineral species, and Co-rich maucherite from the Ognit ultramafic complex, Eastern Sayans, Russia. *Mineralogical Magazine*, **83**, 695–703, Cambridge University Press. doi:10.1180/mgm.2019.31

Bassett, W.A. (2009) Diamond anvil cell, 50th birthday. *High Pressure Research*, **29**, 163–186, Taylor & Francis. doi:10.1080/08957950802597239

Bernier, J.V., Barton, N.R., Lienert, U. & Miller, M.P. (2011) Far-field high-energy diffraction microscopy: a tool for intergranular orientation and strain analysis. *The Journal of Strain Analysis for Engineering Design*, **46**, 527–547. doi:10.1177/0309324711405761

Bernier, J.V., Suter, R.M., Rollett, A.D. & Almer, J.D. (2020) High-Energy X-Ray Diffraction Microscopy in Materials Science. *Annu. Rev. Mater. Res.*, **50**, 395–436. doi:10.1146/annurev-matsci-070616-124125

Blackman, D.K., Wenk, H.-R. & Kendall, J.M. (2002) Seismic anisotropy of the upper mantle 1. Factors that affect mineral texture and effective elastic properties. *Geochemistry, Geophysics, Geosystems*, **3**, 1–24. doi:https://doi.org/10.1029/2001GC000248

Blackman, D.K. (2007) Use of mineral physics, with geodynamic modelling and seismology, to investigate flow in the Earth. *Rep. Prog. Phys.*, **70**, 659–689, IOP Publishing. doi:10.1088/0034-4885/70/5/R01

Blacic, J.D. Effect of Water on the Experimental Deformation of Olivine. in *Flow and Fracture of Rocks*, Edit. H.C. Heard, I.Y. Borg, N. L. Carter, C. B. Raleigh., American Geophysical Union Monograph Series 16. (1972); pp. 109–115. doi:10.1029/GM016p0109

Boyce, D., Shade, P., Musinski, W., Obstalecki, M., Pagan, D., Bernier, J. & Turner, T. (2020) Estimation of anisotropic elastic moduli from high energy X-Ray data and finite element simulations. *Materialia*, **12**, 100795. doi:10.1016/j.mtla.2020.100795

Bragg, W.L. (1913) The diffraction of short electromagnetic waves by a crystal. *Proceedings of the Cambridge Philosophical. Society*, **17**, 43-57.

Buffett, B.A. & Becker, T.W. (2012) Bending stress and dissipation in subducted lithosphere. *Journal of Geophysical Research: Solid Earth*, **117**. doi:https://doi.org/10.1029/2012JB009205

Burnley, P.C. & Green, H.W. (1989) Stress dependence of the mechanism of the olivine–spinel transformation. *Nature*, **338**, 753–756. doi:10.1038/338753a0

Chai, M.; Brown, J.M.; Wang, Y. (1998) Yield strength, slip systems and deformation induced phase transition of San Carlos olivine up to the transition zone pressure at room temperature. In "Properties of Earth and Planetary Materials at High Pressure and Temperature"; Edit .M.H. Manghnani and T. Yagi, American Geophysical Union Monograph 101; pp. 483–493.doi:10.1029/GM101p0483

Chen, J., Weidner, D.J. & Vaughan, M.T. (2002) The strength of $Mg_{0.9}Fe_{0.1}SiO_3$ perovskite at high pressure and temperature. *Nature*, **419**, 824–826. doi:10.1038/nature01130

Chen, K., Kunz, M., Li, Y., Zepeda-Alarcon, E., Sintubin, M. & Wenk, H.-R. (2016) Compressional residual stress in Bastogne boudins revealed by synchrotron X-ray microdiffraction: Compressional Origin of Bastogne Boudins. *Geophysical Research Letters*, **43**, 6178–6185. doi:10.1002/2016GL069236

Chien-Min, S. & Burns, R.G. (1976) Kinetics of high-pressure phase transformations: Implications to the evolution of the olivine → spinel transition in the downgoing lithosphere and its consequences on the dynamics of the mantle. *Tectonophysics*, **31**, 1–32. doi:10.1016/0040-1951(76)90165-7

Cordier, P., Demouchy, S., Beausir, B., Taupin, V., Barou, F. & Fressengeas, C. (2014) Disclinations provide the missing mechanism for deforming olivine-rich rocks in the mantle | Nature. *Nature*, **507**, 51–56. doi:10.1038/nature13043

Cottaar, S. & Romanowicz, B. (2013) Observations of changing anisotropy across the southern margin of the African LLSVP. *Geophysical Journal International*, **195**, 1184–1195. doi:10.1093/gji/ggt285

Cottaar, S., Li, M., McNamara, A.K., Romanowicz, B. & Wenk, H.-R. (2014) Synthetic seismic anisotropy models within a slab impinging on the core–mantle boundary. *Geophysical Journal International*, **199**, 164–177. doi:10.1093/gji/ggu244

Couvy, H., Frost, D.J., Heidelbach, F., Nyilas, K., Ungar, T., Mackwell, S. & Cordier, P. (2004) Shear deformation experiments of forsterite at 11 GPa - 1400°C in the multianvil apparatus. *European Journal of Mineralogy*, **16**, 877–889. doi:10.1127/0935-1221/2004/0016-0877

Demouchy, S., Mussi, A., Barou, F., Tommasi, A. & Cordier, P. (2014) Viscoplasticity of polycrystalline olivine experimentally deformed at high pressure and 900°C. *Tectonophysics*, **623**, 123–135. doi:10.1016/j.tecto.2014.03.022

Deng, J. & Lee, K.K.M. (2017) Viscosity jump in the lower mantle inferred from melting curves of ferropericlase. *Nature Communications*, **8**. doi:10.1038/s41467-017-02263-z

Dobson, D.P., Miyajima, N., Nestola, F., Alvaro, M., Casati, N., Liebske, C., Wood, I.G., *et al.* (2013) Strong inheritance of texture between perovskite and post-perovskite in the D″ layer. *Nature Geoscience*, **6**, 575.

Durham, W.B.; Ricoult, D.L.; Kohlstedt, D.L. (1985) Interaction of slip systems in olivine. In "Point Defects in Minerals"; Edit. R.N. Schock, American Geophysical Union Monograph 31; pp.185-193.10.1029/GM031p0185

Durinck, J., Devincre, B., Kubin, L. & Cordier, P. (2007) Modeling the plastic deformation of olivine by dislocation dynamics simulations. *American Mineralogist*, **92**, 1346–1357. doi:10.2138/am.2007.2512

Evans, B. & Goetze, C. (1979) The temperature variation of hardness of olivine and its implication for polycrystalline yield stress. *Journal of Geophysical Research: Solid Earth*, **84**, 5505–5524. doi:https://doi.org/10.1029/JB084iB10p05505

Ewald, P.P. (1969) Introduction to the dynamical theory of X-ray diffraction. *Acta Cryst A*, **25**, 103–108, International Union of Crystallography. doi:10.1107/S0567739469000155

Faccenda, M. & Capitanio, F.A. (2013) Seismic anisotropy around subduction zones: Insights from three-dimensional modeling of upper mantle deformation and SKS splitting calculations. *Geochemistry, Geophysics, Geosystems*, **14**, 243–262. doi:10.1002/ggge.20055

Faccenda, M. & Dal Zilio, L. (2017) The role of solid–solid phase transitions in mantle convection. *Lithos*, **268–271**, 198–224. doi:10.1016/j.lithos.2016.11.007

French, S.W. & Romanowicz, B.A. (2014) Whole-mantle radially anisotropic shear velocity structure from spectral-element waveform tomography. *Geophysical Journal International*, **199**, 1303–1327. doi:10.1093/gji/ggu334

Fujino, K. & Irifune, T. (1992) TEM Studies on the Olivine to Modified Spinel Transformation in Mg2SiO4. in *High-Pressure Research: Application to Earth and Planetary Sciences*, pp. 237–243, American Geophysical Union (AGU). doi:10.1029/GM067p0237

Fukao, Y. & Obayashi, M. (2013) Subducted slabs stagnant above, penetrating through, and trapped below the 660 km discontinuity. *Journal of Geophysical Research: Solid Earth*, **118**, 5920–5938. doi:10.1002/2013JB010466

Funamori, N., Yagi, T., Utsumi, W., Kondo, T., Uchida, T. & Funamori, M. (1996) Thermoelastic properties of MgSiO3 perovskite determined by in situ X ray observations up to 30 GPa and 2000 K. *Journal of Geophysical Research: Solid Earth*, **101**, 8257–8269. doi:10.1029/95JB03732

Garnero, E.J., Maupin, V., Lay, T. & Fouch, M.J. (2004) Variable Azimuthal Anisotropy in Earth's Lowermost Mantle. *Science*, **306**, 259–261. doi:10.1126/science.1103411

Garnero, E.J. & McNamara, A.K. (2008) Structure and Dynamics of Earth's Lower Mantle. *Science*, **320**, 626–628. doi:10.1126/science.1148028

Girard, J., Amulele, G., Farla, R., Mohiuddin, A. & Karato, S. (2016) Shear deformation of bridgmanite and magnesiowüstite aggregates at lower mantle conditions. *Science*, **351**, 144–147. doi:10.1126/science.aad3113

Gleason, A.E. & Mao, W.L. (2013) Strength of iron at core pressures and evidence for a weak Earth's inner core. *Nature Geoscience*, **6**, 571–574, Nature Publishing Group. doi:10.1038/ngeo1808

Goto, K., Suzuki, Z. & Hamaguchi, H. (1987) Stress distribution due to olivine-spinel phase transition in descending plate and deep focus earthquakes. *Journal of Geophysical Research: Solid Earth*, **92**, 13811–13820. doi:https://doi.org/10.1029/JB092iB13p13811

Green II, H.W. & Burnley, P.C. (1989) A new self-organizing mechanism for deep-focus earthquakes. *Nature*, **341**, 733–737. doi:10.1038/341733a0

Gualtieri, A.F. (2000) Accuracy of XRPD QPA using the combined Rietveld–RIR method. *Journal of Applied Crystallography*, **33**, 267–278. doi:https://doi.org/10.1107/S002188989901643X

Girard, J., Amulele, G., Farla, R., Mohiuddin, A. & Karato, S. (2016) Shear deformation of bridgmanite and magnesiowüstite aggregates at lower mantle conditions. *Science*, **351**, 144–147. doi:10.1126/science.aad3113

Girard, J., Chen, J., Raterron, P. & Holyoke, C.W. (2013) Hydrolytic weakening of olivine at mantle pressure: Evidence of [100](010) slip system softening from single-crystal deformation experiments. *Physics of the Earth and Planetary Interiors*, **216**, 12–20. doi:10.1016/j.pepi.2012.10.009

Gloaguen, D., Oum, G., Legrand, V., Fajoui, J. & Branchu, S. (2013) Experimental and theoretical studies of intergranular strain in an alpha titanium alloy during plastic deformation. *Acta Materialia*, **61**, 5779–5790. doi:10.1016/j.actamat.2013.06.022

Hansen, L.N., Kumamoto, K.M., Thom, C.A., Wallis, D., Durham, W.B., Goldsby, D.L., Breithaupt, T., *et al.* (2019) Low-Temperature Plasticity in Olivine: Grain Size, Strain Hardening, and the Strength of the Lithosphere. *Journal of Geophysical Research: Solid Earth*, **124**, 5427–5449. doi:https://doi.org/10.1029/2018JB016736

Henningsson, N.A., Hall, S.A., Wright, J.P. & Hektor, J. (2020) Reconstructing intragranular strain fields in polycrystalline materials from scanning 3DXRD data. *Journal Applied Crystallography*, **53**, 314–325, International Union of Crystallography. doi:10.1107/S1600576720001016

Hirose, K., Sinmyo, R. & Hernlund, J. (2017) Perovskite in Earth's deep interior. *Science*, **358**, 734–738. doi:10.1126/science.aam8561

Holland, T.J.B. & Redfern, S. a. T. (1997) Unit cell refinement from powder diffraction data: the use of regression diagnostics. *Mineralogical Magazine*, **61**, 65–77, Cambridge University Press. doi:10.1180/minmag.1997.061.404.07

Horiuchi, H. & Sawamoto, H. (1981) β-Mg2SiO4: Single-crystal X-ray diffraction study. *American Mineralogist*, **66**, 568–575.

Horiuchi, H., Ito, E. & Weidner, D.J. (1987) Perovskite-type $MgSiO_3$; single-crystal X-ray diffraction study. *American Mineralogist*, **72**, 357–360.

Idrissi, H., Bollinger, C., Boioli, F., Schryvers, D. & Cordier, P. (2016) Low-temperature plasticity of olivine revisited with in situ TEM nanomechanical testing. *Science Advances*, **2**, e1501671. doi:10.1126/sciadv.1501671

Jung, H. & Karato, S.-I. (2001) Effects of water on dynamically recrystallized grain-size of olivine. *Journal of Structural Geology*, **23**, 1337–1344. doi:10.1016/S0191-8141(01)00005-0

Kaercher, P., Miyagi, L., Kanitpanyacharoen, W., Zepeda-Alarcon, E., Wang, Y., Parkinson, D., Lebensohn, R.A., *et al.* (2016) Two-phase deformation of lower mantle mineral analogs. *Earth and Planetary Science Letters*, **456**, 134–145. doi:10.1016/j.epsl.2016.09.030

Kamaya, M. (2009) Measurement of local plastic strain distribution of stainless steel by electron backscatter diffraction. *Materials Characterization*, **60**, 125–132. doi:10.1016/j.matchar.2008.07.010

Kantor, I., Prakapenka, V., Kantor, A., Dera, P., Kurnosov, A., Sinogeikin, S., Dubrovinskaia, N., *et al.* (2012) BX90: A new diamond anvil cell design for X-ray diffraction and optical measurements. *Review of Scientific Instruments*, **83**, 125102, American Institute of Physics. doi:10.1063/1.4768541

Karato, S. & Weidner, D.J. (2008) Laboratory Studies of the Rheological Properties of Minerals under Deep-Mantle Conditions. *Elements*, **4**, 191–196. doi:10.2113/GSELEMENTS.4.3.191

Kasemer, M., Zepeda-Alarcon, E., Carson, R., Dawson, P. & Wenk, H.-R. (2020) Deformation heterogeneity and intragrain lattice misorientation in high strength contrast, dual-phase bridgmanite/periclase. *Acta Materialia*, **189**, 284–298. doi:10.1016/j.actamat.2020.02.061

Keken, P.E. van & Yuen, D.A. (1995) Dynamical influences of high viscosity in the lower mantle induced by the steep melting curve of perovskite: Effects of curvature and time dependence. *Journal of Geophysical Research: Solid Earth*, **100**, 15233–15248. doi:10.1029/95JB00923

Kendrick, J.E., Lavallée, Y., Mariani, E., Dingwell, D.B., Wheeler, J. & Varley, N.R. (2017) Crystal plasticity as an indicator of the viscous-brittle transition in magmas. *Nature Communications*, **8**, 1926, Nature Publishing Group. doi:10.1038/s41467-017-01931-4

Knittle, E. & Jeanloz, R. (1987) Synthesis and Equation of State of $(Mg,Fe)SiO_3$ Perovskite to Over 100 Gigapascals. *Science*, **235**, 668–670. doi:10.1126/science.235.4789.668

Kerschhofer, L., Sharp, T.G. & Rubie, D.C. (1996) Intracrystalline Transformation of Olivine to Wadsleyite and Ringwoodite Under Subduction Zone Conditions. *Science*, **274**, 79–81. doi:10.1126/science.274.5284.79

Kohlstedt, D.L. & Goetze, C. (1974) Low-stress high-temperature creep in olivine single crystals. *Journal of Geophysical Research (1896-1977)*, **79**, 2045–2051. doi:10.1029/JB079i014p02045

Kumamoto, K.M., Thom, C.A., Wallis, D., Hansen, L.N., Armstrong, D.E.J., Warren, J.M., Goldsby, D.L., *et al.* (2017) Size effects resolve discrepancies in 40 years of work on low-temperature plasticity in olivine. *Science Advances*, **3**, e1701338, doi:10.1126/sciadv.1701338

Kunz, M., Yan, J., Cornell, E., Domning, E.E., Yen, C.E., Doran, A., Beavers, C.M., *et al.* (2018) Implementation and application of the peak scaling method for temperature measurement in the laser heated diamond anvil cell. *Review of Scientific Instruments*, **89**, 083903. doi:10.1063/1.5028276

Langrand, C., Hilairet, N., Nisr, C., Roskosz, M., Ribárik, G., Vaughan, G.B.M. & Merkel, S. (2017) Reliability of multigrain indexing for orthorhombic polycrystals above 1 Mbar: application to MgSiO $_3$ post-perovskite. *Journal of Applied Crystallography*, **50**, 120–130. doi:10.1107/S1600576716018057

Lay, T. (2008) Sharpness of the D″ discontinuity beneath the Cocos Plate: Implications for the perovskite to post-perovskite phase transition. *Geophysical Research Letters*, **35**. doi:10.1029/2007GL032465

Levien, L., Prewitt, C.T. & Weidner, D.J. (1980) Structure and elastic properties of quartz at pressure. *American Mineralogist*, **65**, 920–930.

Li, L., Weidner, D., Raterron, P., Chen, J. & Vaughan, M. (2004) Stress measurements of deforming olivine at high pressure. *Physics of the Earth and Planetary Interiors* New Developments in High-Pressure Mineral Physics and Applications to the Earth's Interior, **143–144**, 357–367. doi:10.1016/j.pepi.2003.09.022

Lin, Giannetta, Jugle, Couper, Dunleavy, & Miyagi. (2019) Texture Development and Stress–Strain Partitioning in Periclase + Halite Aggregates. *Minerals*, **9**, 679. doi:10.3390/min9110679

Long, H., Weidner, D.J., Li, L., Chen, J. & Wang, L. (2011) Deformation of olivine at subduction zone conditions determined from in situ measurements with synchrotron radiation. *Physics of the Earth and Planetary Interiors*, **186**, 23–35. doi:10.1016/j.pepi.2011.02.006

Lutterotti, L., Vasin, R. & Wenk, H.-R. (2014) Rietveld texture analysis from synchrotron diffraction images. I. Calibration and basic analysis. *Powder Diffraction*, **29**, 76–84, Cambridge University Press. doi:10.1017/S0885715613001346

Madon, M. & Poirier, J.P. (1983) Transmission electron microscope observation of α, β and γ (Mg, Fe)$_2$SiO$_4$ in shocked meteorites: planar defects and polymorphic transitions. *Physics of the Earth and Planetary Interiors*, **33**, 31–44. doi:10.1016/0031-9201(83)90005-5

Mainprice, D., Tommasi, A., Couvy, H., Cordier, P. & Frost, D.J. (2005) Pressure sensitivity of olivine slip systems and seismic anisotropy of Earth's upper mantle. *Nature*, **433**, 731–733, Nature Publishing Group. doi:10.1038/nature03266

Mainprice, D., Hielscher, R. & Schaeben, H. (2011) Calculating anisotropic physical properties from texture data using the MTEX open-source package. *Geological Society, London, Special Publications*, **360**, 175–192. doi:10.1144/SP360.10

Marquardt, H., Speziale, S., Reichmann, H.J., Frost, D.J. & Schilling, F.R. (2009) Single-crystal elasticity of $(Mg_{0.9}Fe_{0.1})O$ to 81 GPa. *Earth and Planetary Science Letters*, **287**, 345–352. doi:10.1016/j.epsl.2009.08.017

Marquardt, H. & Miyagi, L. (2015) Slab stagnation in the shallow lower mantle linked to an increase in mantle viscosity. *Nature Geoscience*, **8**, 311–314. doi:10.1038/ngeo2393

Martinez, I., Wang, Y., Guyot, F., Liebermann, R.C. & Doukhan, J.-C. (1997) Microstructures and iron partitioning in $(Mg,Fe)SiO_3$ perovskite-(Mg,Fe)O magnesiowüstite assemblages: An analytical transmission electron microscopy study. *Journal of Geophysical Research: Solid Earth*, **102**, 5265–5280. doi:10.1029/96JB03188

Masters, G., Laske, G., Bolton, H. & Dziewonski, A. (2000) The relative behavior of shear velocity, bulk sound speed, and compressional velocity in the mantle: Implications for chemical and thermal structure. in *Geophysical Monograph Series* 117 eds. Karato, S., Forte, A., Liebermann, R., Masters, G. & Stixrude, L., pp. 63–87. doi:10.1029/GM117p0063

Mattern, E., Matas, J., Ricard, Y. & Bass, J. (2005) Lower mantle composition and temperature from mineral physics and thermodynamic modelling. *Geophysical Journal International*, **160**, 973–990. doi:10.1111/j.1365-246X.2004.02549.x

Matthies, S. (2012) GEO-MIX-SELF calculations of the elastic properties of a textured graphite sample at different hydrostatic pressures. *Journal Applied Crystallography*, **45**, 1–16, International Union of Crystallography. doi:10.1107/S002188981104338X

Maupin, V., Garnero, E.J., Lay, T. & Fouch, M.J. (2005) Azimuthal anisotropy in the D″ layer beneath the Caribbean. *Journal of Geophysical Research: Solid Earth*, **110**. doi:10.1029/2004JB003506

McNamara, A.K., Keken, P.E. van & Karato, S.-I. (2002) Development of anisotropic structure in the Earth's lower mantle by solid-state convection. *Nature*, **416**, 310–314. doi:10.1038/416310a

McNamara, A.K., Keken, P.E. van & Karato, S.-I. (2003) Development of finite strain in the convecting lower mantle and its implications for seismic anisotropy. *Journal of Geophysical Research: Solid Earth*, **108**. doi:10.1029/2002JB001970

Meade, C. & Jeanloz, R. (1990) The strength of mantle silicates at high pressures and room temperature: implications for the viscosity of the mantle. *Nature*, **348**, 533–535, Nature Publishing Group. doi:10.1038/348533a0

Means, W.D. (1976) The Stress Ellipsoid, I. in *Stress and Strain: Basic Concepts of Continuum Mechanics for Geologists* ed. Means, W.D., pp. 53–61, New York, NY: Springer New York. doi:10.1007/978-1-4613-9371-9_7

Merkel, S., Wenk, H.R., Shu, J., Shen, G., Gillet, P., Mao, H. & Hemley, R.J. (2002) Deformation of polycrystalline MgO at pressures of the lower mantle. *Journal of Geophysical Research: Solid Earth*, **107**, ECV 3-1-ECV 3-17. doi:10.1029/2001JB000920

Merkel, S., McNamara, A.K., Kubo, A., Speziale, S., Miyagi, L., Meng, Y., Duffy, T.S., *et al.* (2007) Deformation of $(Mg,Fe)SiO_3$ Post-Perovskite and D'' Anisotropy. *Science*, **316**, 1729–1732. doi:10.1126/science.1140609

Meyers, M.A. & Chawla, K.K. (2009) Mechanical Behavior of Materials, 2nd edition, 882.

Miyagi, L., Kanitpanyacharoen, W., Raju, S., Kaercher, P., Knight, J., Macdowell, A., Wenk, H.-R., *et al.* (2013) Combined resistive and laser heating technique for in situ radial X-ray diffraction in the diamond anvil cell at high pressure and temperature. *The Review of scientific instruments*, **84**, 025118. doi:10.1063/1.4793398

Miyagi, L., Merkel, S., Yagi, T., Sata, N., Ohishi, Y. & Wenk, H.-R. (2009) Diamond anvil cell deformation of $CaSiO_3$ perovskite up to 49GPa. *Physics of the Earth and Planetary Interiors* Advances in High Pressure Mineral Physics: from Deep Mantle to the Core, **174**, 159–164. doi:10.1016/j.pepi.2008.05.018

Miyagi, L., Kanitpanyacharoen, W., Stackhouse, S., Militzer, B. & Wenk, H.-R. (2011) The enigma of post-perovskite anisotropy: deformation versus transformation textures. *Physical Chemistry of Minerals*, **38**, 665–678. doi:10.1007/s00269-011-0439-y

Miyagi, L. & Wenk, H.-R. (2016) Texture development and slip systems in bridgmanite and bridgmanite + ferropericlase aggregates. *Physics and Chemistry of Minerals*, **43**, 597–613. doi:10.1007/s00269-016-0820-y

Miyahara, M., Ohtani, E., Ozawa, S., Kimura, M., Goresy, A.E., Sakai, T., Nagase, T., *et al.* (2011) Natural dissociation of olivine to $(Mg,Fe)SiO_3$ perovskite and magnesiowüstite in a shocked Martian meteorite. *PNAS*, **108**, 5999–6003, doi:10.1073/pnas.1016921108

Muir, J.M.R. & Brodholt, J.P. (2016) Ferrous iron partitioning in the lower mantle. *Physics of the Earth and Planetary Interiors*, **257**, 12–17. doi:10.1016/j.pepi.2016.05.008

Murakami, M., Hirose, K., Sata, N. & Ohishi, Y. (2005) Post-perovskite phase transition and mineral chemistry in the pyrolitic lowermost mantle. *Geophysical Research Letters*, **32**. doi:10.1029/2004GL021956

Mussi, A., Cordier, P., Demouchy, S. & Vanmansart, C. (2014) Characterization of the glide planes of the [001] screw dislocations in olivine using electron tomography. *Phys Chem Minerals*, **41**, 537–545. doi:10.1007/s00269-014-0665-1

Nisr, C., Ribárik, G., Ungár, T., Vaughan, G.B.M., Cordier, P. & Merkel, S. (2012) High resolution three-dimensional X-ray diffraction study of dislocations in grains of MgGeO3 post-perovskite at 90 GPa. *Journal of Geophysical Research: Solid Earth*, **117**. doi:https://doi.org/10.1029/2011JB008401

Nakagawa, T. & Tackley, P.J. (2011) Effects of low-viscosity post-perovskite on thermo-chemical mantle convection in a 3-D spherical shell. *Geophysical Research Letters*, **38**. doi:https://doi.org/10.1029/2010GL046494

Nomura, R., Hirose, K., Uesugi, K., Ohishi, Y., Tsuchiyama, A., Miyake, A. & Ueno, Y. (2014) Low Core-Mantle Boundary Temperature inferred from the solidus of pyrolite. *Science*, **343**, 522–525. doi:10.1126/science.1248186

Nowacki, A., Wookey, J. & Kendall, J.-M. (2010) Deformation of the lowermost mantle from seismic anisotropy. *Nature*, **467**, 1091–1094, Nature Publishing Group. doi:10.1038/nature09507

Nowacki, A. (2013) Deformation of the Lowermost Mantle from Seismic Anisotropy. in *Plate Deformation from Cradle to Grave: Seismic Anisotropy and Deformation at Mid-Ocean Ridges and in the Lowermost Mantle* Springer Theses ed. Nowacki, A., pp. 99–122, doi:10.1007/978-3-642-34842-6_4

Noyan, I.C. & Cohen, J.B. (1987) *Residual Stress: Measurement by Diffraction and Interpretation*. Materials Research and Engineering, New York: Springer-Verlag. doi:10.1007/978-1-4613-9570-6

Nye, J.F., 1957. Physical Properties of Crystals. Their Representation by Tensors and Matrices, Oxford Clarendon Press, 322pp.

Oganov, A.R., Brodholt, J.P. & Price, G.D. (2001) The elastic constants of $MgSiO_3$ perovskite at pressures and temperatures of the Earth's mantle. *Nature*, **411**, 934–937, Nature Publishing Group. doi:10.1038/35082048

Oganov, A.R. & Ono, S. (2004) Theoretical and experimental evidence for a post-perovskite phase of MgSiO3 in Earth's D″ layer. *Nature*, **430**, 445–448. doi:10.1038/nature02701

Oddershede, J., Schmidt, S., Poulsen, H.F., Sørensen, H.O., Wright, J. & Reimers, W. (2010) Determining grain resolved stresses in polycrystalline materials using three-dimensional X-ray diffraction. *Journal Applied Crystallography*, **43**, 539–549, International Union of Crystallography. doi:10.1107/S0021889810012963

Ogi, H., Ohmori, T., Nakamura, N. & Hirao, M. (2006) Elastic, anelastic, and piezoelectric coefficients of α-quartz determined by resonance ultrasound spectroscopy. *Journal of Applied Physics*, **100**, 053511, American Institute of Physics. doi:10.1063/1.2335684

Offerman, S.E., Dijk, N.H. van, Sietsma, J., Grigull, S., Lauridsen, E.M., Margulies, L., Poulsen, H.F., *et al.* (2002) Grain Nucleation and Growth During Phase Transformations. *Science*, **298**, 1003–1005, doi:10.1126/science.1076681

Pagan, D.C. & Miller, M.P. (2014) Connecting heterogeneous single slip to diffraction peak evolution in high-energy monochromatic X-ray experiments. *Journal Applied Crystallography*, **47**, 887–898. doi:10.1107/S1600576714005779

Panning, M. & Romanowicz, B. (2006) A three-dimensional radially anisotropic model of shear velocity in the whole mantle. *Geophysical Journal International*, **167**, 361–379. doi:10.1111/j.1365-246X.2006.03100.x

Parise, J.B., Wang, Y., Yeganeh-Haeri, A., Cox, D.E. & Fei, Y. (1990) Crystal structure and thermal expansion of $(Mg,Fe)SiO_3$ perovskite. *Geophysical Research Letters*, **17**, 2089–2092. doi:10.1029/GL017i012p02089

Pisconti, A., Thomas, C. & Wookey, J. (2019) Discriminating Between Causes of D″ Anisotropy Using Reflections and Splitting Measurements for a Single Path. *Journal of Geophysical Research: Solid Earth*, **124**, 4811–4830. doi:10.1029/2018JB016993

Pokharel, R. (2018) Overview of High-Energy X-Ray Diffraction Microscopy (HEDM) for Mesoscale Material Characterization in Three-Dimensions. in *Materials Discovery and Design: By Means of Data Science and Optimal Learning* Springer Series in Materials Science eds. Lookman, T., Eidenbenz, S., Alexander, F. & Barnes, C., pp. 167–201, Cham: Springer International Publishing. doi:10.1007/978-3-319-99465-9_7

Poulsen, H.F., Garbe, S., Lorentzen, T., Jensen, D.J., Poulsen, F.W., Andersen, N.H., Frello, T., *et al.* (1997) Applications of High-Energy Synchrotron Radiation for Structural Studies of Polycrystalline Materials. *Journal of Synchrotron Radiation*, **4**, 147–154. doi:10.1107/S0909049597002021

Prescher, C. & Prakapenka, V.B. (2015) DIOPTAS: a program for reduction of two-dimensional X-ray diffraction data and data exploration. *High Pressure Research*, **35**, 223–230, Taylor & Francis. doi:10.1080/08957959.2015.1059835

Proietti, A., Bystricky, M., Guignard, J., Béjina, F. & Crichton, W. (2016) Effect of pressure on the strength of olivine at room temperature. *Physics of the Earth and Planetary Interiors*, **259**, 34–44. doi:10.1016/j.pepi.2016.08.004

Raterron, P., Wu, Y., Weidner, D.J. & Chen, J. (2004) Low-temperature olivine rheology at high pressure. *Physics of the Earth and Planetary Interiors*, **145**, 149–159. doi:10.1016/j.pepi.2004.03.007

Raterron, P., Chen, J. & Weidner, D.J. (2002) A process for low-temperature olivine-spinel transition under quasi-hydrostatic stress. *Geophysical Research Letters*, **29**, 36-1-36–4. doi:https://doi.org/10.1029/2002GL015003

Ricolleau, A., Fei, Y., Cottrell, E., Watson, H., Deng, L., Zhang, L., Fiquet, G., *et al.* (2009) Density profile of pyrolite under the lower mantle conditions. *Geophysical Research Letters*, **36**. doi:10.1029/2008GL036759

Ringwood, A.E. (1982) Phase Transformations and Differentiation in Subducted Lithosphere: Implications for Mantle Dynamics, Basalt Petrogenesis, and Crustal Evolution. *The Journal of Geology*, **90**, 611–643, The University of Chicago Press. doi:10.1086/628721

Ringwood, A.E. (1991) Phase transformations and their bearing on the constitution and dynamics of the mantle. *Geochimica et Cosmochimica Acta*, **55**, 2083–2110. doi:10.1016/0016-7037(91)90090-R

Rokosky, J.M., Lay, T. & Garnero, E.J. (2006) Small-scale lateral variations in azimuthally anisotropic D″ structure beneath the Cocos Plate. *Earth and Planetary Science Letters*, **248**, 411–425. doi:10.1016/j.epsl.2006.06.005

Romanowicz, B. & Wenk, H.-R. (2017) Anisotropy in the deep Earth. *Physics of the Earth and Planetary Interiors*, **269**, 58–90. doi:10.1016/j.pepi.2017.05.005

Rosa, A.D., Hilairet, N., Ghosh, S., Garbarino, G., Jacobs, J., Perrillat, J.-P., Vaughan, G., *et al.* (2015) In situ monitoring of phase transformation microstructures at Earth's mantle pressure and temperature using multi-grain XRD. *Journal Applied Crystallography*, **48**, 1346–1354. doi:10.1107/S1600576715012765

Rosa, A.D., Hilairet, N., Ghosh, S., Perrillat, J.-P., Garbarino, G. & Merkel, S. (2016) Evolution of grain sizes and orientations during phase transitions in hydrous Mg_2SiO_4. *Journal of Geophysical Research: Solid Earth*, **121**, 7161–7176. doi:10.1002/2016JB013360

Sasaki, S., Prewitt, C.T., Sato, Y. & Ito, E. (1982) Single-crystal X ray study of γ Mg_2SiO_4. *Journal of Geophysical Research: Solid Earth*, **87**, 7829–7832. doi:https://doi.org/10.1029/JB087iB09p07829

Shen, R.R. & Efsing, P. (2018) Overcoming the drawbacks of plastic strain estimation based on KAM. *Ultramicroscopy*, **184**, 156–163. doi:10.1016/j.ultramic.2017.08.013

Shim, S.-H., Grocholski, B., Ye, Y., Alp, E.E., Xu, S., Morgan, D., Meng, Y., *et al.* (2017) Stability of ferrous-iron-rich bridgmanite under reducing mid mantle conditions. *PNAS*. doi:10.1073/pnas.1614036114

Simmons, N.A. & Grand, S.P. (2002) Partial melting in the deepest mantle. *Geophysical Research Letters*, **29**, 47-1-47–4. doi:10.1029/2001GL013716

Sinmyo, R. & Hirose, K. (2010) The Soret diffusion in laser-heated diamond-anvil cell. *Physics of the Earth and Planetary Interiors* Transport properties of the lower mantle, **180**, 172–178. doi:10.1016/j.pepi.2009.10.011

Soignard, E. & McMillan, P.F. (2004) An Introduction to Diamond Anvil Cells and Loading Techniques. *High-Pressure Crystallography* NATO Science Series eds. Katrusiak, A. & McMillan, P., pp. 81–100, Dordrecht: Springer Netherlands. doi:10.1007/978-1-4020-2102-2_6

Solomatov, V.S. & Reese, C.C. (2008) Grain size variations in the Earth's mantle and the evolution of primordial chemical heterogeneities. *Journal of Geophysical Research: Solid Earth*, **113**. doi:https://doi.org/10.1029/2007JB005319

Sørensen, H.O., Schmidt, S., Wright, J.P., Vaughan, G.B.M., Techert, S., Garman, E.F., Oddershede, J., *et al.* (2012) Multigrain crystallography. *Zeitschrift für Kristallographie*, **227**, 63–78. doi:10.1524/zkri.2012.1438

Spencer, L.J. (1937) The Tenham (Queensland) meteoritic shower of 1879 (With Plates XIV-XVII.). *Mineralogical magazine and journal of the Mineralogical Society*, **24**, 437–452, Cambridge University Press. doi:10.1180/minmag.1937.024.156.02

Stein, S.A. & Rubie, D.C. (1999) Deep Earthquakes in Real Slabs. *Science*, **286**, 909–910, American Association for the Advancement of Science. doi:10.1126/science.286.5441.909

Stixrude, L. & Karki, B. (2005) Structure and Freezing of $MgSiO_3$ Liquid in Earth's Lower Mantle. *Science*, **310**, 297–299. doi:10.1126/science.1116952

Sturgeon, W., Ferreira, A.M.G., Faccenda, M., Chang, S.-J. & Schardong, L. (2019) On the Origin of Radial Anisotropy Near Subducted Slabs in the Midmantle. *Geochemistry, Geophysics, Geosystems*, **20**, 5105–5125. doi:10.1029/2019GC008462

Sun, J., Jin, L., Dong, J., Ding, W. & Luo, A.A. (2016) Microscopic deformation compatibility during monotonic loading in a Mg-Gd-Y alloy. *Materials Characterization*, **119**, 195–199. doi:10.1016/j.matchar.2016.08.003

Sun, D., Helmberger, D., Lai, V.H., Gurnis, M., Jackson, J.M. & Yang, H.-Y. (2019) Slab Control on the Northeastern Edge of the Mid-Pacific LLSVP Near Hawaii. *Geophysical Research Letters*, **46**, 3142–3152. doi:https://doi.org/10.1029/2018GL081130

Thielmann, M. & Kaus, B.J.P. (2012) Shear heating induced lithospheric-scale localization: Does it result in subduction? *Earth and Planetary Science Letters*, **359–360**, 1–13. doi:10.1016/j.epsl.2012.10.002

Thomas, C., Wookey, J. & Simpson, M. (2007) D″ anisotropy beneath Southeast Asia. *Geophysical Research Letters*, **34**. doi:10.1029/2006GL028965

Tommasi, A., Goryaeva, A., Carrez, P., Cordier, P. & Mainprice, D. (2018) Deformation, crystal preferred orientations, and seismic anisotropy in the Earth's D″ layer. *Earth and Planetary Science Letters*, **492**, 35–46. doi:10.1016/j.epsl.2018.03.032

Tomioka, N. & Okuchi, T. (2017) A new high-pressure form of Mg_2SiO_4 highlighting diffusionless phase transitions of olivine. *Scientific Reports*, **7**, 17351, Nature Publishing Group. doi:10.1038/s41598-017-17698-z

Tomioka, N., Bindi, L., Okuchi, T., Miyahara, M., Iitaka, T., Li, Z., Kawatsu, T., *et al.* (2021) Poirierite, a dense metastable polymorph of magnesium iron silicate in shocked meteorites. *Communications Earth & Environment*, **2**, 1–8, Nature Publishing Group. doi:10.1038/s43247-020-00090-7

Tsuchiya, T., Tsuchiya, J., Umemoto, K. & Wentzcovitch, R.M. (2004) Elasticity of post-perovskite MgSiO3. *Geophysical Research Letters*, **31**. doi:10.1029/2004GL020278

Tyrrell, H.J.V. & Colledge, R. (1954) Thermal Diffusion Potentials and the Soret Effect. *Nature*, **173**, 264–265, Nature Publishing Group. doi:10.1038/173264a0

Van der hilst, R.D., Widiyantoro, S. & Engdahl, E.R. (1997) Evidence for deep mantle circulation from global tomography. *Nature*, **386**, 578–584. doi:10.1038/386578a0

Verma, R.K. (1960) Elasticity of some high-density crystals. *Journal of Geophysical Research (1896-1977)*, **65**, 757–766. doi:https://doi.org/10.1029/JZ065i002p00757

Vinet, N., Flemming, R.L. & Higgins, M.D. (2011) Crystal structure, mosaicity, and strain analysis of Hawaiian olivines using in situ X-ray diffraction. *American Mineralogist*, **96**, 486–497. doi:10.2138/am.2011.3593

Vinnik, L.P., Farra, V. & Romanowicz, B. (1989) Observational evidence for diffracted SV in the shadow of the Earth's core. *Geophysical Research Letters*, **16**, 519–522. doi:10.1029/GL016i006p00519

Walker, A.M., Forte, A.M., Wookey, J., Nowacki, A. & Kendall, J.-M. (2011) Elastic anisotropy of D″ predicted from global models of mantle flow: Predicting anisotropy in D″. *Geochem. Geophys. Geosyst.*, **12**, n/a-n/a. doi:10.1029/2011GC003732

Walker, A.M. & Wookey, J. (2012) MSAT—A new toolkit for the analysis of elastic and seismic anisotropy. *Computers & Geosciences*, **49**, 81–90. doi:10.1016/j.cageo.2012.05.031

Walker, A.M., Dobson, D.P., Wookey, J., Nowacki, A. & Forte, A.M. (2018) The anisotropic signal of topotaxy during phase transitions in D″. *Physics of the Earth and Planetary Interiors* Special Issue:15th SEDI conference, **276**, 159–171. doi:10.1016/j.pepi.2017.05.013

Wang, Y., Zhu, L., Shi, F., Schubnel, A., Hilairet, N., Yu, T., Rivers, M., *et al.* (2017) A laboratory nanoseismological study on deep-focus earthquake micromechanics. *Science Advances*, **3**, e1601896, doi:10.1126/sciadv.1601896

Wang, Y., Guyot, F., Yeganeh-Haeri, A. & Liebermann, R.C. (1990) Twinning in $MgSiO_3$ Perovskite. *Science*, **248**, 468–471. doi:10.1126/science.248.4954.468

Wang, Y., Guyot, F. & Liebermann, R.C. (1992) Electron microscopy of (Mg, Fe)SiO_3 Perovskite: Evidence for structural phase transitions and implications for the lower mantle. *Journal of Geophysical Research: Solid Earth*, **97**, 12327–12347. doi:10.1029/92JB00870

Watanabe, T. (1993) Effects of water and melt on seismic velocities and their application to characterization of seismic reflectors. *Geophysical Research Letters*, **20**, 2933–2936. doi:10.1029/93GL03170

Wehinger, B., Bosak, A., Nazzareni, S., Antonangeli, D., Mirone, A., Chaplot, S.L., Mittal, R., *et al.* (2016) Dynamical and elastic properties of $MgSiO_3$ perovskite (bridgmanite). *Geophysical Research Letters*, **43**, 2568–2575. doi:10.1002/2016GL067970

Weidner, D.J., Wang, Y; Chen, G; Ando, J; Vaugn, M.T. (1998) Rheology measurements at high pressure and temperature. In "Properties of earth and planetary materials at high pressure and temperature". Edit. M.H. Manghnani and T. Yagi, *Geophysical Monograph series 101*, 473–482, American Geophysical Union Monograph 101.

Wenk, H.-R. & Tomé, C.N. (1999) Modeling dynamic recrystallization of olivine aggregates deformed in simple shear. *Journal of Geophysical Research: Solid Earth*, **104**, 25513–25527. doi:https://doi.org/10.1029/1999JB900261

Wenk, H.-R., Lonardelli, I., Merkel, S., Miyagi, L., Pehl, J., Speziale, S. & Tommaseo, C.E. (2006) Deformation textures produced in diamond anvil experiments, analysed in radial diffraction geometry. *Journal of Physics: Condensed Matter*, **18**, S933–S947. doi:10.1088/0953-8984/18/25/S02

Wenk, H.-R., Kanitpanyacharoen, W. & Voltolini, M. (2010) Preferred orientation of phyllosilicates: Comparison of fault gouge, shale and schist. *Journal of Structural Geology*, **32**, 478–489. doi:10.1016/j.jsg.2010.02.003

Wenk, H.-R., Chandler, B.C., Chen, K., Li, Y., Tamura, N. & Yu, R. (2020) Residual lattice strain in quartzites as a potential palaeo-piezometer. *Geophysical Journal International*, **222**, 1363–1378. doi:10.1093/gji/ggaa226

Wenk, H.-R., Lutterotti, L., Kaercher, P., Kanitpanyacharoen, W., Miyagi, L. & Vasin, R. (2014) Rietveld texture analysis from synchrotron diffraction images. II. Complex multiphase materials and diamond anvil cell experiments. *Powder Diffraction*, **29**, 220–232, Cambridge University Press. doi:10.1017/S0885715614000360

Wheeler, J. (2009) The preservation of seismic anisotropy in the Earth's mantle during diffusion creep. *Geophysical Journal International*, **178**, 1723–1732, Oxford Academic. doi:10.1111/j.1365-246X.2009.04241.x

Williams, Q. & Garnero, E.J. (1996) Seismic Evidence for Partial Melt at the Base of Earth's Mantle. *Science*, **273**, 1528–1530, doi:10.1126/science.273.5281.1528

Withers, P.J. & Bhadeshia, H.K.D.H. (2001) Residual stress. Part 1 – Measurement techniques. *Materials Science and Technology*, **17**, 355–365, Taylor & Francis. doi:10.1179/026708301101509980

Withers, P.J. & Bhadeshia, H.K.D.H. (2001) Residual stress. Part 2 – Nature and origins. *Materials Science and Technology*, **17**, 366–375, Taylor & Francis. doi:10.1179/026708301101510087

Wookey, J. & Kendall, J.-M. (2007) Seismic anisotropy of post-perovskite and the lowermost mantle. in *Geophysical Monograph Series 174.* eds. Hirose, K., Brodholt, J., Lay, T. & Yuen, D., Vol. 174, pp. 171–189, doi:10.1029/174GM13

Wu, T. -C. & Bassett, W.A. (1994) Measuring deviatoric stress in the diamond anvil cell using two x-ray diffraction geometries. *AIP Conference Proceedings*, **309**, 1625–1628, American Institute of Physics. doi:10.1063/1.46398

Wu, Z. (2016) Velocity structure and composition of the lower mantle with spin crossover in ferropericlase. *Journal of Geophysical Research: Solid Earth*, **121**, 2304–2314. doi:https://doi.org/10.1002/2015JB012667

Wu, X., Lin, J.-F., Kaercher, P., Mao, Z., Liu, J., Wenk, H.-R. & Prakapenka, V.B. (2017) Seismic anisotropy of the D″ layer induced by (001) deformation of post-perovskite. *Nature Communications*, **8**, 14669. doi:10.1038/ncomms14669

Xie, L., Yoneda, A., Yamazaki, D., Manthilake, G., Higo, Y., Tange, Y., Guignot, N., *et al.* (2020) Formation of bridgmanite-enriched layer at the top lower-mantle during magma ocean solidification. *Nature Communications*, **11**, 548, Nature Publishing Group. doi:10.1038/s41467-019-14071-8

Xu, Y., Shankland, T.J., Linhardt, S., Rubie, D.C., Langenhorst, F. & Klasinski, K. (2004) Thermal diffusivity and conductivity of olivine, wadsleyite and ringwoodite to 20 GPa and 1373 K. *Physics of the Earth and Planetary Interiors* New Developments in High-Pressure Mineral Physics and Applications to the Earth's Interior, **143–144**, 321–336. doi:10.1016/j.pepi.2004.03.005

Yamazaki, D. & Karato, S. (2001) Some mineral physics constraints on the rheology and geothermal structure of Earth's lower mantle. *American Mineralogist*, **86**, 385–391, GeoScienceWorld. doi:10.2138/am-2001-0401

Yamazaki, D., Yoshino, T. & Nakakuki, T. (2014) Interconnection of ferro-periclase controls subducted slab morphology at the top of the lower mantle. *Earth and Planetary Science Letters*, **403**, 352–357. doi:10.1016/j.epsl.2014.07.017

Yang, J., Tong, X., Lin, J.-F., Okuchi, T. & Tomioka, N. (2015) Elasticity of Ferropericlase across the Spin Crossover in the Earth's Lower Mantle. *Scientific Reports*, **5**, 17188, Nature Publishing Group. doi:10.1038/srep17188

Yang, J., Lin, J.-F., Jacobsen, S.D., Seymour, N.M., Tkachev, S.N. & Prakapenka, V.B. (2016) Elasticity of ferropericlase and seismic heterogeneity in the Earth's lower mantle. *Journal of Geophysical Research: Solid Earth*, **121**, 8488–8500. doi:10.1002/2016JB013352

Yu, T., Du, Y., Fan, G., Xu, R., Barabash, R., Hansen, N., Huang, X., *et al.* (2021) In-situ synchrotron X-ray micro-diffraction investigation of ultra-low-strain deformation

microstructure in laminated Ti-Al composites. *Acta Materialia*, **202**, 149–158. doi:10.1016/j.actamat.2020.10.050

Yuan, K. & Romanowicz, B. (2017) Seismic evidence for partial melting at the root of major hot spot plumes. *Science*, **357**, 393–397. doi:10.1126/science.aan0760

Yuan, H. & Zhang, L. (2017) In situ determination of crystal structure and chemistry of minerals at Earth's deep lower mantle conditions. *Matter and Radiation at Extremes*, **2**, 117–128. doi:10.1016/j.mre.2017.01.002

Zha, C., Duffy, T.S., Downs, R.T., Mao, H. & Hemley, R.J. (1998) Brillouin scattering and X-ray diffraction of San Carlos olivine: direct pressure determination to 32 GPa. *Earth and Planetary Science Letters*, **159**, 25–33. doi:10.1016/S0012-821X(98)00063-6

Zhang, L., Yuan, H., Meng, Y. & Mao, H.-K. (2019) Development of High-Pressure Multigrain X-Ray Diffraction for Exploring the Earth's Interior. *Engineering*, **5**, 441–447. doi:10.1016/j.eng.2019.02.004

Zhang, L., Popov, D., Meng, Y., Wang, J., Ji, C., Li, B. & Mao, H. (2016) In-situ crystal structure determination of seifertite SiO2 at 129 GPa: Studying a minor phase near Earth's core–mantle boundary. *American Mineralogist*, **101**, 231–234. doi:10.2138/am-2016-5525

Zhang, L., Meng, Y., Yang, W., Wang, L., Mao, W.L., Zeng, Q.-S., Jeong, J.S., *et al.* (2014) Disproportionation of (Mg,Fe)SiO3 perovskite in Earth's deep lower mantle. *Science*, **344**, 877–882. doi:10.1126/science.1250274

Zhong, S. & Watts, A.B. (2013) Lithospheric deformation induced by loading of the Hawaiian Islands and its implications for mantle rheology. *Journal of Geophysical Research: Solid Earth*, **118**, 6025–6048. doi:https://doi.org/10.1002/2013JB010408

Appendix 1
Multigrain Crystallography: using *HEXRD*

What follows is a descriptive procedure that describes certain processes that are needed when using the *HEXRD* software package that was used during the production of this work which makes use of a mixture of the graphical user interface (GUI) provided by *HEXRD* as well as individual python scripts. Figure A1 reiterates the general *HEXRD* workflow

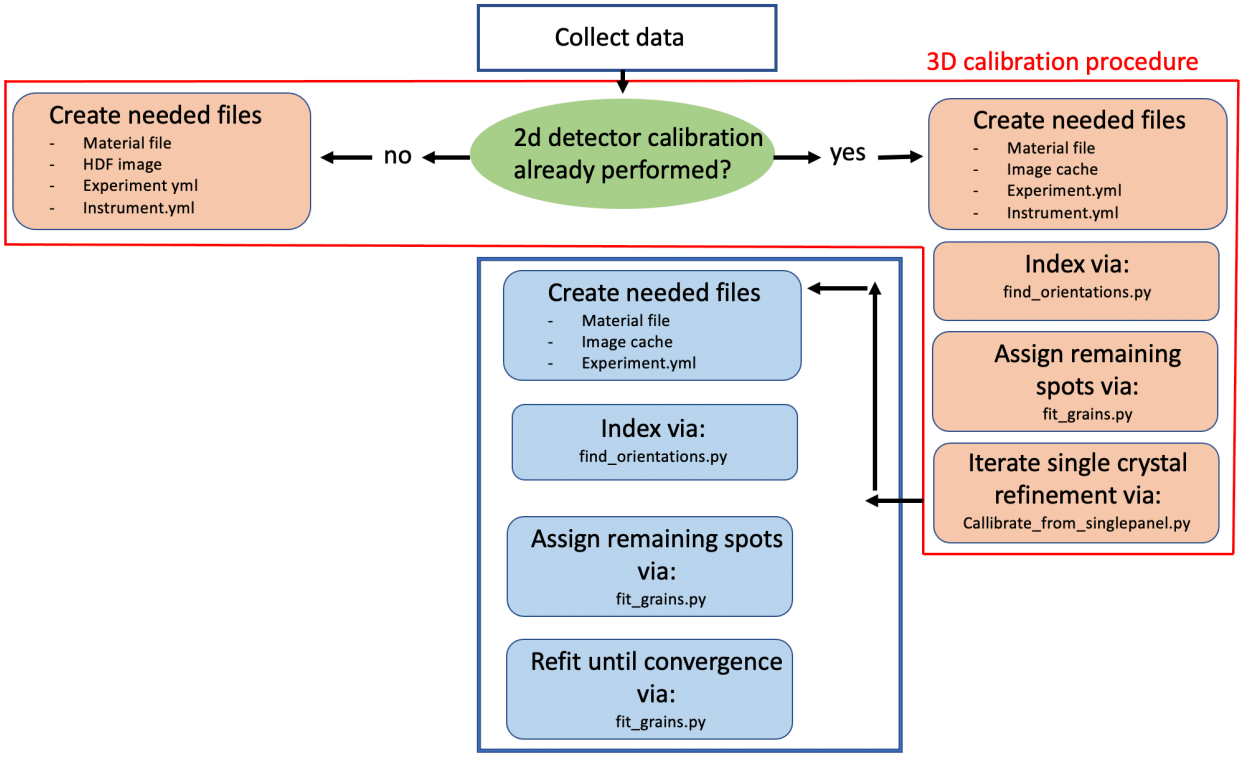

Figure A1. Multigrain analysis workflow using HEXRD. *Showing flowchart moving from data collection, file generation, 2D detector calibration, 3D detector calibration, indexing, and grain fitting.*

The creation and saving of the materials.h5 file were described in Chapter 2. There are expanded capabilities in the materials creation process where if the atomic positions are known entire crystal structure can be created. This can also be achieved by loading a crystal.cif file containing the structure. This feature was not used in these experiments, but future users should exploit this feature.

For the 2D calibration a .tiff file can be loaded directly into the *HEXRD* GUI and the calibration procedure performed as instructed in Chapter 2. The rotation series can be loaded in the same manner. In these experiments however, an external script was used to generate the aggregate diffraction image in the accepted .npz format. This process and the general rotational series description is provided below.

1. Make rotational image series.

Once the rotational data set has been collected it needs to be uploaded to the *HEXRD* software. The *HEXRD* GUI takes many image types but ultimately the python native frame-cache in .npz format is ideal in that it is easily portable for large datasets. For instance, a typical .npz file ranges from 1-10 Mb while the same images stored in a .tiff format can range from 50 Mb to 30 GB depending on the number of images. Detectors and processing software used at synchrotron facilities use various file types but using .tiff is the most ideal for this approach. An aggregate or "ω-collapsed" image series can be made by the native functions inside the GUI or by an external script provided below. In either case the calibrated *instrument.yml* file needs to be created in the GUI first from the powder diffraction calibration procedure as described in Chapter 2; or at a minimum a template instrument file that contains the detector distance, estimated x/y beam center, detector face dimensions in pixels and pixel size which will then be iteratively calibrated in 3D. Once this file has been created the aggregate image can then be produced using the instruction below. In the event the calibration was not performed, or the image taken for some reason, a template instrument.yml is provided below. It is possible to use this file in conjunction with single crystal images to bypass the 2D calibration going straight to the 3D calibration, but it will take several iterations.

Instrument_template.yml:

```
beam:
  energy: 29.984664278952753
  vector:
    azimuth: 90.0
    polar_angle: 90.0
calibration_crystal:
  0:
    inv_stretch:
    - 0.9991001336702174
    - 0.9986565122371246
    - 0.9988087658175581
    - 0.0001474921624213055
    - 6.510210995975127e-05
    - -0.0001392214250843584
    orientation:
    - 0.0
    - 0.0
    - 0.0
    position:
    - 0.0
    - 0.0
    - 0.0
detectors:
  pilatus_3M:
    buffer: null
    distortion:
      function_name: GE_41RT
      parameters:
```

```
      - 0.0036306480156830215
      - -0.002714213721719885
      - -0.0012118685211435136
      - 2.0
      - 2.0
      - 2.0
    pixels:
      columns: 981
      rows: 1043
      size:
      - 0.172
      - 0.172
    saturation_level: 1600000
    transform:
      tilt:
      - -0.00683143684673381
      - -0.009542442045741149
      - -0.004376291444653499
      translation:
      - 0.03149536331255768   # this is the x beam center coordinate
      - 0.480041767132194     # this is the y beam center coordinate
      - -217.76489642711243   # this is the detector distance in mm
(negative distance!)

id: instrument
oscillation_stage:
  chi: -0.005356057978024881
  translation:
  - 0.0
  - 0.0
  - 0.0
```

Instruction set :

Using the script *Appendix 2: make_image_series.py* or *make_dac_imageseries.py* performs the same function except that *make_dac_imageseries.py* creates a symmetric scan aggregate image. This can only be used if the sample stage allows for 180° rotation of the DAC during experiment. These scripts are entirely general and can be copied from this document and placed in a python/spyder interface and the user specific values. The working directory and raw_data_directory are where the script resides and where the image collection to be used resides respectively. Absolute paths are recommended. It is good practice to create a new experiment directory with two folders (1) scripts and (2) images. All native raw image files are placed in the image folder and all processing scripts are placed in the scripts folder for each experiment. Lines in the scripts with user required inputs in either script are highlighted in yellow. Once all inputs are added the script can be run in any python terminal or IDE like spyder or Jupiter notebook (the latter two are recommended).

The image series generation proceeds by dividing the provided angular range by the number of images in the image series and assigning an ω key to each image. It is crucial to make sure the

correct start and stop values as well as **n_wedges** was entered. The corresponding omega tags should reflect the angular step size used in the experiment (i.e., if a 0.25-degree step was used there should be 0.25 degrees between each image, if this is not the case, the ranges need to be adjusted accordingly). The image series is then filtered by the threshold input and converted into a sparse matrix. This is a very efficient way of taking a file of 1000 tiff images that may normally have a size of 30 Gb and convert it to 20 Mb by only keeping spot intensity information and making the rest 0. This means that for a diffraction pattern where there may be a one to a hand full of spots in each individual image ultimately it will be a mostly blank image. In the event the detector background is high, and the user input threshold is low, an error will be thrown that the image is not sparse and these parameters should be adjusted. This also greatly decreases the computational time for the image analysis to be done in the next steps. Below is a summary checklist of operations that should have been completed thus far. The output file for from this script is a frame-cache with extension .npz.

2. Setting up the experiment.yml file.

Once the frame-cache of the image series has been created, another .yml file is needed that will guide the remaining process. The file *Ruby.yml* below provides a copyable template that can be modified as needed. The areas for specific user input are highlighted. This file that acts as the "master" file to guide the analysis process by integrating all the needed file locations as well as thresholding and tolerances during the indexation and refinement processes. Creating this file correctly and making sure things are pointing to the right places is crucial so care must be taken. There are certain sections of this file not used by the version described here and these will be explicitly stated. Below, each section that requires user input is described followed by a copyable version of the file.

- **Analysis_name:** Will be the name of the output folder automatically generated during the analysis.
- **Working_dir:** absolute path to the material.yml file location.
- **Material: definitions:** the name of the material file created for the analysis.
- **Material:active:** sets the active material from the material list in the materials.cpl file that was created in the *HEXRD* GUI.
- **Image_series:** Input the image series cache file name as well as the angular ranges over which it was taken.
- **Instrument:Parameters:** file name of the instrument.yml file created during the 2D calibration (this will be generated in the next section).

- **Instrument rows, columns, size:** defines the size of the detector being used in rows, columns, and pixel size.

From here the analysis proceeds in two steps: (1) grain indexing and orientation determinations and (2) fitting each grain found. The material.yml file is organized in the same way listed as **find_orientations** and **fit_grains**.

In the **find_orientation** section of the material.yml file:

- **threshold:** sets the global threshold on the image series. (Take care that there is also another manual threshold that was set when the rotational series was generated using the above prescribed script. Ensure this value is set to what you would like.
- **Active_hkls:** Corresponds to the 0 based indexing of the highlighted hkls selected in the GUI. An error will occur if for instance you set this value to [0 1 2 3 4 5] but only highlighted the first 5 when creating the material file.
- **hkl_seeds:** Selects which *hkl*s from the active hkl list to use when searching for orientations. This is advantageous because in the event the material consists of two phases and has an overlapping hkl, it can be excluded to minimize the chance of erroneous assignment of diffraction intensities.
- **fiber_step:** in general use 2x the omega angular range used when collecting the image series.
- **threshold:** intensity threshold allowed on the pole figures (described more in detail below)
- **omega:tolerance:** Sets the tolerance in omega in a +/- fashion to search for an expected peak intensity. I.e., 0.5 would allow + 0.25 and – 0.25 in omega meaning that when searching for a specific intensity the algorithm with search +1 image and -1 image from the anticipated frame where the intensity should be.
- **eta:tolerance:** this defines the azimuthal tolerance applied to the grain indexation algorithm. It is helpful to use the image viewing screen in the *HEXRD* GUI and investigate individual diffraction intensities to get a feel for this tolerance. The bottom bar of the HEXRD GUI provides the d-spacing, 2θ, η, and ω of the cursor position on the image. This way the user can measure the η at both bounds on a reflection. In the event there is an orientation gradient smaller than about 0.4° this may be un-measurable but as will be shown in sections 2.5-2.6 this can be a very insightful tolerance when multiple grains have the same orientation.
- **mask:** this value should be set to 5 generally and removes +/- 2.5° from the rotational axis of the image since reflections there precess around the rotational axis and may constantly be in the Bragg condition.
- **clustering:radius:** set to 1 by default
- **completeness:** this is a key parameter that is based on a ratio displayed as a % of hit : miss for whether an anticipated diffraction intensity is measured above background within the angular tolerances provided using the list of seed *hkl*s defined in the *material.cpl* file and also input above in **active_hkls** and **hkl_seeds**.

3. 3D detector calibration

As stated in the main document, at the time of writing this thesis, the 3D detector calibration was performed externally to the HEXRD GUI. Once the indexing and initial grain fitting is performed, the grains.out (Figure A2) file contains the information of each grain that was possible to fit. In the event of a single crystal standard there should be only one identified

unique orientation. The script provided below 3D_calibration_from_rotational_series should be copied and added to the scripts folder of the experimental directory. The input grain id = 0 for the first grain (only grain if a single crystal was used). The needed user input is highlighted in the script. Key inputs here are:

- the config filename (experiment.yml file described above)
- ***Overwrite_parfile*** = true; this allows the detector parameter file to be adjusted and fit in 3D thereby calibrating the detector rotation about its own normal as well as other parameters.
- ***Grain_ids*** = [0,]; which grain to use during the calibration
- ***Clobber_strain*** = true; if it is certain the sample is a strain free standard set to true. This allows refitting of the strain under this assumption.
- ***Clobber_centroid*** = False, this should be set to false because there is a small likelihood the grain is perfectly centered but this parameter should be tested.
- ***Clobber_grain_y*** = True; this is a crucial parameter during calibration because the crystal y component and the sample y component (height) are correlated. By setting this value to be fixed the y component is fixed going forward. This is key if the sample is slightly elevated during the calibration.

  The calibration is then run 2-3 times or until convergence. If the script is run in a spyder console the fit will be printed to the screen. The script also provides several autogenerated plots allowing visualization of the reflection assignment before and after the calibration.

  Once this is complete the experiment can proceed with the sample as the detector and software are now calibrated to all experimental parameters. The resulting instrument.yml should be renamed to something that will not be confused with an older uncalibrated version.

```
# grain ID    completeness  chi^2         exp_map_c[0]              exp_map_c[1]
exp_map_c[2]              t_vec_c[0]                t_vec_c[1]                t_vec_c[2]
inv(V_s)[0,0]             inv(V_s)[1,1]             inv(V_s)[2,2]             inv(V_s)[1,2]*sqrt(2)
inv(V_s)[0,2]*sqrt(2)     inv(V_s)[0,2]*sqrt(2)     ln(V_s)[0,0]              ln(V_s)[1,1]
ln(V_s)[2,2]              ln(V_s)[1,2]              ln(V_s)[0,2]              ln(V_s)[0,1]
0             0.929752      1.314896e-03  -1.0467672270978885e+00  7.6837218291013387e-01
-8.2942405406707276e-01  4.2437965258615151e-03   -1.7933634383558755e-01  -1.9275278579063589e-03
1.0005651240065740e+00   9.9972273833241088e-01   1.0003289159002042e+00   3.7178403164915119e-04
-1.2273803390966745e-04  -1.0695736801777761e-05  -5.6496059317432518e-04  2.7733470123868654e-04
-3.2882350917637121e-04  -2.6288390708611466e-04  8.6749125956525692e-05   7.5505369414703142e-06
```

Figure A2. *Grains.out file with columns for: grain number, grain id, completeness %, goodness of fit, orientation in 3-vector exponential map notation, 3-volume averaged grain centroid components, 6-vector notation of inverse stretch and 6-vector notation of strain tensor.*

Experiment.yml:

```
analysis_name: Ruby_Calibration # defaults to analysis

# working directory defaults to current working directory
# all relative paths specified herein are assumed to be in the
working_dir
# any files not in working_dir should be specified with an absolute
path
#
# working_dir:

# "all", "half", or -1 means all but one, defaults to -1
multiprocessing: all

material:
  definitions: ruby.h5
  active: ruby
  dmin: 0.65 # defaults to 1.0 angstrom
  tth_width: 0.25 # defaults to 0.25 degrees
  min_sfac_ratio: 0.05 # min percentage of max |F|^2 to exclude;
default None

image_series:
  format: frame-cache
  data:
    - file: Ruby30keVFullSweep_00001-fc_pilatus_3M.npz
      args: {}
      panel: pilatus_3M  # must match detector key
   # - file: ../imageseries/mruby-0129_000004_ff2_000012-cachefile.npz
   #   args: {}
   #   panel: ff2  # must match detector key

instrument: ruby_instrument.yml

find_orientations:
  orientation_maps:
    # A file name must be specified. If it doesn't exist, one will be
created
    file: null

    threshold: 1000
    bin_frames: 1 # defaults to 1

    # "all", or a list of hkl orders used to find orientations
    # defaults to all orders listed in the material definition
    active_hkls: [0,1,2,3,4]
```

```
  # either search full quaternion grid, or seed search based on sparse
  # orientation maps.  For input search space:
  #
  # use_quaternion_grid: some/file/name
  #
  # otherwise defaults to seeded search:
  seed_search: # this section is ignored if use_quaternion_grid is
defined
    hkl_seeds: [0, 1, 2,3,4] # hkls ids to use, must be defined for
seeded search
    fiber_step: 0.5 # degrees, defaults to ome tolerance
    # Method selection:
    #   Now 3 choices: label (the original), 'blob_dog', and
'blob_log'
    #   Each has its own parameter names, examples below.
    #
    method:
       label:
         filter_radius: 1
         threshold: 1000 # defaults to 1
    #
    # method:
    #   blob_dog:
    #     min_sigma: 0.5
    #     max_sigma: 5
  #     sigma_ratio: 1.6
    #     threshold: 0.01
    #     overlap: 0.1
    #
    #method:
    #  blob_log:
    #    min_sigma: 0.5
    #    max_sigma: 5
    #    num_sigma: 10
    #    threshold: 0.01
    #    overlap: 0.1
  # this is the on-map threshold using in the scoring
  # defaults to 1
  threshold: 1000

  omega:
    tolerance: 1.0  # in degrees, defaults to 2x ome step

    # specify the branch cut, in degrees. The range must be 360
degrees.
    # defaults to full 360 starting at the first omega value in
imageseries.
    # !!! THIS OPTION IS DEPRECATED.
    # period: [0, 360]
```

```
  eta:
    tolerance: 1.0  # in degrees, defaults to 2x ome step
    mask: 5  # degrees, mask angles close to ome rotation axis,
defaults to 5

  clustering:
    # algorithm choices are
    #   sph-dbscan
    #   ort-dbscn
    #   dbscan <default>
    #   fclusterdata; this is a fallback and won't work for large
problems
    radius: 1.0
    completeness: 0.70 # completeness threshold
    algorithm: dbscan

fit_grains:
  do_fit: true # if false, extracts grains but doesn't fit. defaults
to true

  estimate: null

  npdiv: 4 # number of polar pixel grid subdivisions, defaults to 2

  threshold: 25

  tolerance:
    tth: [0.35, 0.25] # tolerance lists must be identical length
    eta: [1.0, 0.5]
    omega: [0.5, 0.5]

  refit: [2, 1]

  tth_max: False #false # true, false, or a non-negative value,
defaults to true
```

Appendix 2

Scripts:

make_image_series.py:

```
from __future__ import print_function

import os
import yaml
import numpy as np
from hexrd import config
from hexrd import instrument
from hexrd import imageseries
Pims = imageseries.process.ProcessedImageSeries

#=============================================================================
=========
# INITIALIZATION
#=============================================================================
=========

# ############################################################
# make input yaml files
working_dir = '/Users/brianchandler/…” '
raw_data_dir = '/Users/brianchandler/……/ruby/images'
filename_stem = 'Scan1_%05d.tif'
cfg_filename = '/scripts/new-instrument-0.yml'
scan_number = 0
n_wedges = 1279
first_scan = 0   # !!! careful to be consistent with scan number
empty_frames = 0  # start at first in file
max_frames = 1279 # read all
# omegas
start_ome = 0
stop_ome = 320.0  # angular range of image

# frame-cache threshold
threshold = 1000

# processing options
popts = [('flip', None)] #('mask','pilatus')
```

```
instr_cfg_file = os.path.join(working_dir,
'scripts/new_instrument.yml')
#
# ##########################################################

output_stem = filename_stem.split('.')[0] % (scan_number)

scan_numbers = range(first_scan, first_scan + n_wedges)
filenames_str = '\n'.join([filename_stem % scan for scan in
scan_numbers])

icfg = yaml.load(open(instr_cfg_file, 'r'))
instr = instrument.HEDMInstrument(instrument_config=icfg)

raw_img_tmplate = '''
image-files:
  directory: %%s
files: "%s"
options:
  empty-frames: %%d
  max-frames: %%d
meta:
  panel: %%s
''' % filenames_str

#============================================================================
=========
# LOOP WRITES OVER DETECTOR PANELS
#============================================================================
=========

for det_id in instr.detectors:
    fill_tmpl = [raw_data_dir] \
        + [empty_frames, max_frames, det_id]
    # make yml string
    output_str = raw_img_tmplate % tuple(fill_tmpl)
    rawfname = "raw_images_%s-%s.yml"
    with open(rawfname % (output_stem, det_id), 'w') as f:
        print(output_str, file=f)

    # load basic imageseries: no flip, no omegas
    ims = imageseries.open(
        rawfname % (output_stem, det_id),
        'image-files')


    # generate omegas
    nf = len(ims)
    w = imageseries.omega.OmegaWedges(nf)
```

```
w.addwedge(start_ome, stop_ome, nf)
meta = ims.metadata
meta['omega'] = w.omegas
w.save_omegas('omegas_FF.npy')
print(ims.metadata)

# make dark
print("making dark image")
dark = imageseries.stats.median(ims, nframes=120)
np.save('background_%s-%s.npy' % (output_stem, det_id), dark)



# add flips
pims = Pims(ims, [('dark', dark), ] + popts)

##### mask test


# save as frame-cache
print("writing frame cache")
imageseries.write(pims, '%s-fc_%s.yml' % (output_stem, det_id),
                  'frame-cache',
                      cache_file="%s-fc_%s.npz" %
(output_stem,det_id), threshold=threshold,output_yaml=False)
```

make_dac_image_series.py:

```
#!/usr/bin/env python2
# -*- coding: utf-8 -*-
"""
Created on Mon Jul  1 11:44:06 2019

@author: brianchandler
"""


from __future__ import print_function

import os
import yaml

import numpy as np

from hexrd import config
from hexrd import instrument
from hexrd import imageseries

Pims = imageseries.process.ProcessedImageSeries

#=============================================================================
=========
# INITIALIZATION
#=============================================================================
=========

# ######################################################

working_dir = '/Users/brianchandler/Desktop/dac_scan_test'
raw_data_dir = 'scans/'
filename_stem1 = 'OL_30keV_30GPa_LH5_01_%04d.sfrm'
filename_stem2 = 'OL_30keV_30GPa_LH5_02_%04d.sfrm'
cfg_filename = 'new-instrument-0.yml'
scan_number = 0

#################### Create wedges
%%%%%%%%%%%%%%%%%%%%%%%%%%%%%%%%%%%%%%%%%%%%%%%%%%%%
n_wedges1 = 240
first_scan1 = 1    # !!! careful to be consistent with scan number
empty_frames = 0  # start at first in file
max_frames = 0    # 0 = read all
n_wedges2 = 240   # second scan, (cell flipped)
first_scan2 = 1
```

```
# omegas
start_ome1 = -30  # first scan range
stop_ome1 = 30

start_ome2 = 150.00 # second scan range
stop_ome2 = 210.00

# frame-cache threshold
threshold = 1000

# processing options
popts = [('flip', 'ccw90'), ]

#instrument configuration file generated from calibration
instr_cfg_file = os.path.join(working_dir, 'new-instrument-0.yml')
#
# ############################################################

output_stem = filename_stem1.split('.')[0] % (scan_number)

scan_numbers1 = range(first_scan1, first_scan1 + n_wedges1) ##changes
to scan_numbers 1 and n_wedges1
scan_numbers2 = range(first_scan2, first_scan2 + n_wedges2)
filenames_str = '\n'.join([filename_stem1 % scan for scan in
scan_numbers1] + [filename_stem2 % scan for scan in scan_numbers2])
#changed to scan numbers 1

icfg = yaml.load(open(instr_cfg_file, 'r'))
instr = instrument.HEDMInstrument(instrument_config=icfg)

raw_img_tmplate = '''
image-files:
  directory: %%s
  files: "%s"

options:
  empty-frames: %%d
  max-frames: %%d
  dtype: int32
meta:
  panel: %%s
''' % filenames_str

#============================================================================
=========
# LOOP WRITES OVER DETECTOR PANELS
#============================================================================
=========

for det_id in instr.detectors:
```

```
    fill_tmpl = [raw_data_dir] \
        + [empty_frames, max_frames, det_id]
    # make yml string
    output_str = raw_img_tmplate % tuple(fill_tmpl)
    rawfname = "raw_images_%s-%s.yml"
    with open(rawfname % (output_stem, det_id), 'w') as f:
print(output_str, file=f)

    # load basic imageseries: no flip, no omegas
    ims = imageseries.open(
        rawfname % (output_stem, det_id),
        'image-files')

    # generate omegas
    nf = 480 #len(ims)
    w = imageseries.omega.OmegaWedges(nf)
    w.addwedge(start_ome1, stop_ome1, 240)
    w.addwedge(start_ome2, stop_ome2, 240)
    meta = ims.metadata
    meta['omega'] = w.omegas
    w.save_omegas('omegas_FF.npy')
    print(ims.metadata)

    # make dark
    print("making dark image")
    dark = imageseries.stats.median(ims, nframes=10)
    np.save('background_%s-%s.npy' % (output_stem, det_id), dark)

    # add flips
    pims = Pims(ims, [('dark', dark), ] + popts)

    # save as frame-cache
    print("writing frame cache")
    imageseries.write(pims, '%s-fc_%s.yml' % (output_stem, det_id),
                      'frame-cache',
                      cache_file="%s-fc_%s.npz" % (output_stem,
det_id),
                      threshold=threshold,
                      output_yaml=False)
```

3D_calibration_from_rotational_series.py:

```
import os

import numpy as np

from hexrd import config
from hexrd import constants as cnst
from hexrd import matrixutil as mutil
from hexrd.fitting import grains as grainutil
from hexrd.transforms import xfcapi

from scipy.optimize import leastsq, least_squares

from matplotlib import pyplot as plt

# panel
panel_flags_DFLT = np.ones(6, dtype=bool)
panel_flags_fixed_Y = np.array(
    [1, 1, 1, 1, 0, 1],
    dtype=bool
)

# distortion dicts
distortion_flags_DFLT = dict(
    GE_41RT=np.array([1, 1, 1, 0, 0, 0], dtype=bool),
    Dexela_2923=np.array([0, 0, 1, 1, 1, 1, 1, 1], dtype=bool)
)

# grains
grain_flags_DFLT = np.array(
    [1, 1, 1,
     1, 0, 1,
     0, 0, 0, 0, 0, 0],
    dtype=bool
)


#
================================================================================
=======
# %% *USER INPUT*
#
================================================================================
=======


# hexrd yaml config file
```

```
cfg_filename = 'Ruby.yml'
block_id = 0    # only change this if you know what you are doing!

overwrite_parfile = True    # if you want to overwrite the instr par

# select which orientaion to use (in case of more than one...)
grain_ids = [0, ]  # selects which indexed grain to use

# if you know this is a strain-free standard, then set the following
to True
clobber_strain = True

# if you know this is centered grain, then set the following to True
clobber_centroid = False

# if you know this is a line beam, then set the following to True
clobber_grain_Y = True

#
==========================================================================
=======
# %% *USER INPUT*
#
==========================================================================
=======


# load config
cfg = config.open(cfg_filename)[block_id]

# grab instrument
instr = cfg.instrument.hedm

# load imageseries dict
ims_dict = cfg.image_series
ims = next(iter(ims_dict.values()))    # grab first member
delta_ome = ims.metadata['omega'][:, 1] - ims.metadata['omega'][:, 0]
assert np.all(np.diff(delta_ome) == 0.), \
    "something funky going one with your omegas"
delta_ome = delta_ome[0]   # any one member witll do

# refit tolerances
if cfg.fit_grains.refit is not None:
    n_pixels_tol = cfg.fit_grains.refit[0]
    ome_tol = cfg.fit_grains.refit[1]*delta_ome
else:
    n_pixels_tol = 2
    ome_tol = 2.*delta_ome
```

```
#
=============================================================================
=======
# %% Local function definitions
#
=============================================================================
=======


def calibrate_instrument_from_sx(
        instr, grain_params, bmat, xyo_det, hkls_idx,
        param_flags=None, grain_flags=None,
        ome_period=None,
        xtol=cnst.sqrt_epsf, ftol=cnst.sqrt_epsf,
        factor=10., sim_only=False, use_robust_lsq=False):
    """
    arguments xyo_det, hkls_idx are DICTs over panels

    """

    pnames = [
        '{:>24s}'.format('beam energy'),
        '{:>24s}'.format('beam azimuth'),
        '{:>24s}'.format('beam polar'),
        '{:>24s}'.format('chi'),
        '{:>24s}'.format('tvec_s[0]'),
        '{:>24s}'.format('tvec_s[1]'),
        '{:>24s}'.format('tvec_s[2]'),
    ]

    for det_key, panel in instr.detectors.items():
        pnames += [
            '{:>24s}'.format('%s tilt[0]' % det_key),
            '{:>24s}'.format('%s tilt[1]' % det_key),
            '{:>24s}'.format('%s tilt[2]' % det_key),
            '{:>24s}'.format('%s tvec[0]' % det_key),
            '{:>24s}'.format('%s tvec[1]' % det_key),
            '{:>24s}'.format('%s tvec[2]' % det_key),
        ]
        # now add distortion if there
        if panel.distortion is not None:
            for j in range(len(panel.distortion.params)):
                pnames.append(
                    '{:>24s}'.format('%s dparam[%d]' % (det_key, j))
                )

    grain_params = np.atleast_2d(grain_params)
    ngrains = len(grain_params)
    for ig, grain in enumerate(grain_params):
        pnames += [
```

```
            '{:>24s}'.format('grain %d expmap_c[0]' % ig),
            '{:>24s}'.format('grain %d expmap_c[0]' % ig),
            '{:>24s}'.format('grain %d expmap_c[0]' % ig),
            '{:>24s}'.format('grain %d tvec_c[0]' % ig),
            '{:>24s}'.format('grain %d tvec_c[1]' % ig),
            '{:>24s}'.format('grain %d tvec_c[2]' % ig),
            '{:>24s}'.format('grain %d vinv_s[0]' % ig),
            '{:>24s}'.format('grain %d vinv_s[1]' % ig),
            '{:>24s}'.format('grain %d vinv_s[2]' % ig),
            '{:>24s}'.format('grain %d vinv_s[3]' % ig),
            '{:>24s}'.format('grain %d vinv_s[4]' % ig),
            '{:>24s}'.format('grain %d vinv_s[5]' % ig)
        ]

    # reset parameter flags for instrument as specified
    if param_flags is None:
        param_flags = instr.calibration_flags
    else:
        # will throw an AssertionError if wrong length
        instr.calibration_flags = param_flags

    # re-map omegas if need be
    if ome_period is not None:
        for det_key in instr.detectors:
            for ig in range(ngrains):
                xyo_det[det_key][ig][:, 2] = xfcapi.mapAngle(
                        xyo_det[det_key][ig][:, 2],
                        ome_period
                )

    # first grab the instrument parameters
    # 7 global
    # 6*num_panels for the detectors
    # num_panels*ndp in case of distortion
    plist_full = instr.calibration_parameters

    # now handle grains
    # reset parameter flags for grains as specified
    if grain_flags is None:
        grain_flags = np.tile(grain_flags_DFLT, ngrains)

    plist_full = np.concatenate(
        [plist_full, np.hstack(grain_params)]
    )

    # concatenate refinement flags
    refine_flags = np.hstack([param_flags, grain_flags])
    plist_fit = plist_full[refine_flags]
    fit_args = (plist_full,
                param_flags, grain_flags,
```

```
                instr, xyo_det, hkls_idx,
                bmat, ome_period)
    if sim_only:
        return sxcal_obj_func(
            plist_fit, plist_full,
            param_flags, grain_flags,
            instr, xyo_det, hkls_idx,
            bmat, ome_period,
            sim_only=True)
    else:
        print("Set up to refine:")
        for i in np.where(refine_flags)[0]:
            print("\t%s = %1.7e" % (pnames[i], plist_full[i]))

        # run optimization
        if use_robust_lsq:
    result = least_squares(
                sxcal_obj_func, plist_fit, args=fit_args,
                xtol=xtol, ftol=ftol,
                loss='soft_l1', method='trf'
            )
            x = result.x
            resd = result.fun
            mesg = result.message
            ierr = result.status
        else:
            # do least squares problem
            x, cov_x, infodict, mesg, ierr = leastsq(
                sxcal_obj_func, plist_fit, args=fit_args,
                factor=factor, xtol=xtol, ftol=ftol,
                full_output=1
            )
            resd = infodict['fvec']
        if ierr not in [1, 2, 3, 4]:
            raise RuntimeError("solution not found: ierr = %d" % ierr)
        else:
            print("INFO: optimization fininshed successfully with
ierr=%d"
                  % ierr)
            print("INFO: %s" % mesg)

        # ??? output message handling?
        fit_params = plist_full
        fit_params[refine_flags] = x

        # run simulation with optimized results
        sim_final = sxcal_obj_func(
            x, plist_full,
            param_flags, grain_flags,
            instr, xyo_det, hkls_idx,
```

```
            bmat, ome_period,
            sim_only=True)

        # ??? reset instrument here?
        instr.update_from_parameter_list(fit_params)

        return fit_params, resd, sim_final


def sxcal_obj_func(plist_fit, plist_full,
                   param_flags, grain_flags,
                   instr, xyo_det, hkls_idx,
                   bmat, ome_period,
                   sim_only=False, return_value_flag=None):
    """
    """
    npi = len(instr.calibration_parameters)
    NP_GRN = 12

    # stack flags and force bool repr
    refine_flags = np.array(
        np.hstack([param_flags, grain_flags]),
        dtype=bool)
# fill out full parameter list
    # !!! no scaling for now
    plist_full[refine_flags] = plist_fit

    # instrument update
    instr.update_from_parameter_list(plist_full)

    # assign some useful params
    wavelength = instr.beam_wavelength
    bvec = instr.beam_vector
    chi = instr.chi
    tvec_s = instr.tvec

    # right now just stuck on the end and assumed
    # to all be the same length... FIX THIS
    xy_unwarped = {}
    meas_omes = {}
    calc_omes = {}
    calc_xy = {}

    # grain params
    grain_params = plist_full[npi:]
    if np.mod(len(grain_params), NP_GRN) != 0:
        raise RuntimeError("parameter list length is not consistent")
    ngrains = len(grain_params) // NP_GRN
    grain_params = grain_params.reshape((ngrains, NP_GRN))
```

```
    # loop over panels
    npts_tot = 0
    for det_key, panel in instr.detectors.items():
        rmat_d = panel.rmat
        tvec_d = panel.tvec

        xy_unwarped[det_key] = []
        meas_omes[det_key] = []
        calc_omes[det_key] = []
        calc_xy[det_key] = []

        for ig, grain in enumerate(grain_params):
            ghkls = hkls_idx[det_key][ig]
            xyo = xyo_det[det_key][ig]

            npts_tot += len(xyo)

            xy_unwarped[det_key].append(xyo[:, :2])
            meas_omes[det_key].append(xyo[:, 2])
            if panel.distortion is not None:    # do unwarping
                xy_unwarped[det_key][ig] = panel.distortion.apply(
                    xy_unwarped[det_key][ig]
                )
                pass

            # transform G-vectors:
            # 1) convert inv. stretch tensor from MV notation in to
3x3
            # 2) take reciprocal lattice vectors from CRYSTAL to
SAMPLE frame
            # 3) apply stretch tensor
            # 4) normalize reciprocal lattice vectors in SAMPLE frame
            # 5) transform unit reciprocal lattice vetors back to
CRYSAL frame
            rmat_c = xfcapi.makeRotMatOfExpMap(grain[:3])
            tvec_c = grain[3:6]
            vinv_s = grain[6:]
            gvec_c = np.dot(bmat, ghkls.T)
vmat_s = mutil.vecMVToSymm(vinv_s)
            ghat_s = mutil.unitVector(np.dot(vmat_s, np.dot(rmat_c,
gvec_c)))
            ghat_c = np.dot(rmat_c.T, ghat_s)

            match_omes, calc_omes_tmp = grainutil.matchOmegas(
                xyo, ghkls.T,
                chi, rmat_c, bmat, wavelength,
                vInv=vinv_s,
                beamVec=bvec,
                omePeriod=ome_period)
```

```
            rmat_s_arr = xfcapi.makeOscillRotMatArray(
                chi, np.ascontiguousarray(calc_omes_tmp)
            )
            calc_xy_tmp = xfcapi.gvecToDetectorXYArray(
                    ghat_c.T, rmat_d, rmat_s_arr, rmat_c,
                    tvec_d, tvec_s, tvec_c
            )
            if np.any(np.isnan(calc_xy_tmp)):
                print("infeasible parameters: "
                      + "may want to scale back finite difference step
size")

            calc_omes[det_key].append(calc_omes_tmp)
            calc_xy[det_key].append(calc_xy_tmp)
            pass
        pass

    # return values
    if sim_only:
        retval = {}
        for det_key in calc_xy.keys():
            # ??? calc_xy is always 2-d
            retval[det_key] = []
            for ig in range(ngrains):
                retval[det_key].append(
                    np.vstack(
                        [calc_xy[det_key][ig].T,
calc_omes[det_key][ig]]
                    ).T
                )
    else:
        meas_xy_all = []
        calc_xy_all = []
        meas_omes_all = []
        calc_omes_all = []
        for det_key in xy_unwarped.keys():
            meas_xy_all.append(np.vstack(xy_unwarped[det_key]))
            calc_xy_all.append(np.vstack(calc_xy[det_key]))
            meas_omes_all.append(np.hstack(meas_omes[det_key]))
            calc_omes_all.append(np.hstack(calc_omes[det_key]))
            pass
        meas_xy_all = np.vstack(meas_xy_all)
        calc_xy_all = np.vstack(calc_xy_all)
        meas_omes_all = np.hstack(meas_omes_all)
        calc_omes_all = np.hstack(calc_omes_all)

        diff_vecs_xy = calc_xy_all - meas_xy_all
        diff_ome = xfcapi.angularDifference(calc_omes_all,
meas_omes_all)
        retval = np.hstack(
```

```
            [diff_vecs_xy,
             diff_ome.reshape(npts_tot, 1)]
        ).flatten()
if return_value_flag == 1:
            retval = sum(abs(retval))
        elif return_value_flag == 2:
            denom = npts_tot - len(plist_fit) - 1.
            if denom != 0:
                nu_fac = 1. / denom
            else:
                nu_fac = 1.
            nu_fac = 1 / (npts_tot - len(plist_fit) - 1.)
            retval = nu_fac * sum(retval**2)
    return retval


def parse_reflection_tables(cfg, instr, grain_ids, refit_idx=None):
    """
    make spot dictionaries
    """
    hkls = {}
    xyo_det = {}
    idx_0 = {}
    for det_key, panel in instr.detectors.items():
        hkls[det_key] = []
        xyo_det[det_key] = []
        idx_0[det_key] = []
        for ig, grain_id in enumerate(grain_ids):
            spots_filename = os.path.join(
                cfg.analysis_dir, os.path.join(
                    det_key, 'spots_%05d.out' % grain_id
                )
            )

            # load pull_spots output table
            gtable = np.loadtxt(spots_filename)

            # apply conditions for accepting valid data
            valid_reflections = gtable[:, 0] >= 0  # is indexed
            not_saturated = gtable[:, 6] < panel.saturation_level
            print("INFO: panel '%s', grain %d" % (det_key, grain_id))
            print("INFO: %d of %d reflections are indexed"
                  % (sum(valid_reflections), len(gtable))
                  )
            print("INFO: %d of %d"
                  % (sum(not_saturated), sum(valid_reflections)) +
                  " valid reflections be are below" +
                  " saturation threshold of %d" %
(panel.saturation_level)
                  )
```

```
            # valid reflections index
            if refit_idx is None:
                idx = np.logical_and(valid_reflections, not_saturated)
                idx_0[det_key].append(idx)
            else:
                idx = refit_idx[det_key][ig]
                idx_0[det_key].append(idx)
                print("INFO: input reflection specify " +
                      "%d of %d total valid reflections"
                      % (sum(idx), len(gtable))
                      )
  hkls[det_key].append(gtable[idx, 2:5])
            meas_omes = gtable[idx, 12].reshape(sum(idx), 1)
            xyo_det[det_key].append(np.hstack([gtable[idx, -2:],
meas_omes]))
    return hkls, xyo_det, idx_0


# %% Initialization...

# read config
cfg = config.open(cfg_filename)[block_id]

# output for eta-ome maps as pickles
working_dir = cfg.working_dir
analysis_name = cfg.analysis_name
analysis_dir = cfg.analysis_dir
analysis_id = "%s_%s" % (analysis_name, cfg.material.active)

# instrument
instr = cfg.instrument.hedm
num_panels = instr.num_panels
det_keys = instr.detectors.keys()

# plane data
plane_data = cfg.material.plane_data
bmat = plane_data.latVecOps['B']

# the maximum pixel dimension in the instrument for plotting
max_pix_size = 0.
for panel in instr.detectors.values():
    max_pix_size = max(max_pix_size,
                       max(panel.pixel_size_col, panel.pixel_size_col)
                       )
    pass

# grab omega period
# !!! data should be consistent
# !!! this is in degrees
```

```
ome_period = cfg.find_orientations.omega.period

# load reflection tables from grain fit
hkls, xyo_det, idx_0 = parse_reflection_tables(cfg, instr, grain_ids)

# load grain parameters
grain_parameters = np.loadtxt(
    os.path.join(cfg.analysis_dir, 'grains.out'),
    ndmin=2)[grain_ids, 3:15]
if clobber_strain:
    for grain in grain_parameters:
        grain[6:] = cnst.identity_6x1
if clobber_centroid:
    for grain in grain_parameters:
        grain[3:6] = cnst.zeros_3
if clobber_grain_Y:
    for grain in grain_parameters:
        grain[4] = 0.
ngrains = len(grain_parameters)

#
================================================================================
=======
# %% plot initial guess
#
================================================================================
=======

xyo_i = calibrate_instrument_from_sx(
    instr, grain_parameters, bmat, xyo_det, hkls,
    ome_period=np.radians(ome_period), sim_only=True
)

for det_key, panel in instr.detectors.items():
    fig, ax = plt.subplots(1, 2, sharex=True, sharey=False,
figsize=(9, 5))
    fig.suptitle("detector %s" % det_key)
    for ig in range(ngrains):
        ax[0].plot(
            xyo_det[det_key][ig][:, 0],
            xyo_det[det_key][ig][:, 1],
            'k.'
        )
        ax[0].plot(xyo_i[det_key][ig][:, 0], xyo_i[det_key][ig][:, 1],
'rx')
        ax[0].grid(True)
        ax[0].axis('equal')
        ax[0].set_xlim(-0.5*panel.col_dim, 0.5*panel.col_dim)
        ax[0].set_ylim(-0.5*panel.row_dim, 0.5*panel.row_dim)
        ax[0].set_xlabel('detector X [mm]')
```

```
        ax[0].set_ylabel('detector Y [mm]')

        ax[1].plot(
            xyo_det[det_key][ig][:, 0],
            np.degrees(xyo_det[det_key][ig][:, 2]), 'k.'
        )
        ax[1].plot(
            xyo_i[det_key][ig][:, 0],
            np.degrees(xyo_i[det_key][ig][:, 2]),
            'rx'
        )
        ax[1].grid(True)
        ax[1].set_xlim(-0.5*panel.col_dim, 0.5*panel.col_dim)
        ax[1].set_ylim(ome_period[0], ome_period[1])
        ax[1].set_xlabel('detector X [mm]')
        ax[1].set_ylabel(r'$\omega$ [deg]')

    fig.show()

#
=============================================================================
=======
# %% RUN OPTIMIZATION
#
=============================================================================
=======
instr_param_flags = np.array(
    [0,
     0, 0,
     1,
     0, 0, 0], dtype=bool
 )

# !!! careful about distortion flags here; omit if none for your
instrument
panel_param_flags = []
for ip, panel in enumerate(instr.detectors.values()):
    if ip == 0:
        this_panel_flags = panel_flags_DFLT  # often want to fix Y
here
    else:
        this_panel_flags = panel_flags_DFLT
    if panel.distortion is not None:
        this_panel_flags = np.hstack(
            [this_panel_flags,
             distortion_flags_DFLT[panel.distortion.maptype]]
        )
panel_param_flags.append(this_panel_flags)
panel_param_flags = np.hstack(panel_param_flags)
```

```
# assemble flags
param_flags = np.hstack([instr_param_flags, panel_param_flags])
grain_flags = np.tile(grain_flags_DFLT, (len(grain_ids), 1)).flatten()

# %%
params, resd, xyo_f = calibrate_instrument_from_sx(
    instr, grain_parameters, bmat, xyo_det, hkls,
    ome_period=np.radians(ome_period),
    param_flags=param_flags,
    grain_flags=grain_flags
)

# define difference vectors for spot fits
for det_key, panel in instr.detectors.items():
    for ig in range(ngrains):
        x_diff = abs(xyo_det[det_key][ig][:, 0] -
xyo_f[det_key][ig][:, 0])
        y_diff = abs(xyo_det[det_key][ig][:, 1] -
xyo_f[det_key][ig][:, 1])
        ome_diff = np.degrees(
            xfcapi.angularDifference(
                xyo_det[det_key][ig][:, 2],
                xyo_f[det_key][ig][:, 2])
        )

        # filter out reflections with centroids more than
        # a pixel and delta omega away from predicted value
        idx_1 = np.logical_and(
            x_diff <= n_pixels_tol*panel.pixel_size_col,
            np.logical_and(
                y_diff <= n_pixels_tol*panel.pixel_size_row,
                ome_diff <= ome_tol
            )
        )

        print("INFO: Will keep %d of %d input reflections "
              % (sum(idx_1), sum(idx_0[det_key][ig]))
              + "on panel %s for re-fit" % det_key)

        idx_new = np.zeros_like(idx_0[det_key][ig], dtype=bool)
        idx_new[np.where(idx_0[det_key][ig])[0][idx_1]] = True
        idx_0[det_key][ig] = idx_new

#
================================================================
=======
# %% Look ok? Then proceed
#
================================================================
=======
```

```
#
# define difference vectors for spot fits
# for det_key, panel in instr.detectors.items():
#     hkls_refit = hkls[det_key][idx_new[det_key], :]
#     xyo_det_refit = xyo_det[det_key][idx_0[det_key], :]
#     pass

# update calibration crystal params
grain_parameters_fit = params[-
grain_parameters.size:].reshape(ngrains, 12)
grain_parameters = grain_parameters_fit

# reparse data
hkls_refit, xyo_det_refit, idx_0 = parse_reflection_tables(
    cfg, instr, grain_ids, refit_idx=idx_0
)

# perform refit
params2, resd2, xyo_f2 = calibrate_instrument_from_sx(
    instr, grain_parameters, bmat, xyo_det_refit, hkls_refit,
    ome_period=np.radians(ome_period),
    param_flags=param_flags,
    grain_flags=grain_flags
)


#
================================================================================
=======
# %% perform refit
#
================================================================================
=======

for det_key, panel in instr.detectors.items():
    fig, ax = plt.subplots(1, 2, sharex=True, sharey=False,
figsize=(9, 5))
    fig.suptitle("detector %s" % det_key)
    for ig in range(ngrains):
        ax[0].plot(
            xyo_det[det_key][ig][:, 0],
            xyo_det[det_key][ig][:, 1],
            'k.'
        )
        ax[0].plot(xyo_i[det_key][ig][:, 0], xyo_i[det_key][ig][:, 1],
'rx')
        ax[0].plot(xyo_f2[det_key][ig][:, 0], xyo_f2[det_key][ig][:,
1], 'b+')
        ax[0].grid(True)
        ax[0].axis('equal')
```

```
        ax[0].set_xlim(-0.5*panel.col_dim, 0.5*panel.col_dim)
        ax[0].set_ylim(-0.5*panel.row_dim, 0.5*panel.row_dim)
        ax[0].set_xlabel('detector X [mm]')
        ax[0].set_ylabel('detector Y [mm]')

        ax[1].plot(
            xyo_det[det_key][ig][:, 0],
            np.degrees(xyo_det[det_key][ig][:, 2]), 'k.'
        )
        ax[1].plot(
            xyo_i[det_key][ig][:, 0],
            np.degrees(xyo_i[det_key][ig][:, 2]),
            'rx'
        )
        ax[1].plot(
            xyo_f2[det_key][ig][:, 0],
            np.degrees(xyo_f2[det_key][ig][:, 2]),
            'b+'
        )
        ax[1].grid(True)
        ax[1].set_xlim(-0.5*panel.col_dim, 0.5*panel.col_dim)
        ax[1].set_ylim(ome_period[0], ome_period[1])
        ax[1].set_xlabel('detector X [mm]')
        ax[1].set_ylabel(r'$\omega$ [deg]')

        ax[0].axis('equal')

    fig.show()
#
=========================================================================
=======
# %% output results
#
=========================================================================
=======

# update calibration crystal params
grain_parameters_fit = params2[-
grain_parameters.size:].reshape(ngrains, 12)
grain_parameters = grain_parameters_fit

calibration_dict = dict.fromkeys(grain_ids)
for grain_id, grain in zip(grain_ids, grain_parameters):
    calibration_dict[grain_id] = {
        'inv_stretch': grain[6:].tolist(),
        'orientation': grain[:3].tolist(),
        'position': grain[3:6].tolist(),
    }

# write out
```

```
output_name = 'new_instrument.yml'
if overwrite_parfile:
    output_name = cfg.instrument.configuration
instr.write_config(filename=output_name,
                   calibration_dict=calibration_dict)
```